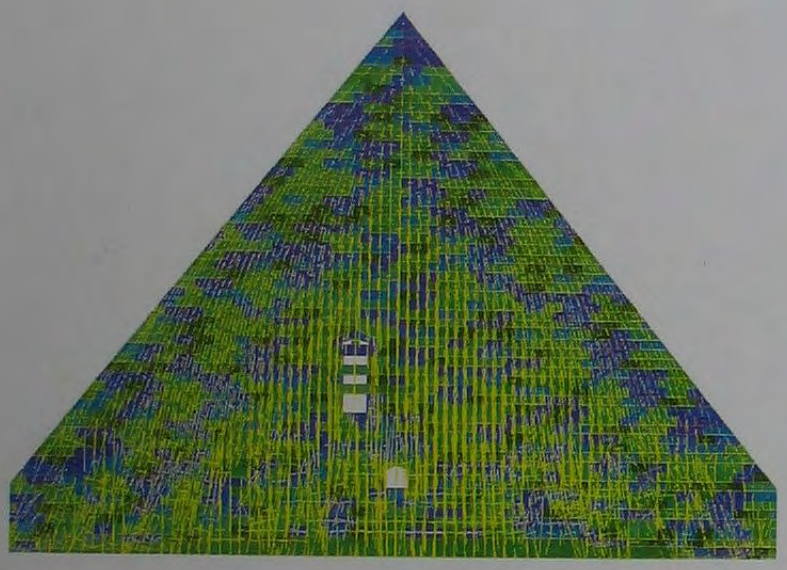
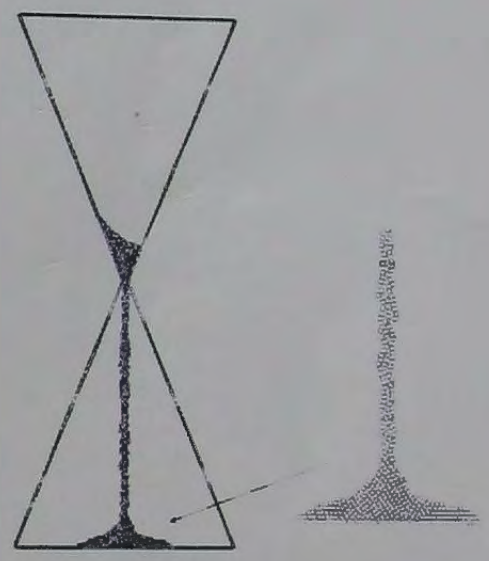
PROCEEDINGS OF

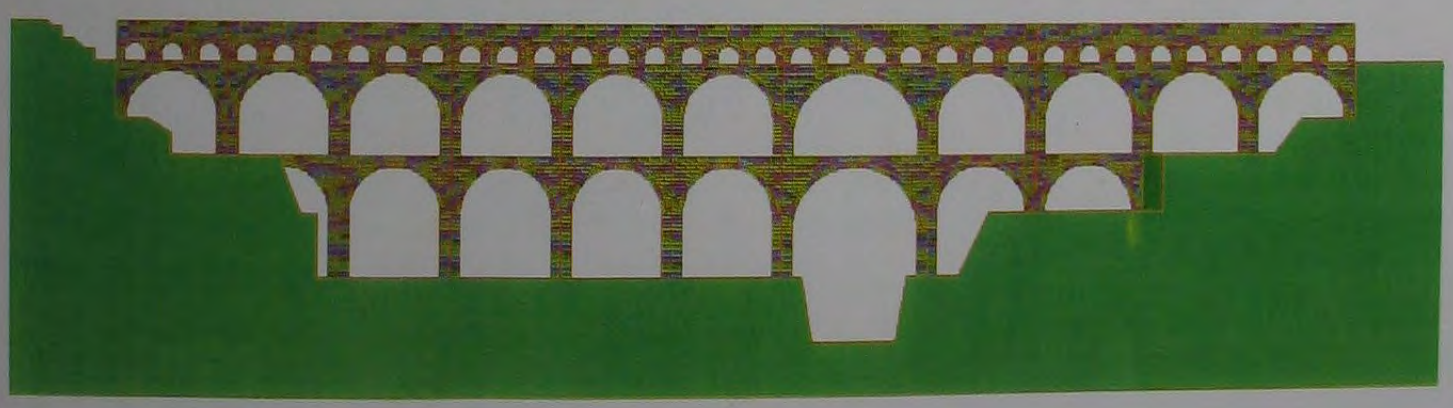
International Mini-Symposium for Numerical Discontinuous Analyses

- The 20th anniversary of Japanese society for discontinuous analyses-

November 21, 2008
Kona, *Hawaii*







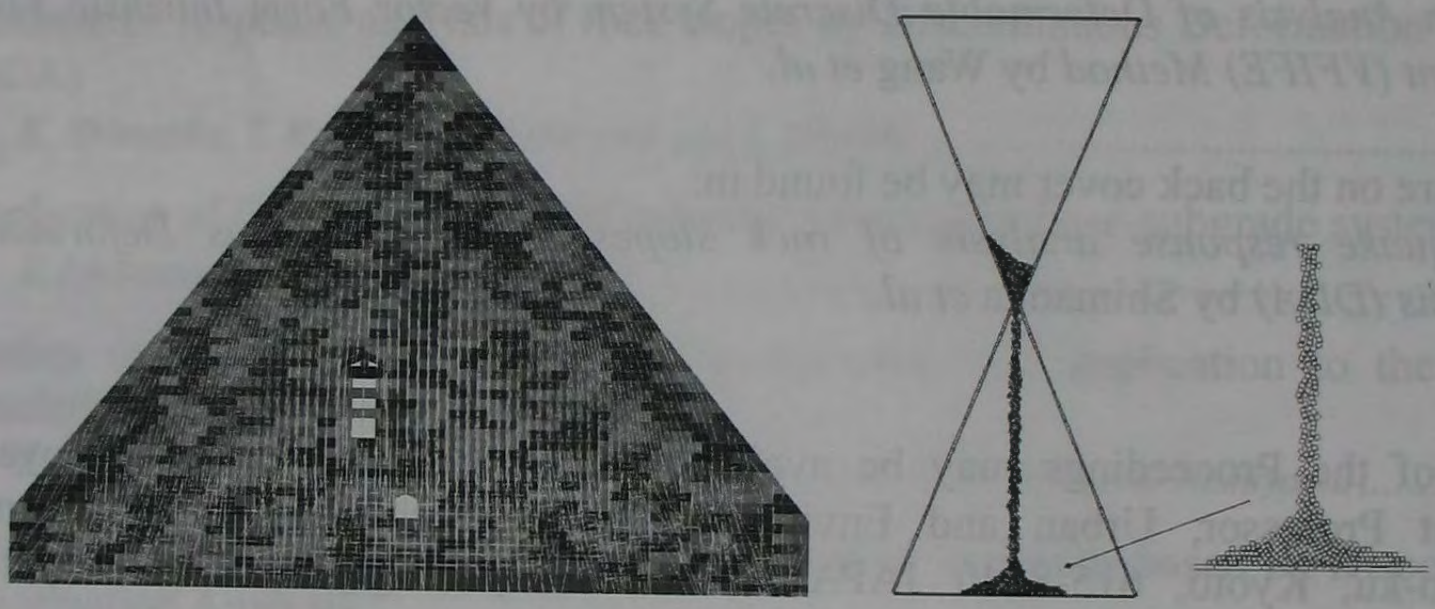
Proceedings Compiled & Edited by
Yuzo Ohnishi and Tomofumi Koyama, Kyoto University

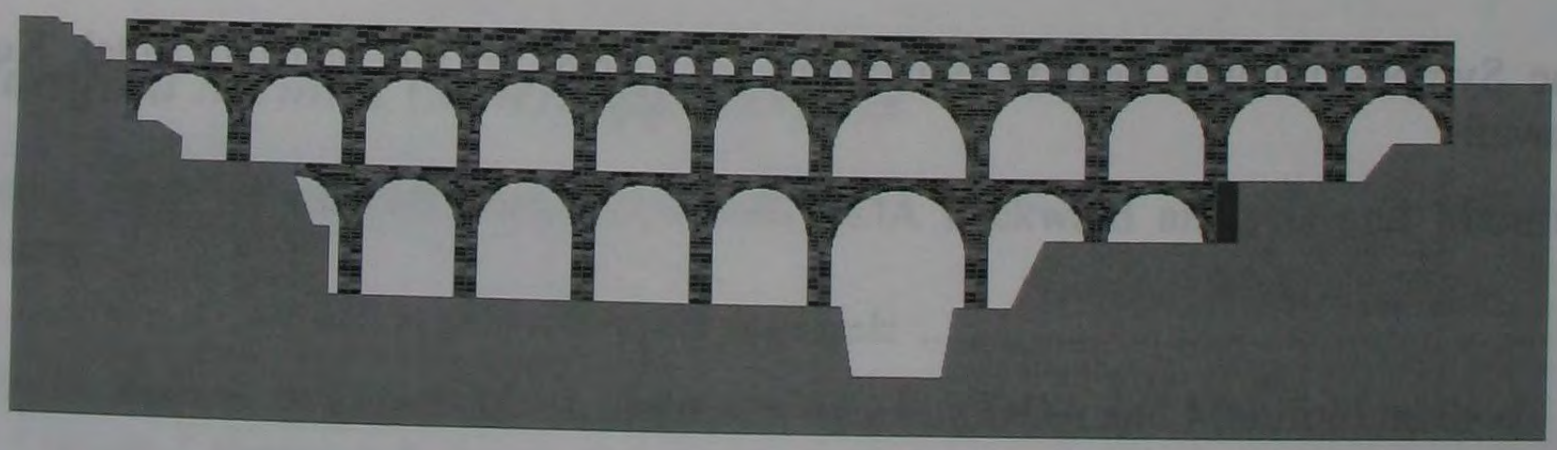
PROCEEDINGS OF

International Mini-Symposium for Numerical Discontinuous Analyses

- The 20th anniversary of Japanese society for discontinuous analyses-

November 21, 2008
Kona, *Hawaii*





Proceedings Compiled & Edited by
Yuzo Ohnishi and Tomofumi Koyama, Kyoto University

International Mini-Symposium for Numerical Discontinuous Analyses in Hawaii
Organizing Committee:
Yuzo Ohnishi, Kyoto University, *Conference Chair*
Gen-hua Shi, DDA Company, *Honorary Chair*
Tomofumi Koyama, Kyoto University, *Technical Program Chair*
Satoshi Nishiyama, Kyoto University
Sasaki Takeshi, SANCOH Consultant Co. Ltd.
Shigeru Miki, KISO-JIBAN Consultants Co. Ltd.

The organizing committee would like to express appreciation to the Japan Committee for ISRM, Japanese Society for Rock Engineering, West Japan Rock Engineering Research Society, Japan Society for Computational Science & Engineering and DDA Company for supporting *Int Mini-Symp for Numerical Discontinuous Analyses*.

The figures shown on the front cover may be found in the following papers:
Stability analysis of ancient block structures by using DDA and Manifold method by Sasaki *et al.*
Motion Analysis of Deformable Discrete System by Vector Form Intrinsic Finite Element (VFIFE) Method by Wang *et al.*

The figure on the back cover may be found in:
Earthquake response analysis of rock slopes by Discontinuous Deformation Analysis (DDA) by Shimaoka *et al.*

Copies of the Proceedings may be available by contacting Tomofumi Koyama, Assistant Professor, Urban and Environmental Engineering, Kyoto University, Nishikyo-ku, Kyoto, 615-8540 JAPAN (e-mail: koyama@geotech.kuciv.kyoto-u.ac.jp)

The Symposium was held in November, 21, 2008, on the Marriott Hotel, Kona, Hawaii



Table of Contents iii
Preface v

Keynote Lectures

The development of Analyses using discontinuous deformation methods: contact computations
Yuzo Ohnishi, Satoshi Nishiyama and Tomofumi Koyama 1

Cutting Joint Blocks and Block Analysis of Underground Excavation
Gen-hua Shi 11

Discontinuous Deformation Analysis (DDA), fundamentals and applications

Earthquake response analysis of rock slopes by Discontinuous Deformation Analysis (DDA)
K. Shimaoka, T. Koyama, S. Nishiyama and Y. Ohnishi 31

Application of DDA to mechanical behavior of granular base-subgrade system
T. Ishikawa, E. Sekine and Y. Ohnishi 41

Studies on the property of impact velocity ratio and application to the rockfall simulation by DDAball
T. Shimauchi, K. Nakamura, N. Sakai, I. Hagiwara, Y. Ohnishi and S. Nishiyama 53

Study on Prediction of flow movement of shallow landslide based on Discontinuous Deformation Analysis
N. Sakai, H. Ikei and S. Miki 63

Manifold Method (MM), applications

A case study of rockfall phenomena with DDA backward analysis and Manifold Method
T. Tobase, Z. Cao, T. Itou, H. Asaka and N. Kumazaki. 73

Stability analysis of ancient block structures by using DDA and Manifold method
T. Sasaki, I. Hagiwara, K. Sasaki, R. Yoshinaka Y. Ohnishi 83

Proceedings International Mini-Symposium for Numerical Discontinuous Analyses, edited by T. Koyama, Hawai, November, 2008

Other methods for discontinuous analyses and their applications

Motion Analysis of Deformable Discrete System by Vector Form Intrinsic Finite Element (VFIFE) Method
C. Y. Wang, S. H. Chen and R. Z. Wang 97

Motion Analysis of the Interaction among Discrete Solid Bodies and Multi-Phase Fluid
T. R. Wu, M. Cuang, C. J. Huang and C. Y. Wang 113

Stability analysis of reinforced slope by using hybrid-type penalty method
N. Takeuchi and M. Kusabuka 129

Development of simplified discrete limit analysis for three-dimensional slope stability problem
E, Hamasaki, N. Takeuchi and Y. Ohnishi 143

A Simulation Analysis of Loading Test on Two-layer Brickwork Arch Model by RBSM
N. Okano,Y. Shigeta, T. Matsunaga, K. Yasui and T. Asakura 161

Three-dimensional core picture system
T. Nakai, K. Ando, P. Bruines and Y. Ohnishi 165

Preface

International Mini-Symposium for Numerical Discontinuous Analyses in Hawaii

This volume contains the papers presented at the International Mini-Symposium for Numerical Discontinuous Analyses which was held at Waikoloa Beach Marriott Resort & Spa in Hawaii, on the 21st of November 2008. Over the past decades there have been very rapid developments of analysis and numerical approximations for discontinuous materials. To review the recent developments and to explore exciting new directions in this area, this conference was organized around certain topics of current interest. The aim of this conference was to bring together active scientists and engineers working on analyses using discontinuous methods in physics and engineering, and to provide a forum so that they would meet and exchange ideas in a stimulating environment.

We are grateful to the contributors, who worked very hard to meet the deadlines and resent this quality special issue to the reader now. We hope that the resulting special issue will be useful to this research community and will introduce these fascinating problems to outsiders whose interest and effort may in turn contribute in the field. We were delighted that Dr. Gen-hua Shi responded positively to our proposal and that this collection of contributions has therefore appeared here in this conference. Here, we wish to express our heartfelt thanks to Dr. Sasaki, Dr. Miki, and Dr. Koyama. We hope that you will find many articles of interest to you in this special issue.

Yuzo Ohnishi
Kyoto University
October 15

Proceedings of International Mini-Symposium for Numerical Discontinuous Analyses, edited by T. Koyama, Hawaii, November, 2008

The Development of Analyses using Discontinuous Deformation Methods: contact computations

Yuzo Ohnishi, Satoshi Nishiyama and Tomofumi Koyama
School of Urban & Environment Engineering, Kyoto University, Kyoto, 615-8540, JAPAN

ABSTRACT: DDA can compute the contact forces when blocks contact each other. Specific parameters such as normal contact spring and time increment etc. are employed to consider good performance of contact behaviors. These specific parameters are the most difficult part to be decided in analysis. The problems with lots of blocks and complicated contacts can be very sensitive to these parameters. Bad parameter selections can cause poor computation results. In this paper, we will focus on explaining the meaning of these parameters and discussing the setting of this contact parameter.

1. SPECIFIC PARAMETERS IN DDA ANALYSIS

The contact parameters are very important but difficult to obtained optimal values during computations. In this analysis, some problems can happen when solving large span problems composing small blocks. The vibrations of small block stress occur, and if the stiff contact spring is introduced to the analysis, the vibration does not converge. When the static analysis is used to avoid the effect of gravity turn-on, the vibrations can be neglected during static computation. However, the blocks start to vibrate again when the full dynamic analysis is introduced again. Two major methods to solve this problem are to employ more exact contact parameters and to choose softer contact spring. In this study, the stress distributions of discrete blocks in a box are investigated. Fig. 1 shows simulation geometric model used in this study. The stress of each block comes only from the overburden.

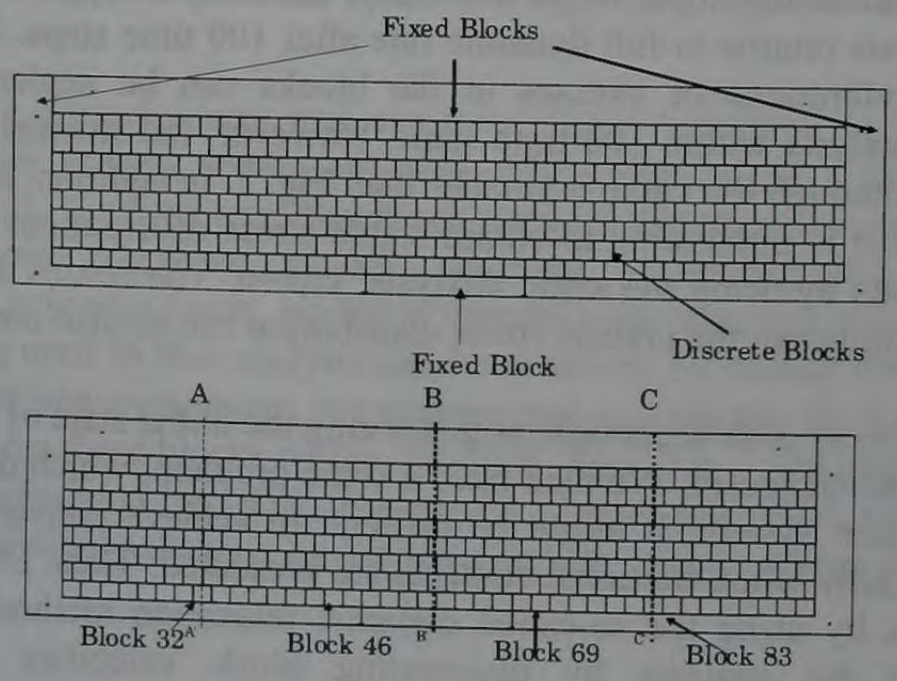


Fig.1 Illustration of Geometric Model for Parameter Studies

The Young's modulus of blocks is 62 MPa, and the Poisson's ratio equals to 0.2. The joints have properties with the frictional angle equal to 20°. No cohesion and no tensile strength are considered for the joints. In addition, some DDA analysis parameters, including displacement allowed ratio and maximum time increment, are also shown in Table 1.
DDA needs contact spring stiffness to calculate contacts, however, it is very sensitive to the computations. In this simulatuion, the proper contact spring stiffness is studied to obtain correct stress distributions in Fig. 2. In this case, external forces come from the overburden and contacts among blocks. The vertical stress changes of block 32, 46, 69, and 83 at each time step are used as an index to check proper contact spring stiffness for the analysis. Fig. 3 presents the results with contact spring stiffness up to 2 times of block Young's modulus.

Table 1 Parameters for the DDA Simulation

Item		*Value*
DDA Analysis Parameters	Displacement Allowed Ratio	0.01
	Maximum Time Increment (sec)	0.001
Blocks	Unit Weight (kN/m^3)	26.4
	Poisson's Ratio	0.2
	Young's Modulus (MPa)	62
Discontinuity	Frictional Angle (°)	20.0
	Cohesion (MPa)	0.0
	Tensile Strength (MPa)	0.0

The sudden turn-on of gravity at the beginning of the first time step produces displacements due to elastic deformation of the blocks and "seating" of the contacts. Although these displacements are very small, they lead to propagation of initial block velocities and accelerations and affect the generations of initial stress distributions. In this study, the static analysis is introduced before 100 time steps. The analysis returns to full dynamic one after 100 time steps. With this method, it is considered that the vibrations of stresses in the blocks can be neglected. Fig.3 shows the efficiency of static analysis within 100 time steps. However, the stresses of blocks still vibrate after 100 time steps although the value is smaller than Fig. 2. In addition, the vibrations of blocks do not converge, and it is impossible to obtain stable stress distributions by this method. Fig.4 shows the DDA results by using the static analysis, k01=0. The results show that although the stress vibration is diminished, the precise stress distribution can be also obtained hardly with stiff contact spring.
If the deformation process is slow enough, as generating the initial state of rock masses, the effect of inertia forces can be neglected. We then have a static problem, which demands the solution of a simultaneous equation system. It might be difficult to achieve convergence in general non-linear analysis, especially when frictional contacts are presented. Thus, DDA is made to analyze quasi-static problems by using the so-called dynamic relaxation method. DDA introduces the damping effects to the analysis by discounting block velocities for each time step. Mathematically it can be shown as equation (1):

$$V_i^{(n+1)} = k01 \cdot V_f^{(n)} \tag{1}$$

Where, "$V_i^{(n+1)}$" is the initial velocity at time step n+1. "k01" is the Type of Analysis parameter, and "$V_f^{(n)}$" indicates the final velocity at time step n.
In the full dynamic analysis, the initial velocities of blocks at time step n+1 are acceded from the final velocities of step n. In DDA, a value of 1 is entered to k01 for a full dynamic analysis and a value of 0 for static analysis. Certainly, a value for k01 of between 0 and 1 can be entered. The value corresponds to different degrees of damping or energy dissipation.
To obtain the stable stress distributions of the discrete blocks, it is necessary to investigate the reason to cause stress vibrations during calculations. It is found that the discrete block is relative small compared to the span of the model. The contact computations and the model span are related.

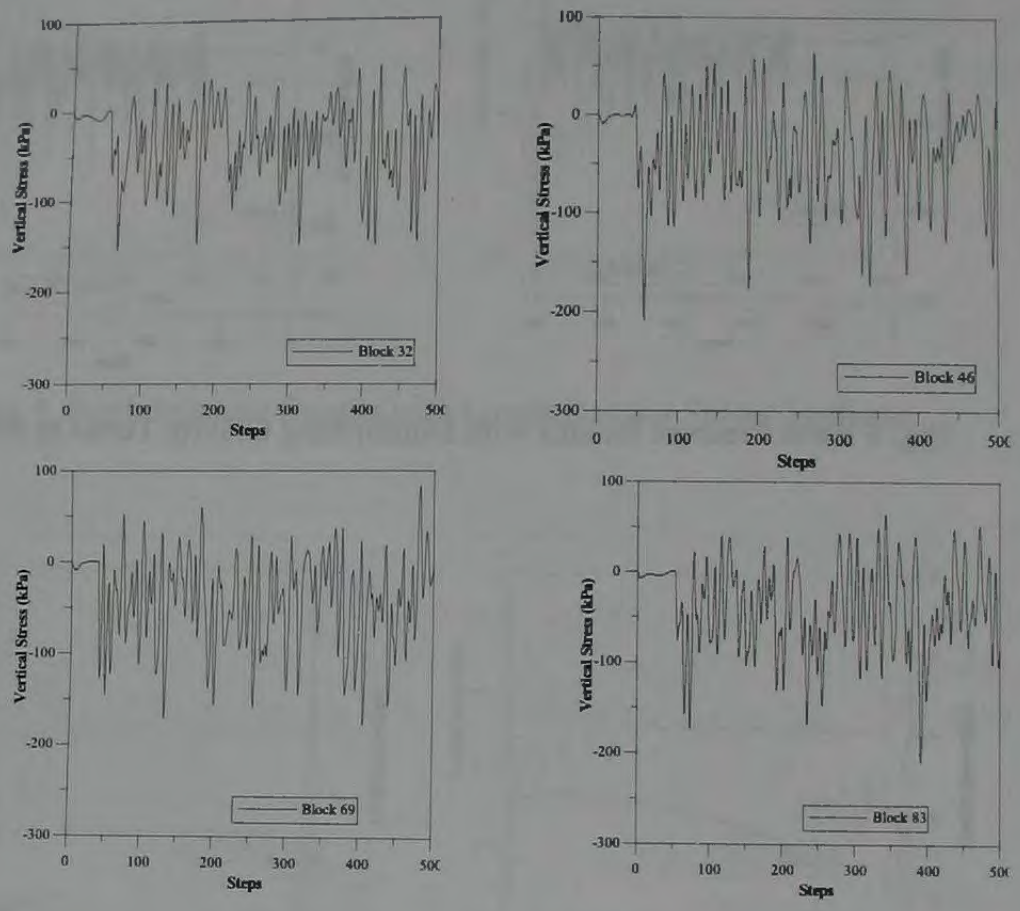


Fig. 2 Earth Pressure Results with High Contact Spring Stiffnes

To diminish exceeding contact forces and unwanted stress vibrations in Fig. 2 and Fig.3, the author introduced lower contact spring stiffness, 620 kN/m (about 1/100 of block Young's modulus), to the analysis. Fig.5 presents that block stresses converge to a constant in the analysis, however, some unwanted vibrations are still observed. To neglect the effects of unwanted vibrations and make it converge faster, we try to introduce the damping effect is introduced to the analysis. The damping used in this analysis can be achieved by setting the analysis type index, k01, as 0.99. With these new parameters, the stresses tend to converge to -5 kPa in Fig.6, which is the analytical solution for these blocks within 200 time steps. Fig.7 illustrates the stresses change accompany to depth calculated by DDA. The results present that DDA simulation results have good agreement to analytical solutions by introducing new contact spring stiffness and damping to the analysis.

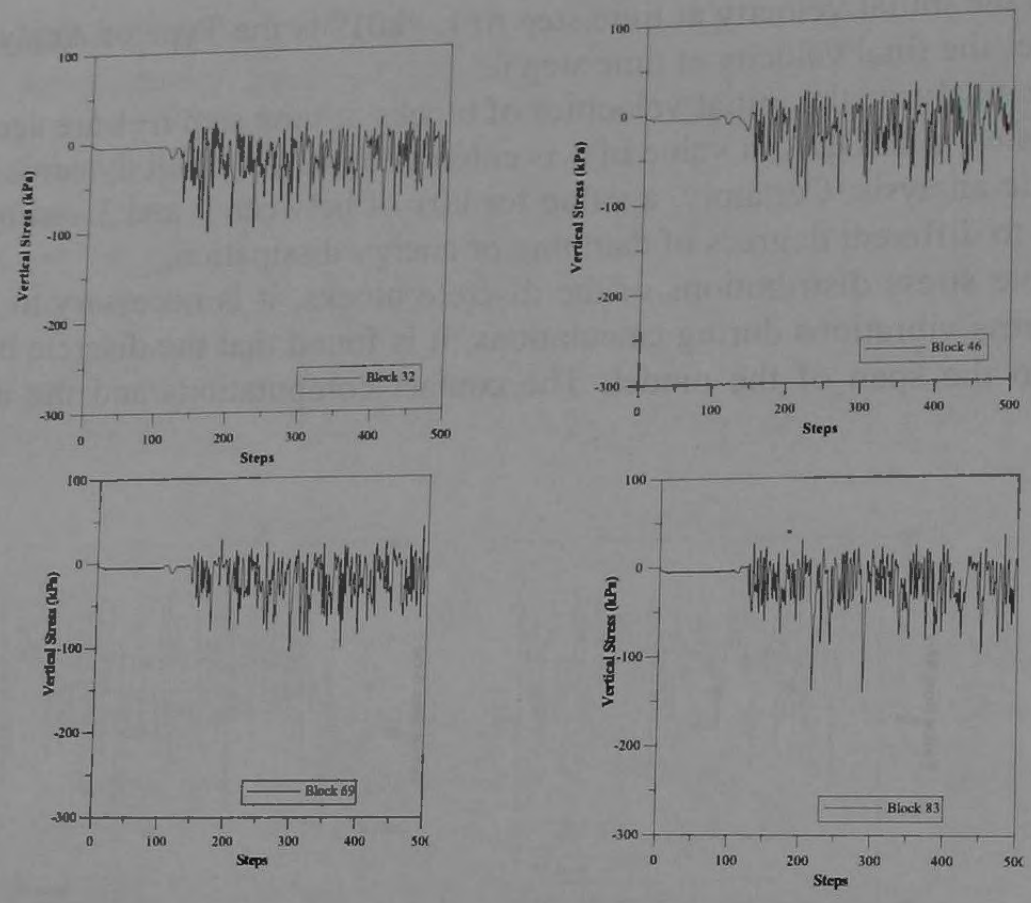


Fig. 3 Earth Pressure Results with Diminishing Gravity Turn-On Effects

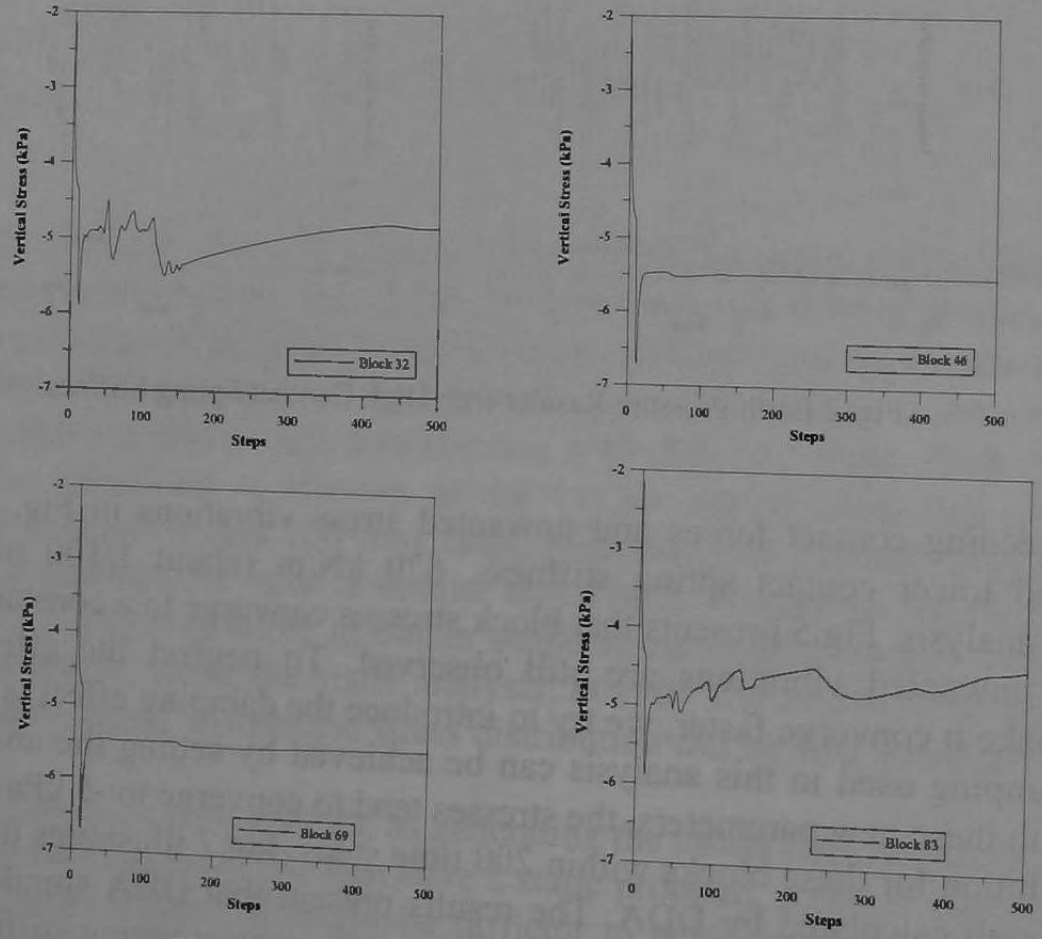


Fig. 4 Earth Pressure Results with Static Analysis

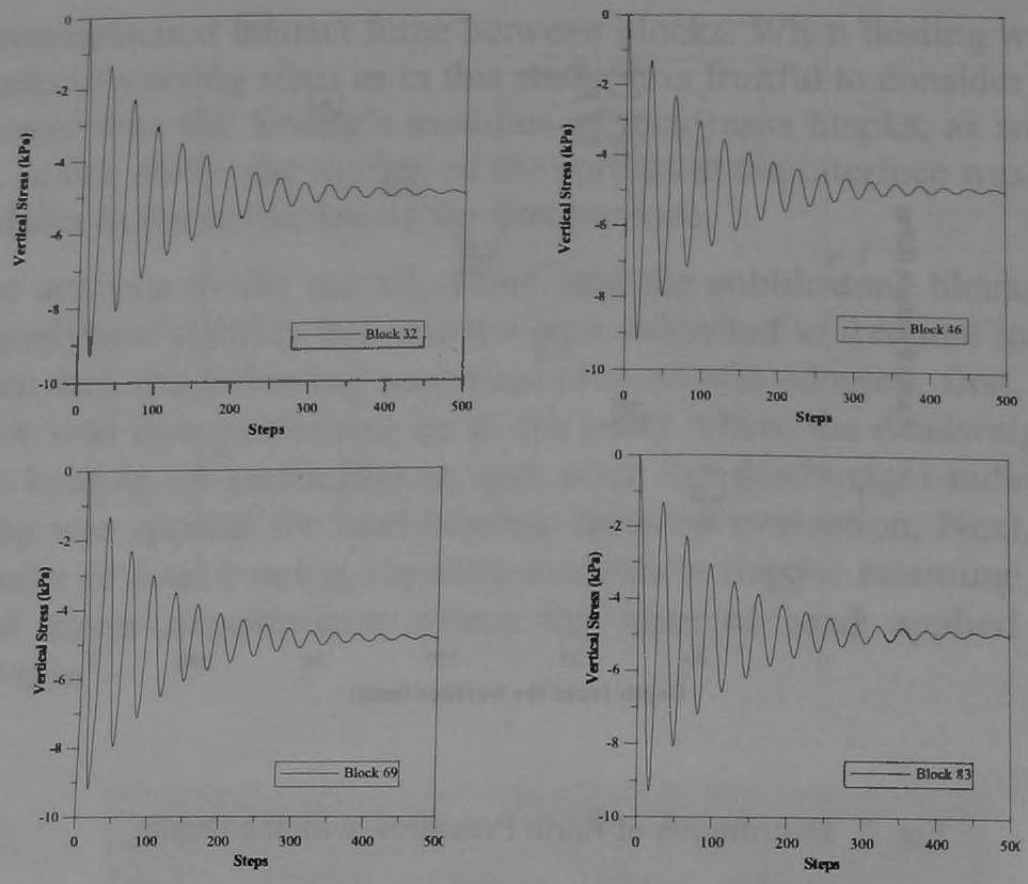


Fig. 5 Earth Pressure Results with Lower Contact Spring Stiffness

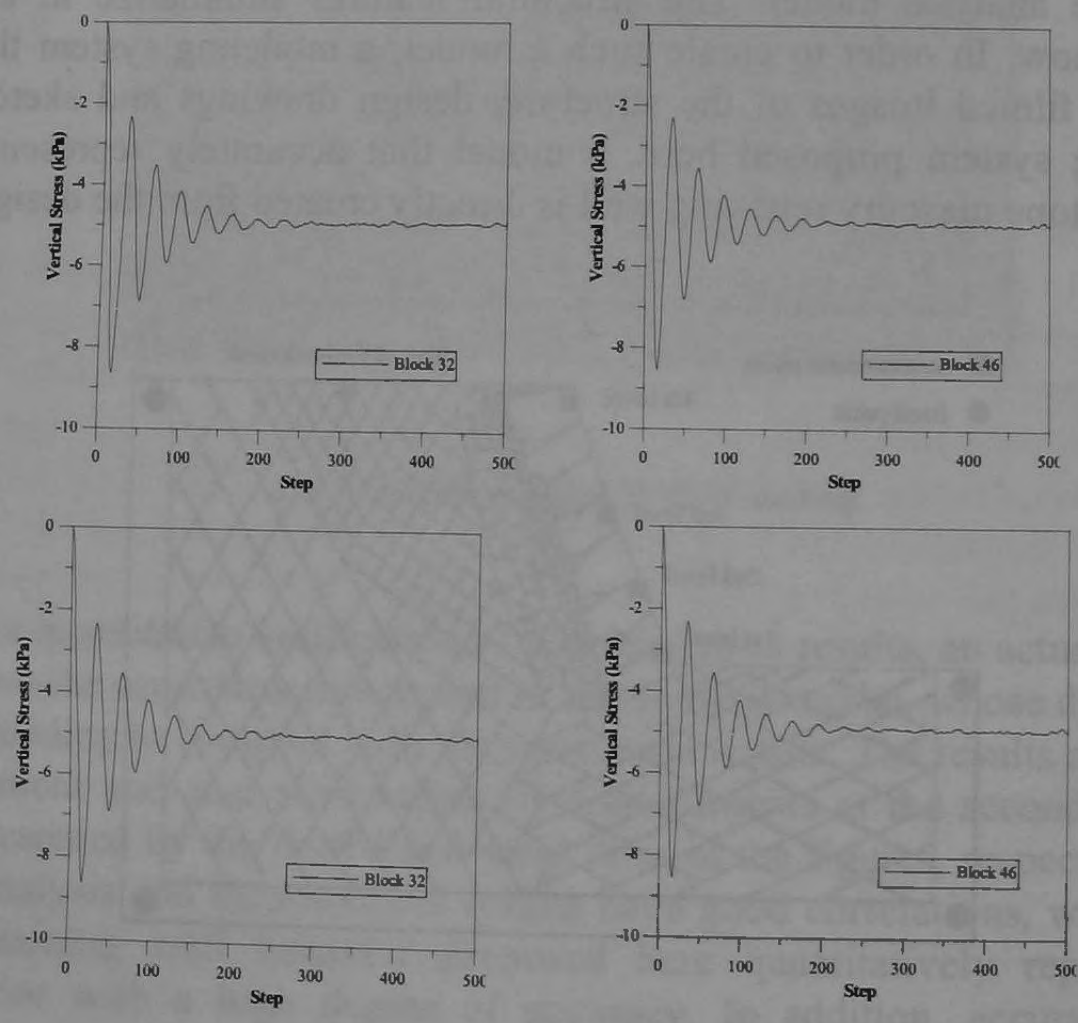


Fig.6 Earth Pressure Results with Lower Contact Spring Stiffness and Damping

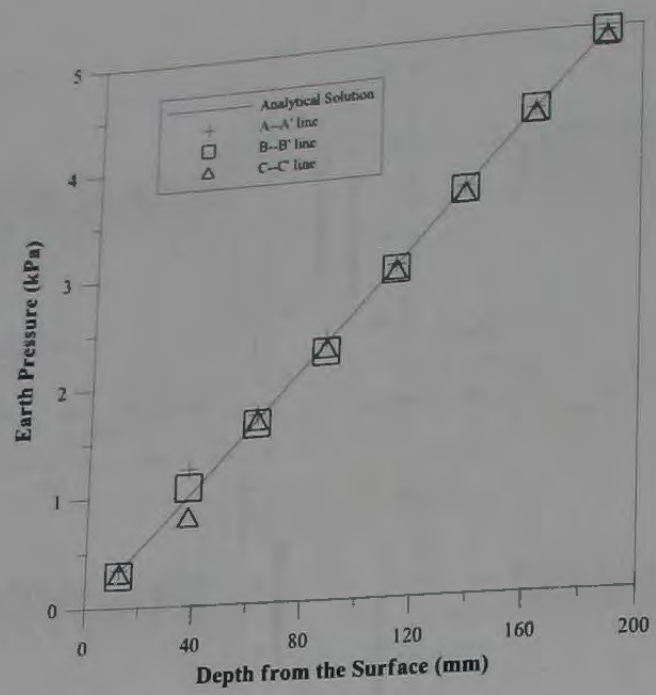


Fig. 7 Distribution of Earth Pressures with the Depth

2. NUMERICAL EXAMPLE

Figure 8 shows the analysis model. The structural features summarize in a way stonewall construction know-how. In order to create such a model, a modeling system that allows direct modeling based on filmed images of the structure, design drawings and sketches is required. Using the modeling system proposed here, a model that accurately represents the structural characteristics of a stone masonry retaining wall is directly created from the design drawings.

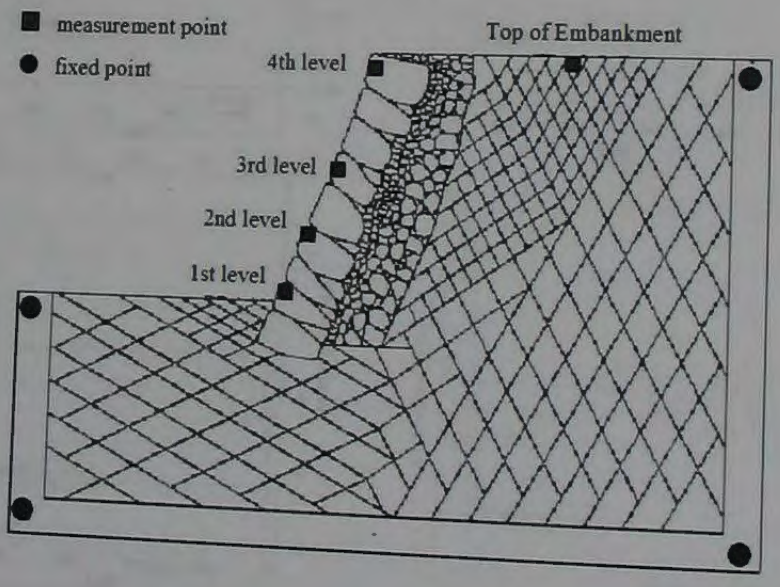


Fig.8 Analytical model produced

When blocks are in contact with each other in DDA, springs are applied and the contact condition is computed repeatedly until the blocks are free from mutual penetration and tension. Generally, the applied springs have rigidity larger than the Young's modulus of contiguous rock mass blocks. However, when dealing with models composed of numerous complex blocks like the cobblestones in this analysis, it is difficult to define parameters to control the vibration of blocks

because of the overestimated contact force between blocks. When dealing with models composed of numerous blocks of varying sizes as in this study, it is fruitful to consider applying soft springs with a rigidity lower than the Young's modulus of rock mass blocks, as an attempt to solve the above problems. In this study, the rigidity of the springs at the interface was set at 15 MN/m, half the Young's modulus in the embankment for this purpose.

The blocks in the analysis model are all elastic, and the cobblestone blocks in particular have a large impact on analytical stability because they are subjected to frequent individual rotation, slip and contact. Given this, the following analytical process was adopted: first, only deadweight was input; computation was then performed up to the point where the deadweight ceased to have an effect before the loading of embankment; and after the deadweight-induced deformation was controlled, loading was applied for load-bearing capacity evaluation. Next, in order to illustrate the analytical results of load-bearing capacity evaluation for the retaining wall, Figure 9 shows deformations and stress distributions where the size of load applied to the ground was approximately 55 tf/m^2.

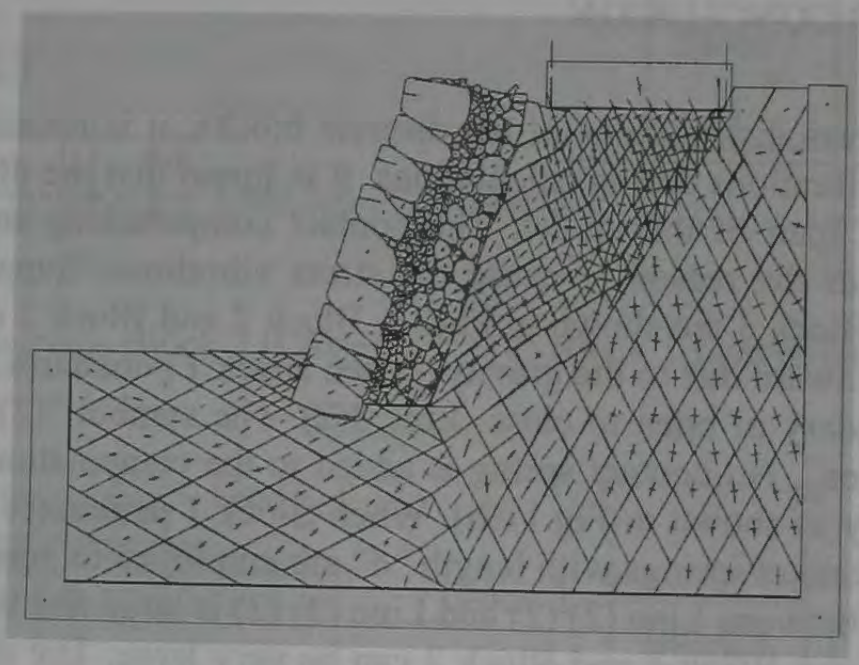


Fig.9 Condition under 55 tf/㎡ loading

In order to make a quantitative verification of the simulation results, an actual retaining wall was constructed to have the same structure as that of the analysis model, whose deformation was then measured under loading to compare with the simulation results. The results are shown in Figures 10. The measurement and analytical values of displacements at the second and third levels in Figure 8 are represented by the dotted and solid lines in the figures, respectively. According to the figures, the analysis and measurement results have good correlations, which proves that the simulation of retaining wall behavior proposed here quantitatively reproduced the actual structure's behavior with a high degree of accuracy. In addition, accurately simulating the behavior of each stone enables the identification of load value causing the bulging of stonewall. This further allows prediction of the load value that affects the stability of the structure. Based on these results, it is shown that through DDA, an analytical technique that allows the specific examination of various design parameters, such as those related to the embankment height, has successfully been established.

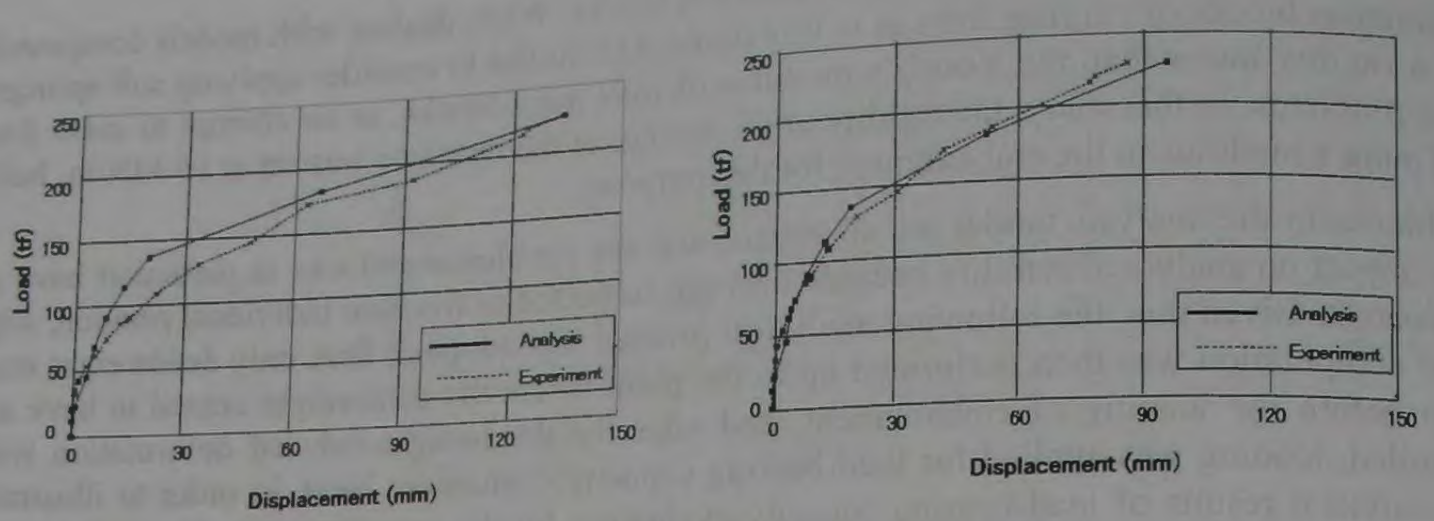
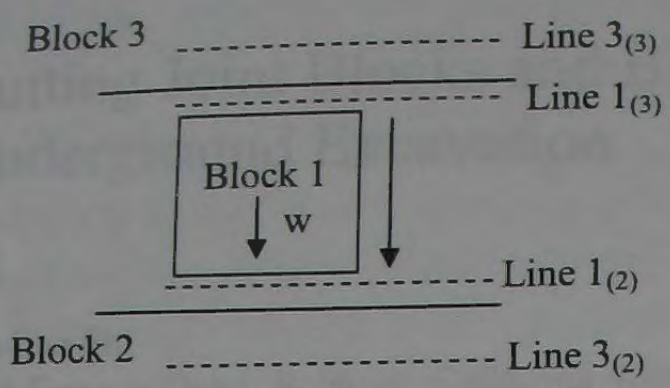


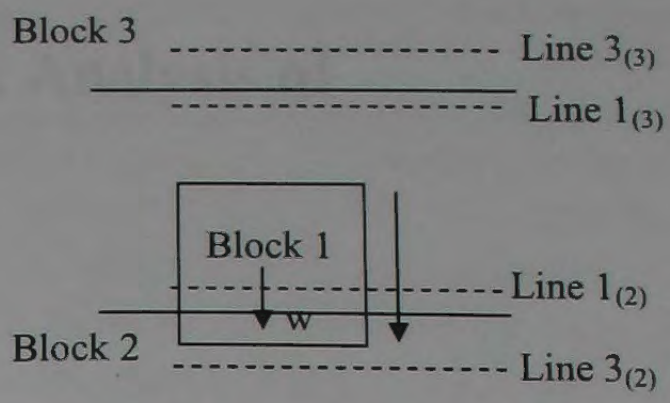
Fig.10 Load-displacement curves for 2nd level and 3rd level

3. DISCUSSION AND CONCLUSION

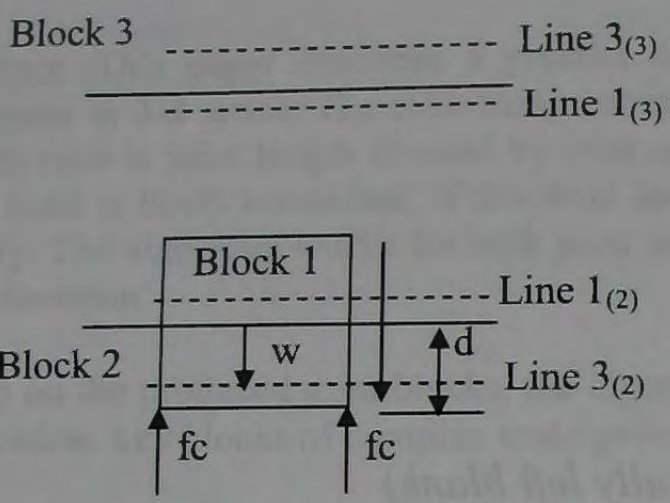
To obtain the stable stress distributions of the discrete blocks, it is necessary to investigate the reason to cause stress vibrations during calculations. It is found that the discrete block is relative small compared to the span of the model. The contact computations and the model span are related. Fig.11 illustrates the reason to cause the stress vibrations. Supposing the locations of Block 1, Block 2, and Block 3 are shown in Fig.11. Block 2 and Block 3 are fixed. Block 1 with weight "w" moves downward due to the gravity. When Block 1 penetrates an edge of Block 2 but locates above the boundary of open to close, Line 3(2). The symbol "(2)" means Block 2. It is still considered as "Open". No contact spring is added to the computations, and Block 1 moves downward continuously as shown in Fig.11(b). When Block 1 penetrates Line 3(2) presented in Fig.11(c), the normal contact springs with length "d" are employed to generate contact forces, fc, upward. When the gap between Line (2) (2) and Line (3) (2) is large and the contact spring is stiff, the contact forces between Block 1 and Block 2 can be very large. The contact forces are larger than the weight of discrete block and drive it moving upward if Block 1 is small or light. When the vertex moves upward to the position between Line (1) (2) and Line (2) (2), the tension can be produced to Block 1 shown in Fig.11(d). After Bock 1 moves above Line (1) (2), the contact is judged as "Open", and the contact spring is deleted. When Block 1 moves upward continuously and hits Block 3 above. The contact sequence mentioned above is done again. Finally, the block stresses vibrate as above mentioned. When DDA is applied to produce highly accurate static and dynamic analyses, the influences of the Criteria of Opening and Criteria of Open-Close to the contacts should be considered.



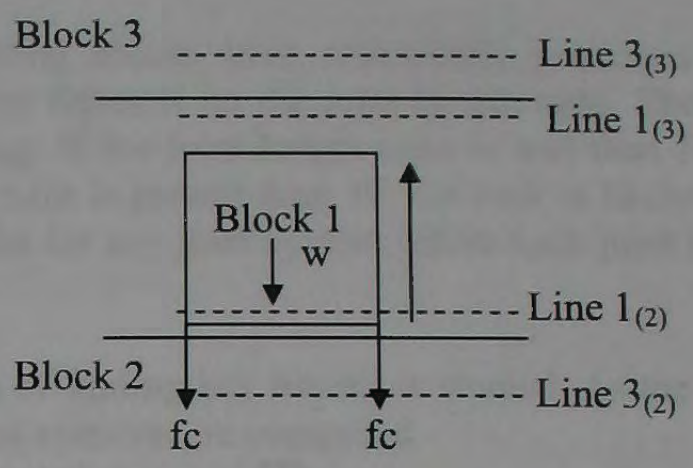
(a) Initial State (Open)



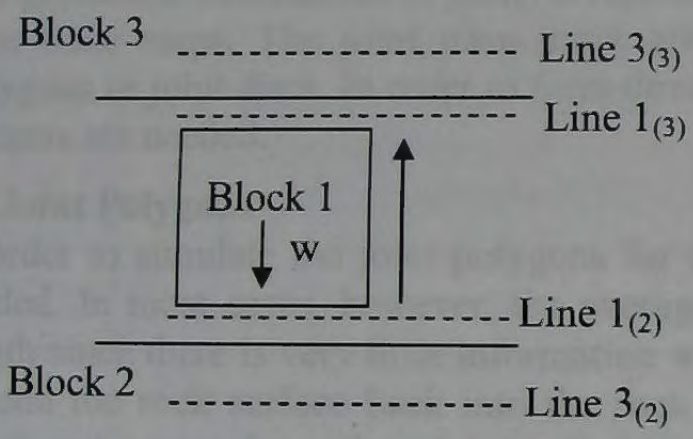
(b) Block 1 Penetrates Block 2 (Open)



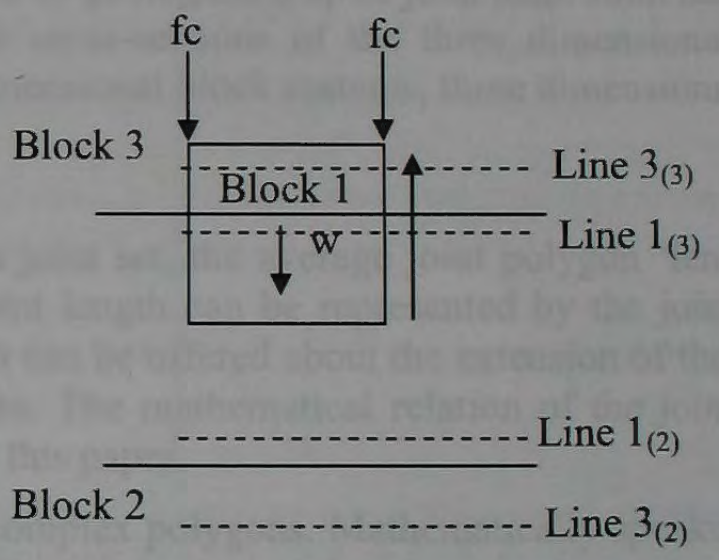
(c) Block 1 Penetrates Block 2 (Close)



(d) Block 1 Leaves Block 2 (Close)



(e) Block 1 Leaves Block 2 (Open)



(f) Block 1 Penetrates Block 3 (Close)

Fig.11 Illustrations of the Reason to Cause Stresses Vibrations

References

1. WU, J.H. 2003. Doctoral Dissertation. Kyoto University.

Proceedings of International Mini-Symposium for Numerical Discontinuous Analyses, edited by T. Koyama, Hawaii, November, 2008

Cutting Joint Blocks and Block Analysis of Underground Excavation

Gen-hua Shi
1746 Terrace Drive, Belmont, California 94002

Abstract :This paper describes a process of cutting blocks from statistically generated joint polygons in 3-d space. The rock mass connectivity depends on the joint length ratio. The joint length ratio is joint length divided by joint spacing. If the joint length ratio is less than 10, the rock mass is likely connected; if this joint length ratio is greater than 10, the rock is likely to be blocky. The algorithm works for both joint sets and for any joint system where each joint has its own direction.

Based on the produced joint blocks, the algorithm of finding key blocks is studied. As the direct application, key blocks of complex underground excavations are computed.

1. THREE DIMENSIONAL JOINTS

The geometric information of joints is represented by geological map or joint map. Joint maps are joint trace maps. The joint trace maps are the cross-sections of the three dimensional joint polygons or joint discs. In order to form three dimensional block systems, three dimensional joint systems are needed.

(1) Joint Polygons

In order to simulate the joint polygons for each joint set, the average joint polygon 'length' is needed. In most cases, however, the average joint length can be represented by the joint trace length since there is very little information which can be offered about the extension of the joints beyond the rock surface back into the rock mass. The mathematical relation of the joint trace length and joint polygon length is studied here in this paper.

The real shapes of three dimensional joints are complex polygons. Mathematically speaking any complex shape can be represented by polygons. The joint polygons may be complex and variable. However, very limited information can be given about the joint polygon shapes from joint trace maps. The joint polygons are often to be simplified as discs with different diameters, different locations and different directions. This is a popular choice.

(2) Representation of Joint Polygons

Assume the horizontal tectonic force is the main factor of forming the rock fractures. In this paper, the joint polygons are simplified as squares where the edges are parallel to joint dip direction and joint strike direction respectively.

However, using the joint squares to compute blocks, the joint squares are divided to triangles. The actual input joint shapes of this block computation code are triangle combinations or general polygons. Therefore the joint squares can be change to joint polygons if more joint shape

information can be obtain in the future. The block computation code still works without any modification.

(3) Joint Trace Length and Joint Disc Diameter

The simplest representation of a joint in 3-D is a disc. Denote the average joint trace length of a joint set as L_{tr}. Denote the joint disc diameter as D. The edge length of the circumscribed square of joint disc is D. The average length L_{tr} of joint traces is equal to the area of the joint disc divided by edge length of circumscribed square D. (See Figure 1)

$$L_{tr} = \pi (D/2)^2 / D = (\pi/4) D$$

$$D = (4/\pi) L_{tr} = 1.2732 L_{tr}$$

(4) Joint Trace Length and Square Edge Length of Joints

Another simplest representation of a joint in 3-D is a square. Denote the average joint trace length of a joint set as L_{tr}. Denote the edge length of joint squares as E. Denote the angle of section line and square edge as α.

A circumscribed square of the joint square with edge E will contain the joint square. All of four nodes of the joint square are in the four edges of the circumscribed square. The circumscribed square with two edges parallel to the section line has edge length C: (See Figure 2)

$$C = (\sin\alpha + \cos\alpha) E$$

The average length L_{tr} of joint traces equal to the joint square area divided by the edge length of the circumscribed square C:

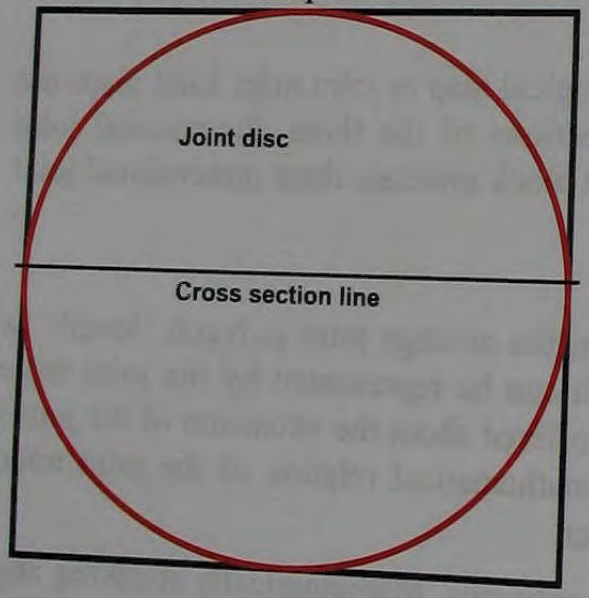


Fig. 1 Joint disc and cross section line

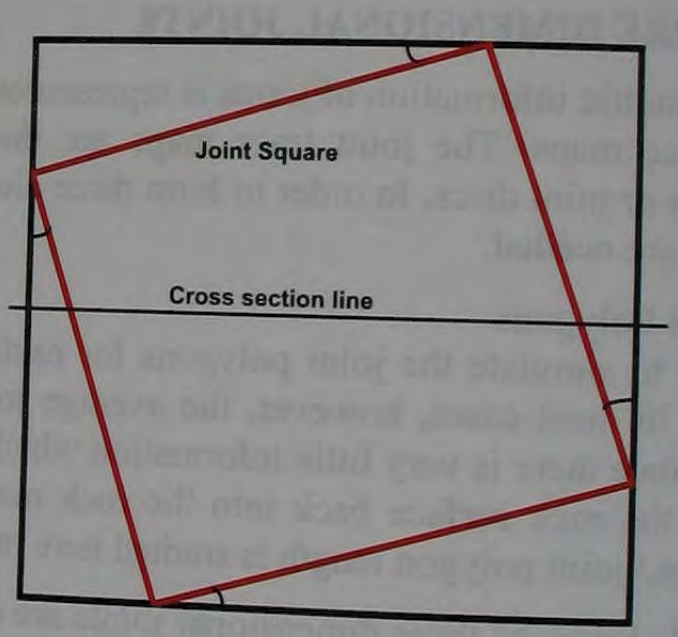


Fig. 2 Joint square and cross section line

$$L_{tr} = E^2 / C = E^2 / ((\sin\alpha + \cos\alpha) E)$$

$$L_{tr} = E / (\sin\alpha + \cos\alpha)$$

$$E = (\sin\alpha + \cos\alpha) L_{tr}$$

Compute average square edge length E_{av} over the angle α

$$E_{av} = \left(\int_0^{\pi/2} E d\alpha \right) / (\pi/2)$$

$$E_{av} = \left(\int_0^{\pi/2} (\sin\alpha + \cos\alpha) L_{tr} d\alpha \right) / (\pi/2)$$

$$E_{av} = (4/\pi) L_{tr} = 1.2732 L_{tr}$$

It is seems a wonderful coincident that the formulae for disc diameter D and square edge E_{av} are exactly the same. Theoretically, the edge length E_{av} of joint squares is 1.2732 times of the average joint trace length. Again, the joint trace is the intersection line segment of a joint square with the section plane. Therefore, the three dimensional joint polygon is longer than its joint traces.

(5) Joint Trace Spacing and Joint Plane Spacing

Joint plane spacing is measured along the joint plane normal direction. Joint plane spacing is the distance of two parallel joint planes. In any section plane, the joint trace spacing is generally larger than the joint plane spacing. The joint trace spacing is different in different section plane directions. The joint spacing should be the joint plane spacing in the direction perpendicular to the joint plane. Therefore, the joint spacing is independent of the directions of the section plane.
Denote the joint plane spacing as S_{3d}

Denote the joint trace spacing as S_{tr}

Denote the angle between the upward normal of joint plane and section plane as β

The mathematical relation of S_{3d} and S_{tr} is:

$$S_{3d} = S_{tr} \sin\beta$$

2. CUTTING 3-D BLOCKS FROM JOINT POLYGONS

(1) What Kind of Three-Dimensional Blocks the Joint Polygons Can Possibly to Produce

To determine the joint blocks, all joint sets must be simulated or the individual joint polygons must be input. The produced joint polygons of all joint sets, all input joint polygons and all boundary faces are the input data for the three dimensional DDA cutting program DC. Figure 3 shows statistically produced joint polygons of four joint sets.

The cutting program DC computes 3-d blocks. Figure 4 to Figure 9 show a portion of produced three dimensional blocks.

If the individual joints are all much longer compare with the dimension of the target block, all intersected blocks are convex block. In this case, the blocks are simple and the computation, the algorithm and the related theory are all simple.

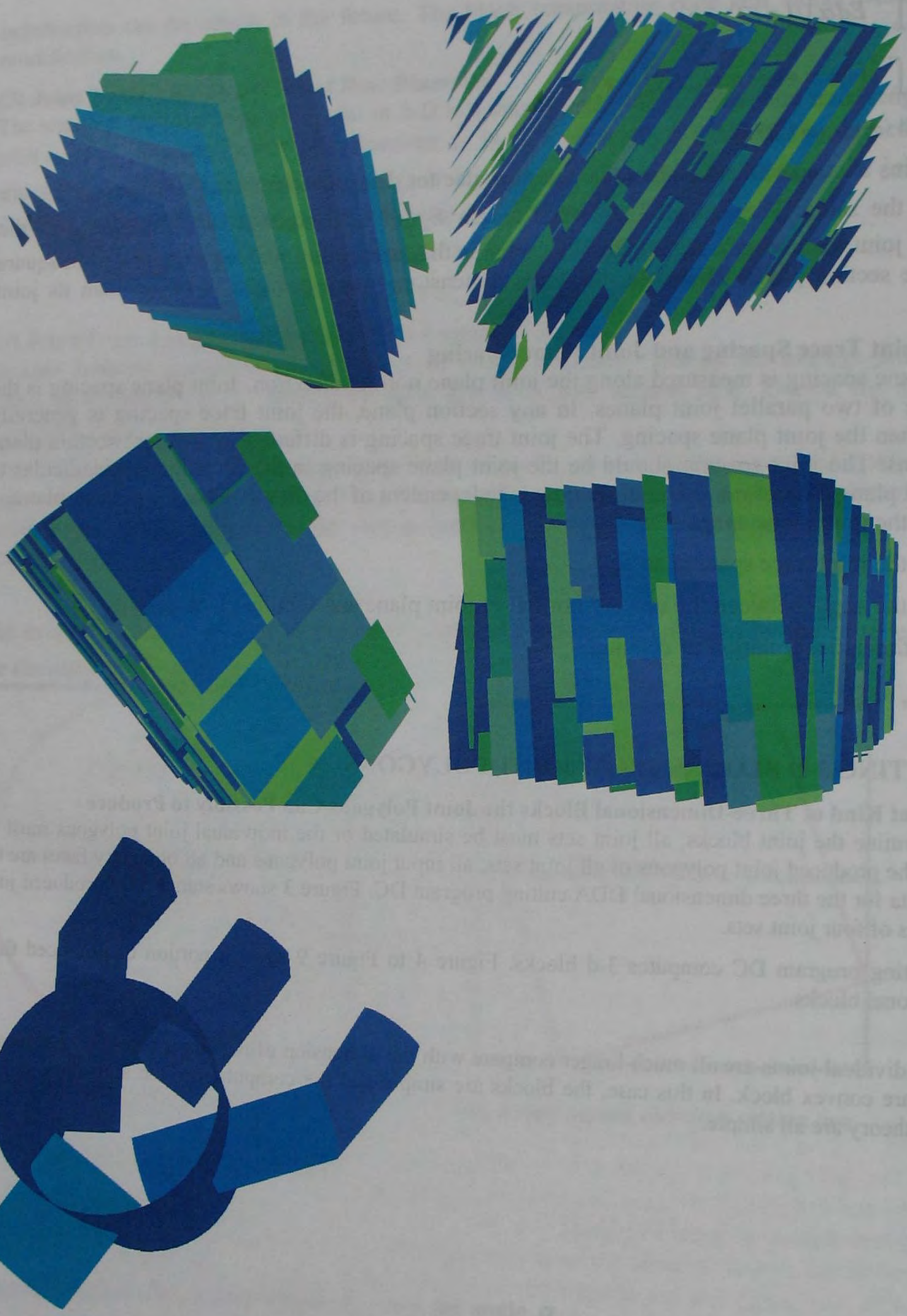


Fig. 3 Statistically produced joint polygons of four joint set and tunnel surfaces

However, if the joint polygons are shorter than the diameter of the target block, the joint polygons are terminated in the middle of the target block. In the later case, the computation, the algorithm and the

related theory could be substantially complex. Also, the produced blocks could be complex in the following ways:

- The blocks can be concave
- The polygon faces of the blocks can be concave
- The number of polygon faces of one block can be unusually large
- Inside a block there can have other smaller blocks which are sub-blocks
- Inside a block, the sub-block can contain its own sub-blocks
- The blocks can have through holes such as a ring
- Inside a block, the sub-blocks and holes can be connected in points or edges
- As block faces, a polygon can contain other polygons which are sub-polygons
- Inside a polygon, a sub-polygon can contain its own sub-polygons

(2) The Differences from the Other Three-Dimensional Block Producing Methods

Most block cutting codes produce convex blocks. It is assumed that the joint polygons are long enough to cut through the target block.

DC in itself is a block cutting code. DC uses polygons to cut blocks. These polygons can be of any length. The input polygons of DC can terminate in the middle of the target block. The produced blocks can be of any shape: convex, concave or blocks with bubble and holes.

(3) The Self-Checking of the Three-Dimensional Block Cutting Code

Self-checking of the block cutting code DC is important for both programmer and user. Also the three-dimensional graphic can directly see the polygons and the produced blocks. If there are only few polygons, the results of DC code can be checked intuitively. For large number blocks, the major checks of DC code are:

Two-dimensional topological check: for any formed polygon P_i double boundary operation is zero.

$$\partial\partial P_i = 0$$

Three-dimensional topological check: for any formed block B_i double boundary operation is zero and the sum of all block boundaries are the boundary of the target block T.

$$\partial\partial B_i = 0$$

$$\sum_i \partial B_i = \partial T$$

Bock volume summation check: the summation of the block volumes $V(B_i)$ should equal to the volume $V(T)$ of the target block.

$$\sum_i V(B_i) = V(T)$$

The volume checking is a convincing examination. For example, if the target block is simply a cube and the six square faces of the cube are also the cutting polygons, the summation of the block volumes should equal to the cube volume.

3. JOINTED LENGTH RATIO

(1) Definition of Joint Length Ratio

Denote the average joint plane spacing of a joint set as S_{3d}. Denote the average joint trace length of a joint set as L_{tr}. Given S_{3d}, as the average joint trace length L_{tr} is longer, more blocks are formed. The joint length ratio R_{ls} is defined as:

$R_{ls} = L_{tr} / S_{3d}$

The joint length ratio R_{ls} will be the most important factor for forming blocks. The total volume and the number of the joint blocks will be the most important factor of the rock global stability.

(2) Joint Sets Information

The following are examples of joint set data for producing joint polygons by statistics.

Table 1 Joint set angle data

Joint set	Dip angle	Dip direction
1	84°	221°
2	83°	299°
3	9°	59°

Table 2 Joint spacing and joint trace length data

Joint set	Spacing S_{3d}	Length L_{tr}	Bridge
1	0.60 m	2.54m	0.10m
2	1.92m	2.71m	0.10m
3	0.59m	3.23m	0.10m

(3) Joint Length Ratio and Global Rock Stability

In the next two sections, four cases with different edge lengths of joint squares are studied. Here E_{av} is the edge length of the produced joint square. Table 3 shows the results of the computation of the following two sections.

Table 3 Joint length ratio data

Case	Square Edge Length	Length Ratio R_{ls}	Volume of inner blocks
1	$E_{av} = 1.3L_{tr}$	4.82	2.54%
2	$E_{av} = 2.0L_{tr}$	7.84	12.24%
3	$E_{av} = 3.0L_{tr}$	11.11	44.54%
4	$E_{av} = 4.0L_{tr}$	14.83	65.06%

These results provide valuable guidelines for the type of analysis required for excavations.

4. JOINTED AND CONNECTED ROCK MASSES

(1) Connected Rock Masses

When $R_{ls} < 10$, the majority of the rock mass is connected, only local stability or key block need to be examined. The Main boundary block is a very complex and connected block with large number of faces.

(2) Jointed Rock Masses with Less Than 5% Volume of Inner Blocks

The space for producing joint polygons and computing blocks is the target block. One of the target blocks is a three-dimensional cube with dimensions:
20m × 20m × 20m

As the checking sum, the volume summation of all blocks is 8,000.0000000000 cubic meters. It indicates that the whole computation is accurate.

The average joint length ratio in this simulation is $R_{ls} = 4.82$

The total inner block volume is 2.54 % of the total rock volume.

Figure 4 shows the connected main boundary blocks with 4354 polygons. The surfaces of the main blocks are mainly the cubic boundary surfaces.

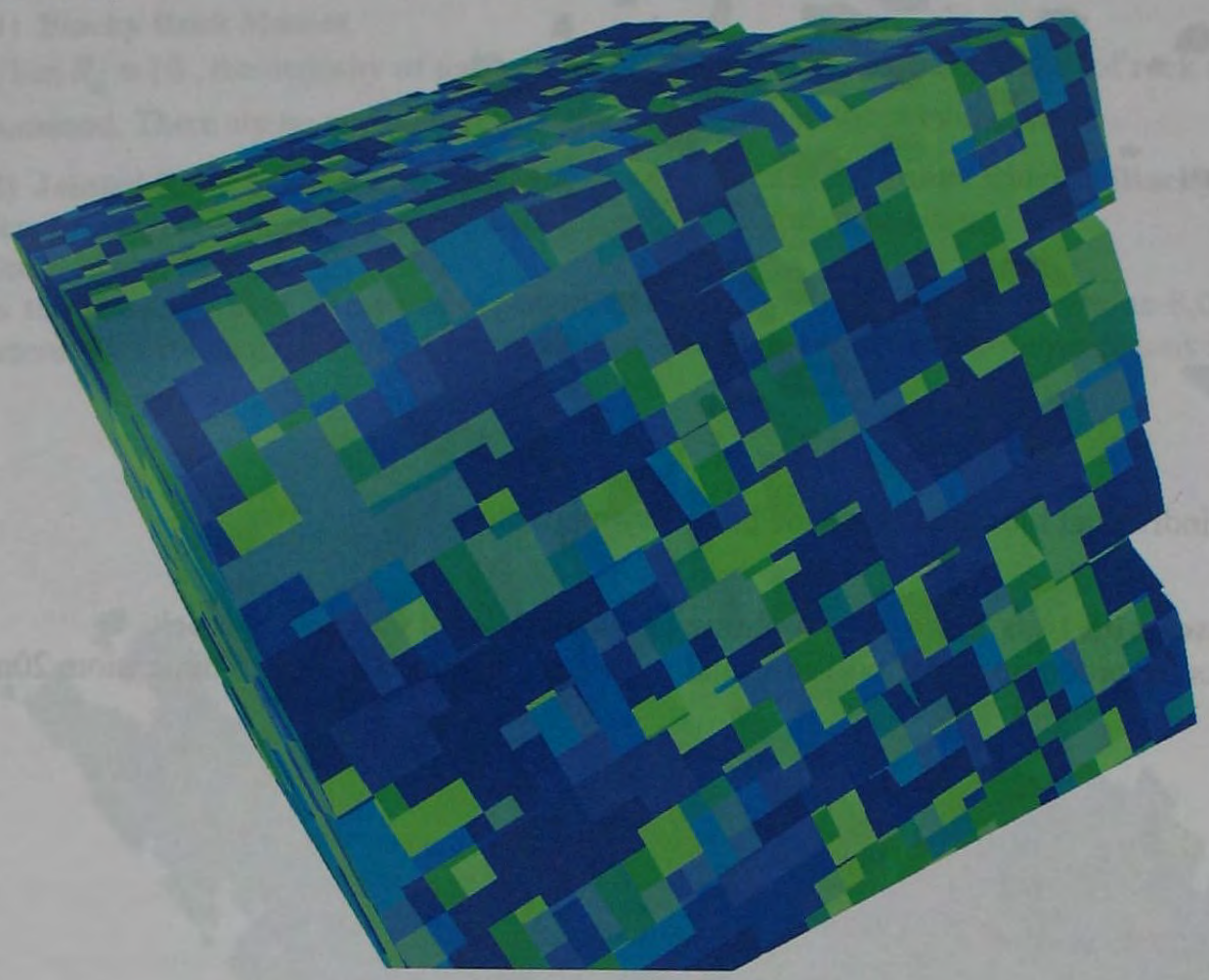


Fig. 4 The single connected main boundary block with 4354 polygons

Figure 5 shows one fifth of the individual blocks excluding the connected boundary main block

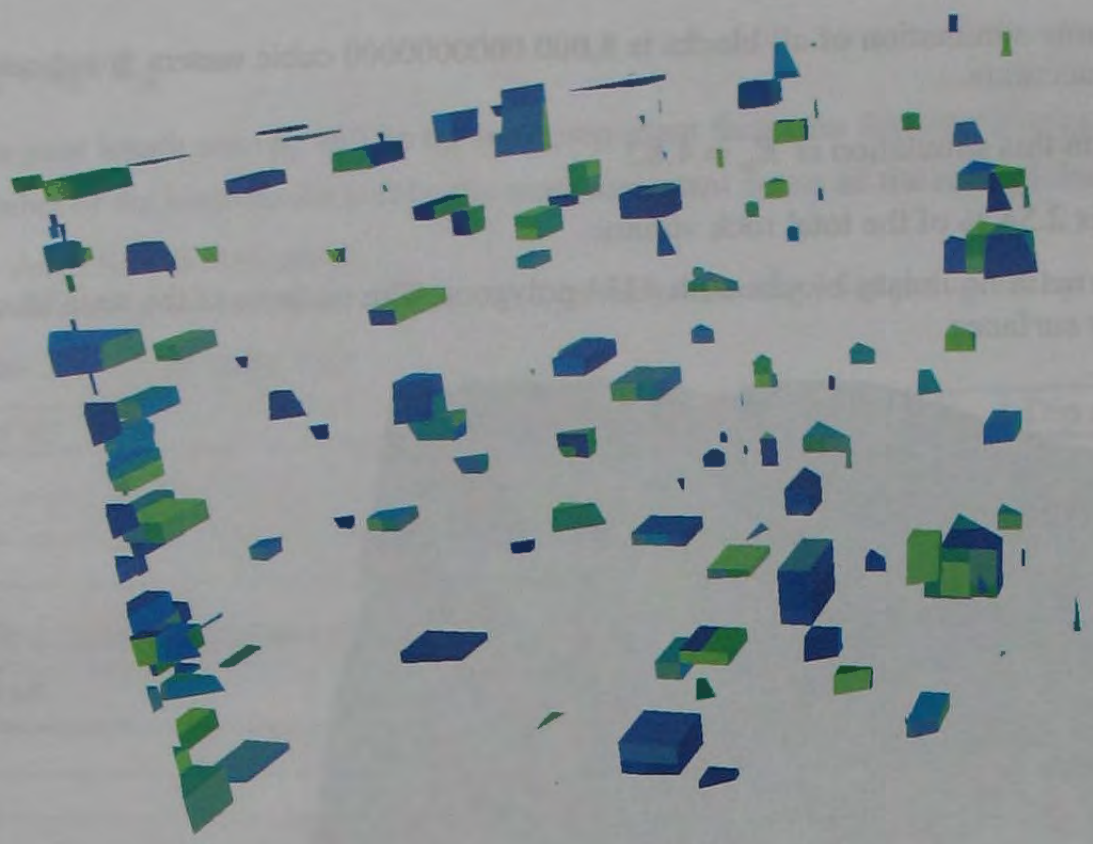


Fig. 5 One fifth of the individual blocks exclude the boundary main block

(3) Jointed Rock Masses with Less Than 20% Volume of Inner Blocks: Connected Rock

One of the target blocks for producing joint polygons and computing blocks is a cube of dimension: 20m × 20m × 20m

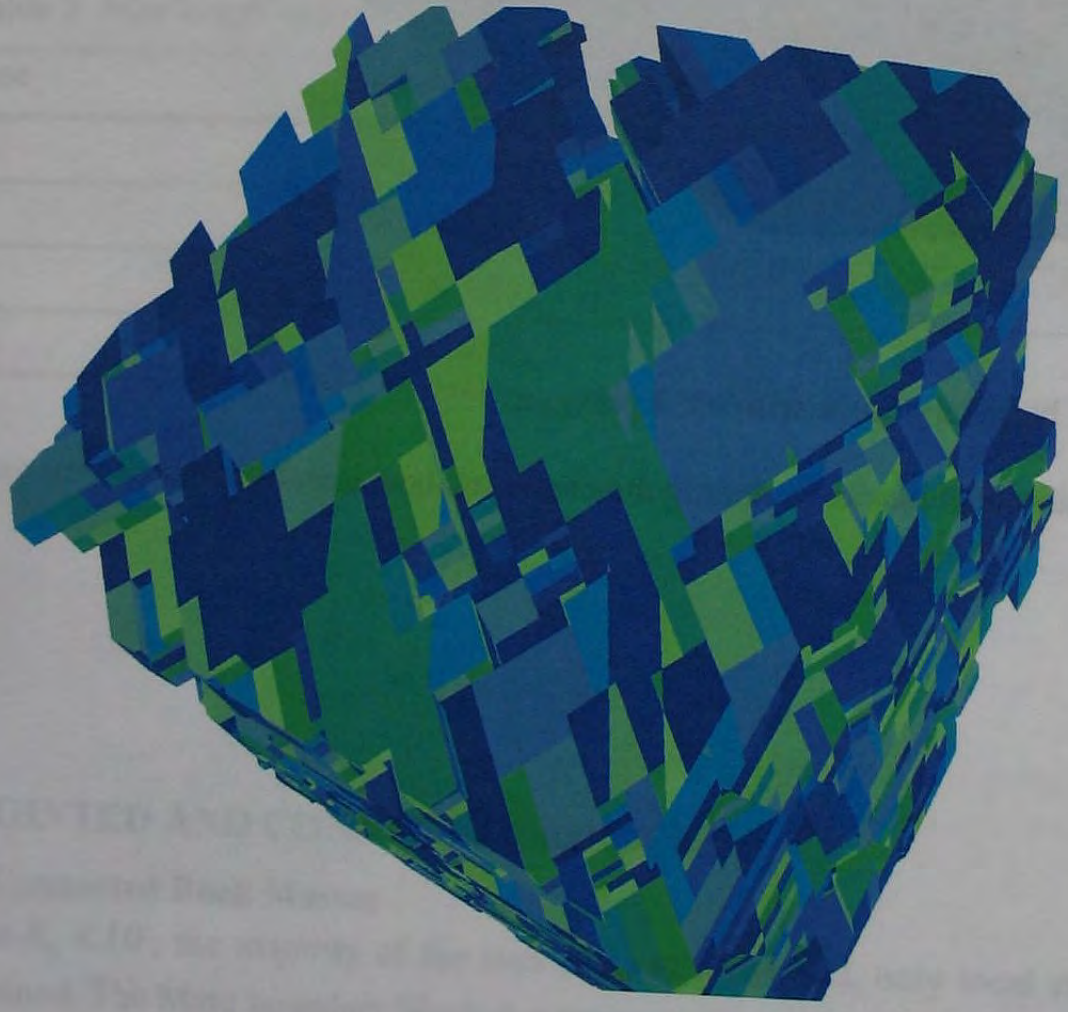


Fig. 6 The single connected main boundary block with 7655 polygons

As the checking sum, the volume summation of all blocks is 8,000.0000000000 cubic meters. It indicates the whole computation is accurate.

The average joint length ratio in this simulation is $R_{ls} = 7.84$

Total inner block volume is 12.24 % of the total rock volume.

Figure 6 shows the connected main boundary blocks with 7655 polygons respectively.

5. BLOCKY OR DISCONNECTED ROCK MASSES

(1) Blocky Rock Masses

When $R_{ls} > 10$, the majority of the rock mass is blocky. The global stability of rock masses must be examined. There are no very complex major blocks like in the previous case.

(2) Jointed Rock Masses with More Than 40% Volume of Inner Blocks: Blocky Rock

Here the target block is a three-dimensional cube with the dimension:
20m × 20m × 20m
As the checking sum, the volume summation of all blocks is as accurate as 8,000.0000000000 cubic meters. This summation kept 14 correct digits. The numbers with double precisions have only 16 digits.

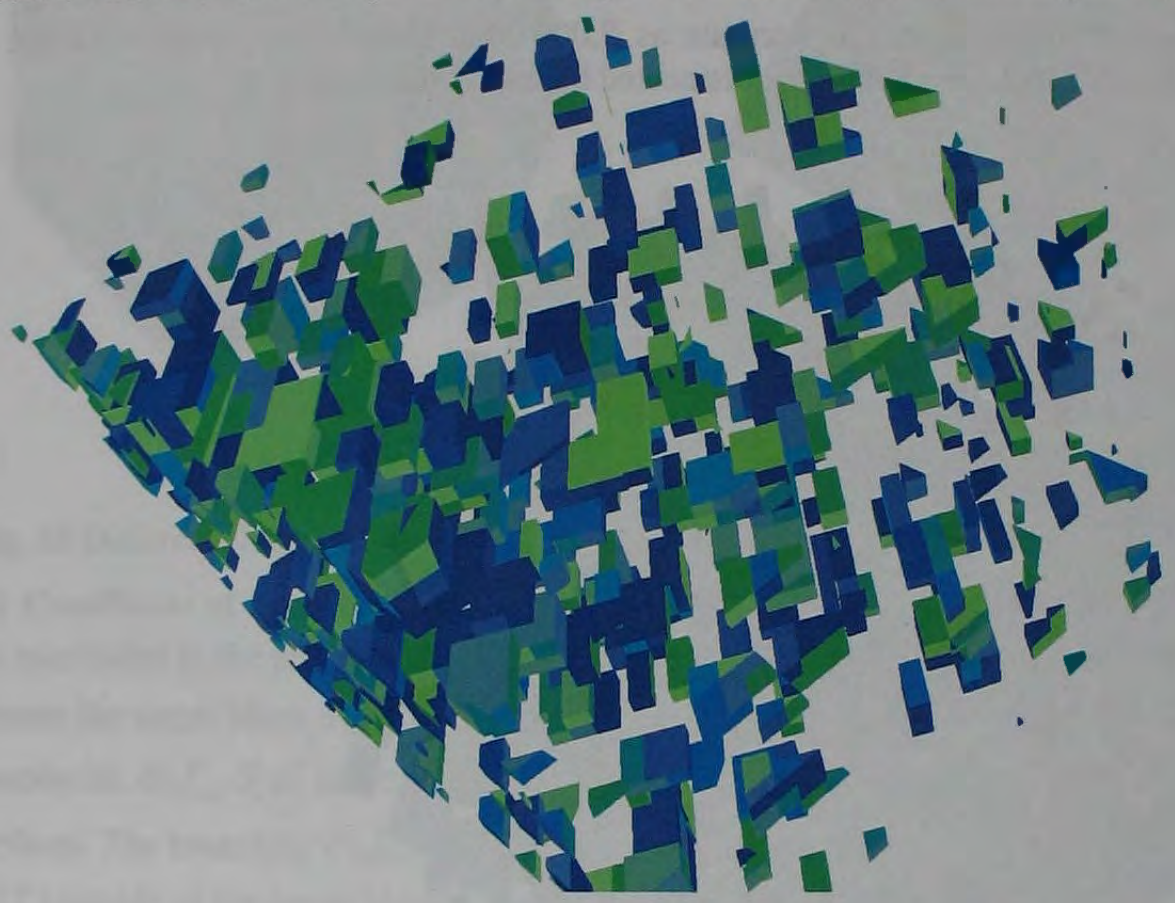


Fig. 7 One fifth of the individual blocks exclude the boundary main block

The average joint length ratio $R_{ls} = 11.11$

The total inner block volume is 44.54 % of the total rock volume.

Figure 7 shows one fifth of the individual blocks exclude the boundary main block

Figure 8 shows the connected main block with 601 polygons respectively.



Fig. 8 The single connected main block delimited by 601 polygons

(3) Jointed Rock Masses with More Than 60% Volume of Inner Blocks: Blocky Rock

Here the average joint length ratio $R_{ls} = 14.83$. Total inner block volume is 65.06 % of the total rock volume. The graphic results are shown Figure 9.

The volume summation of all blocks is still as accurate as 8,000.0000000000 cubic meters. Figure 9 shows one fifth of the individual blocks excluding the connected boundary main block.

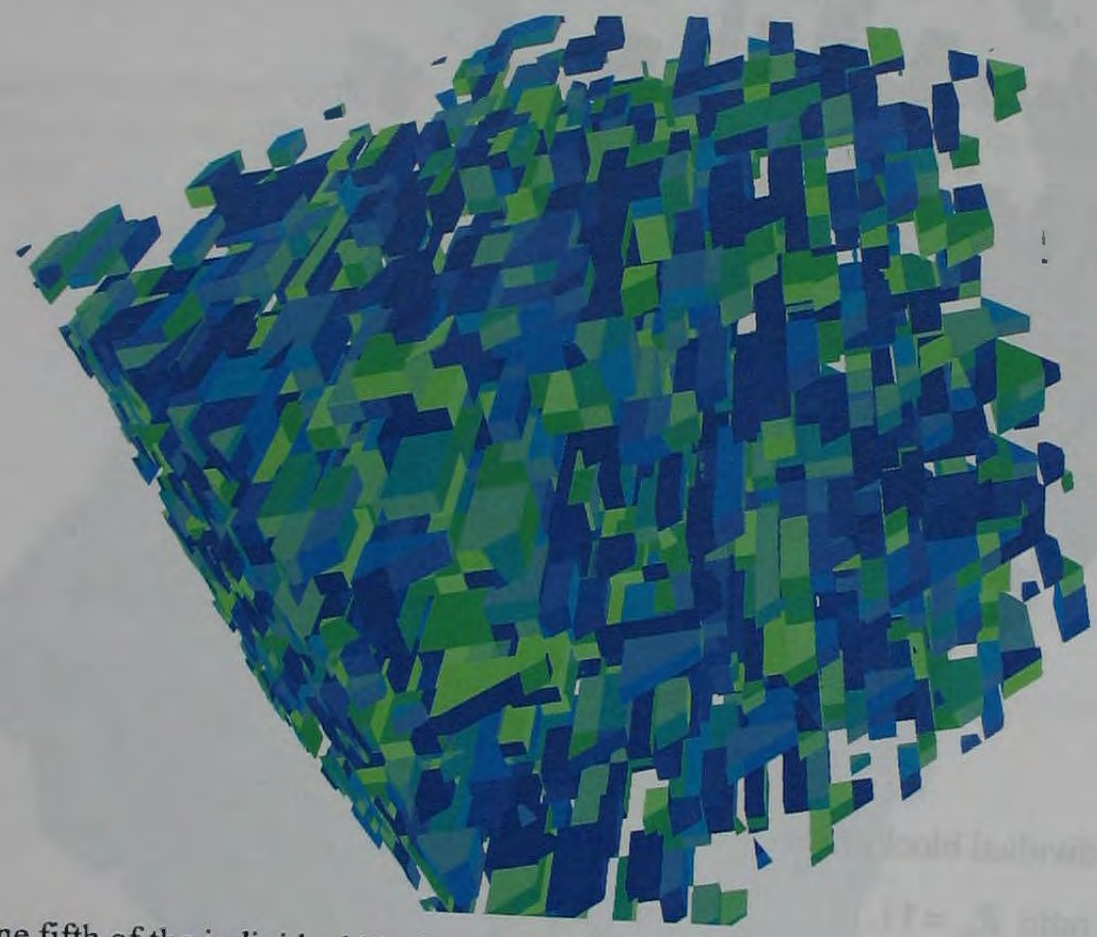


Fig. 9 One fifth of the individual blocks excluding the main block

6. FREE SURFACES OF TARGET BLOCK

(1) Target Block Is Convex Block

The joint polygons are produced in a space lager than the target block. Target blocks are defined as convex blocks. Convex blocks are simple. It is convenient to compute the part of polygon which is inside of the convex target block. The equations of target block boundary faces are plane equations:

$$A_i x + B_i y + C_i z + D_i = 0 \qquad i = 1, 2, 3, \ldots, n$$

The equation of target block is

$$A_i x + B_i y + C_i z + D_i \geq 0 \qquad i = 1, 2, 3, \ldots, n$$

Each produced polygon is trimmed by all boundary face planes $A_i x + B_i y + C_i z + D_i = 0$. If the plane divides the polygon to two sub-polygons, only the sub-polygon satisfying $A_i x + B_i y + C_i z + D_i \geq 0$ keeps.

The boundary of target block is shown by Figure 10.

(2) Free Surfaces Are Defined by Their Oriented Boundary Triangles

The free surfaces of the rock mass are polygons in three dimensional spaces. These polygons are not necessarily convex. However the boundary polygon can be subdivided into oriented triangles. The rotation directions of the oriented triangles are pointing into the rock mass.

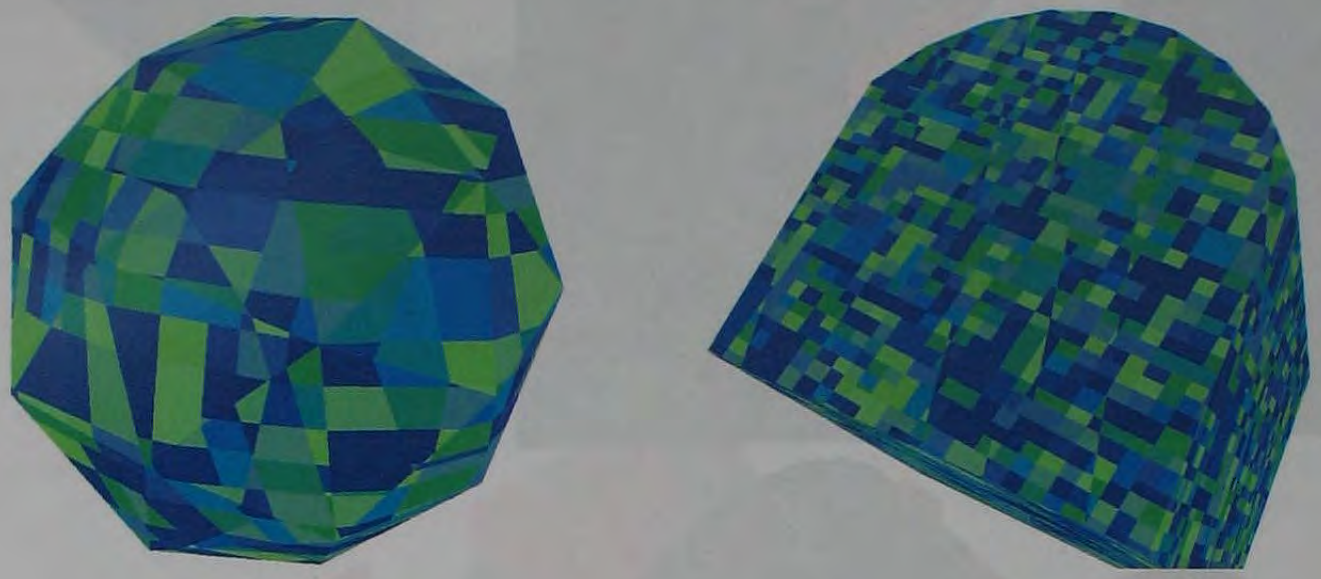


Fig. 10 Different shapes of convex target blocks

(3) Conditions of Free Surfaces

As mentioned in the previous paragraph, the boundaries of rock mass are a set of oriented triangles $\bigcup_{i=1}^{n} S_i$. Denote the target block as T. Denote the set of points outside of the target block T as $C(T)$. The boundaries $\partial \bigcup_{i=1}^{n} S_i$ of all oriented triangles of the free surfaces $\bigcup_{i=1}^{n} S_i$ consist of outer edges of the free surfaces. The boundary $\partial \bigcup_{i=1}^{n} S_i$ is in the union of the boundary ∂T of the target block T and the set $C(T)$ outside of the target block T. Intuitively speaking, the input free surfaces will cut through the entire target block. The free surface can not end inside of the target block.

$$\partial(\bigcup_{i=1}^{n} S_i) \subseteq (\partial T \bigcup C(T))$$

The target block is divided by the free surfaces. These blocks are divided to two groups: rock mass blocks and the excavated blocks.

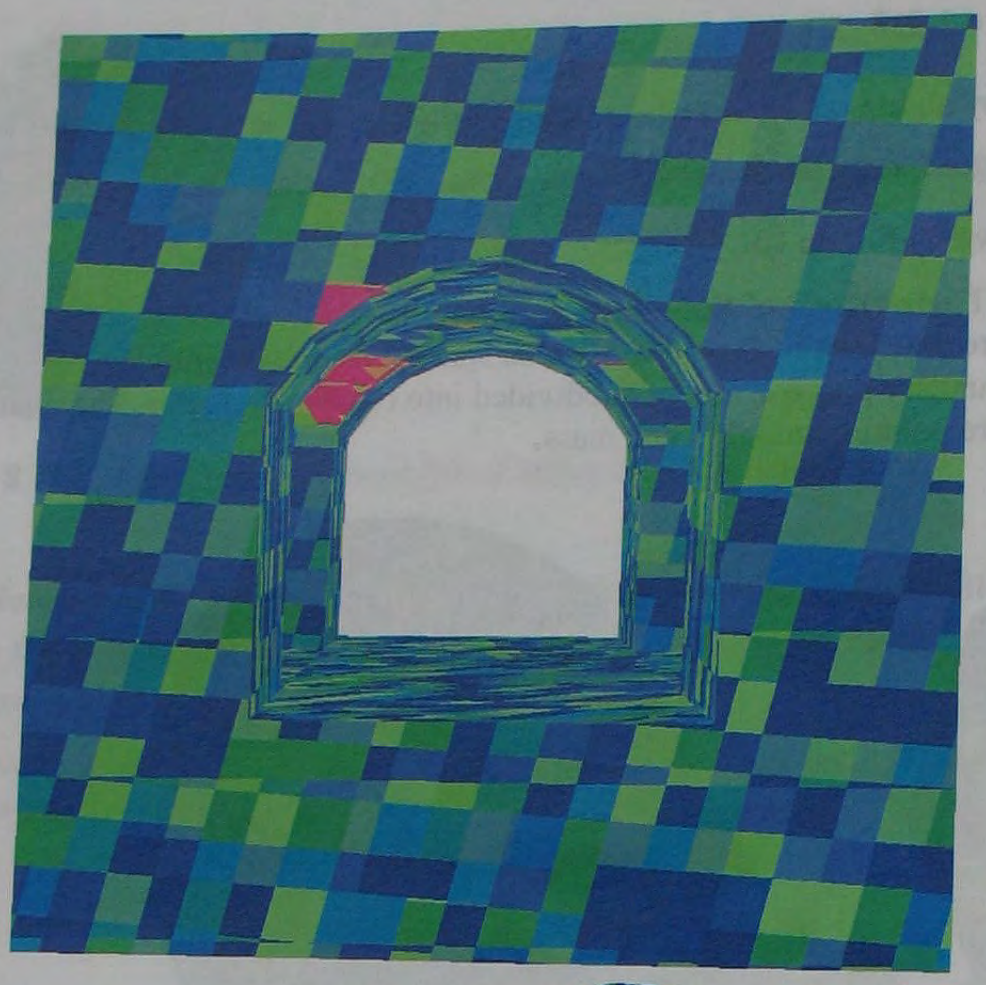


Fig. 11 Tunnel and Tunnel intersection as free surfaces of a cubic target block

Figure 11 shows part of the rock mass joint blocks and the excavated joint blocks. The target block is a cube. The free surfaces are the surfaces of two intersecting tunnels.

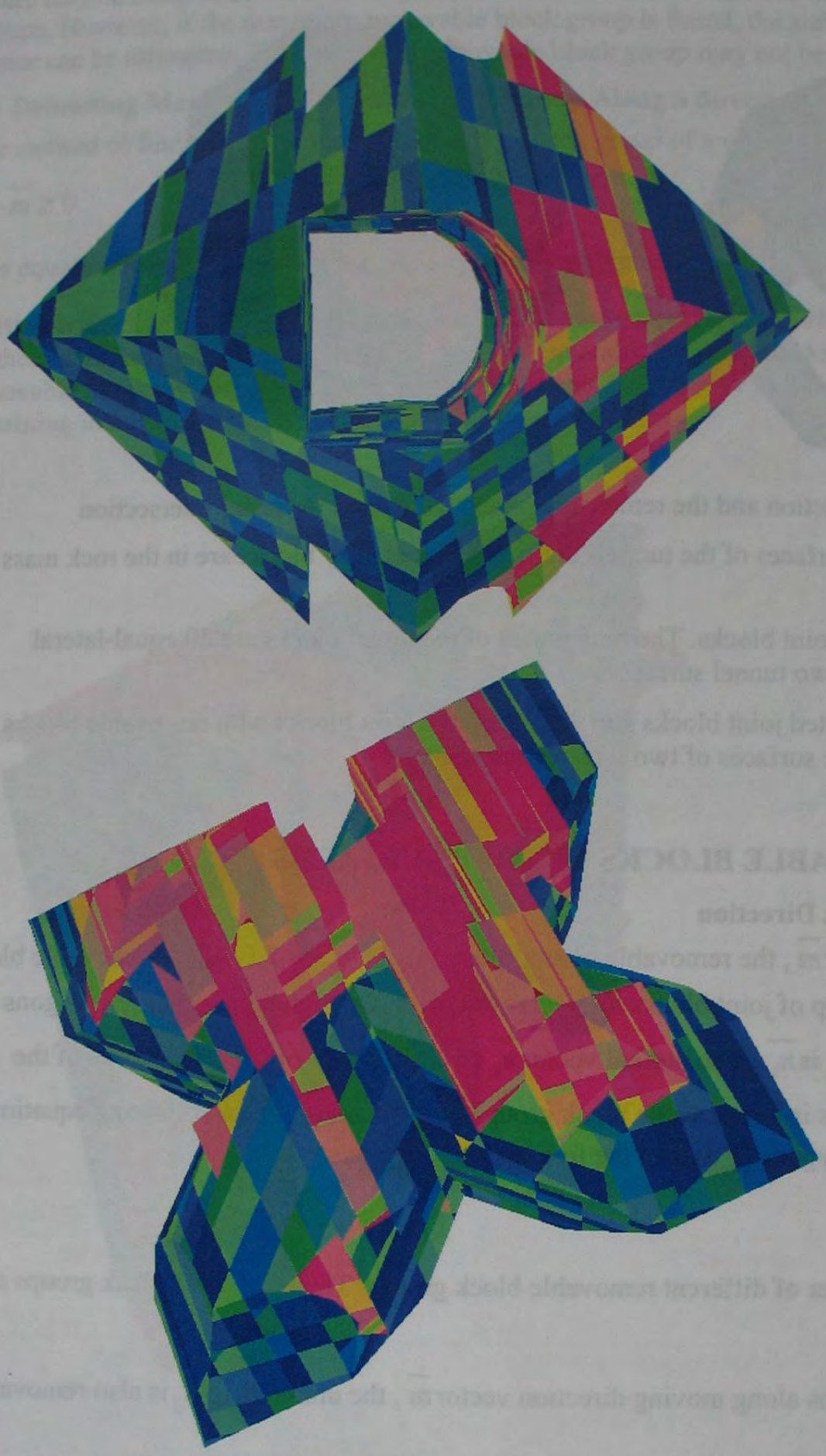


Fig. 12 Tunnels are the free surfaces of target blocks, key blocks are in the rock mass out side of tunnels

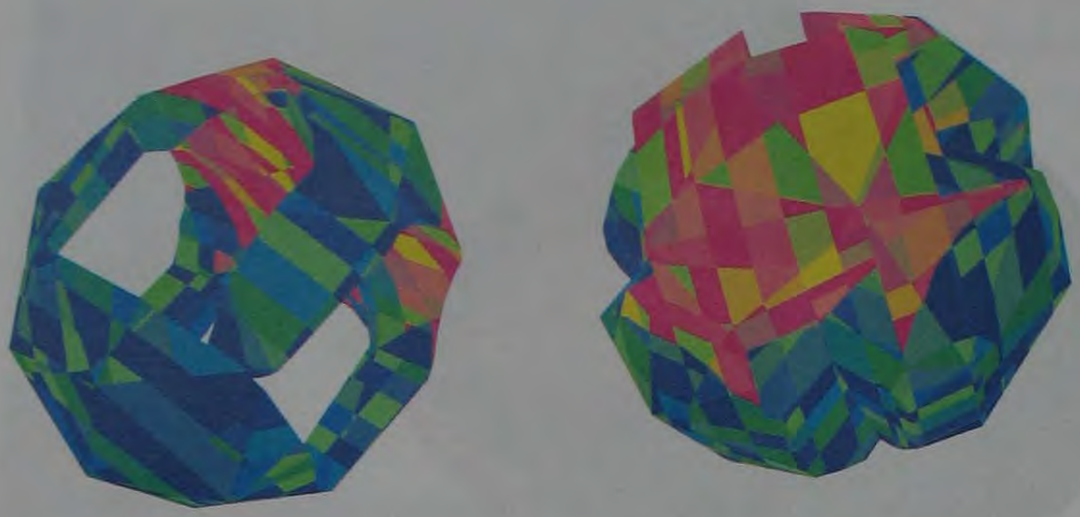


Fig. 13 Excavated tunnel intersection and the removable blocks on the top of tunnel intersection

Figure 12 shows tunnels. The surfaces of the tunnels are free surfaces. Key blocks are in the rock mass out side of tunnels.

Figure 13 shows the rock mass joint blocks. The boundaries of the target blocks are 20 equal-lateral triangles. The free surfaces are two tunnel surfaces.

Figure 13 also shows the excavated joint blocks and the excavated joint blocks with removable blocks on the top. The free surfaces are the surfaces of two intersecting tunnels.

7. FINDING ALL REMOVABLE BLOCKS OF FREE SURFACES

(1) Removable Blocks Along a Direction

Given a moving direction vector $\vec{m}$, the removable blocks along vector $\vec{m}$ are defined. A removable block group along vector $\vec{m}$ is the group of joint blocks R_i. The boundaries ∂R_i of the group R_i are polygons P_k. The normal vector of polygon P_k is $\vec{n_k}$. The normal vector $\vec{n_k}$ points the side of the joint blocks of the group. This group of joint blocks is a removable block group along vector $\vec{m}$, if the following equation is satisfied for all its boundary polygons P_k except the free surface polygons.

$$\vec{n_k} \cdot \vec{m} \geq 0$$

There could be very large number of different removable block groups. The removable block groups along the same vector $\vec{m}$ are additive.

If R_i and R_j are removable groups along moving direction vector $\vec{m}$, the union $R_i \bigcup R_j$ is also removable block group along vector $\vec{m}$.

(2) Maximum Removable Blocks Along a Direction

Union of all removable block groups along a vector $\vec{m}$ is still a removable block group along the same moving direction vector $\vec{m}$. This union is the maximum removable block group along vector $\vec{m}$. Therefore for a given vector $\vec{m}$, there is only one unique maximum removable block group. It is more convenient to find this unique maximum removable block group.

There may be many removable block groups of a vector. It is too hard to find all of the removable block groups. However, if the maximum removable block group is found, the stability of the rock mass along the vector can be estimated. The maximum removable block group may not be connected.

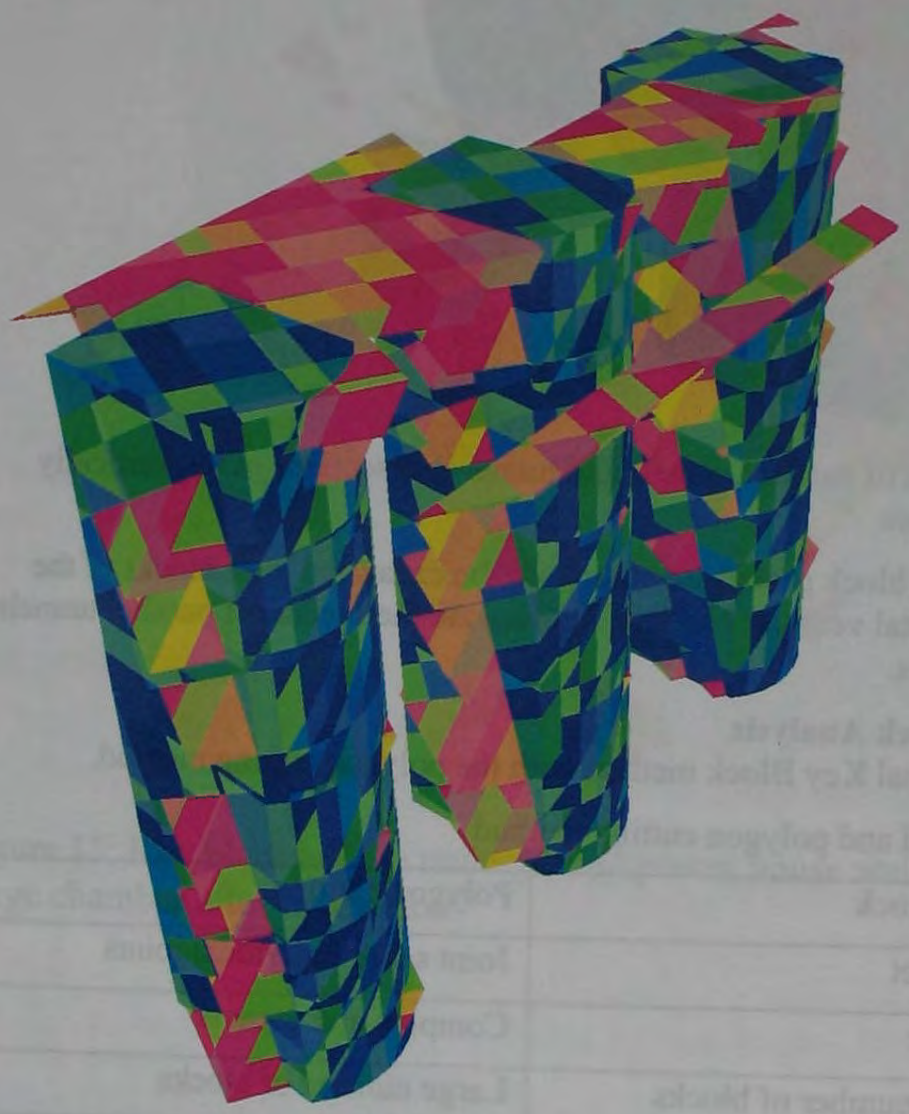
(3) Delimiting Maximum Removable Block Group Along a direction

The method of finding the maximum removable block group of a vector $\overline{m}$ is based on the equation:

$$\overline{n_k} \cdot \overline{m} \geq 0$$

This equation has to be satisfied for all its boundary polygons P_k except the free surface polygons.

Starting with all of the joint blocks on the rock side of the target block surfaces, compute the boundary of all the remaining joint blocks. Using the previous equation, the joint blocks outside of the maximum removable block group are deleted one-by-one. If there are no more joint blocks to be deleted, the remaining joint blocks are the maximum removable block group.



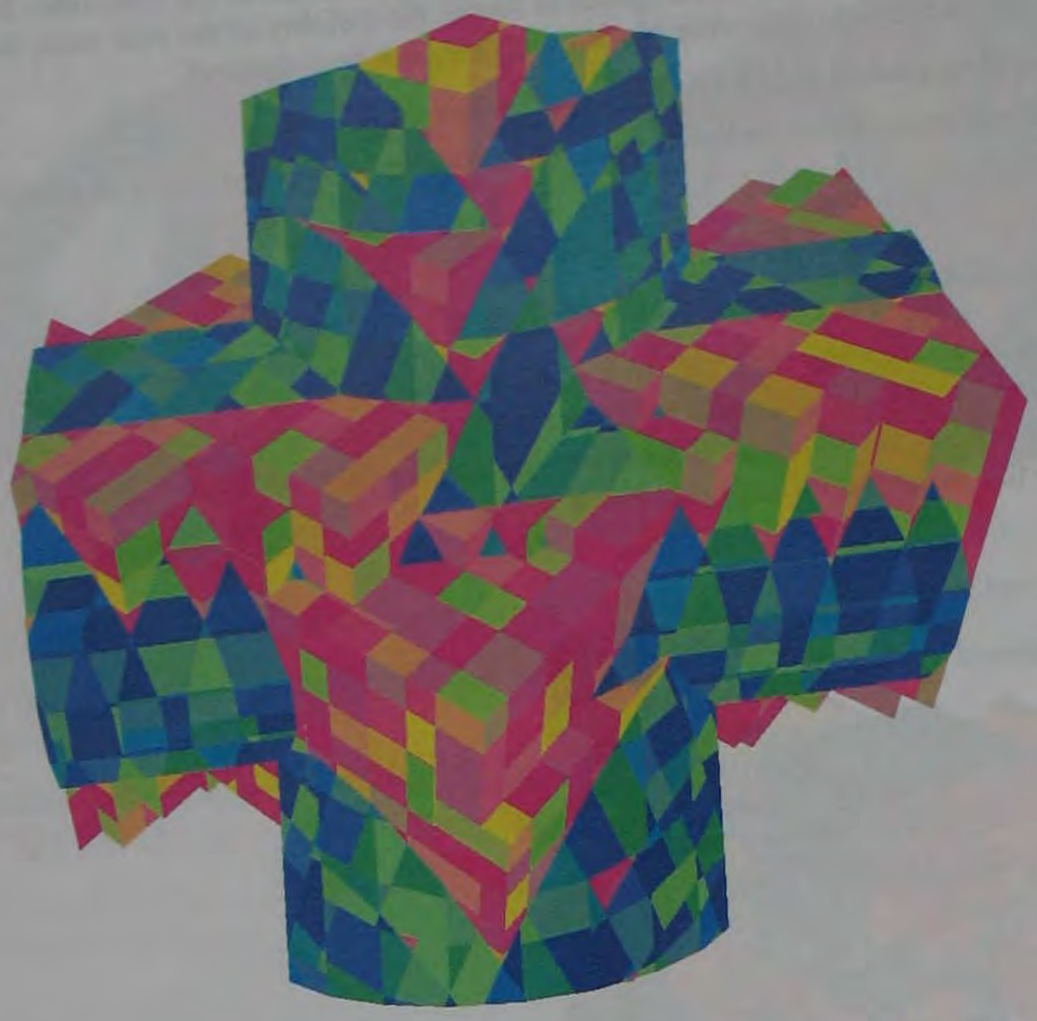


Fig. 14 Maximum removable block groups of parallel tunnels and tunnel intersections of the vertically downward vector and two horizontal vectors

Figure 14 shows the maximum removable block groups together with the excavated joint blocks of the vertical downward vector and two horizontal vectors. The free surfaces are the surface of parallel tunnels and the surfaces of two intersecting tunnels.

(4) Comparison With Original Key Block Analysis

The following table compares the traditional Key Block method with the polygon cutting method.

Table 4 Comparison of key block method and polygon cutting method

Methods	Key Block	Polygon Cutting
Joint system	Joint set	Joint set or individual joints
Free surface	Simple	Complex and general
Block system	Small number of blocks	Large number of blocks
Moving directions	Few moving directions	Large number of moving directions
Finiteness	Infinite	Finite
Secondary removable blocks	No	Yes

8. ROCK BLOCK FALLING ESTIMATION OF UNDERGROUND POWER CHAMBERS BY CUTTING PROGRAM OF THREE DIMENSIONAL DDA

In this section, the cutting program and other programs of three dimensional DDA are used for finding key blocks of underground power chambers and tunnel system of surge chambers.

Joint polygons are produced based on the geometric data of joint sets. Based on produced joint polygons and input geometry of the underground power chamber, blocks are computed by the cutting program. The key blocks are found by a special searching program based on block geometry and moving directions.

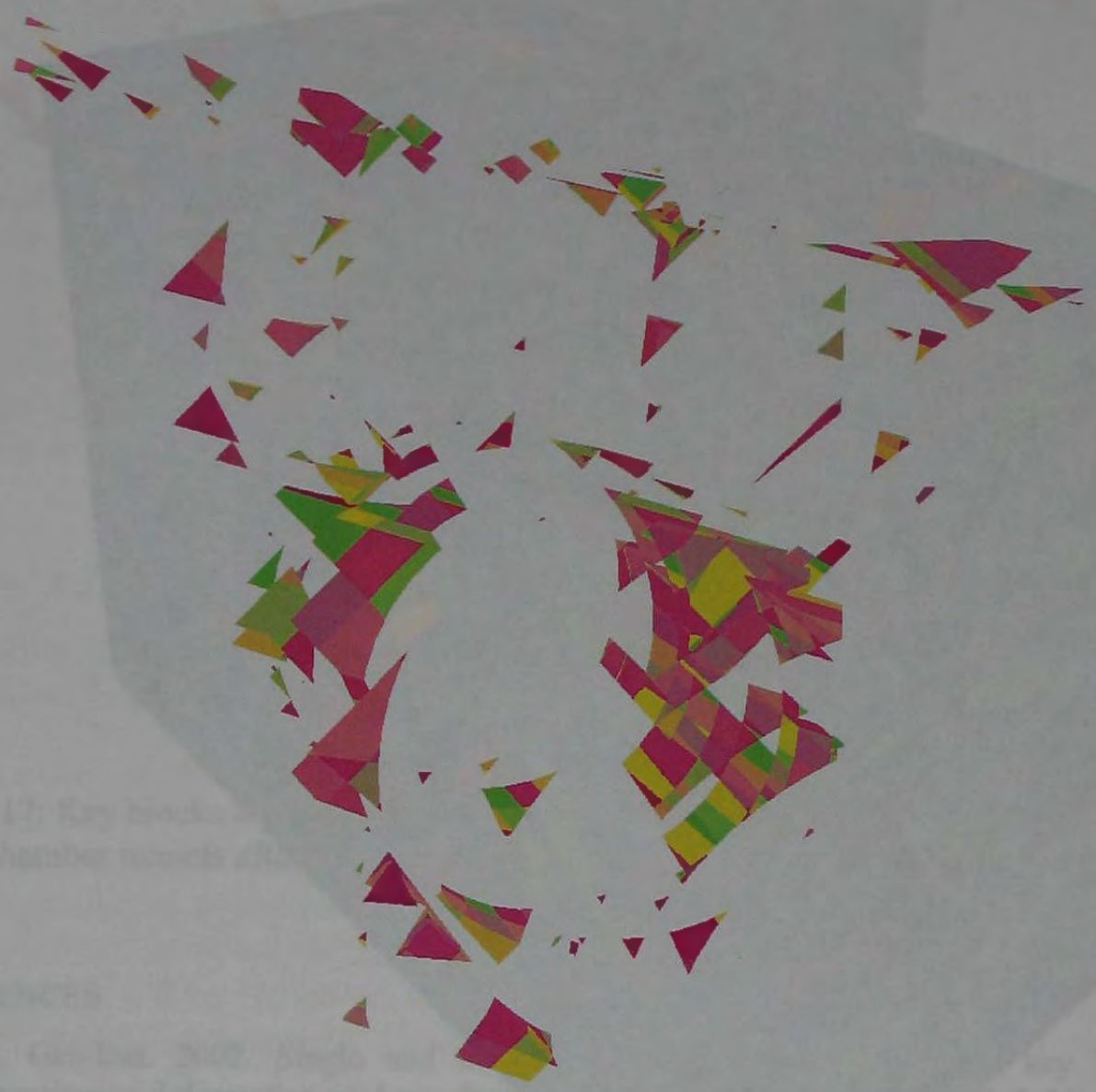


Figure 15: Key blocks of the underground power house wall and connected tunnel system of surge chamber after excavation

Figure 15 shows key blocks of the underground power house wall and connected tunnel system of surge chamber after excavation.

Figure 16 shows key blocks and the rock masses of the underground power chamber wall and connected tunnel system of surge chamber after excavation.

Figure 17 shows key blocks and excavated rock masses of the underground power house and connected tunnel system of surge chamber after excavation.

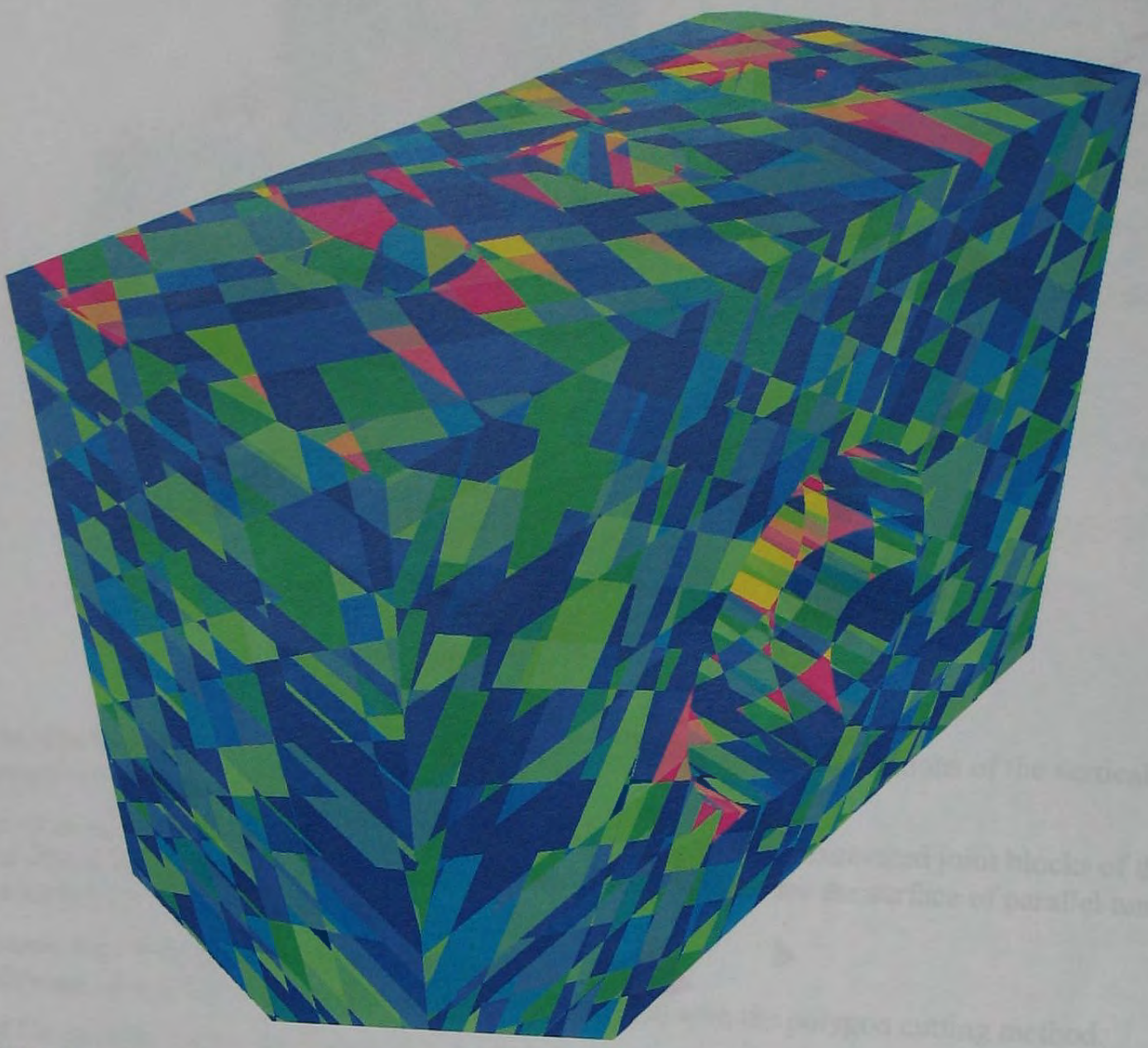


Figure 16: Key blocks and rock masses of the underground power house wall and connected surge chamber tunnels after excavation

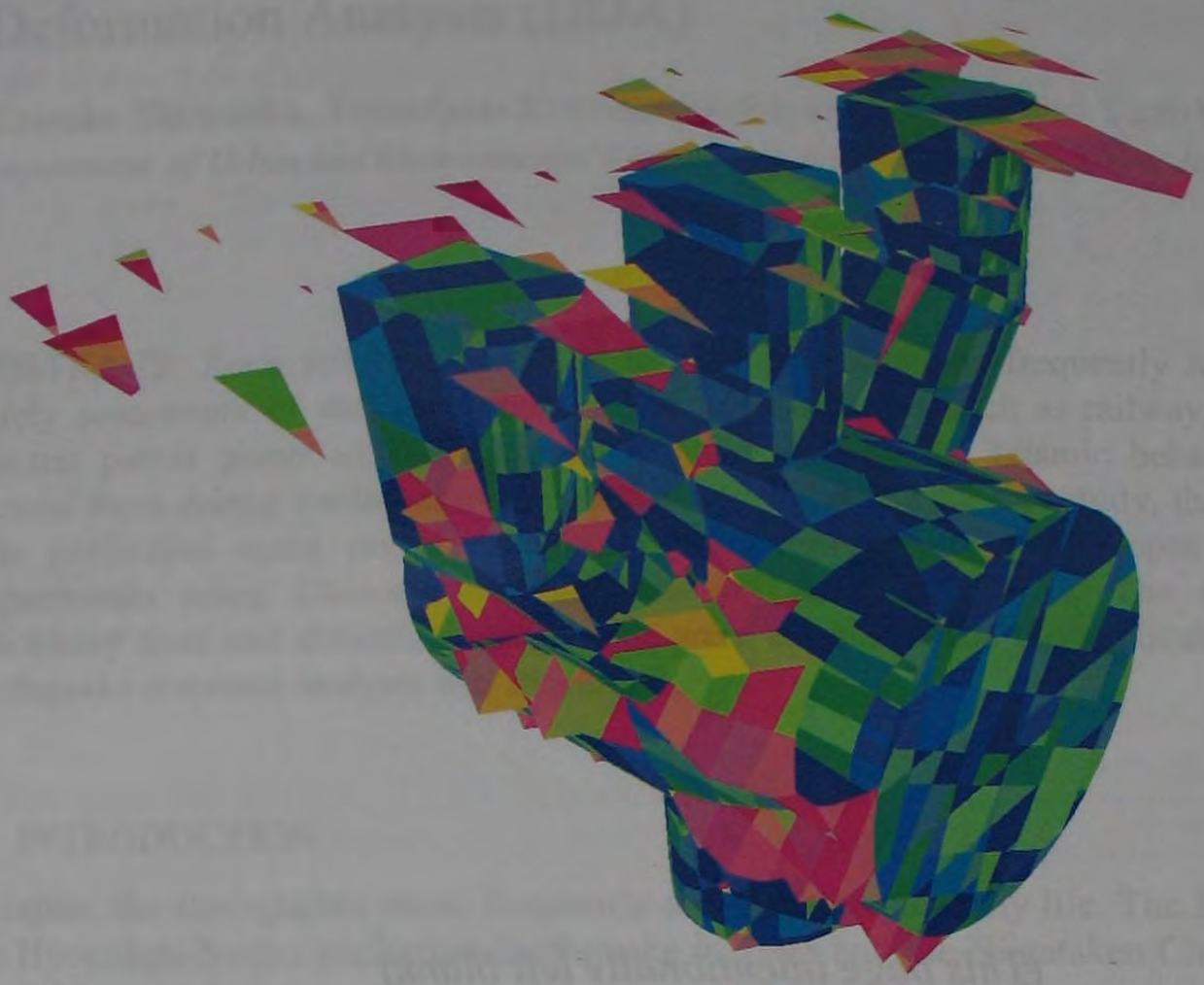


Figure 17: Key blocks and excavated rocks of the underground power house wall and connected surge chamber tunnels after excavation

REFERENCES

1. Shi, Gen-hua. 2002. Single and multiple block limit equilibrium of key block method and discontinuous deformation analysis. *Stability of Rock Structures, ICADD-5,* 3-46. Beer Sheva, Israel.

2. Shi, Gen-hua. 1999. Applications of discontinuous deformation analysis (DDA) and manifold method. *The Third International Conference on Analysis of Discontinuous Deformation, ICADD-3,* 3-15. Vail, Colorado.

3. Shi, Gen-hua. 1993. Block system modeling by discontinuous deformation analysis. *Computational Mechanics Publications,* Southampton, UK and Boston, USA.

Proceedings of International Mini-Symposium for Numerical Discontinuous Analyses, edited by T. Koyama, Hawaii, November, 2008

Earthquake response analysis of rock slopes by Discontinuous Deformation Analysis (DDA)

Keisuke Shimaoka, Tomofumi Koyama, Nishiyama Satoshi and Yuzo Ohnishi
Department of Urban and Environmental Engineering, Kyoto University, Kyoto, Japan

ABSTRACT: Rock failure caused due to earthquakes occurs frequently in Japan and for the safety assessment of various structures and infrastructures such as railway, roads, tunnels and electric power plants against earthquake, understanding the seismic behavior of rock slopes around them during earthquake is necessary and important. In this study, the shaking table tests was performed using multilayer block model representing rock slopes and simulated the experiments using Discontinuous Deformation Analysis (DDA). The results obtain from laboratory tests and numerical simulations were compared and the applicability of DDA to the earthquake response analysis was examined.

1. INTRODUCTION

In Japan, the earthquakes occur frequently and threaten our daily life. The huge earthquakes like the Hyogoken-Nanbu prefecture Earthquake in 1995 and the Niigataken Chuetsu-oki Earthquake in 2007 caused serious damage to various structures and infrastructures. Hence, the safety assessment of the important structures such as electric power plants during earthquakes is required. For the safety assessment, it is important to investigate not only the earthquake-resistance strengths of structures but also the stability of the ground and/or slopes around structures during earthquakes and the behavior of falling rocks so called secondary influence of slope failure. To assess the secondary influence, capture the travel paths and final distribution of falling rocks during and after the failure is required and understanding the seismic behavior of discontinuous rock slopes with enough accuracy during earthquakes becomes more important.

In general, the rock masses include many faults and cracks and should be treated as a discontinuous body. Hence, it is necessary to consider the effects of discontinuities in order to understand the mechanical behaviors of fractured rock masses. This discontinuous behavior cannot be treated sufficiently using the continuum based approaches such as Finite Element Method (FEM) which have been used conventionally for the safety assessment of rock slopes. Therefore, the safety assessment of the fractured rock slopes, discontinuum based numerical models is required.

In this study, Discontinuous Deformation Analysis (DDA) developed by Shi and Goodman [1-2] was used. The DDA is one of the discontinuum based numerical approaches and has been applied to the static problems such as the stability of underground spaces and the tunnels [3] as well as dynamic problems such as falling rock [4], etc. However, DDA has not been used practically for the earthquake response analysis and the applicability of DDA has not been discussed in detail in terms of parameters for DDA such as contact stiffness of the springs etc, even though the applications to the earthquake response analysis of the very simple block models compared with the analytical solutions have been reported by some researchers [5-6]. Therefore, in this study, the shaking table tests was performed using multilayer block model representing rock slopes and simulated the experiments using Discontinuous Deformation Analysis (DDA). The results obtain

from laboratory tests and numerical simulations were compared and the applicability of DDA to the earthquake response analysis was examined.

2. BASIC CONCEPT OF DDA

In DDA, fractured rock masses are treated as an assemblage of many independent blocks separated by discontinuities and mechanical behaviors of each block are represented by six deformation parameters in 2-dimensional problems; displacements of a rigid body at the center of gravity of blocks, angle of rotation around the center of gravity of blocks and normal and shear strain of the block. These unknowns can be calculated by solving the equilibrium equation derived by minimizing the potential energy of the whole block systems, which is similar to the finite element method (FEM). The algorithm for contact is included in DDA to handle the contact behaviors between blocks and the penalty method is introduced to prevent penetration of the blocks. Friction along the interface between the blocks is modeled according to the Mohr-Coulomb failure criterion. In DDA, the kinematic equations are based on Hamilton's principle expressed as,

$$M\ddot{u} + C\dot{u} + Ku = F \tag{1}$$

where, M: mass matrix, C: viscosity matrix, K: stiffness matrix, F: external force vector, u: displacements, $\dot{u}$: velocity, and $\ddot{u}$: acceleration of the blocks at the center.

The kinematic equation (1) is discretized in time by using Newmark's β method and finally the increase of displacement is solved in each time increment by the following three equations

$$\tilde{K} \cdot \Delta u = \tilde{F} \tag{2a}$$

$$\tilde{K} = \frac{2}{\Delta t^2} M + \frac{2\eta}{\Delta t} + K_e + K_f \tag{2b}$$

$$\tilde{F} = \frac{2}{\Delta t} M\dot{u} + (\Delta F - f) \tag{2c}$$

where, Δt: time increment, Δu: incremental displacement, K_e: elastic matrix, K_f: displacement constraint and contact matrix, f: initial stress vector, ΔF: body force and point road vector, etc. In addition, DDA is brought in penalty method for contacts and replicates contact force by setting contact spring stiffness. The details for DDA can be seen in the papers [1-2] and text book [7]. In this study, seismic vibration was given by inputting the displacement time history to displacement constraint point.

3. SHAKING TABLE TEST

The shaking table tests were performed to investigate the seismic response of the multilayer block model representing a rock slope, which consists of many blocks. The mechanical behavior was observed by a video camera and the displacement of focused blocks was calculated from the image in order to compare with the results obtained from the DDA simulation presented in the next section.

3.1. Multilayer block model and testing equipment

The multilayer block model representing a rock slope shown in Fig. 1a and 1b was used for the shaking table tests. The multilayer block model consists of the basic and element parts. The basic part is composed of a horizontal surface and three slopes with different angles as shown in Fig.1.

The element part is composed of quadratic and triangle prism blocks. The several element blocks with the slash in Fig.1 were fixed to the basic part in order to prevent the collapse of the model with self weight. Both basic and element parts are made of aluminum with the thickness of 50 mm, and physical properties data are shown in Table 1.

The small shaking table used in this study is shown in Fig. 2. For the shaking table tests, the model was fixed on the horizontal shaking table and shaken only in the horizontal direction. The size of the shaking table is 80 × 150 cm. The acceleration waveform was created by a function generator and formalized as digital value. The created waveform in digital format was converted into analog format, and given to the controller of the shaking table.

3.2. Input waveform

The waveform used in this study is shown in Fig. 3. The waveform was created based on the earthquake accelerogram observed in Hachinohe city at the Tokachi-oki Earthquake in 1968 with the maximum acceleration of about 800 Gal.

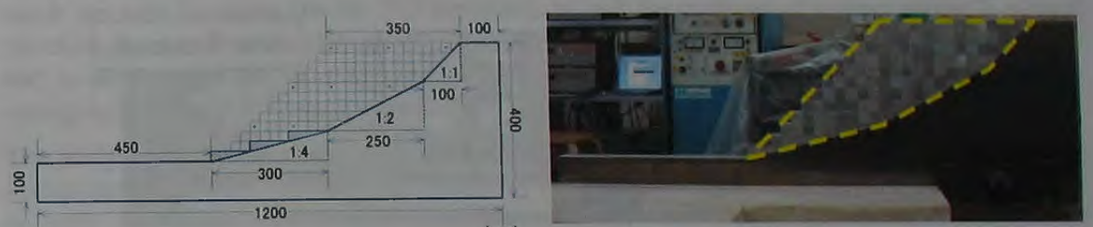


Fig. 1. Multilayer block model representing discontinuous a rock slope.

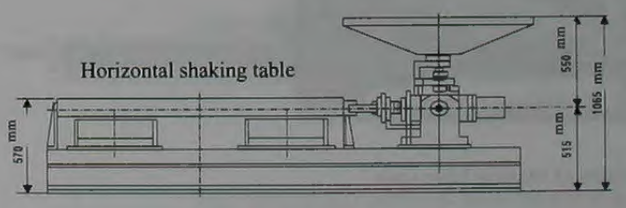


Fig. 2. Shaking table.

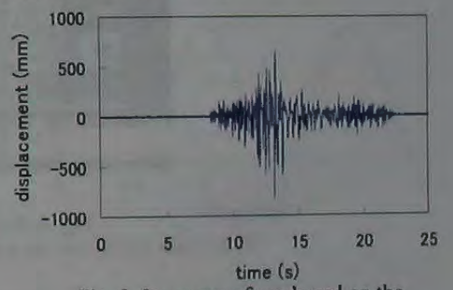


Fig. 3. Input waveform based on the Tokachi-oki earthquake in 1968.

Table.1 Physical properties of aluminum blocks

Unit Weight (kN/m³)	26.4	Friction Angle (°)	20
Young's Modulus (kN/m²)	62000	Viscosity Force (kN/m)	0
Poisson's Ratio	0.2	Tension Strength (kN/m²)	0

3.3. Testing results

The dynamic behavior of the multilayer block model recorded by the video was shown in Fig. 4. The dynamic behavior of the block model can be explained separately two regions as shown in

from laboratory tests and numerical simulations were compared and the applicability of DDA to the earthquake response analysis was examined.

2. BASIC CONCEPT OF DDA

In DDA, fractured rock masses are treated as an assemblage of many independent blocks separated by discontinuities and mechanical behaviors of each block are represented by six deformation parameters in 2-dimensional problems; displacements of a rigid body at the center of gravity of blocks, angle of rotation around the center of gravity of blocks and normal and shear strain of the block. These unknowns can be calculated by solving the equilibrium equation derived by minimizing the potential energy of the whole block systems, which is similar to the finite element method (FEM). The algorithm for contact is included in DDA to handle the contact behaviors between blocks and the penalty method is introduced to prevent penetration of the blocks. Friction along the interface between the blocks is modeled according to the Mohr-Coulomb failure criterion. In DDA, the kinematic equations are based on Hamilton's principle expressed as,

$$M\ddot{u} + C\dot{u} + Ku = F \tag{1}$$

where, M: mass matrix, C: viscosity matrix, K: stiffness matrix, F: external force vector, u: displacements, $\dot{u}$: velocity, and $\ddot{u}$: acceleration of the blocks at the center.

The kinematic equation (1) is discretized in time by using Newmark's β method and finally the increase of displacement is solved in each time increment by the following three equations

$$\widetilde{K} \cdot \Delta u = \widetilde{F} \tag{2a}$$

$$\widetilde{K} = \frac{2}{\Delta t^2} M + \frac{2\eta}{\Delta t} + K_e + K_f \tag{2b}$$

$$\widetilde{F} = \frac{2}{\Delta t} M\dot{u} + (\Delta F - f) \tag{2c}$$

where, Δt : time increment, Δu : incremental displacement, K_e: elastic matrix, K_f: displacement constraint and contact matrix, f: initial stress vector, ΔF : body force and point road vector, etc. In addition, DDA is brought in penalty method for contacts and replicates contact force by setting contact spring stiffness. The details for DDA can be seen in the papers [1-2] and text book [7]. In this study, seismic vibration was given by inputting the displacement time history to displacement constraint point.

3. SHAKING TABLE TEST

The shaking table tests were performed to investigate the seismic response of the multilayer block model representing a rock slope, which consists of many blocks. The mechanical behavior was observed by a video camera and the displacement of focused blocks was calculated from the image in order to compare with the results obtained from the DDA simulation presented in the next section.

3.1. Multilayer block model and testing equipment

The multilayer block model representing a rock slope shown in Fig. 1a and 1b was used for the shaking table tests. The multilayer block model consists of the basic and element parts. The basic part is composed of a horizontal surface and three slopes with different angles as shown in Fig.1.

The element part is composed of quadratic and triangle prism blocks. The several element blocks with the slash in Fig.1 were fixed to the basic part in order to prevent the collapse of the model with self weight. Both basic and element parts are made of aluminum with the thickness of 50 mm, and physical properties data are shown in Table 1.

The small shaking table used in this study is shown in Fig. 2. For the shaking table tests, the model was fixed on the horizontal shaking table and shaken only in the horizontal direction. The size of the shaking table is 80 × 150 cm. The acceleration waveform was created by a function generator and formalized as digital value. The created waveform in digital format was converted into analog format, and given to the controller of the shaking table.

3.2. Input waveform

The waveform used in this study is shown in Fig. 3. The waveform was created based on the earthquake accelerogram observed in Hachinohe city at the Tokachi-oki Earthquake in 1968 with the maximum acceleration of about 800 Gal.

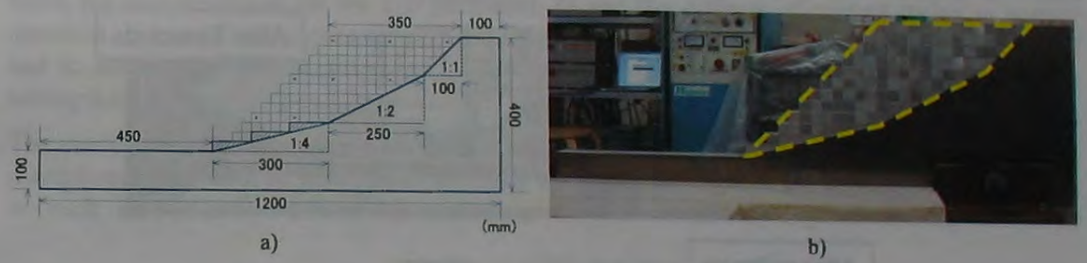


Fig. 1. Multilayer block model representing discontinuous a rock slope.

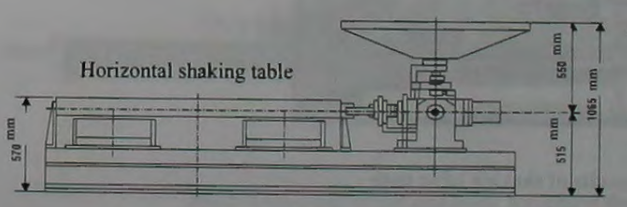


Fig. 2. Shaking table.

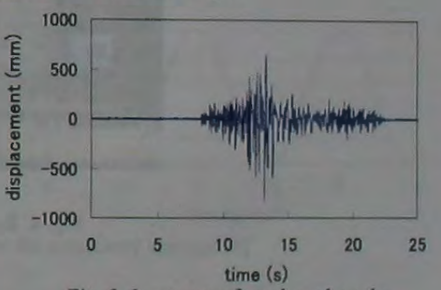


Fig. 3. Input waveform based on the Tokachi-oki earthquake in 1968.

Table.1 Physical properties of aluminum blocks

Unit Weight (kN/m^3)	26.4	Friction Angle (°)	20
Young's Modulus (kN/m^2)	62000	Viscosity Force (kN/m)	0
Poisson's Ratio	0.2	Tension Strength (kN/m^2)	0

3.3. Testing results

The dynamic behavior of the multilayer block model recorded by the video was shown in Fig. 4. The dynamic behavior of the block model can be explained separately two regions as shown in

Fig. 4; ① the area with toppling and sliding and ② the area with only sliding. From Fig. 4, at four seconds after start shaking, sliding occurred gradually in the entire blocks. At seven seconds, the acceleration amplitude of input waveform became largest and toppling failure occurred in the region ①, and the blocks in the region ② slid continuously following the blocks in region ①. After seven seconds, the acceleration amplitude became smaller, and no more topping and sliding did not occur and the shape of the entire blocks did not change very much. The final shape of the multilayer blocks is shown in the bottom figure in Fig. 4.

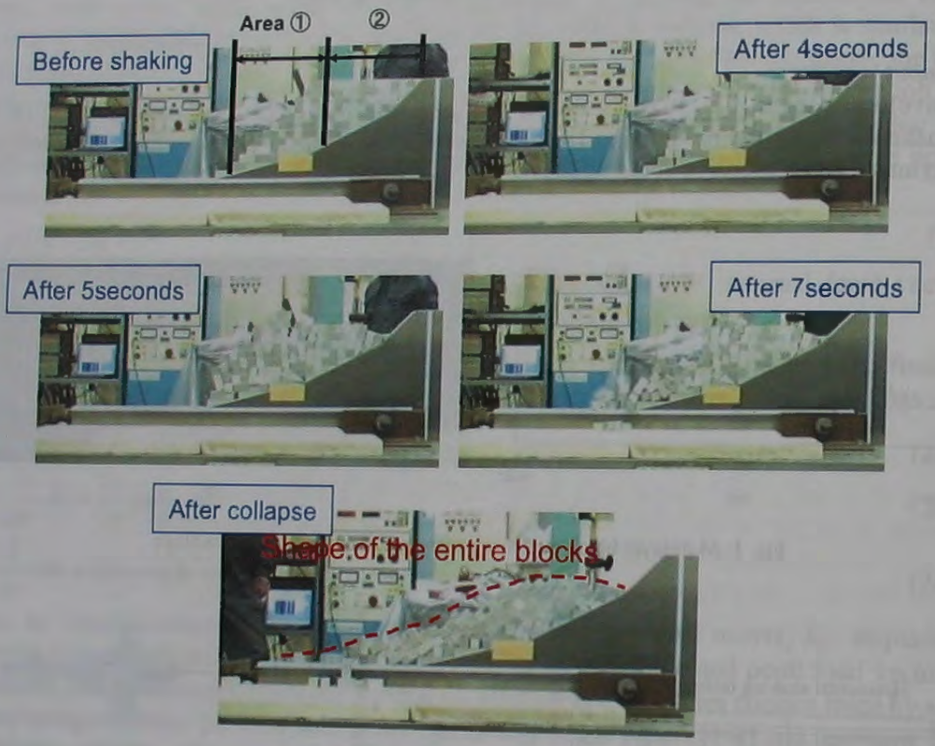


Fig. 4. Results of shaking table tests

4. DDA SIMULATION

To investigate the applicability of DDA to the earthquake response analysis, the results obtained from the shaking table tests presented in the previous section were compared with the results obtained from the numerical simulations using DDA. As for DDA simulations for seismic problems, the shaking table tests using the single block model [5] and the simple two-tiered block model [6] have been simulated by DDA so far and the applicability of DDA to the earthquake response analysis has been discussed. However, in these works, only very simple block models were tested and simulated. Hence, first of all, based on the findings obtained from the previous studies of DDA for the earthquake response analysis, how to determine the stiffness of the contact springs for the multilayer block models was discussed. Then, the DDA simulations of the

shaking table tests with multilayer block model were performed and the obtained results were compared and then the failure mechanism of discontinuous rock slopes was discussed.

4.1. Indicator for determining contact spring stiffness

The relatively large contact spring stiffness has been recommended in DDA in order not to occur too much penetration between two blocks. For the dynamic behavior of the blocks during the shaking table tests, the frictional force between blocks mainly acts along the boundaries of the blocks. In the actual rock slope, the frictional force mainly acts along discontinuous surface and therefore it is important to consider the frictional force acting properly in the numerical simulations for a discontinuous body and accurately acting frictional force is required in order to perform the earthquake response analysis with good accuracy. In the previous DDA simulations for the shaking tests using simple two-tiered block model [6], the sensitivity analysis for contact spring stiffness and the upper block mass was performed and then the result of the simulation by DDA was compared with the analytical solutions of the displacement of upper block. The numerical model and input waveform (regular sine wave) are shown in Fig. 5. The results obtained from this sensibility analysis was summarized in Fig. 6 in terms of the weight of upper block per unit thickness (in the 2-D problem), M and the stiffness of contact spring in normal direction, k_n as well as the contact spring stiffness per the upper block mass, k_n/M. The units of M and k_n are ton and KN/m, respectively. From Fig. 6, the frictional force will act properly by setting k_n/M is about 10^5, and this result was used as an indicator in this study.

The model used in the present tests has so many discontinuous surfaces that the stiffness of the contact springs cannot be determined uniquely because the weight of the upper blocks is different in each discontinuity. Hence, the stiffness of the contact springs should be determine

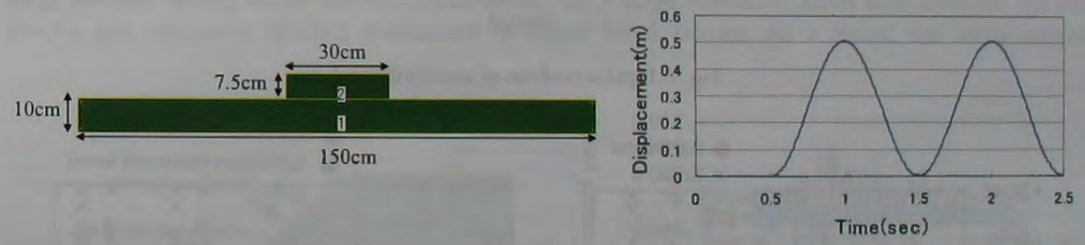


Fig.5 Analytical model and input waveform for the sensitivity analysis [6]

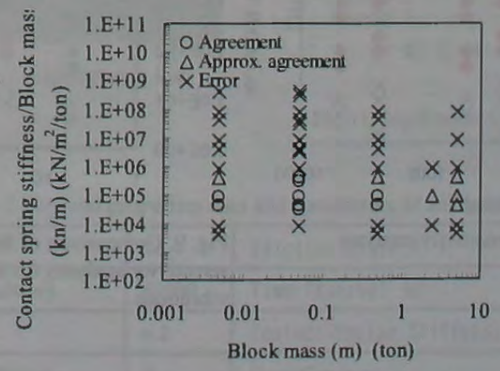


Fig. 6 Results of the sensitivity analysis [6]

systematically and how to determine the stiffness of contact springs will be described in detail in the next section.

In addition, the real earthquake includes the acceleration not only in the horizontal direction but also in the vertical direction. For the wider applicability of DDA to the earthquake response analysis, the similar sensitivity analysis in terms of contact springs for the vertical vibration will be necessary. Hence, the response analysis of a single block for the vertical vibrations was also investigated in this study. As for the behavior of blocks during vertical vibrations, the normal force between the blocks mainly acts along the discontinuous boundary of blocks. Therefore, the appropriate stiffness of the contact springs will be required to be applied the normal force accurately for the seismic response analysis with vertical vibrations. In this study, the sensitivity analysis for contact spring stiffness and the upper block mass using the block model was performed. Fig. 7 shows the input wave form for this sensitivity analysis. The results obtained from the sensitivity analysis are shown in Fig. 8, and the results of the sensitivity analysis for both horizontal and vertical vibrations were compared in Fig. 9 (plot Fig. 6 and Fig. 8 in the same graph). From Fig. 9, to apply the normal force on the discontinuous boundaries accurately, the stiffness per unit wait, kn/M of 10^5 should be selected, which is the same condition for the frictional force.

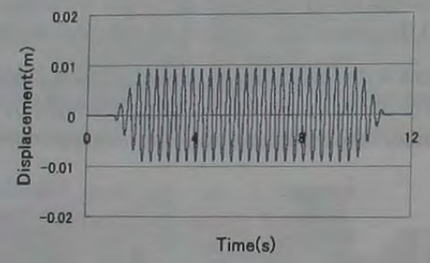


Fig. 7. Input waveform of sensitivity analysis

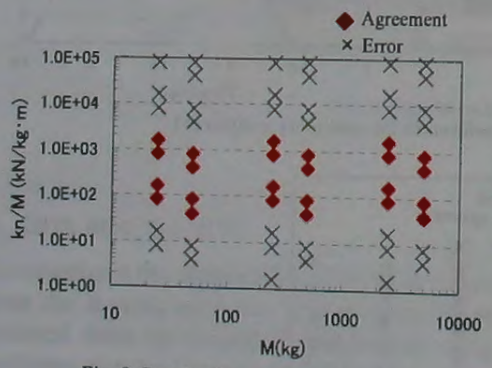


Fig. 8. Results from sensitivity analysis for vertical vibration

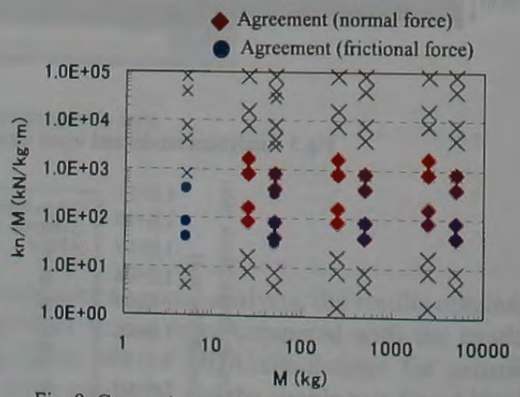


Fig. 9. Comparison of the results obtained from the sensitivity analyses for both horizontal and vertical vibrations.

4.2. Simulation of the shaking table tests

4.2.1. Analytical model, input waveform, physical properties and DDA parameters

Fig. 10 shows the DDA model of the multilayer blocks used in the laboratory shaking table tests. The element blocks were fixed to the basic part, which is the same condition in the experiments. In addition, the displacement of the focused blocks called No.1 and No.2, which was surrounded by thick line in Fig. 10, was monitored.

Fig. 11 shows the input waveform (the history of horizontal displacement) measured during the shaking table tests and this displacement history was given to the basic part of the model.

The physical properties and DDA parameters used in the simulations are summarized in Table 2. The physical properties of the blocks used in the simulations are the same as those used in the laboratory shaking table tests. As for the contact spring stiffness, the stiffness cannot be determined uniquely using the indicator mentioned in the previous section because the DDA model has many contact surfaces. In the simulations, the indicator was applied to the contact surface A in Fig. 10, where the weight of blocks is largest initially. The contact stiffness should be determined in order not to penetrate too much between blocks at the surface A and determined as 6.2×10^3 kN/m. However, in this case, too much bounce may occur around along the contact surface for the upper blocks because the stiffness is too large for the upper blocks. Hence, in DDA, to consider the contact situation, open and close criteria were proposed (see Fig. 12). After the block A moves downward and passes over the close criterion for the block B, the contact spring is introduced at the contact point to prevent the penetration of two blocks. The deformation of the contact spring is calculated as the distance from the surface of the block B. The contact springs are installed as long as the blocks are under the "close" condition. In addition, when the block A under the "close" condition is pulled back from the surface of the block B by repulsive force, the contact spring is installed not to affect on the separation of the blocks by attractive force until the block A crosses over the "open" criterion for the block B. However, when too large contact spring is set for the upper block, very large repulsive force acts between the two blocks and excessive upward movement of upper block occurs. As a result, the block crosses

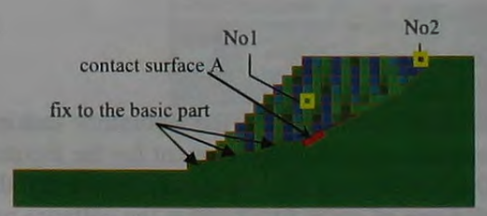


Fig. 10. DDA model for the shaking table test

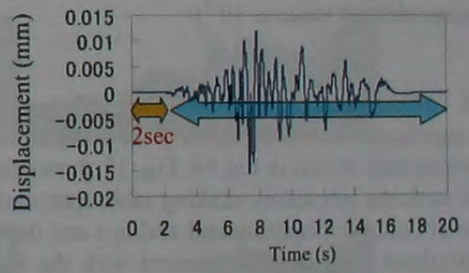
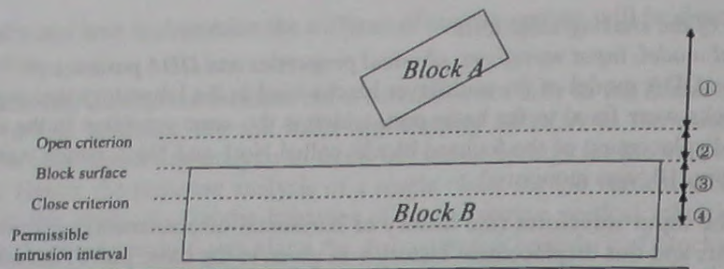


Fig.11. Input waveform for the simulations

Table.2 Physical properties data and parameters of analytical model

Unit Weigh (kN/m³)	26.4	Friction Angle (°)	20.0
Young's Modulus (kN/m²)	62000	Time Interval (s)	0.0005
Poisson's Ratio	0.2	Contact Spring Stiffness (kN/m)	6200
Viscosity Force (kN/m)	0	Open Criterion	1.0×10^{-7}
Tension Strength (kN/m²)	0	Close Criterion	1.0×10^{-6}



Previous condition	Present condition			
	①	②	③	④
OPEN	OPEN	OPEN	OPEN	CLOSE
CLOSE	OPEN	CLOSE	LOCK	LOCK
LOCK	OPEN	CLOSE	LOCK	LOCK

Open condition・・・There is a possibility that two blocks will contact

Close condition・・・Two blocks are in contact

Lock condition・・・Two blocks are in contact and does not slide by friction

Fig.12. Open-close iteration for the contact between two blocks

over "open" criterion and will be under the "open" condition, then the bounce of upper block occurs. Since the above mentioned trend was observed during the simulations, to avoid the bounce of the upper block, the "close" criterion was changed by giving the smaller value. In this case, the influence of changing close criterion on the indicator for setting the stiffness of contact springs should be investigated. Since, the sensitivity analysis for the stiffness of contact springs stiffness and close criterion was performed based on the previous work [6], and Fig. 13 show the results of the sensitivity analysis. From this figure, the range of contact spring stiffness for acting the frictional force accurately becomes wider by giving the smaller value of 10^{-6} for "close" criterion (default value is 10^{-4}).

4.2.3. Simulation results

The simulation results by DDA were compared with those obtained from the laboratory shaking table tests and shown in Fig.14. Fig. 15 shows the comparison of the displacement for the focused block between laboratory shaking table tests and DDA simulations. Fig. 14 clearly shows that the mode of collapse (toppling and sliding) and the final shape of entire blocks after the collapse can be simulated with good agreement with the results obtained from the laboratory shaking table tests, although the displacement of entire blocks by simulated by DDA is slightly larger than that measured in the laboratory experiments (see Fig. 15) and the toppling occurs earlier in DDA simulations.

Proceedings of International Mini-Symposium for Numerical Discontinuous Analyses, edited by T. Koyama, Hawaii, November, 2008

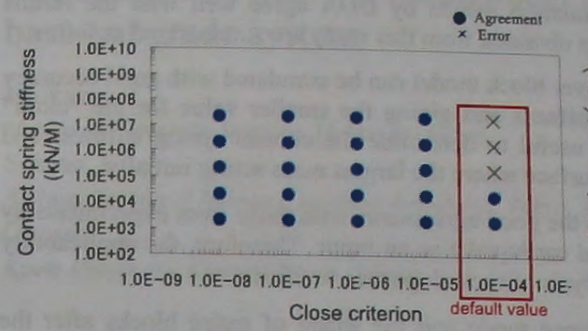


Fig.13 Result of the sensitivity analysis

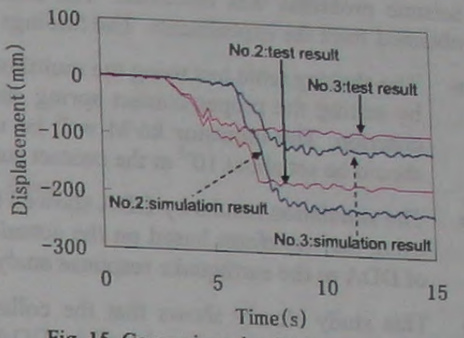


Fig. 15. Comparison the displacements for the focused blocks between laboratory tests and DDA simulation

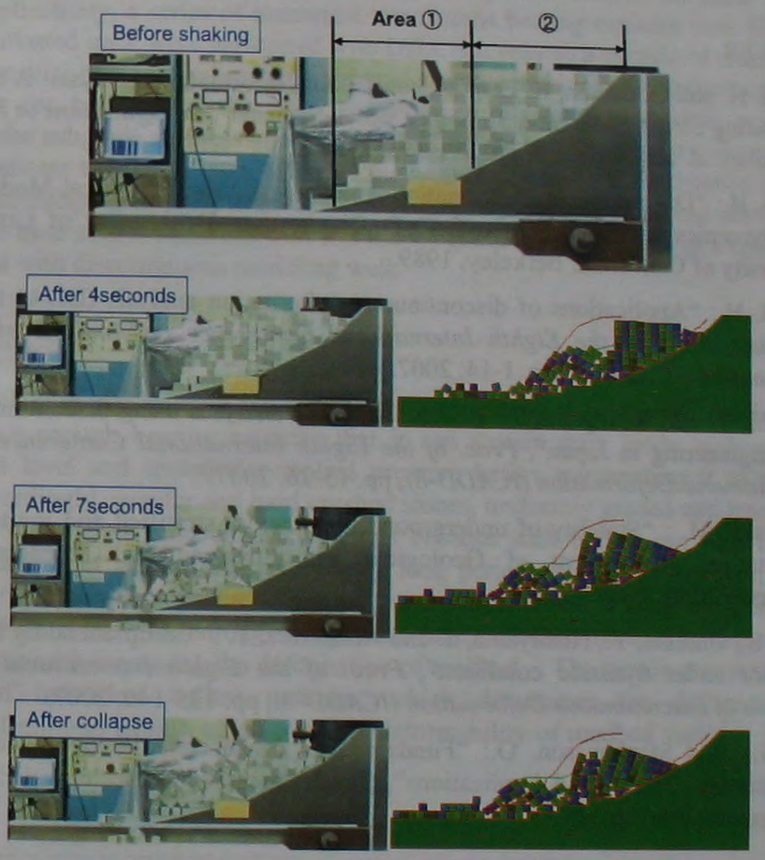


Fig. 14. Simulation results and their comparison with the laboratory tests

5. CONCLUSION

In the present study, we conducted the shaking table tests using the multilayer block model representing the rock slope and the seismic response of the model was investigated. The laboratory shaking table tests were simulated by DDA and the applicability of DDA for the

seismic problems was discussed. The simulation results by DDA agree well with the results obtained from the experiments. The findings ohtained from this study are summarized as follow.

- The shaking table test using the multilayer block model can be simulated with good accuracy by setting the proper contact spring stiffness and giving the smaller value for the "close" criterion. The indicator kn/M will be useful to determine the contact spring stiffness and should be set about 10^{-5} at the contact surface where the largest mass acting initially.
- The simulation results by DDA showed the good agreements with those from experiments by using the waveform based on the actual earthquake as an input. Therefore, the applicability of DDA to the earthquake response analysis of rock slope was verified.
- This study clearly shows that the collapse mode and the shape of entire blocks after the collapse can be reproduced well by DDA using the multilayer block model representing rock slopes.

REFERENCES

1. Shi, G. H. and Goodman, R. E. : "Discontinuous Deformation Analysis- A new Method for Computing Stress, Strain and Sliding of Block Systems", *Key Questions in Rock Mechanics*, Cundall et. al. eds, Balkema, pp. 381-393, 1988.
2. Shi, G. H.: "Discontinuous Deformation Analysis- A New Numerical Model for the Static and Dynamics of Block System", Ph.D Dissertation, Department of Civil Engineering, University of California, Berkeley, 1989.
3. Shi, G. H.: "Applications of discontinuous deformation analysis (DDA) to rock stability analysis", *Proc. of the Eighth International Conference on Analysis of Discontinuous Deformation (ICADD-8)*, pp. 1-14, 2007.
4. Ohnishi, Y. and Nishiyama S. "Recent insight of analyses using discontinuous methods in rock engineering in Japan", *Proc. of the Eighth International Conference on Analysis of Discontinuous Deformation (ICADD-8)*, pp. 15-26, 2007.
5. Tsesarsky, M. : "Stability of underground openings in stratified and jointed rock", Ph. D Dissertation, Department of Geological and Environmental Sciences, Ben Gurion University of the Negev, 2004.
6. Akao, S., Ohnishi, Y., Nishiyama, S. and Nishimura, T. : "Comprehending DDA for a block behavior under dynamic condition", *Proc. of the Eighth International Conference on Analysis of Discontinuous Deformation (ICADD-8)*, pp. 135-140, 2007.
7. Jing, L., and Stephansson, O.: "Fundamentals of Discrete Element Methods for Rock Engineering - Theory and Applications", Developments in Geotechinical Enginnering, Vol. 85, Elsevier, 2007, p.545.

Proceedings of International Mini-Symposium for Numerical Discontinuous Analyses, edited by T. Koyama, Hawaii, November, 2008

Application of DDA to mechanical behavior of granular base-subgrade system

Ishikawa, T.
Hokkaido University,Sapporo, Hokkaido, Japan
Sekine, E.
Railway Technical Research Institute, Kokubunji, Tokyo, Japan
Ohnishi, Y.
Kyoto University, Katsura, Kyoto, Japan

ABSTRACT: The paper proposes a new analytical procedure with discontinuous analysis to estimate the bearing capacity of granular base-subgrade systems used in ballasted track. To examine the applicability, a series of numerical simulations bearing capacity tests for 1/5 scale model of real ballasted track were performed with DDA that regards a particle of crush stone as a regular or an irregular polygon and assumes subgrade as an assemblage of discontinuous bodies. As the result, it can be observed that the element shape of numerical models, especially the angularity, and the subgrade stiffness has a great effect on the bearing capacity of granular base. These results indicate that DDA is an effective method to simulate the mechanical behavior of the granular base-subgrade system if an element of discontinuous analysis can imitate the real particle shape of base course materials well and the subgrade which behaves as a continuum can be approximated with discontinuous modeling well.

1. INTRODUCTION

In ballasted track (Fig. 1), railroad ballast, that is a pile of well-compacted crushed stone, is expected to have enough bearing capacity that it can sustain train loads without losing the evenness of rail level and spread the applied pressure before transmitting it to roadbed and subgrade. Accordingly, angular and hard crushed stones, uniformly graded and free of dust and dirt, have been considered good ballast materials because such ballast can bear high contact pressures from a sleeper at train passages over a long period of time. Moreover, in case the bearing capacity of roadbed drops due to rainfall, raise of ground water level and freeze-thawing, even if railroad ballast itself has strong strength and hard stiffness, the uneven settlement of rail level may increase with increasing the deformation of roadbed. The reason seems to be because the mobility of individual ballast particles, which determines the deformation-strength characteristics of railroad ballast, changes as the deformability of roadbed varies. Therefore, it

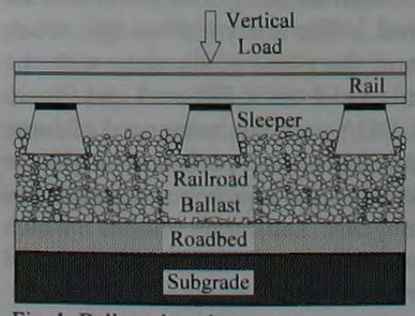


Fig. 1. Ballasted track structure.

is necessary for rationalizing a present design method for ballasted track to elucidate the bearing capacity characteristics of granular base-subgrade systems like railroad ballast - roadbed systems at ballasted tracks in terms of the particle properties of constituent particles such as particle shape and grain size distribution, and the interaction between granular base and other continuum components like sleeper and roadbed.

By some past researches [1, 2, 3], it has been showed that discontinuous analysis, which regards a ballast particle as an element, is effective in simulating the mechanical behavior of railroad ballast because it can evaluate the mobility of individual ballast particles directly. However, the precision of the numerical simulations for ballasted track with discontinuous analysis seriously depends on how to model the imhomogeneous granular assemblage of railroad ballast and the interactive multi-layer system of ballasted track. However, unfortunately, little is known about the effects of particle properties of ballast particles in discontinuous analysis and the effects of interaction between ballast particles and other components of ballasted track, especially roadbed, on the mechanical behavior of ballasted track from the viewpoint of the mechanics of granular materials. Therefore, this paper comprehensively examines the effects of particle shape and grain size distribution of ballast and the effects of roadbed stiffness on the bearing capacity of granular base-subgrade systems used in ballasted track to improve the prediction accuracy of numerical simulations with discontinuous analysis.

In this paper, a series of numerical simulations of bearing capacity tests for a model ballasted track are performed with DDA (Discontinuous Deformation Analysis [4]) models, which regard a ballast particle as a regular or an irregular polygon and assume that a roadbed is composed of one or some discontinuous blocks. Here, three types of element shapes, namely regular icosagon, regular hexagon and expanded hexagon, are employed for a ballast block and two kinds of grain size distribution are employed for railroad ballast blocks. Moreover, three types of roadbed materials, namely steel, hard rubber and soft rubber, are adopted for roadbed blocks. Based on the comparison of experimental results of model tests with analytical results of DDA simulations, the effects of particle properties such as particle shape and grain size distribution of granular base and the deformability of subgrade such as deformation modulus on the bearing capacity of granular base-subgrade systems are examined.

2. ANALYTICAL METHOD

2.1. Modeling

Numerical simulations of bearing capacity tests for small scale model ballasted track at longitudinal section [5] were performed with two-dimensional DDA models. Figure 2 shows the size, dimension and boundary condition of DDA models, which simulates a one-fifth scale model of a full-scale track. However, for bearing capacity tests, both the analytical model and the real model tracks have a single aluminum sleeper and no rail. The analytical model, which simulates a longitudinal section of model ballasted track, is in the plane strain state with the longitudinal section assumed to infinitely continue like the real model track. Figure 3 and Figure 4 shows element meshes of DDA models before loading. A DDA model is composed of some polygon blocks, namely "ballast blocks" which represent andesite ballast particles, "a sleeper block" which represents an aluminum sleeper, "roadbed block(s)" which represents various types of roadbed, "a subgrade block" which represents steel subgrade and "side blocks" which represent a rigid soil container. With regards to preparation method of the above-mentioned DDA models, the paper [6] of the authors is available for reference.

Proceedings of International Mini-Symposium for Numerical Discontinuous Analyses, edited by T. Koyama, Hawaii, November, 2008

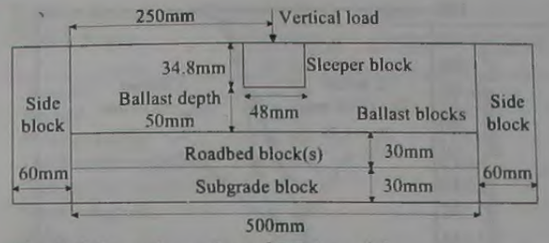
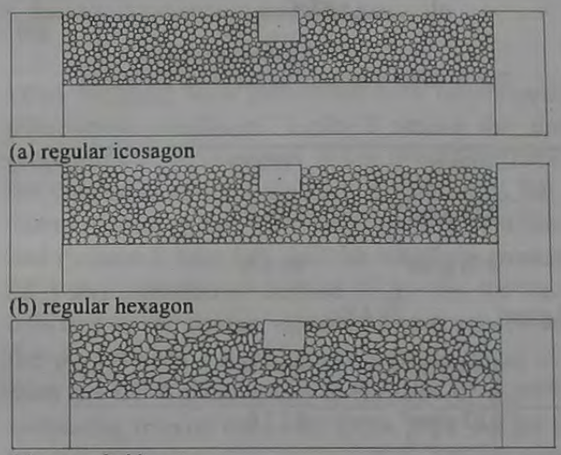


Fig. 2. Schematic section of DDA model.

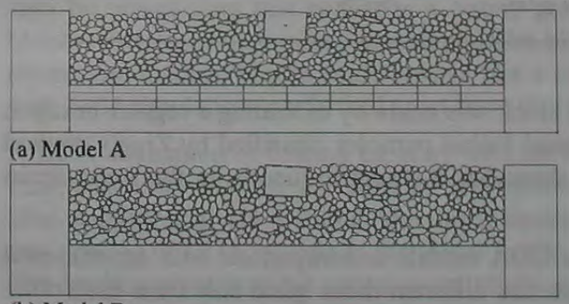


(a) regular icosagon

(b) regular hexagon

(c) expanded hexagon

Fig. 3. Element mesh (A Ballast, Ballast depth 50mm).



(a) Model A

(b) Model B

Fig. 4. Element mesh (Expanded hexagon, A Ballast, Ballast depth 50mm).

Note that DDA models in case of examining the effects of particle properties differ in the modeling method for roadbed and the element shape of ballast blocks from those in case of examining the effects of modeling method for roadbed as follows. The former DDA models have only one DDA block as roadbed unified with subgrade (Fig. 3), while the latter DDA models have either of two types of roadbeds, which differ in element discretization (Fig. 4), with a subgrade block. Here, in Figure 4, the term "Model A" is used to refer to DDA model which roadbed is divided into three blocks in height and ten blocks in width, and the term "Model B" is used to refer to the other. Moreover, the former DDA models employed either of three types of element shape, namely regular icosagon, regular hexagon and expanded hexagon, for a ballast block (Fig. 3), while the shape of ballast blocks in the latter DDA models was fixed for expanded

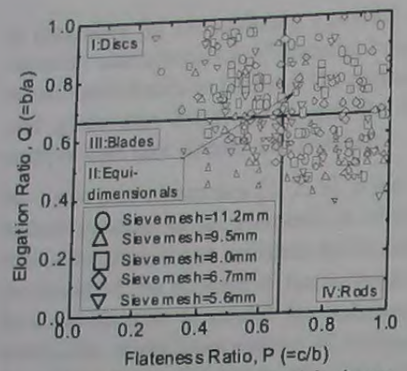


Fig. 5. Classification of ballast particle shapes.

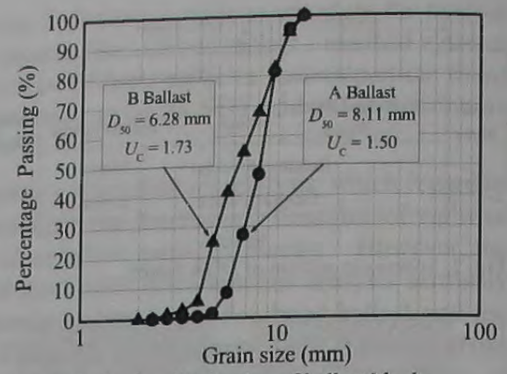


Fig. 6. Grain size distribution of ballast blocks.

Table 1. Features of railroad ballast in DDA models.

Ballast Type	Ballast Shape	Density	Porocity
Number of blocks			
A Ballast	regular icosagon	2.19 g/cm^3	19.0 %
610			
	regular hexagon	2.16 g/cm^3	20.1 %
598			
	expanded hexagon	2.12 g/cm^3	21.4 %
451			
	Experiment	1.46 g/cm^3	46.0 %
B Ballast	regular icosagon	2.22 g/cm^3	17.7 %
913			
	regular hexagon	2.21 g/cm^3	18.3 %
853			
	expanded hexagon	2.24 g/cm^3	16.9 %
552			

hexagon (Fig. 4). Here, an expanded hexagon block was made by extending a regular hexagon block in consideration for the aspect ratio of actual ballast particles classified by Zigg's method [7] as shown in Figure 5 because the particle shape has a strong influence on the stress-strain behavior of granular materials [8].

Table 1 shows the feature of railroad ballast in DDA models in comparison with experimental conditions. Two types of railroad ballast which had different mean grain size from each other were employed in this paper. The gradation curves for railroad ballast of DDA models, which are equivalent to the gradation curves of railroad ballast employed in real bearing capacity tests of the one-fifth scale model ballasted track, are shown in Figure 6 together with their mean grain sizes (D_{50}) and uniformity coefficients (U_c). Here, in Figure 6, the term "A Ballast" is used to refer to model ballast which uniformity coefficient is smaller, and the term "B Ballast" is used to refer to the other. Seeing Table 1, it is recognized that for the same grain size distribution, the total number of ballast blocks increases in order of regular icosagon, regular hexagon and expanded hexagon, and that for the same element shape, the total number of ballast blocks in DDA models using A Ballast is larger than those in DDA models using B Ballast. In the meantime, the porosity of DDA models is much smaller than that of experiments, though there is little difference in the porosity among all DDA models. This phenomenon seems to be mainly caused by the reason that the DDA models used in this study are two-dimensional while the laminated state of real railroad ballast is three-dimensional.

Proceedings of International Mini-Symposium for Numerical Discontinuous Analyses, edited by T. Koyama, Hawaii, November, 2008

Table 2. Material properties of DDA models.

Block Name	Unit mass ρ	Young's modulus E	Poisson's ratio ν	Cohesion C_μ	Friction Angle ϕ_μ
	g/cm^3	GPa		kPa	deg.
Sleeper	2.70	70.0	0.30	0	37.0
Ballast	2.70	0.02	0.10	0	55.0
Steel roadbed	7.80	210.0	0.30	400.0	37.0
Hard rubber roadbed	0.94	0.004	0.48	150.0	37.0
Soft rubber roadbed	0.94	0.001	0.48	10.0	37.0
Steel subgrade	7.80	210.0	0.30	0	37.0
Side	7.80	210.0	0.30	0	37.0

2.2. *Analytical conditions*

DDA analyses were performed with two-dimensional models using linear elastic blocks under plane-strain condition. Table 2 shows the material properties of blocks and the interface proper-ties of block edges. When two DDA blocks come in contact, springs and a frictional slider are created at contact points. Accordingly, the analytical input parameters of DDA blocks are characterized by the material properties of a block, namely unit mass (γ), Young's modulus (E) and Poisson's ratio (ν), and the interface properties of block edges, namely block friction angle (ϕ_μ) and cohesion of surface (C_μ). As for the material properties, the parameters were set by referring to the design values and past experimental results [9]. As for the interface properties, the ϕ_μ between ballast blocks was set equal to 55° because the internal friction angle derived from the DDA simulations in the case of ϕ_μ=55° indicated the best fit to experimental results in simulating triaxial tests with DDA [9]. As for the ϕ_μ between a ballast block and other kinds of blocks, the value was set equal to 37° by referring to the real test results. Besides, the C_μ between ballast blocks and the C_μ between a ballast block and all other blocks were set equal to zero by considering that ballast is a coarse granular material, while the C_μ between roadbed blocks when dividing roadbed into some DDA blocks was set at a specified value so that element discretized roadbed blocks could behave like a continuum body by comparing DDA simulations with FEM simulations performed apart from this paper.

A DDA simulation of bearing capacity tests for model ballasted track was performed as follows. First, a stability analysis was done by gravity force of 9.8 m/s^2. Here, the state of DDA models after stability analysis is called "the initial loading state" (Fig. 3, Fig. 4). Second, vertical load was applied to DDA models in the initial loading state while the gravity force was also applied. The loading point was the center point of the sleeper block as shown in Figure 2. A vertical load was slowly increased from 0 kN to 5 kN at the constant loading speed, which was regarded as a static load like the actual experimental condition. Here, for the experiments, stage loading was adopted pursuant to a plate loading test, while for the analyses, monotonic loading was adopted for a saving of calculation time. However, in case of static loading, it may safely be assumed that the difference in loading methods has little influence on the load-displacement relation.

3. RESULTS AND DISCUSSION

This chapter examines the effects of particle properties such as particle shape and grain size distribution of granular base and the effects of deformability for subgrade such as deformation

mudulus on the bearing capacity of granular base-subgrade systems. Here, the bearing capacity of DDA models can be defined as the vertical displacement at the vertical load (P) of 2 kN and 5 kN. Accordingly, it is considered that the DDA model has stronger bearing capacity in case of obtaining smaller vertical displacement at the specified vertical load.

3.1. Effect of Particle Properties

First, discussed is the difference in the load-displacement relations of ballasted tracks due to the difference in the element shape of a ballast block. Figure 7 and Figure 8 show the relations between the applied vertical load (P) and the vertical displacement (u) at the center of gravity of the sleeper block obtained from DDA simulations which differ in particle shape for A Ballast and B Ballast, respectively. For plots with the same grain size distribution, it is clearly shown that the bearing capacities of DDA models decrease in order of expanded hexagon, regular hexagon, and regular icosagon. This indicates that the difference in the element shape of a ballast block has a considerable influence on the load-displacement relations of ballasted tracks in DDA simulations. Figure 7 also compares analytical results with experimental results. The load-displacement relation in case of regular icosagon blocks has much smaller stiffness than experimental results, while the load-displacement relations in case of expanded hexagon or regular hexagon blocks resembles experimental results.

Figure 9 compares the vertical displacement at P=5kN derived from analytical results of each DDA models. In Figure 9, though the bearing capacity of DDA model using regular icosagon blocks is much smaller than analytical results using expanded hexagon blocks or regular hexagon blocks, the bearing capacities in case of expanded hexagon blocks and regular hexagon blocks are

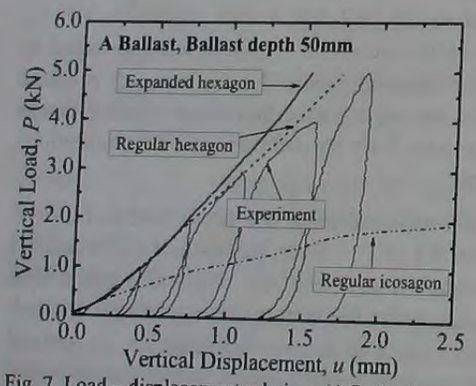


Fig. 7. Load – displacement relations (A Ballast).

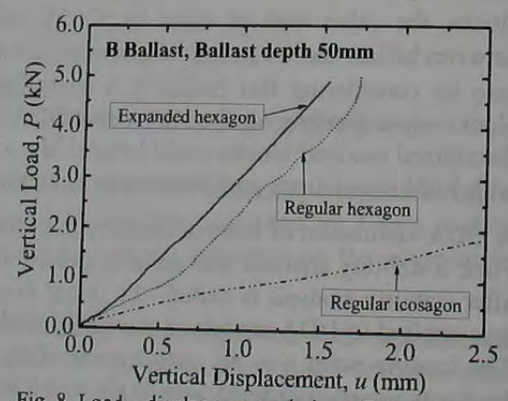


Fig. 8. Load – displacement relations (B Ballast).

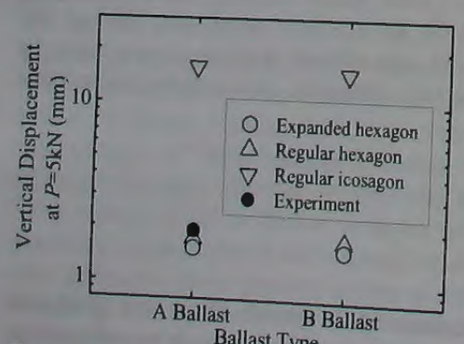


Fig. 9. Comparison of bearing capacity.

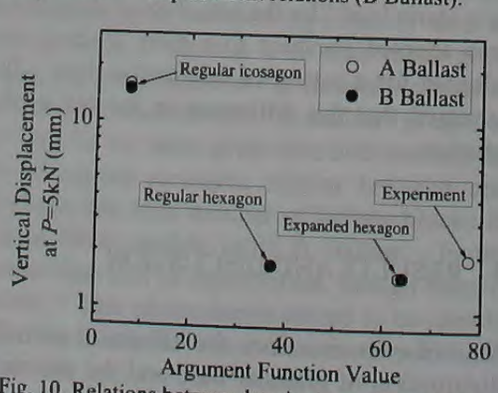
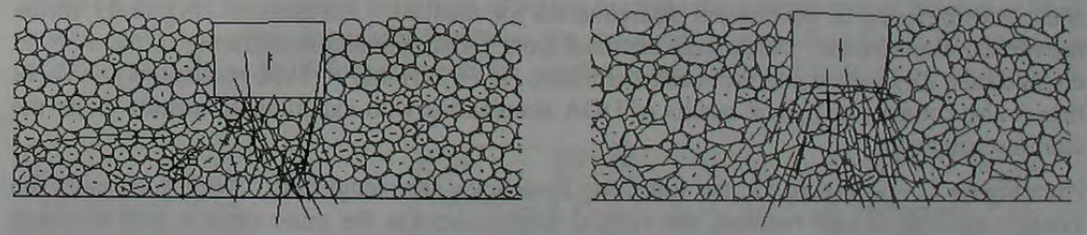


Fig. 10. Relations between bearing capacity and NA_{fv}

approximately the same. In terms of the mechanics of granular materials, the difference between expanded hexagon blocks and regular hexagon blocks is the sphericity of DDA blocks, while the difference between regular hexagon blocks and regular icosagon blocks is the angularity of DDA blocks. Accordingly, these results indicate that the angularity of ballast blocks has greater effect on the bearing capacity of ballasted tracks in discontinuous analysis than the sphericity.

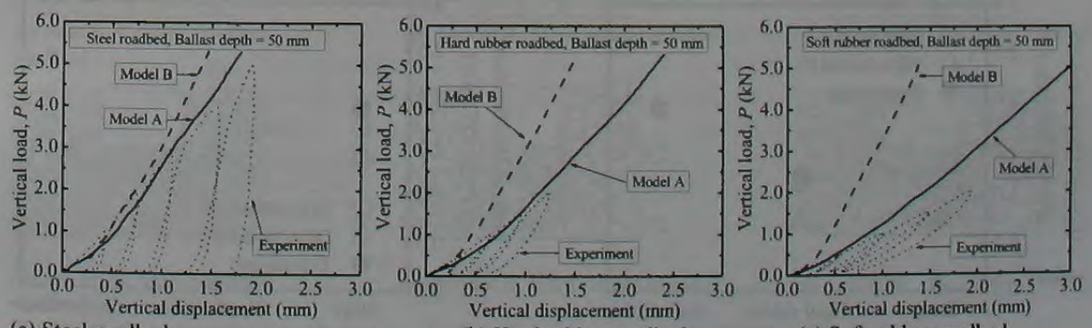
Figure 10 compares the relations between the vertical displacement at P=5kN and the normalized argument function value (NA_{fv}) of each DDA models with experimental results. Here, the normalized argument function (NA_{fv}) is a kind of evaluation indexes for the angularity of a particle propsed by Kono et al. [10]. In Figure 10, it is recognized that though the bearing capacity of DDA models using regular icosagon blocks is much smaller than that of experimental results, with approaching the NA_{fv} value of DDA models to that of real ballast particles, the bearing capacity of DDA models is approximately equal to experimental results. This indicates that the imitation of the shape of real ballast particles makes the reliability of analytical results improved, and that the NA_{fv} value is one of effective indexes to evaluate the analytical precision in simulating the mechanical behavior of granular assemblage with discontinuous analysis.

Next, discussed is the difference in the load-displacement relations due to the difference in the grain size distributions of ballast blocks. Comparing Figure 7 with Figure 8, for plots with the same element shape, the bearing capacity of DDA models for A Ballast is larger than that for B Ballast in case of regular icosagon blocks. However, in case of the other shapes, the clear tendency cannot be recognized. These results indicate that the difference in the grain size distributions of model ballast has a little influence on the bearing capacity of ballasted tracks in discontinuous analysis compared with the influence of particle shape. The same is true for Figure 9.



(a) Regular icosagon, A Ballast. (b) Expanded hexagon, B Ballast.

Fig. 11. Deformation of ballast blocks and distribution of principal stress.



(a) Steel roadbed. (b) Hard rubber roadbed. (c) Soft rubber roadbed.

Fig. 12. Load – displacement relations (A Ballast).

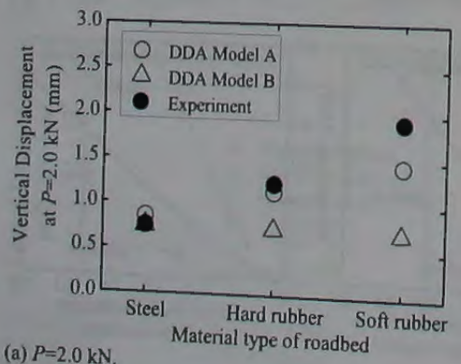
Finally, the influence of the element shape of ballast blocks on the mechanical behavior of railroad ballast in DDA simulations is examined. Figure 11 shows the deformation of ballast blocks and the distribution of principal stress for DDA blocks at P=5kN. In Figure 11, it is recognized that the analytical results in case of regular icosagon blocks differ from those of expanded hexagon blocks in the distribution of principal stress. For example, in case of regular icosagon blocks, there are many ballast blocks underneath the sleeper block which principal stress turns toward horizontal direction. Whereas, in case of expanded hexagon blocks, the principal stress of the ballast blocks mainly turns toward vertical direction. Besides, in Figure 11b, it can be observed that high principal stress appears underneath the sleeper block. However, the principal stresses observed in Figure 11a are smaller compared with those in Figure 11b on the whole.

The reason for this is that DDA models using regular icosagon blocks cannot sustain vertical load by ballast blocks under the sleeper block alone as it has very low bearing capacity, though DDA models using expanded hexagon blocks can sustain it due to their high bearing capacity. Consequently, the lateral flow occurs in railroad ballast around the sleeper block in Figure 11a, and it leads to large settlement of the sleeper block. These results indicate that the element shape of a ballast block is one of the dominant factors to determine the mechanical behavior of railroad ballast in numerical simulations with discontinuous analysis, and that the mobility of individual particles is concerned with the mechanical properties of granular assemblage.

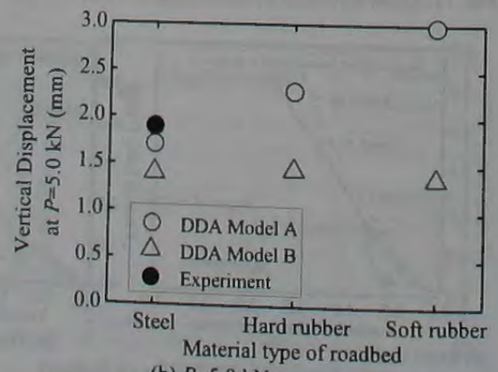
3.2. *Effects of modeling method for roadbed*

First, discussed is the difference in the bearing capacity of ballasted tracks due to the difference in the element discretization for roadbed and the roadbed stiffness. Figure 12 shows the relations for every material type of roadbed between the applied vertical load (P) and the vertical displacement (u) at the center of gravity of the sleeper block, which were obtained from DDA simulations differing in the element discretization for roadbed. Furthermore, Figure 13 shows the vertical displacement, which were obtained from DDA simulations differing in the element discretization for roadbed and the roadbed stiffness, at P=2kN and P=5kN, respectively. These figures also compare analytical results of DDA simulations with experimental results under the same test conditions.

From Figure 12 and Figure 13, the following tendencies are recognized. With decreasing the Young's modulus (E) for roadbed, the vertical displacement at the same vertical load increases regardless of the element discretization for roadbed. Besides, for the same vertical load, the



(a) P=2.0 kN.



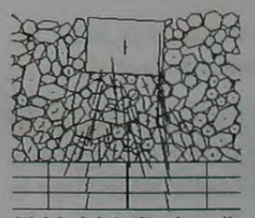
(b) P=5.0 kN.

Fig. 13. Comparison of bearing capacity among models under different types of road

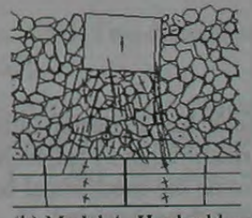
vertical displacement of Model A is larger than that of Model B, irrespective of the Young's modulus (E) for roadbed. In comparing DDA simulations with experimental results under the same test conditions, the analytical result of Model A resembles the experimental result at every the roadbed materials as compared with those of Model B, though the difference between both results becomes larger at low Young's modulus (E) for roadbed. These results indicate that Model A having element discretized roadbed, which deformability is high in comparison with Model B having only one roadbed block, is a numerical modeling appropriate to perform bearing capacity tests of ballasted track on soft roadbed in terms of the prediction accuracy of numerical simulations with discontinuous analysis. In other words, if the roadbed which behaves as a continuum can be approximated well with discontinuous modeling by considering the roadbed stiffness, DDA can simulate the mechanical behavior of ballasted tracks regardless of roadbed materials, without considering the interaction between granular assemblage like ballast and a continuum body like roadbed beforehand.

Next, the influence of the element discretization for roadbed on the mechanical behavior of railroad ballast in DDA simulations is examined. Figure 14 shows the deformation of ballast blocks and the distribution for principal stress vectors of ballast blocks at P=5kN obtained from DDA simulations for every material type of roadbed and every DDA model type, respectively. Figure 15 shows the distribution for displacement vectors of ballast blocks at P=5kN obtained from DDA simulations under various analytical conditions like Figure 14. Here, a displacement vector is defined as the movement of a DDA block from the initial loading state to the state at P=5kN.

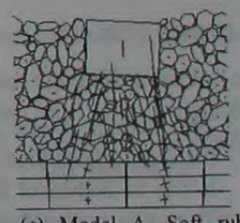
From Figure 14, it is recognized that the analytical results of Model A differ from those of Model B in the distribution of principal stress. For example, in case of Model A, the principal stress of ballast blocks mainly turns toward vertical direction, and high principal stress appears underneath the sleeper block. Whereas, in case of Model B, it can be observed that principal stress vectors spread out toward the diagonal lower part of both sides from the undersurface of the sleeper block. Besides, with decreasing the roadbed stiffness, the deformation of roadbed blocks becomes large in Model A, while the deformation of the roadbed block cannot be discerned in Model B.



(a) Model A, Steel roadbed



(b) Model A, Hard rubber roadbed



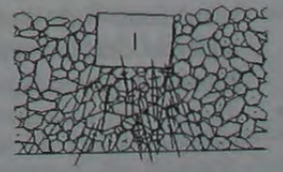
(c) Model A, Soft rubber roadbed



(d) Model B, Steel roadbed



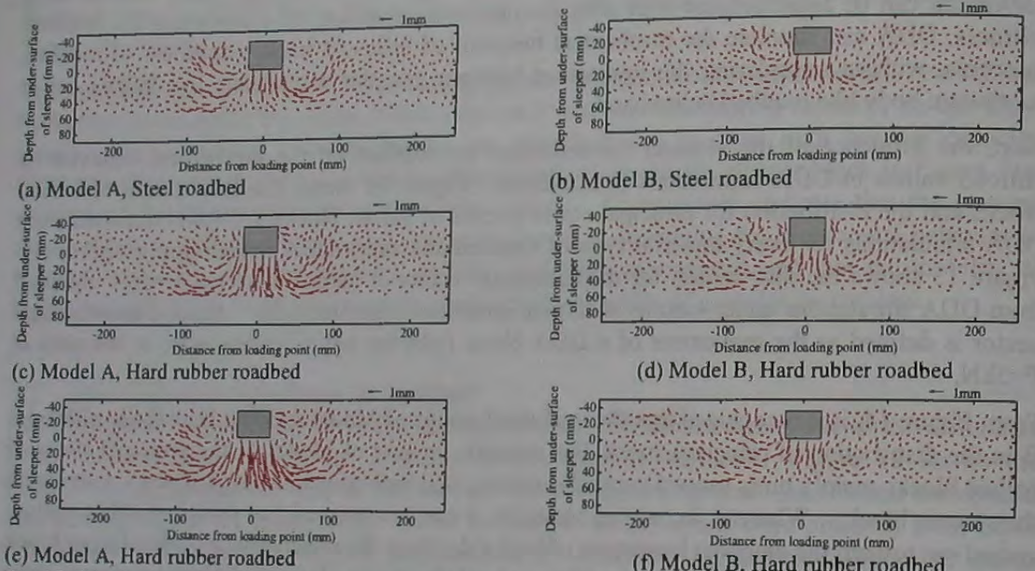
(e) Model B, Hard rubber roadbed



(f) Model B, Soft rubber roadbed

Fig. 14. Deformation of railroad ballast and distribution of principal stress in DDA simulations.

Furthermore, from Figure 15, it is recognized that displacement vectors of ballast blocks underneath the sleeper block in Model B are smaller than those in Model A, and that with decreasing the roadbed stiffness, though the movement of ballast blocks increases in Model A, it hardly changes in Model B. These results indicate that in DDA simulations the element diseretization for roadbed has a strong influence on the stress distribution inside railroad ballast and the movement of ballast blocks. Consequently, one can safely consider that the bearing capacity of granular base has been different according to the modeling method of subgrade.



(a) Model A, Steel roadbed (b) Model B, Steel roadbed

(c) Model A, Hard rubber roadbed (d) Model B, Hard rubber roadbed

(e) Model A, Hard rubber roadbed (f) Model B, Hard rubber roadbed

Fig. 15. Distribution of displacement inside railroad ballast in DDA simulations.

4. CONCLUSIONS

The following findings can be obtained;

- The element shape of a ballast block has a greater influence on the bearing capacity of ballasted tracks than the grain size distribution of ballast blocks. Especially, the angularity is one of dominant factors to determine the mechanical behavior of granular assemblage in discontinuous analysis, compared with the sphericity.
- The imitation of the shape of real ballast particles makes the reliability of numerical simulations with discontinuous analysis improved. In this situation, the normalized argument function value is one of effective indexes to evaluate the analytical precision in simulating the mechanical behavior of granular assemblage with discontinuous analysis.
- The element discretization for roadbed has a strong influence on the bearing capacity of ballasted tracks as well as the deformation modulus of roadbed because the stress distribution inside railroad ballast and the mobility of a ballast block differ according to the roadbed stiffness. Therefore, the precision of numerical simulations with discontinuous analysis depends on the modeling method for roadbed.

- A DDA model employing element discretized roadbed with high deformability is a numerical modeling appropriate to perform bearing capacity tests of ballasted track on soft roadbed. In short, DDA can simulate the mechanical behavior of ballasted tracks regardless of roadbed materials, if a continuum like roadbed can be approximated well with aggregate discontinuums.

These findings lead to tbe conclusion that DDA is an effective method to simulate the mechanical behavior of the granular base-subgrade system if an element of discontinuous analysis can imitate the real particle shape of base course materials well and the subgrade which behaves as a continuum can be approximated with discontinuous modeling well.

ACKNOWLEDGEMENT

The authors would like to thank Prof. Seiichi Miura, Hokkaido University for many invaluable discussions and suggestions, and Mr. Takehiko Kamei, Hokkaido University, who performed numerical simulations and arranged the analytical results.

REFERENCES

1. Aikawa, A., A. Namura, M. Ishida, and Y. Takao. 2007. Dynamic behavior and kinetic energies at the rail weld of ballasted track imparted by moving trains. In *Proceedings of the Eleventh Japanease Domestic Conference on Railway Mechanics, Tokyo, July 2007*, 27–32. (in Japanese).
2. Saussine, G., C. Chplet, P.E. Gautier, F. Duboris, C. Bohatier, and J.J. Moreau. 2004. Modeling ballast under cycle loading using discrete element method. In *Proceedings of the International Symposium on Cycle Behavior of Soils and Liquefaction Phenomena, Bochum, 31 March – 2 April 2004*, ed. Triantafylidis, 649–658.
3. Kono, A., and T. Matsushima. 2008. Effect of loading frequency on the settlement of granular layer. In *Proceedings of the First International Conference on Advances in Transportation Geomechanics, Nottingham, 25 – 27 August 2008*, eds. E. Yu et al, 601–606.
4. Shi, G.H. and R.E. Goodman. 1985. Two dimensional discontinuous analysis. *J. Num. Anal. Methods. Geomech.* 9: 541–556.
5. Ishikawa, T., and E. Sekine. 2002. Effects of Moving Wheel Load on Cyclic Deformation of Railroad Ballast. In *Proceedings of the Fifth International Conference on Railway Engineering-2002, London, 3 – 4 July 2002*, eds. M.C. Forde et al, [1/1(CD-ROM)].
6. Ishikawa, T., K. Kobayashi, E. Sekine, and Y. Ohnishi. 2005. Evaluation of the effect of particle shape on the bearing capacity of railroad ballast with discontinuous analysis. In *Proceedings of the Seventh International Conference on Bearing Capacity of Roads, Railways and Airfields, Trondheim, 27 – 29 June 2005*, ed. I. Horvli, [1/1(CD-ROM)52].
7. Zingg, T. 1935. Beitrage zur Schotteranalyse. *Schweiz. Miner. Petrog. Mitt.* 15: 39-140.
8. Kohata, Y., G.L. Jiang, and E. Sekine. 1999. Deformation characteristics of railroad ballast as observed in cyclic triaxial tests. In *Poster Session Proceedings of the Eleventh Asian Regional Conference on Soil Mechanics and Geotechnical Engineering, Seoul, 16 – 20 August 1999*, eds. S.W. Hong et al, 35–40. Rotterdam: Balkema.

9. Ishikawa, T., Y. Ohnishi, and A. Namura. 1997. DDA applied to deformation analysis of coarse granular materials (ballast). In *Proceedings of the second International Conference on Analysis of Discontinuous Deformation, Kyoto, 11 – 12 July 1997*, ed. Y. Ohnishi, 253–262.

10. Kono, A., E. Sekine, and Y. Kohata. 2000. A study on shape evaluation method of granular material. In *Proceedings of the Fifth International Symposium on Unbound Aggregates in Roads, Nottingham, 21 – 23 June 2000*, ed. A.R. Dawson, 35–40. Rotterdam: Balkema.

Proceedings of International Mini-Symposium for Numerical Discontinuous Analyses, edited by T. Koyama, Hawaii, November, 2008

Studies on the Property of Impact Velocity Ratio and Application to the Rockfall Simulation by DDAball

T.SHIMAUCHI.
Meiji-Consultant Co.Ltd,Saitama 333-0801,Japan
K.NAKAMURA.
Depertment of civil Engineering, Faculty of Engineering, Tottori University, Tottori, Japan
N.SAKAI
Natinal research Institute for Earth science and Disaster prevention, Ibaraki ,Japan
I.HAGIWARA
Suncoh Consultants Co.,Ltd., Tokyo,Japan
Y.Ohnishi and S.Nishiyama
Department of Urban and Environmental Engineering, Kyoto University, Kyoto, Japan

ABSTRACT: Rockfall is one of the major hazards in rock slope cuts for highways and railways in the mountainous area of Japan . For the prevention of rockfall disaster, it is important to evaluate the influence on maintenance object beforehand. The rockfall simulation is used for the evaluation..

Recently many rockfall simulations have been developed (DDA, DEM). At present, the analysis taking account of the shape of falling rock mass and the three-dimensional topography are feasible. However, the property of input parameter (for example, the coefficient of restitution and velocity-ratio) needed for analysis and its setting method are still not clear. In this investigation, the property of the input parameter for the rockfall simulation has been clarified through the field and laboratory experiment and the applying method for the simulation by DDAball is proposed.

1 INTRODUCTION

Recently, various rockfall simulations have been developed. They are useful for the prevention of rockfall disaster. In the rockfall simulation, many input parameters are needed. Above all, the parameter for the impact process has a great influence on the range of falling distance and the locus effect, thus it is very important for the design of countermeasure personnel.

Eqs. (1) ~ (3) are the typical parameters for impact used in the rockfall simulation. Every symbol is shown in Fig. 1.

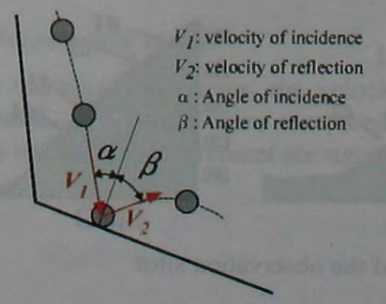


Fig. 1 Properties of bouncing motion

$$R_n = \frac{V_2 \cos\beta}{V_1 \cos\alpha} \quad (1)$$

$$R_t = \frac{V_2 \sin\beta}{V_1 \sin\alpha} \quad (2)$$

$$Ev = \frac{\frac{1}{2}mV_2^2}{\frac{1}{2}mV_1^2} = \left(\frac{V_2}{V_1}\right)^2 \quad (3)$$

Eq. (1) is the normal component of the restitution coefficient. It is used in many rockfall analyses to the central issue of particle analysis and is known as the parameter expressing the material difference of impact ground. Eq. (2) is the tangential component of restitution coefficient and is usually used as the pair of the velocity ratio in the normal direction. This coefficient is also expressed as the value of material distinction but its detailed property is not known. On the other hand, Eq. (3) is the velocity ratio before and after the impact and is usually expressed as the line velocity component of the velocity energy ratio which is designated as the squared velocity ratio. In DDA, it is input as the velocity energy ratio (squared velocity ratio) or the velocity ratio. In Japan , the following typical data were published previously from the field experimental results at more than ten places.

Velocity ratio of normal direction (Rn), soil and sand 0.61±0.23 , bedrock 0.54±0.26 .

Velocity ratio of tangential direction (Rt), soil and sand 0.65±0.24 , bedrock 0.76±0.18.

Velocity energy ratio (Ev), soil and sand 0.71±0.19 , bedrock 0.66±0.23.

However, concerning the above result some problems should be pointed out: for instant, the bedrock exhibits a lower value than the soil and sand which are easier to absorb energy as Rn and Ev. Further, the values of Rn and Rt exceeding 1.0 were often measured. On the other hand, concerning the velocity ratio of normal direction, the property depending on the incident velocity is also known, but the relation of this property with the above-mention values is not clear. (Note: Rn is tbe abbreviation of velocity ratio of normal direction and Rt is that of the velocity ratio of tangential direction) Therefore, (1) we have investigated the property of velocity ratio through the field and laboratory experiment; (2) the applying method of this property has also been examined with the rockfall simulation by DDA.

2 . EXPERIMENT FOR CLARIFYING THE PROPERTY OF VELOCITY RATIO

2.1 Field and laboratory experiment

The field experiment was performed on the slope of four spots. Fig.2 is the typical cross-section. Site A, B are the scenes after the removal of the dangerous rock lump. Site C is the macadam scene and site D is the slope of grass. All of them are the ground with a common characteristic of easily absorbing the impact energy. However site A, B include a great transformation of topography during the falling route; on the other hand site C, D are the comparatively monotonous slopes. Further, the points(a1, a2, d1, d2 etc.) as shown in the symbols of the figure are those where the restitution was measured.

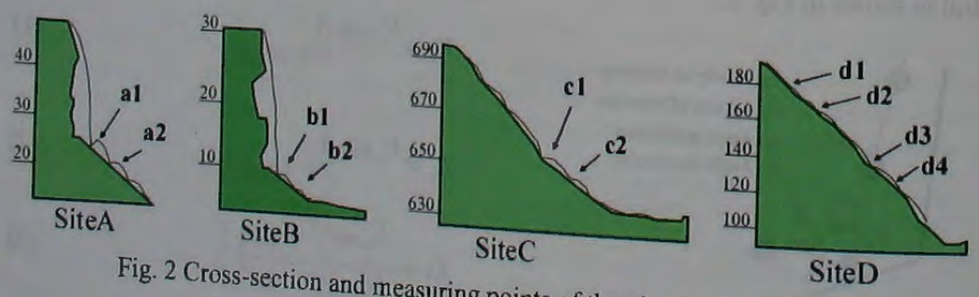


Fig. 2 Cross-section and measuring points of the observation sites

In the measurement, a digital video-camera (lens: 3CCD, 340 thousand pixels) purchased from market was used. In the field where it is possible to photograph from the orthogonal direction against the falling route, the results were analyzed with the two-dimensional method. Nevertheless, in the field where it is difficult to photograph from the orthogonal direction, the photographic results were analyzed in the case while the topography drawn up with photographic results from plural directions by the computer-graphics (CG) and the analyzed results overlapped each other (Fig. 3). The measurement of the impact position and locus of the rockfall was obtained from the overlapped portraits taken within the interval of 3/30 ～ 5/30 seconds

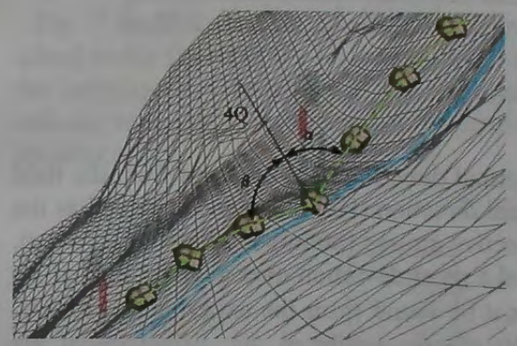


Fig. 3 The record of the moving state of the falling rock and the CG mesh on the computer.

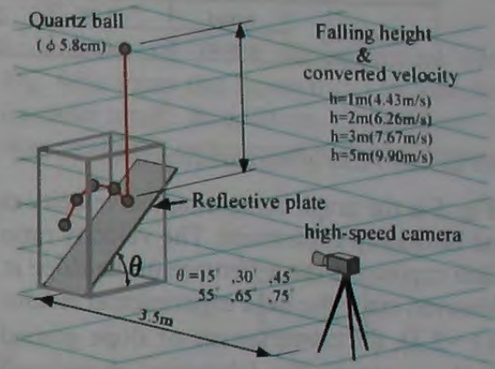


Fig. 4 Data collection set-up in laboratory experiment.

Meanwhile, the laboratory experiment was carried out with a wooden plate of width 0.4 m , length 1.0 m , thickness 5 cm and a granite plate used as the reflective plate. A quartz ball with a diameter of 6 em was allowed to fall. The impact velocity was measured by changing the falling height of the ball. There are four kinds of the converted impact velocity, namely: 4.43, 6.26, 7.67, 9.90 m /se. Moreover the impact angle was measured by changing the inclination of the reflective plate. The incident angle has seven kinds, 0, 15, 30, 45, 55, 65, 75°

In the measurement, a high-speed camera was used. The sampling time was 3/30 seconds, same as that in the field experiment. The measuring items were incident reflective velocity and incident reflective angle.

2.2 Measurement results

From the measuring items, the velocity ratio of normal direction and the velocity ratio were measured. The results were compared with incident velocity of normal direction respectively. These results of measurement are summarized in Table. 1.

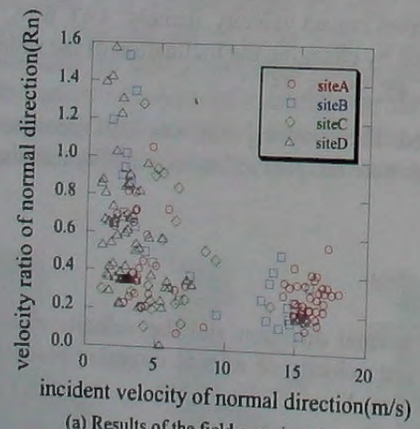
Table. 1 Analytical results of the observations

		incident velocity of normal direction (V_{nin})		Velocity ratio of normal direction (Rn)		Velocity ratio (Rv)	
		mean	stdv	mean	stdv	mean	stdv
field	site A	4.20	6.00	0.48	0.20	0.67	0.21
	site B	8.52	5.79	0.63	0.56	0.49	0.21
	site C	5.77	2.54	0.48	0.33	0.65	0.24
	site D	2.92	1.42	0.61	0.45	0.71	0.37
laboratory	wood	4.45	2.19	0.30	0.09	0.61	0.23
	granit	4.44	2.16	0.77	0.07	0.79	0.09

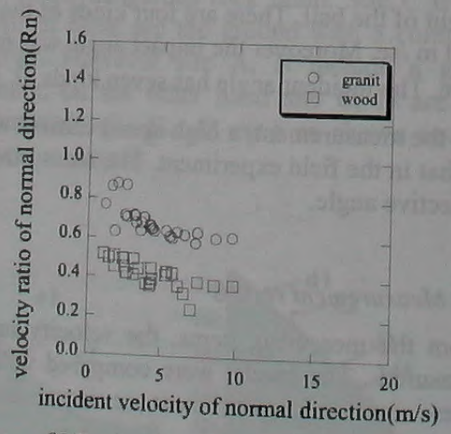
(a)Velocity ratio of normal direction

Fig. 5 is the graph comparing the velocity ratio of normal direction (Rn) obtained from the field and laboratory experiment. The velocity ratio of normal direction (Rn) is generally treated as the value expressing the difference of the slope at the reflective ground (mainly hardness or softness). However, since the field experimental results exhibited a great deviation over a wide range of Rn (0.1～2.1), the characteristic of slope ground could not be found from the experimental results. On the contrary, the laboratory experimental results clearly exhibited the difference of the reflective plate.

In many field experiments, the great deviation of data usually becomes the subject of discussion. The difficulty in the precise measurement of incident reflective angle at the impact point and the difficulty of fully catching the influences of rotation and slipping etc are often regarded as the causes of deviation. In addition, the different destruction state of the ground due to the impact angle and velocity of rockfall may also be regarded as the cause. This effect seems to be the great influence of velocity and angle at the reflective side.



(a) Results of the field experiments



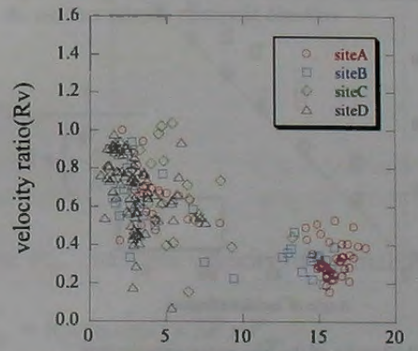
(b) Results of the laboratory experiments

Fig.5 The relation graph of the velocity ratio of the normal direction(Rn) and incident velocity of normal direction

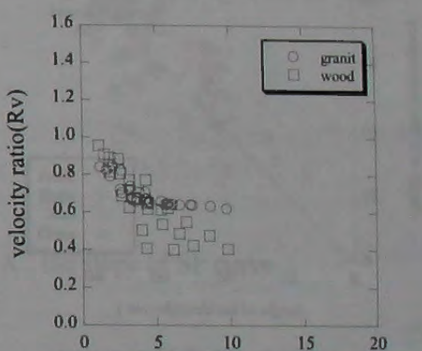
(b)Velocity ratio

Fig. 6 is the graph comparing the velocity ratio obtained from the field and laboratory experiments. It can be seen from this figure that the velocity ratio also depends on the incident velocity of normal direction, similar to the velocity ratio of normal direction. At first sight, the velocity ratio also shows a great deviation, but if it is compared with the laboratory experimental results, the distributions of both cases are similar and the difference of the velocity ratio of normal direction cannot be found. Differing from the velocity ratio of normal direction, the field experimental results did not indicate that Rv >1.0. This might be due to the fact that the component of the incident reflective angle is not included in the velocity ratio and the reading errors during the measurement are not included.

Fig. 7 showed that the incident angle and the incident velocity during the experiment were added to the figure of the laboratory experiment in Fig. 6(b). From this figure it can be seen that the velocity ratio decreases as the incident angle becomes small. In addition, the influence to velocity ratio due to the change of incident velocity was smaller in comparison to the influence of incident angle.



(a) Results of the field experiments



(b) Results of the laboratory experiments

Fig.6 The relation graph of the velocity ratio(Rv) and incident velocity of normal direction

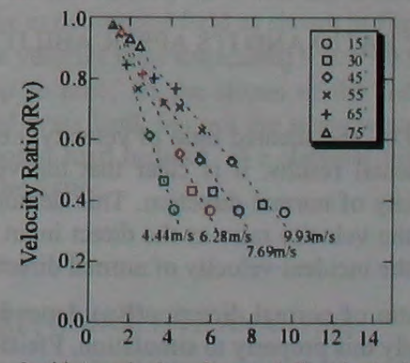


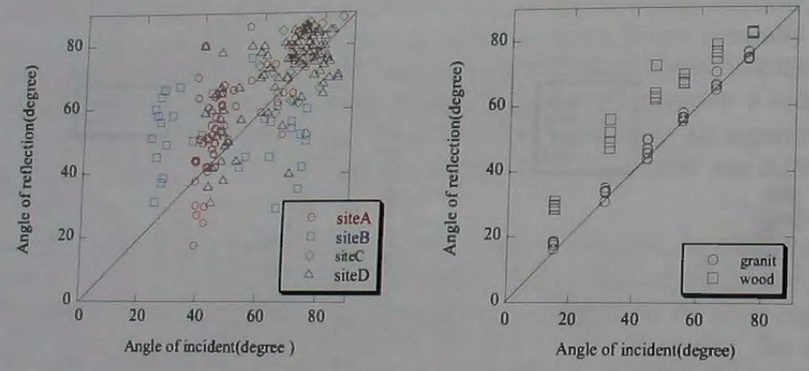
Fig 7 Analytical results of the laboratory experiments

(c)Change of incident reflective angle

From the field measurement results of velocity ratio in the normal direction and the velocity ratio, it is known that the change of incident reflective angle has a great influence on the field measurement results. Fig. 8 shows the relation of incident reflective angle in the field experiment. The laboratory experimental results were also plotted in that figure.

In the laboratory experiment, as in the case of granite, the higher the rigidity of reflective plate is, the closer to the relation of nearly 1:1 the incident reflective angle will be. However in the case of wooden reflective plate, a large hollow would occur. Then the smaller the incident angle is, the greater the tendency of incident angle > reflective angle will be. From the field experimental results, this tendency can also be slightly observed. When the incident angle is greater, the deviation will appear in a wider range.

Considering the properties of such two cases, when discussing the values of velocity ratio and the velocity ratio of normal direction, we should not merely compare their simple values, but have to discuss those values including the velocity and angle at the time of incident reflection.



(a) Results of the field experiments (b)Results of the laboratory experiments

Fig.8 The relation graph of the angle of incident and the Angle of the reflection

3 PROPERTY OF VELOCITY RATIO AND ITS APPLICABILITY

In the rockfall simulation by DDA, the squared ratio of velocity, i.e. the velocity ratio is used as the input value. From experimental results, it is clear that the velocity ratio changes greatly depending on the incident velocity of normal direction. This demonstrates the fact that it is not appropriate to consider merely the velocity ratio as the direct input value. Thus we consider the velocity ratio as the function of the incident velocity of normal direction.

It is known that the velocity ratio of normal direction(Rn) depends on the incident velocity of normal direction. In order to apply this property to simulation, Pfeiffer et al. [1] proposed a method to approximate the property by using the curve designated as "scale factor" as shown in Eq. 5. To apply the "scale factor" to velocity ratio, we proposed Eq. 6, where Rv(scaled) is the starting point when the scale factor is used. Further, K is the slope of SF curve against the incident velocity of normal direction. Concretely, when Rv(scaled)= 1.0, K = 10 and the incident velocity of normal direction equals to 10 m /s, the velocity ratio obtained from the "scale factor is

0.5. Consequently, when K is small, the velocity ratio changes greatly with the small incident velocity of normal direction; but when K is large, the range of change becomes small.

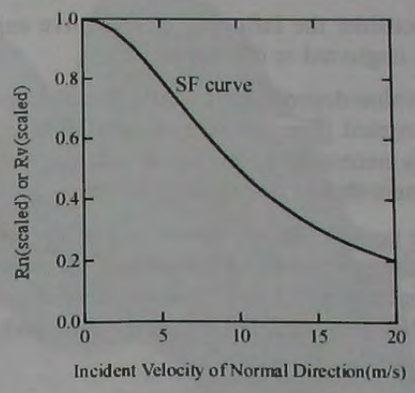


Fig.9 Scaling Factor curve for Rn & Rv as a function of the incident velocity of normal direction.

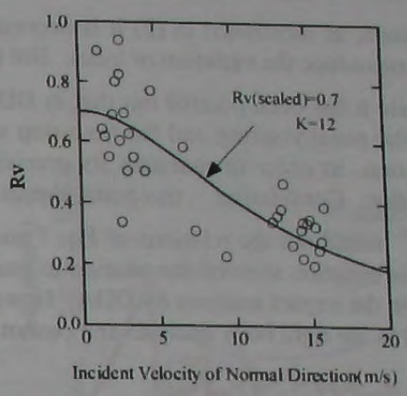


Fig. 10 An average SF curve in observation result of siteB

$$SF = \frac{1}{1+\left(\frac{V_{nin}}{K}\right)} \tag{4}$$

where, V_{nin} : incident velocity of normal direction, K : the slope of SF curve.

$$V_{nout} = R_n(scaled) \times SF \times V_{nin} \tag{5}$$

$$V_{out} = R_V(scaled) \times SF \times V_{in} \tag{6}$$

Fig. 10 is the relation between the velocity ratio and the incident velocity of normal direction obtained from the site B of the experimental field as shown in Fig.2, when Eq. 6 is applied to this relation. The result is that the velocity ratio Rv(scaled) = 0.7～0.98 and K = 8～12. However, as already mentioned in (2), up to now, all the slopes of the field where the measurement was carried out, were the cliff and grass land, but not the scene where the rock mass fell and moved up and down across the exposed hard bedrock. We consider that it is necessary to perform the experiment at such fields in the future.

4 VERIFICATION OF REPRODUCTIVE ANALYSIS

We have investigated the property of velocity ratio and its applying method. Now based on the results, we verified its applicability with the reproductive analysis of field experiments by incorporating Eq. 5 to DDA.

4.1 DDA ball and time step, set-up of spring (other parameters)

In the past, many kinds of DDA were developed. One of them is the rigid ball element model (DDAball)[7],[8]. DDA ball is the three dimensional analysis of the specialized rockfall simulation.

In addition, as mentioned in (2) it is necessary to consider the influence of reflective angle in order to reproduce the variation of locus. But this was neglected in this paper.

Meanwhile it has been pointed out that in DDA, the value-degeneration would occur depending on how the penalty-spring and the time-step were instituted. The problem of rockfall is energy-degeneration. In order to maintain its precision, it is necessary to avoid the useless value of degeneration. Considering this point, theses parameters should be carefully set up.

Fukawa[8] found out the relations of Eq. 7 among the penalty spring, time step and the rockfall mass. This equation showed the relation to guarantee the precision and stability of the numerous analyses in the impact analysis by DDA. However it is known that this equation is valid only for DDA ball in the rigid body analysis and cannot be applied to other DDA treating elastic body.

$$\frac{\Delta t}{2\pi}\sqrt{\frac{K}{M}} \le 0.05 \qquad (7)$$

4.2 Application to field experiment

To verify the validity of Eq. 6, the reproductive analysis of the field experiment using DDA ball was performed. Fig. 2 showed the result of reproductive analysis at siteB. On the slope of siteB together with siteA, there was a large transformation point of topography along the falling route.

The rockfall impacted the first contact point with the falling velocity of 12～15 m/s and incident angle of 13° . The velocity ratio was low (Rv=0.3) at this moment and the velocity energy greatly decreased. On the other hand, at the second contact point, the velocity ratio exhibited a high value of 0.7 even though the energy had greatly decreased at point b1. As it has been already mentioned, the great primary factor of this decrease is the incident angle. The velocity ratio is not the expression of the ground condition, but is the changing relative value being subject to the influence of incident angle and impact velocity.

For the analysis, the SF curve was shown passing through the average at the restitution spot of b1 and b2, which was shown in Fig. 10. The parameters of the SF curve are Rv(scaled) = 0.7, K = 12 m /s. The trajectory of DDAball analysis using these parameters was shown in Fig. 10. Further, the results of velocity were shown in Fig. 11. The 3 cases are analyses as follows; case 2 is only the value of b2(Rv=0.72), case 3 is only the value of b1(Rv=0.33), case 1 used the SF curve for analysis. Case 2 rebounds greatly at the b1 point and is different from the observation. Case 3 resembles the observation result in velocity and trajectory at the b1 point. But the motion changes from the bouncing to the rolling after the b2 point. On the other hand, Case1 is closest in the velocity and the trajectory for the observation result.

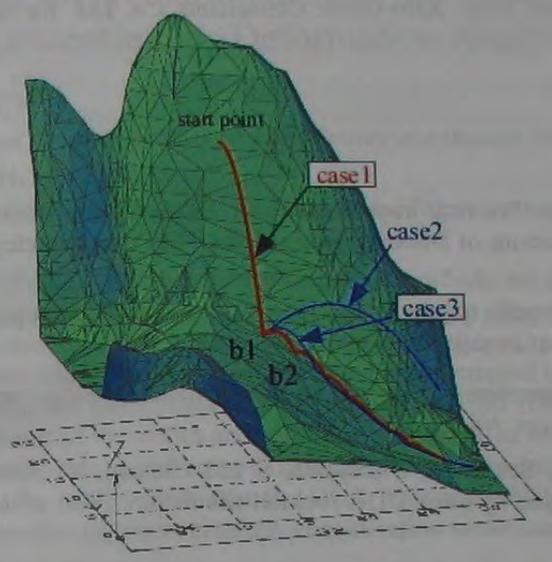


Fig.11 The some trajectory example from the rockfall simulation by DDAball.(siteB)

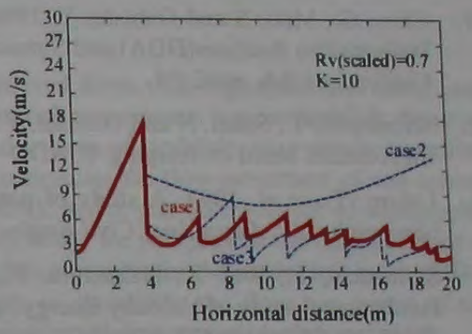


Fig.12 The velocity vs horizontal distance of the each case from the rockfall simulation by DDAball.

5. CONCLUSIONS

In this paper, the applying method of DDA ball to the rockfall simulation was described.

1) From the field experiment, the velocity ratio is greatly dependent on the incident velocity of normal direction.

2) For the reflective angle of rockfall falling to the cliff or grass land, there is a tendency of incident angle < reflective angle as the incident angle becomes smaller. (but except for the case that there is an influence of trees)

3) Pfeiffer et al. used the SF curve which was applied to modify the velocity-dependence of velocity ratio in the normal direction, and adopted the velocity ratio.

4) Using these methods, for the case including a great transformation spot of topography, i.e. the reproductive analysis was performed for the field where there is a great difference between the incident angle and velocity. It has been confirmed that the locus and velocity ratio agree very well with the actual situation.

However concerning the SF curve for the spot where the asphalt of the road and the hard bedrock of slope are exposed, further investigation will be performed. DDA ball is the modeling of the rockfall .with a ball. In the future, it will be necessary to establish a model by taking account of the shape of rockfall. At present, the particle analysis has been performed by incorporating the velocity ratio of the normal direction and the deviation of topography. In the future, it is considered important to take account of these deviations.

ACKNOWLEDGEMENT

The authors would like to thank Dr. Shigeru Miki, Kiso-Giban Consultants Co. Ltd. for his several valuable suggestions.

REFERENCES

1. Chen, G., Miki, S and Ohnishi, Y. 1996. Practical improvements on DDA, Discontinuous Deformation Analysis(DDA) and Simulations of Discontinuous, Media TSI Press Berkeley, California, USA, pp12-14
2. Shimauchi, T., Sakai. N and Ohnishi, Y. 2000. Fundamental study of mechanical behaviors for rockfalls based on imaging. ICADD-4. 473-481
3. Ushiro, T., et al. 1997. A study of parameters for motion of falling rocks on slope and jumping height. *Journals of Civil Engineers. No.581,VI-37*, 49-58.
4. Shimauchi, T., Wei, Z., Nakamura, N., Sakai. N., Nishiyama, S and Ohnishi, Y. 2006. Fundamental study of Velocity Energy ratio by using DDA-rockfall simulation. *Proc. of the JRMS, No.36.Japan*. 473-481
5. Pfeiffer, T, J., Bowen, T. D, 1989, Computer Simulation of Rockfalls; Bulletin of the Association of Engineering Geologists Vol.XXVI. No.1, pp135-146
6. Shimauchi, T., Ohnishi, Y., Nishiyama, S and Sakai, N, 2006, Study on Verification of Rockfall Simulation Using Improved DDA considering the Characteristics of velocity energy ratio at impact, *Journals of Civil Engineers C ,Vol.62,No.3*,pp707-721.
7. Ohnishi,Y., et al. 2003. Development of Spherical Element for DDA and Its Application. *Proc. The Conference on Computational Engineering and Science, Tokyo, Japan. Vol.8, No.1*,171-176
8. Fukawa, Y., Ohnishi, Y., Nishiyama. S., Fukuroi. H., Yonezu. K., Miki. S. 2004. The application of 3-dimentional DDA with spherical rigid block to rockfall simulation. *Proc. of the ISRM International Symposium 3rd ARMS, Kyoto, Japan*. pp1243-1248
9. Ohnishi, Y., Nishiyama, S., Sasaki, T and Nakai, T. 2005. The Spplication of DDA to Practical Rock Engineering Problems: Issues and Recent Insights. *Proc. of the ICADD-7, Honolulu, Hawaii*. pp277-287

Study on prediction of flow movement of shallow landslide based on Discontinuous Deformation Analysis

Sakai, N.
National Research Institute for Earth Science and Disaster Prevention, Tsukuba, Ibaraki, Japan
Ikei, H. and Miki, S.
Kiso-Jiban Consultants Co., Ltd., Chiyoda-ku, Tokyo, Japan

ABSTRACT: Rainfall-induced landslides, which are moved down with high speed and travel long distances, are the most catastrophic phenomenon. Recent risk assessments against landslide disasters need many evaluation items, which are the thickness and volume of landslide mass and the travelling distance and velocities. Therefore, we have attempted to simulate the flow movement of soil masses by using the Discontinuous Deformation Analysis (DDA), which can take account of topographic conditions of the slopes and soil mass properties. In this study, we will present the brief behavior of the large-scale model test of slope failure and the simulation results for the model test by the DDA. Then, the results show that the DDA have a possibility of simulating the flow movement of soil masses after failure in carefully consideration to the contact problem between blocks (particles).

1. INTRODUCTION

Rainfall-induced landslides are causing serious damages associated with urban development and local heavy rainfall. Fig.1 is an example of shallow landslide induced by heavy rainfall, and the houses completely destroyed. Among disastrous landslides, rainfall-induced landslides, which are moved down with high speed and travel long distances, are the most catastrophic phenomenon.



Fig.1 Shallow landslide-induced heavy rainfall (Web site of Hiroshima Pref.)

Recently, great efforts have been made to study the mechanisms that the slope collapses or slides from the source area become fluid. Besides the fluidization mechanisms, it is also important to estimate travelling distances of landslides for the planning against landslide disasters. The travelling distances, in many cases, have been estimated by the empirical relations between the travelling distances and the volumes of collapses soil masses, and several empirical relations have been proposed. However, these empirical methods have the difficulties that geological conditions and/or topographic conditions of the slopes are neglected or simplified.

Recent risk assessments against landslide disasters need many evaluation items, and travelling velocities and spreads of the soil masses are important items for the risk assessments. High accurate methods, which can simulate the behavior of sliding soil masses such as travelling velocities, have been demanded. The Discontinuous Deformation Analysis (DDA) [4], which can take account of topographic conditions of the slopes and soil mass properties, is one of powerful tool for simulating movements of soil masses. Ishikawa et al. [5] already reported the applicability of the DDA by simulating the small scale model test. Hamasaki et al.[6] applied the DDA to the prediction of natural dam formation by landslide.

We focus on estimating traveling distances and spreading of collapses soil masses. Therefore, applicability of the DDA has been studied by simulating the large scale model test of slope failure induced by rainfall as a first step. In this report, we will present the brief results of the large scale model test of slope failure induced by rainfall and simulation results for the large scale model test by the DDA. Moreover, some considerations on the parameter, which are related to the strengths between blocks (particles) in the DDA, will be given.

2. LARGE SCALE MODEL TEST OF SLOPE FAILURE-INDUCED RAINFALL [3]

To study on mechanism of slope failure using model tests are three types. the first is to use centrifuge model(e.g.[1]), the second is to use small-scale model(e.g.[2]), the third is to use large- scale model(e.g.[3]). Among them, It is appropriate for our study to use large scale model test because of the reality of the flow movement after slope failure. In this paper, we show the large scale model test.

2.1. Large-scale model test apparatus with rainfall simulator

The three stage steel flume used in the landslide experiment were 23m length, 7.8m height, 3m width and 1.6m depth, as shown in Fig.2. The main stage of slope was a 10m length with a gradient of 30°. Next stage of slope has 6m length with a gradient of 10°. Third stage of slope has 6 m length with a flat. One wall of entire flume was made of clear reinforced glass to enable direct observation of soil deformation. The lower end of the flume was supported by retaining wall with a metal net for free discharge of water.

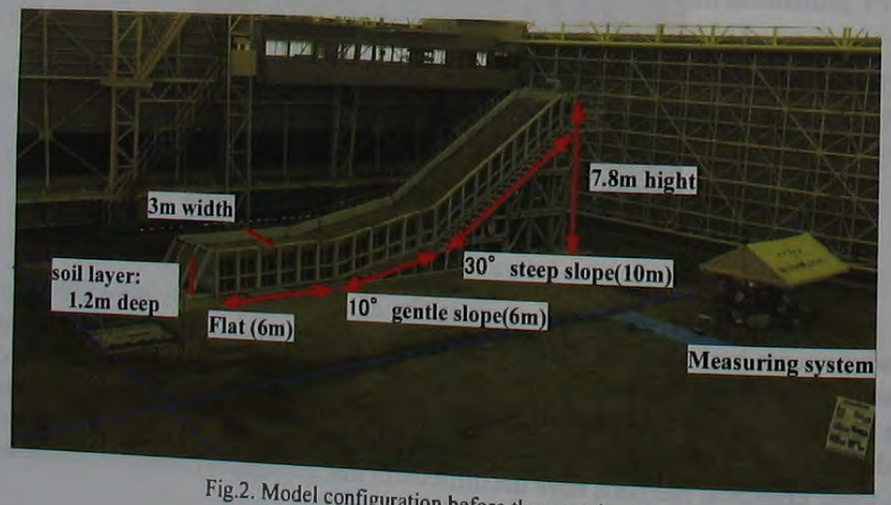


Fig.2. Model configuration before the experiment

Proceedings of International Mini-Symposium for Numerical Discontinuous Analyses, edited by T. Koyama, Hawaii, November, 2008

Fine river sand was placed in the flume with a crane and set to a depth of 1.2 m. To make the sample uniform with packing, the soil sample was placed in a series of 30-cm layers parallel to the flume base and each layer was tamped with foot traffic by using a square wooden compactor. The average dry density of sand was about 1.45 (relative density is low) and the initial water content was about 8% by weight.

We used the rainfall simulator in the National Research Institute for Earth Science and Disaster Prevention (NIED), Japan. It is 75 m length, 50 m width and 22 m height. This simulator is movable between five experimental sites to efficiently conduct many experiments throughout the year. The simulator can sprinkle water at intensities of 15 to 200 mm/h. The height of the nozzles above the ground was 16 m. It's enough for raindrops to reach terminal velocity. In this experiment, we sprinkled the area at a constant intensity of 100 mm/h. The soil properties and the initial conditions are shown in Table 1.

Table 1. Soil properties and initial conditions [3]

Soil material	Sakuragawa sands
Specific gravity	2.69 g/cm3
Uniformity coefficient	3.43
Dry density	1.45 g/cm3
Relative density	3%
Void ratio	0.85
Initial water content	8%
Rainfall intensity (constant)	100 mm/h
Failure time after start of sprinkling	About 154 min
Sliding time	-5s

2.2. Measurements

We measured the following items using the techniques, which are surface displacement, piezometric level at the flume bed, pore-water pressure within the soil, slip surface locations, and landslide motion, listed below:

(i) Surface displacement: extensometers with wire attachments were installed on the 30° slope.

(ii) Basal piezometric levels: sealed diaphragm-type pressure transducers were fixed to the slope bed at regular intervals of 2 m. Transducers could measure up to 3 m of pressure head.

(iii) Internal pore-water pressures: three strain-gauge-type meters were installed at regular interval of 4 m in the soil layer. These gauges were buried at 30, 60, and 90 cm deep respectively, at each location.

(iv) Slip surface and deformation: colored-sand indices with a width of 6 cm were inserted vertically between the soil and the glass wall at regular intervals of 1 m.

(v) Landslide motion: video and digital cameras were used to make recordings. Square markers with a length of 15 cm were attached regularly on the slope surface.

Data from the sensors were digitally analyzed using a personal computer. Some of the sensors were monitored using a pen-recorder. The location of the sensors is shown in Fig. 3.

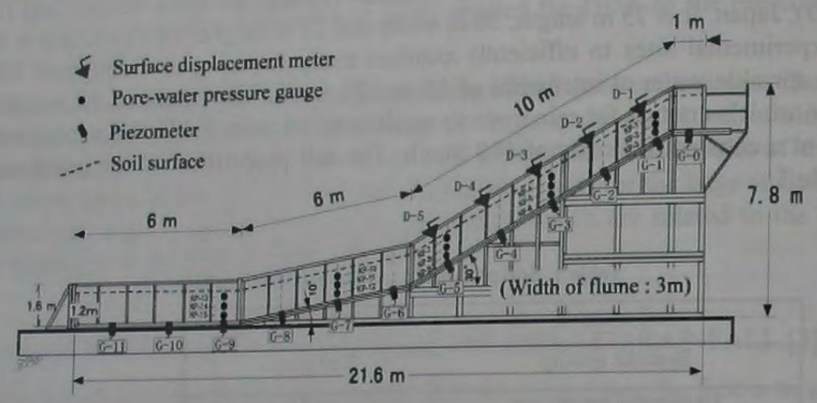


Fig.3. Model slope and location of sensors [3]

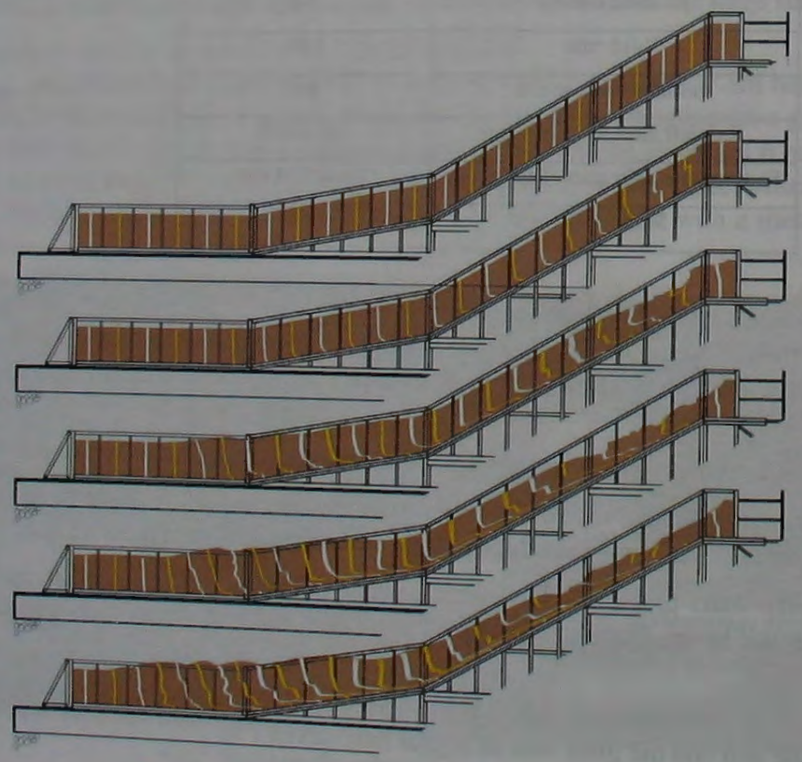


Fig. 4. Illustration of soil deformation during the rapid slide [3]

2.3. *Failure processes*

The rapid movement during failure occurred over 5s after the start of sprinkling, following the long precursory period of deformation down slope. The maximum velocity of the sliding mass was about 1.2m/s. The velocity of the sliding mass at failure was quite different from that before failure.

Fig.4. illustrates the progression of the landslide for 5s on the basis of deformation of white and yellow indices recorded by the digital cameras. The top sketch in Fig.4 is a side view taken just before the rapid slide. The bottom sketch in Fig.4 is after slide stopped. The other sketches are during movement. Overall, the main scrap was located at the top of the 30° slope and toe was in the middle part of horizontal layer.

In the large scale model test, following behavior of soil masses were observed:

(i) Soil masses rapidly moved down at 30° slope entirely.

(ii) Soil masses were sheared along the flume base of 30° slope, and the shear zones in soil layer were located just above the flume base.

(iii) Downing stream of soil masses folded up to soil masses around the 10° slope, and stopped at the flat part.

3. NUMERICAL ANALYSIS OF DDA

A computational simulation of the large scale model test after failure, which is above mentioned test, was carried out by using the DDA. The DDA is a powerful computational method to simulate the behavior of block aggregation, and the DDA is able to take account of the geotechnical features of slope failure, which are slope geometry, geological structure and discontinuous plane. Moreover, the estimation of travel distance, sliding velocity and geometry of landslide mass are to do simulation by using the DDA. Those factors are very important roles to calculate the landslide risk of the slopes.

3.1. *Numerical model and parameters*

In the numerical analysis, soil masses were represented as an aggregation of small polygonal blocks, and the slope was modeled by a large block. The computational model is shown in Fig.5. An average diameter of the small blocks was 11.8cm, and number of the small blocks was 1,822. A general shape of the small blocks was an octagon. It is considers that shapes and arrangements of blocks affect the failure mode. In order to reduce the dependence on block arrangement, octagonal blocks were arranged as Fig.5. It was considers that the mobility of blocks were kept and were freed from interlocking between blocks in this model.

The calculation parameters and block properties are listed in Table 2. All blocks were linear elastic bodies under plane strain condition. The friction angle and cohesion in listed in Table.2 were determined by several trial analyses.

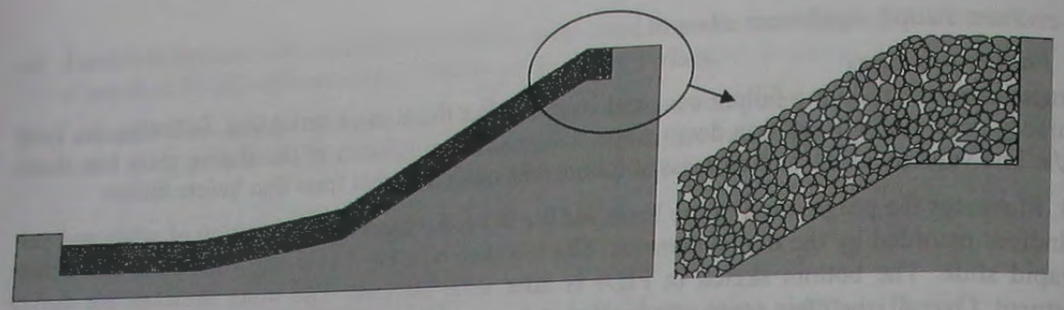


Fig.5. Calculation model and block arrangements

Table 2. Block properties and calculation parameters

Category	Parameters	Values
Properties of blocks	Young's modulus	75GN/m^2
	Poisson's ratio	0.25
	Density	2650kg/m^3
Contact parameters between blocks	Friction angle	45deg
	Cohesion	10kN/m^2
	Tensile strength	0 kN/m^2
	Velocity – energy ratio	0.1
	Normal penalty stiffness	10MN/m
	Shear penalty stiffness	10MN/m
Open-Close parameter	the coefficient of 'Close-to-Open'	1.0E-7 (default value)
Other parameters	Viscosity around block	0.1kNs/m^4
	Maximum. time span	0.0005s
	Total Iteration (Contact generation)	20,000 (2,000)
	Maximum displacement ratio	0.0001

In the analysis, the calculation was processed by two stages. At first stage, gravity was turned on, and contact forces between blocks, where contact strength between blocks were artificially large to prevent shear displacement at the contacts, generated. After first stage, contact strength was set to designated values in Table 2, and it triggered off the slope failure.

3.2. Results

Fig.6. shows the calculation result after 10s by the DDA. In the figure, red colored blocks show large displacement and blue colored blocks show small displacement. Fig.7, which corresponds to Fig.4, illustrates the displacement of marked blocks after 7s. The displacement pattern of the block aggregation can be traced from Fig.7. In the analysis, the rapid movement of the blocks closed down within 10s, and this duration time approximately agreed with that in the large scale model test.

Proceedings of International Mini-Symposium for Numerical Discontinuous Analyses, edited by T. Koyama, Hawaii, November, 2008

As shown in Fig.6, blocks around the 30° slope moved down entirely. Downing stream of blocks fold up to blocks to blocks around the 10° slope, and stopped at the flat part. The displacement of blocks decreased from the surface of the 30° slope layer to the bottom. From Fig.7, upper blocks dragged lower blocks along the 30° slope, and large increment of block displacement appeared along the 30° slope. It was estimated that the slip surface was located along 30° slope slightly above the bottom of soil block layer. Around the 10° slope, it was observed that upper blocks folded up to lower blocks.

Comparing the DDA simulations with the large scale model test, it was revealed that displacement patterns of blocks in the DDA were qualitatively similar to that in the large scale model test. However, there were some differences between the deformations of soil masses after failure in the large scale model test and the DDA simulations. Comparing Fig.6 with Fig.4, the main scrap and toe, which were observed in the large scale model test, were obscure in the DDA simulations.

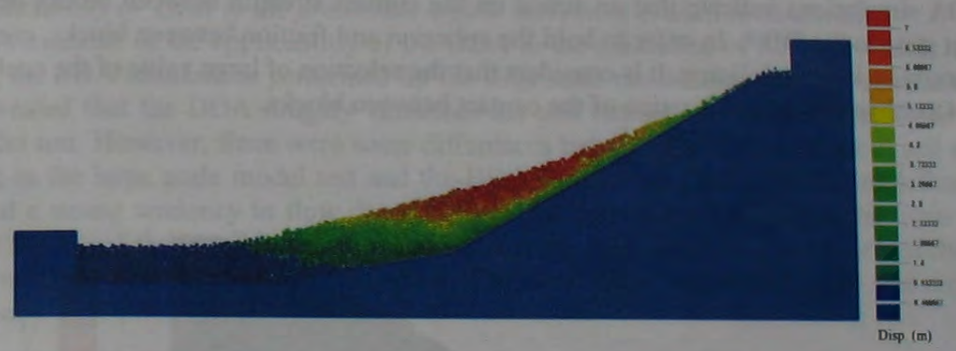


Fig.6. Displacement of blocks after 10s (color division)

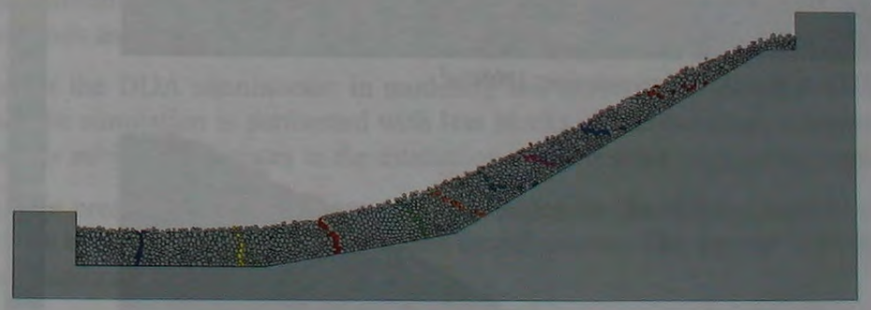


Fig.7. Displacement of blocks after 7s (marked blocks)

4. DISCUSSION

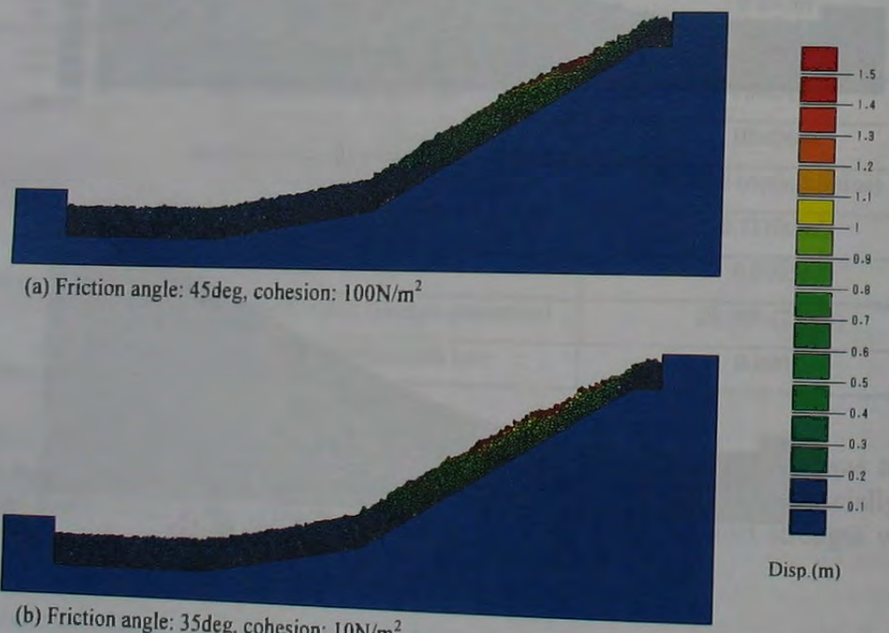
4.1. Consideration on contact parameters between blocks in DDA

As mentioned above, the slope failure in the large scale model test was approximately simulated by the DDA. However, the DDA simulations have shown the difficulties. For example, several DDA simulations indicated that the friction angle and cohesion between blocks hardly affected to the failure mode. It is considered that this phenomenon is related to the contact mechanism in the DDA.

Fig.7 shows the results of the other DDA simulation. In these simulations, analysis models and calculation parameters were same as above-mentioned simulation except the coefficient of 'Close-to-Open', which is the contact control parameter in the DDA. The coefficient of 'Close-to-Open' regulates the distance between the block surface and the judgment line for contact state 'Close' to separate state 'Open', and small value is applied to the coefficient of 'Close-to-Open', as shown in Fig.8. In the DDA simulations shown in Fig.6, the coefficient of 'Close-to-Open' was 1.0^{-7}, and it is default value in the original DDA program. However, the coefficient of 'Close-to-Open' in the DDA simulation shown in Fig.7 was 3.0^{-5}. This value means that the distance between the block surface and the judgment line for 'Close' to 'Open' is larger than the default value.

As shown in Fig.7, the mobility of blocks, as compared with the results in Fig.6, was restricted in spite of weaker friction angle and cohesion than that of the simulation in Fig.6. In Fig.7, the change of the contact strength between blocks was reflected in the displacement of blocks. Moreover, the main scrap at the top of the 30° slope, which was observed in the large scale model test, appeared.

These DDA simulations indicate that an action on the contact strength between blocks depends on the contact state in the DDA. In order to hold the cohesion and friction between blocks, contact state 'Close' should be keep stabilizing. It is considers that the selection of large value of the coefficient of 'Close-to-Open' works on stabilization of the contact between blocks.



(a) Friction angle: 45deg, cohesion: $100N/m^2$

(b) Friction angle: 35deg, cohesion: $10N/m^2$

Fig.7. Displacement of blocks after 7s (color division)

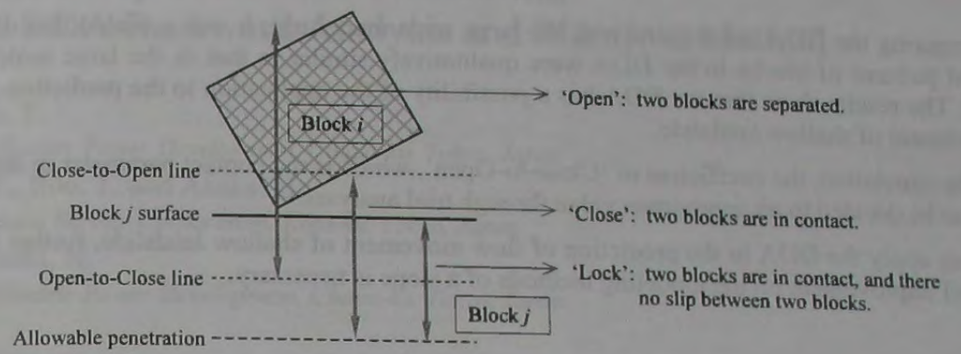


Fig.8. Schematic diagram of the contact between blocks in the DDA

4.2. Applicability of DDA to the prediction of flow movement of shallow landslide

In order to examine of the applicability of the DDA to the prediction of flow movement of shallow landslide, the DDA simulations performed for the large scale model test. From the simulation results, it was revealed that the DDA roughly simulated the soil masses movement observed in the large scale model test. However, there were some differences between the deformations of soil masses after failure in the large scale model test and the DDA simulations. In the DDA simulations, surface blocks had a strong tendency to flow downward. In the large scale model test, the main scrap was located at the top of the 30° slope on the contrary. On the other hand, it was confirmed that the contact parameter in the DDA, the coefficient of 'Close-to-Open', affected friction and cohesion between blocks.

The following subjects have to be cleared in order to apply the DDA to the prediction of flow movement of shallow landslide;

- Methods to translate friction angle and cohesion of soil masses into that of the DDA simulations: rational methods are demanded to estimate the contact strength between blocks.
- Block size for the DDA simulations: in modeling soil masses as granular materials, it is to be desired that the simulation is performed with less blocks in number from a computation time. It seems that this subject also relates to the estimation of the contact strength between blocks.
- Modeling pore pressure and water flow among particles for the DDA: landslide or slope failure closely relates to water flow and pore pressure in soil masses. The current DDA is not equipped with these functions.
- Systematic methods to set the input parameter in the DDA: systematic methods to set the contact parameters, which are the penalty stiffness and contact judgment values, are strongly demanded.

5. CONCLUSIONS

Applicability of the DDA was examined by simulating the large scale model test of slope failure induced by rainfall. The following conclusions can be obtained;

(i) Comparing the DDA simulations with the large scale model test, it was revealed that displacement patterns of blocks in the DDA were qualitatively similar to that in the large scale model test. The results show that the DDA has a possibility of the application to the prediction of flow movement of shallow landslide.

(ii) In the simulation, the coefficient of 'Close-to-Open', which is the contact parameter in the DDA, has to be decided to an appropriate value through trial analyses.

In order to apply the DDA to the prediction of flow movement of shallow landslide, further investigation and improvement on the modeling methods of a slope is necessary.

REFERENCES

1. Take, W., M. D. Bolton, P.C. P. Wong and F. J. Yeung. 2004. Evaluation of landslide triggering mechanisms in model fill slopes, Landslide, 1, 173-184.
2. Sakai N. and S. Sakajo. 2008. Model tests of collapse of unsaturated slopes in rainfall. *10th International Symposium on Landslides and Engineered Slopes, Xi'an, China*, 907-912.
3. Moriwaki, H., T. Inokuchi, T. Hattanji, K. Sassa, H. Ochiai and G. Wang. 2004. Failure processes in a full-scale landslide experiment using a rainfall simulator. *Landslides*, 1, 277-288
4. Shi, G. H. and Goodman, R. E. 1985. Two dimensional discontinuous analysis. *Int. J. Num. Anal. Methods. Geomech, 9*: 541-556.
5. Ishikawa, T., S. Kawamura, S. Miura and Y. Ohnishi. 2007. Fundamental study for slope failure of volcanic soil ground by DDA. *Proceeding of The 8th International Conference on Analysis of Discontinuous Deformation, ICADD-8*, 61-66.
6. Hamasaki, E., A. Sasaki and Y. Ohnishi. 2007. Application of discontinuous deformation analysis in prediction analysis of natural dam formation by landslide. *Proceeding of The 8th International Conference on Analysis of Discontinuous Deformation, ICADD-8*, 147-150.

A Case Study of Rockfall Phenomena With DDA Backward Analysis and Manifold Method

Tobase, T.
Japan Electric Power Development, Chouo-ku, Tokyo, Japan
Cao, Z., Itou, T. and Asaka, H.
JP Business Service Corporation, Koto-ku, Tokyo, Japan
Kumazaki, N.
Japan Electric Power Development, Chouo-ku, Tokyo, Japan

ABSTRACT: A case study of the rockfall occurred in Ikokuma, Aomori Prefecture, Japan on April 20, 2005, has been carried out. The observed creep deformation before falling has been simulated with the DDA backward analysis, and the material properties of the rock blocks, the necessary parameters in the analysis have been identified. Taking the result of creep deformation as the initial condition of falling history and with the identified parameters, the falling behavior of the block has been simulated with manifold method. It has been proved that the method used in study is practical and effective for the mechanism investigation of creep deformations and the analyses of rockfall behaviors.

1. INTRODUCTION

For the prevention and mitigation of natural disasters such as rockfall or landslip, various monitoring and warning systems have been constructed in Japan. Up to now, a great deal of observational data and plenty of experience in the site monitoring have been achieved. However, how to effectively utilize such data for the prevention of such disasters is still a great problem needs our further efforts.

In this study, a feasible way to utilize the observational data for the prevention of rockfall disasters is proposed, which is based on the DDA [1] and manifold method [2].

- DDA backward analysis of the creep deformation of the block recorded before its falling: It is supposed that, based on the analytic results the mechanism of the rock deformation would be presumed, and the material properties could be identified.
- Using the material properties and considering the presumed deformation mechanism, the possibility of rockfall ever since then can be predicated with DDA or manifold method.
- Based on the above analytic results, an advice on engineering measures can be made to the relevant commonality in view of rock engineering.

As the first step of the above attempt, the numerical simulation of a real rockfall phenomenon is curried out by the combined application of DDA backward analysis and manifold forward analysis. Here a brief explanation of the analytic method is given and the main results are presented.

2. AN ACTUAL ROCKFALL EVENT

A rock block about 70 ton fell from a drop-off near a highway in Ikokuma, Aomori Prefecture on April 20, 2005. Fig.1 shows the photo of the rock block, and Fig.2 shows the topographical feature of the slope where the rockfall event occurred.



Fig.1 Photo of the rock block

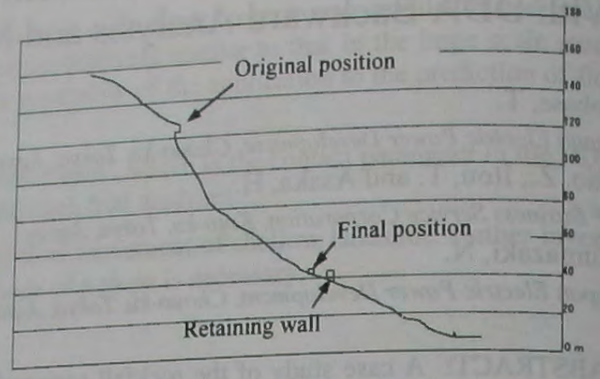


Fig.2 Topographical feature of the slope

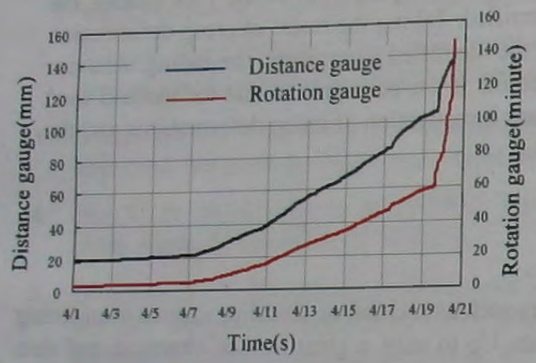


Fig.3 Time histories of the creep deformation before the block falling

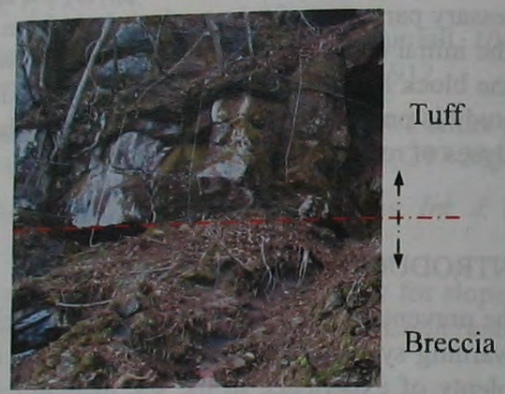


Fig.4 Geological feature of the slope

The creep deformation of the block before its falling has been digitally recorded. Fig.3 shows the time histories of the creep deformation recorded by the distance gauge and rotation gauge. It can be found that the rock moved gradually from April 7 and a sharp increment can be noticed on April 20. Before the block falling, the maximum displacement of the set point is about 15cm, and the maximum rotation is about 137 minutes. No records left about the behaviors of the rock block during its falling process, but finally the block come to standstill at the position about 10m to the retaining wall as shown in Fig.2.

For analyzing the mechanics of the rockfall, site investigation was made first. Fig.4 shows the local geological features of the original position of the rock block. Huge and hard rock blocks exist at the top area of the breccia slope. From the site investigation, it is conjectured that rain and ground water corroded the breccia slope gradually, which exposed the upper rock blocks. Finally the rock block fell down since the bearing power of the subjacent breccia got attenuated.

3. ANALYTIC METHOD

With the application of DDA and manifold method, an analytic method is presented here. Fig.5 shows the main procedure of the method, which combines the DDA and manifold method with the site investigation and laboratorial material tests.

Proceedings of International Mini-Symposium for Numerical Discontinuous Analyses, edited by T. Koyama, Hawaii, November, 2008

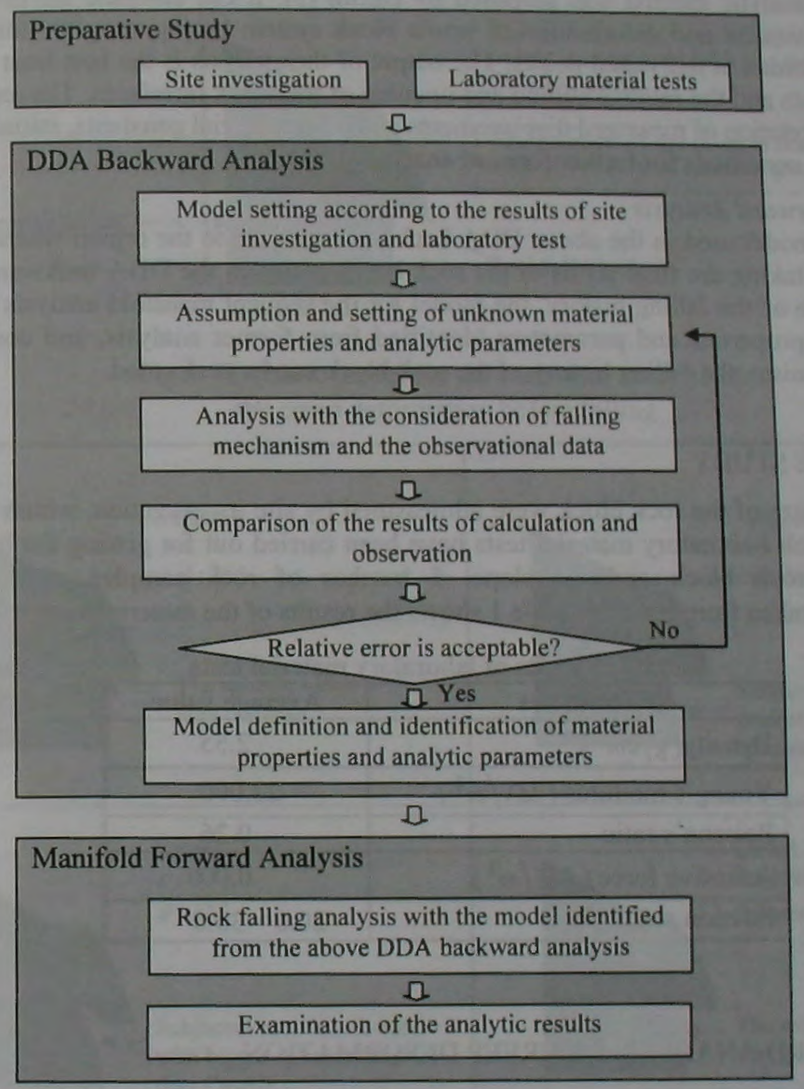


Fig.5 Analytic procedure of the rockfall

3.1. Preparative Study

For establishing a reasonable analytic model, the geographic features of the slope and the shape characteristics of the rock block were made clear by site investigation. Meanwhile, an inference on the trigger of the rockfall was made. Furthermore, laboratory tests with the materials sampled from the site were curried out in order to get the material properties needed in the following numerical analyses.

3.2. DDA Backward Analysis

DDA Backward analytic method was proposed by Dr.Shi [3]. It can compute the continuous and discontinuous movement and deformation of whole block system by inputting the time dependent displacements recorded at individual points. The output of the analysis is the best least square fitted block displacements and the relative sliding and opening of the block interfaces. The analytic results can give an interpretation of measured displacements and offer material constants, initial stresses and possible boundary conditions for further forward analysis.

3.3. Manifold Forward Analysis

By enlarging the model used in the above DDA backward analysis to the region where the rockfall may reach to, and taking the final status of the rock block got from the DDA backward analysis as the initial condition of the falling history, the model for the sequent manifold analysis can be built. With the material properties and parameters identified from former analysis, and considering the deformation mechanism, the falling history of the rock block can be performed.

4. PREPARATIVE STUDY

The shape and the size of the rock block were admeasured by site investigation, which are reflected in the analytic model. Laboratory material tests have been carried out for getting the basic material properties of the rock block and the slope. 5 batches of rock samples of the dimension $\phi 5cm \times H10cm$ were taken from the site. Table 1 shows the results of the material tests.

Table 1 Results of laboratory material tests

Properties	Average value
Density(g/cm^3)	2.55
Young's modulus (MN/m^2)	22,000
Poisson's ratio	0.26
Adhesive force (MN/m^2)	0.00
Friction angle (°)	20.0~30.0

5. DDA BACKWARD ANALYSIS OF CREEP DEFORMATION

For studying the creep deformation mechanism and the contacting status of the blocks, and for identifying the material properties of the rock block, a backward analysis of the creep deformation before its falling is done.

5.1. Analytic Conditions

(i) Model

Since the backward analysis focuses on the creep deformation of the block before its falling, the analytic model is limited to the area including the rock block and the massive rock adjacent to the block. Meanwhile, the failure of the subjacent slope is considered by modeling it with a sphenic rock as mentioned later.

(ii) Material properties and parameters used in the analysis

Material properties shown in the Table 1 are used in the analysis. Adhesive is set at 0, but the friction angle is adjusted slightly for getting a solution of good accordance with the observed one.

Proceedings of International Mini-Symposium for Numerical Discontinuous Analyses, edited by T. Koyama, Hawaii, November, 2008

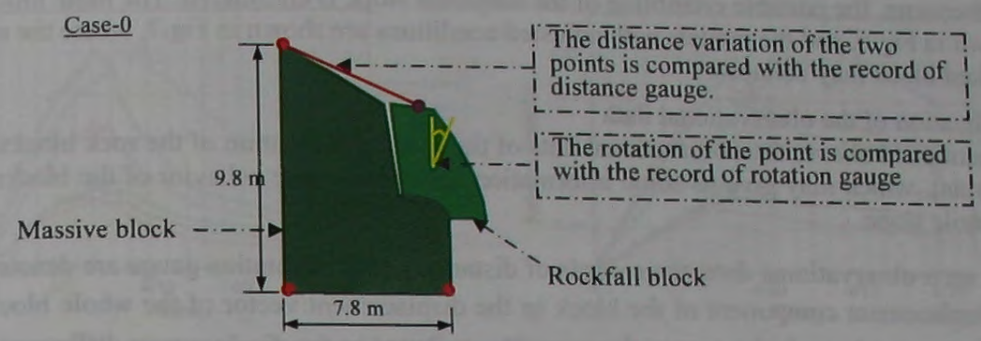


Fig.6 The basic model for the backward analysis of the creep deformation before falling

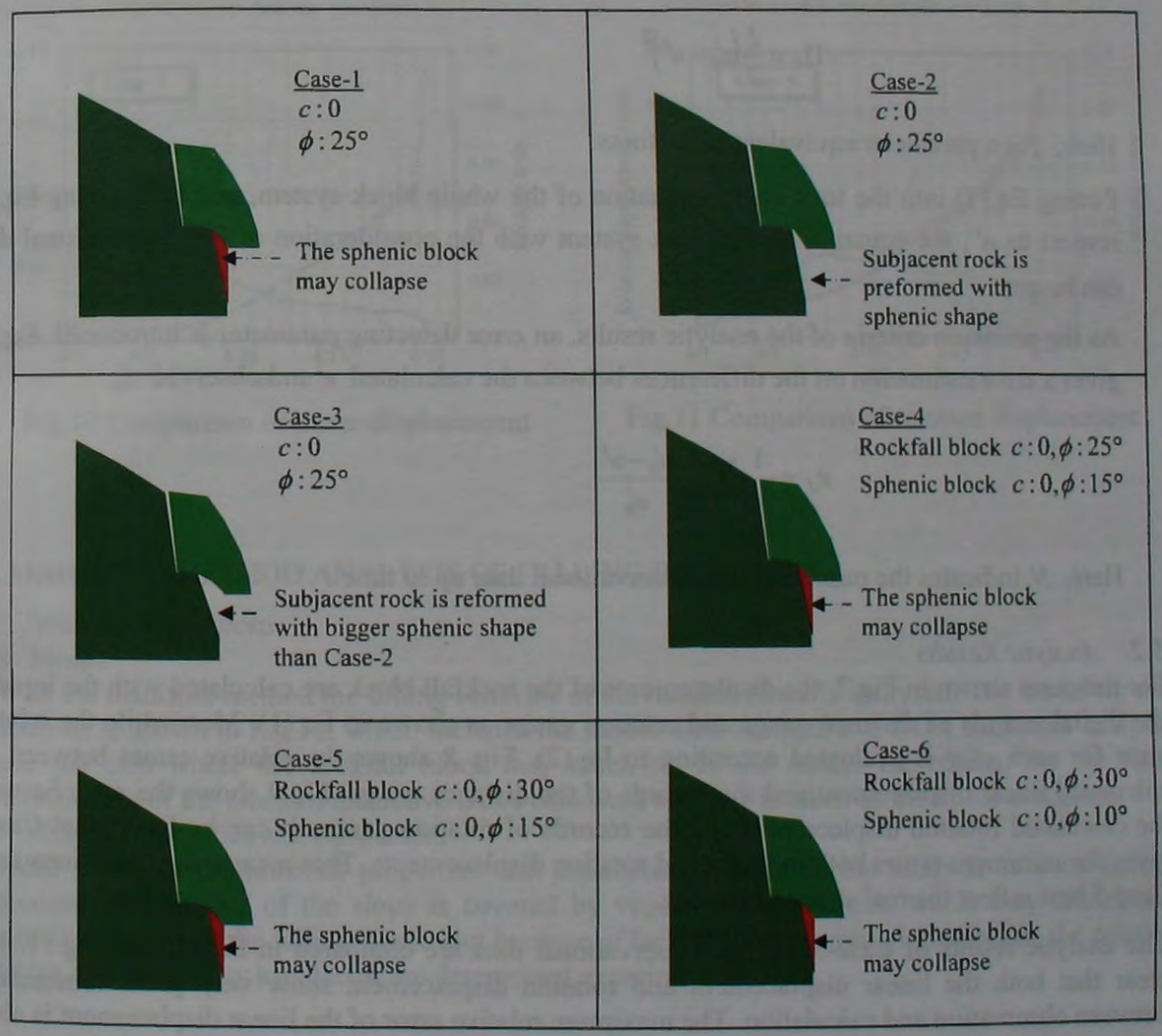


Fig.7 The models for DDA backward analyses of the creep deformation before falling

Furthermore, the possible crumbling of the subjacent slope is considered. The basic model is shown in Fig.6, and the models with adjusted conditions are shown in Fig.7, where the red marked block may collapse.

(iii) Utilization of the observational data

As mentioned above, the observational data of the creep deformation of the rock blocks are very important, which may give us some information about the future behavior of the blocks or even the whole slope.

Here, such observational data, the records of distance gauge or rotation gauge are denoted as u_0^i, and displacement component of the block in the displacement vector of the whole block system can be expressed as u^i, the potential energy Π_0 attributed to the displacement difference between the observed u_0^i and the calculated u^i can be expressed as

$$\Pi_0 = \frac{\xi}{2}\left(u_0^i - u^i\right)^2 \tag{1}$$

Here, ξ is a parameter equivalent to stiffness.

Putting Eq.(1) into the total energy equation of the whole block system, and by deriving Eq.(1) respect to u^i, the equation of the block system with the consideration of the observational data can be got.

As the precision criteria of the analytic results, an error detecting parameter is introduced. Eq.(2) gives a error estimation on the differences between the calculated u^i and observed u_0^i.

$$\varepsilon_J = \frac{1}{N_t}\sum_{i=1}^{N_t}\frac{u_0^i - u^i}{u_0^i} \tag{2}$$

Here, N_t indicates the number of the observational data up to time t.

5.2. Analytic Results

For the cases shown in Fig.7, the displacements of the rockfall block are calculated with the input of the digital records of distance gauge and rotation gauge as shown in Eq.(1). Meanwhile the relative error for each case is evaluated according to Eq.(2). Fig. 8 shows the relative errors between the calculated linear displacement and the records of the distance gauge. Fig.9 shows the error between the calculated rotation displacement and the records of rotation gauge. It can be found that Case-5 gives the minimum errors both in linear and rotation displacements. That means, the conditions set in Case-5 best reflect the real status of the site.

The analytic results of Case-5 and the observational data are compared in Fig.10 and Fig.11. It is clear that both the linear displacement and rotation displacement show very good concordance between observation and calculation. The maximum relative error of the linear displacement is about 3.1% and the maximum error of rotation displacement is about 7.2%.

Proceedings of International Mini-Symposium for Numerical Discontinuous Analyses, edited by T. Koyama, Hawaii, November, 2008

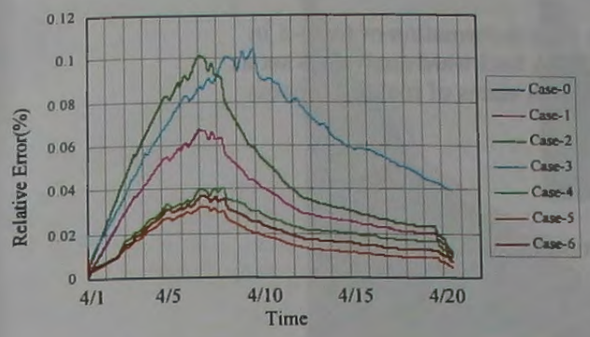


Fig.8 Relative error of linear displacement

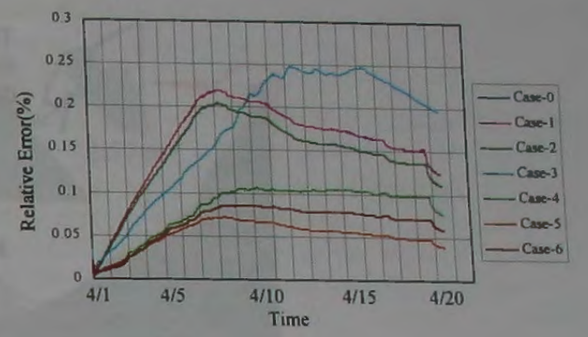


Fig.9 Relative error of rotation displacement

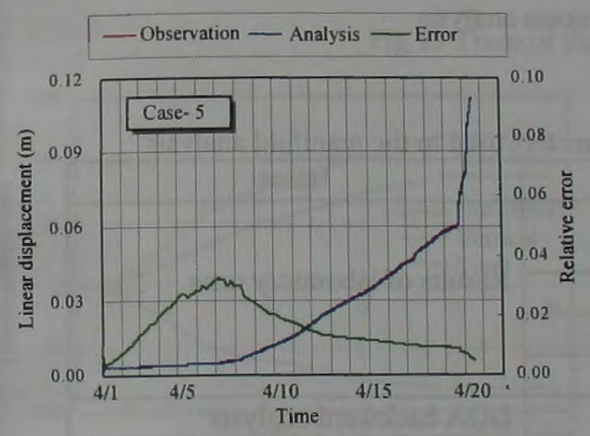


Fig.10 Comparison of linear displacement

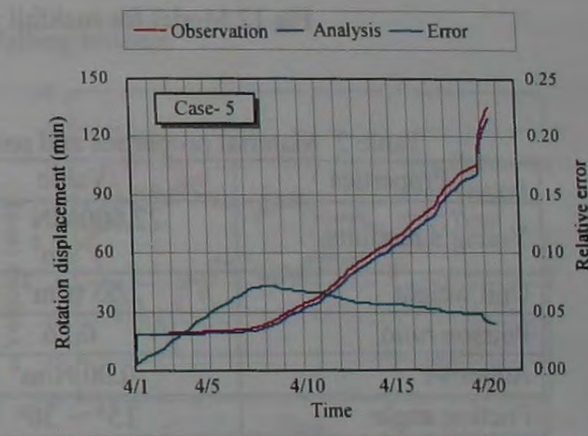


Fig.11 Comparison of rotation displacement

6. MANIFOLD METHOD ANALYSIS OF FALLING BEHAVIOR

6.1. Analytic Conditions

(i) Model

With the manifold method the falling behavior of the rockfall block is analyzed. The model for the analysis is shown in Fig.12, which includes the model used in the above DDA backward analysis and the area where the rockfall block may reach to. In the model the results, i.e. the final deformation of the block in the above DDA backward analysis is taken as the initial condition.

(ii) Material properties and parameters

Table 2 shows the material properties and parameters utilized in the analysis of rock falling process. The surface of the slope is covered by vegetation and humus, which may absorb the collision energy of the falling block. But because of lack of such damping information, the penalty factor and the energy loss factor are determined experimentally.

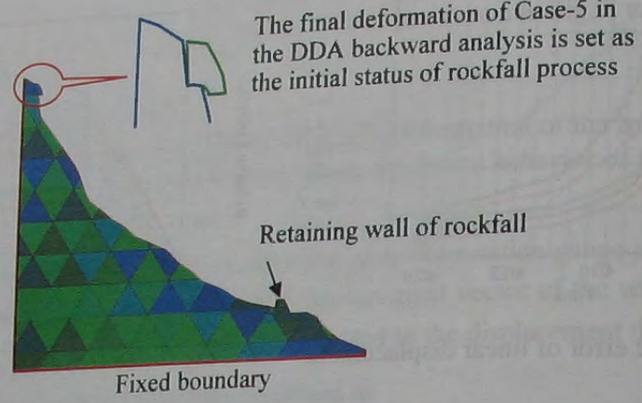


Fig.12 Model for rockfall process analysis

Table 2 Material properties and parameters used in the manifold analysis

Properties	Value	Bases
Young's modulus	22,000MN /m^2	Results of laboratory tests
Unit weight	2.55 tf/m^3	
Poisson ratio	0.26	
Adhesive	0.00 N/m^2	
Friction angle	15°～ 30°	DDA backward analysis
Penalty factor	10,000 MN/m^2	Considering the vegetation and humus of the slope, a relative small value is used.
Dissipative factor	0.99	Experimentally set
Time interval	1/2000 s	Small interval is set for getting a stable solution.
Total calculation time	25.00 s	Estimation

6.2. Analytic Results

The falling trace of the rock block in the falling process is plotted in Fig.13. Since no site record is left about the real falling process, the final position of the rock block is the sole item which can be compared with the analytic result. Incidentally, the final position of the block in the analysis is near exactly same as that of the site investigation (about 10m before the retaining wall). This result intimates that the parameters used in the analysis are generally correct. On the other

Proceedings of International Mini-Symposium for Numerical Discontinuous Analyses, edited by T. Koyama, Hawaii, November, 2008

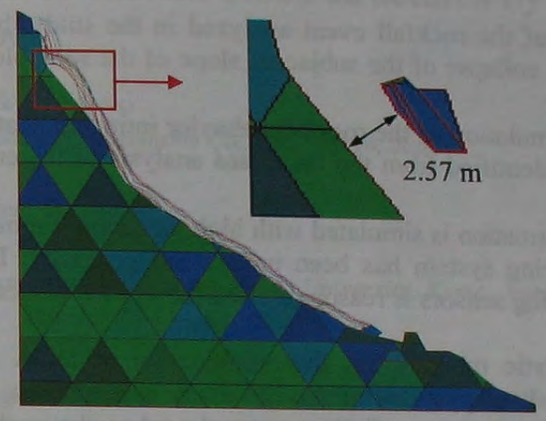


Fig.13 Trace of the falling process



Fig.14 Displaeement history

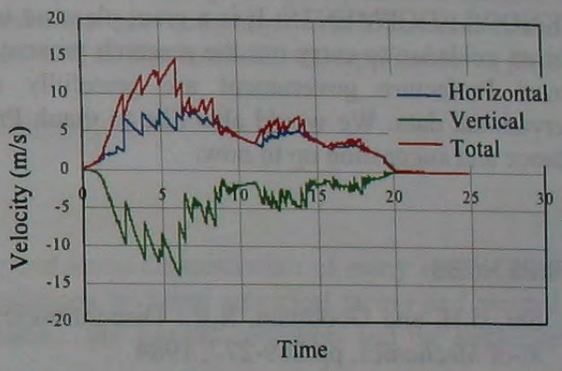


Fig.15 Velocity history

hand, from Fig.13 it can be found that the block bounded about 2.57m high at the upper part of the sharp slope, and after that the block slid most of the lower slope.

Fig.14 shows the displacement history of the rock block. It is clear that the block passed through a distance about 120m from its original position in about 20 seconds. From the velocity history shown in Fig.15, it can be found that during the first 6.05 seconds the block generally moved with an increasing velocity. However, its velocity decreased sharply whenever the block collides with the slope. During the period the block moved over the upper drop-off, gravity accelerated the block. After that, the block got slower gradually, because of the gentle decline of the slope. It can be interpreted that the kinematic energy lost whenever the block collides with the slope. Finally, the block came to a full stop after long slipping behavior.

7. CONLUDING REMARKS

From above study, following matters have been understood.

- The approach presented here is a practical way for mechanism investigation and rockfall behavior study as well as the design of rockfall prevention facilities.

- As for the mechanism of the rockfall event analyzed in the study, besides the groundwater erosion, the progressive collapse of the subjacent slope of the rock block is presumed to be a direct trigger.
- High precision of the simulation of the rockfall behavior intimates that the analytic model and the material properties identified from the backward analysis of the creep deformation reflect the real site situation.
- The observed creep deformation is simulated with high precision. From the analytic results, the accuracy of the monitoring system has been understood generally. It is concluded that the alignment of the monitoring sensors is reasonable and the system works functionally.

In order to improve the analytic method, i.e. the combination of DDA backward analysis and manifold method, it is expected to apply the method to many case studies. And for the prevention and mitigation of the rockfall disasters, a prediction system based on the method will be attempted in the future.

ACKNOWLEDGEMENTS: It is a great pleasure to express our deepest gratitude to Dr. Shi for his constant guidance to carry out the research presented here. Mr. Sasaki T. and Mr. Yamamoto T. of Aomori Prefecture government are gratefully acknowledged for providing us the valuable observational data. We would also like to thank Prof. Ohnishi Y. of Kyoto University for his kind guidance and suggestion up to now.

REFERENCES

1. Shi, G.H. and Goodman, R.E.: Discontinuous Deformation Analysis, *25th US Symposium on Rock Mechanics*, pp.269-277, 1984
2. Shi, G.H.: Manifold Method of Material Analysis, *Transactions of the 9th Army Conference on Applied Mathematics and Computing*, Report No.92-1, U.S. Army Research Office, 1991
3. Shi, G.H.: Discontinuous Deformation Analysis, A New Numerical Model for the Statics and Dynamics of Block System. *Ph.D. Thesis, Department of Civil Engineering, University of California, Berkeley, August,1988*

Stability analysis of ancient block structures by using DDA and Manifold method

T. Sasaki, I. Hagiwara & K. Sasaki
Rock Engineering Lab., Suncoh Consultants Co., Ltd., Tokyo, Japan
R. Yoshinaka
Saitama University, Saitama, Japan
Y. Ohnishi
School of Urban & Environment Engineering, Kyoto University, Kyoto, Japan

ABSTRACT: This paper describes the stabilities of ancient block structures using discontinuous deformation analysis (DDA) and Manifold method. The stress concentration of pyramid of the Pharaoh Khufu (Egypt) and the Pont of Gard are analyzed with continuous and discontinuous models by using DDA, the original triangle and the four node iso-parametric Manifold method. The stress concentration and the settlement of foundations are compared with DDA and Manifold method. The results show qualitative agreement, and so the methods are applicable to physical phenomena.

1. INTRODUCTION

Kerisel, J.(1985) have studied long-term stability and stress concentration of many ancient masonry structures and evaluates settlement of those foundations by using empirical theory and pointed out factors of collapse these are the load concentration, the ground condition and the settlement of foundation[2].

Since, in order to evaluate of sedimentary rock in the long–term stability behavior of deformation, the authors are analyzed the masonry structure of the Pharaoh Khufu's Pyramid located in Giza area constructed B.C. 2551 and the Pont of Gard located in French constructed A.D. 17 by Discontinuous Deformation Analysis (DDA) and Manifold Method (MM). Those ancient structures still standing and carry us a message. Photo-1 shows the Khufu's Pyramid and the Pyramid was constructed on the sedimentary limestone and the formation is not horizontally but little inclined on the hill. The Khufu's Pyramid was measured by F. Pytory in 1880 and Ministry of measurement of Egypt in 1925. And the precise measurement involving the settlement was done by T.Nakagawa in 1978 [1]. The width of foundation is about 230 m and the height is about 147 m. In the Khufu's pyramid, there are three chambers as King's chamber, Queen's chamber and underground unfinished chamber at the 30 m depth from ground level [4].

Those chambers are still stable from after 4500 years in construction. Therefore, the authors expected to get the knowledge of the long-term stability of sedimentary rock to analyze those ancient masonry structures. The objective of the studies are evaluates of rock materials to elucidation of the stress concentrations and the deformation of those ancient structures by using DDA and MM.



Photo-1 The Khufu's pyramid

2. OUTLINE OF THE GEOLOGY AT GIZA AREA

Figure-1 shows the geological map around Giza area as three pyramids constructed [3]. Those pyramids are constructed on the tertiary deposit limestone along a flood plain field of river Nail. The tertiary deposit limestone called Mokattam formation and the area is about 1.5 Km square and surrounded perpendicular two faults. Figure-2 shows the geological section near Giza area and the thickness of Mokattam formation is 120 m and it is not horizontally with little inclined of South-East direction. The structure of formation could see from the Sphinx of side body as shown Photo-2.

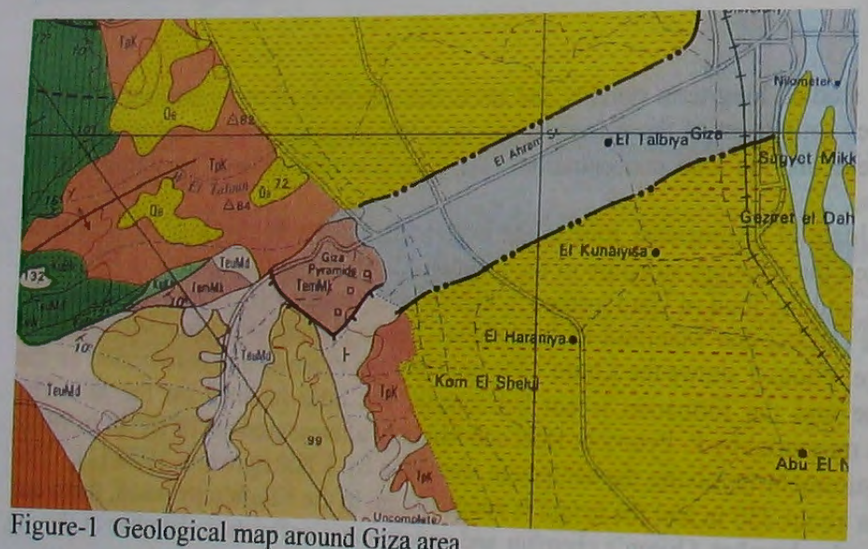


Figure-1 Geological map around Giza area

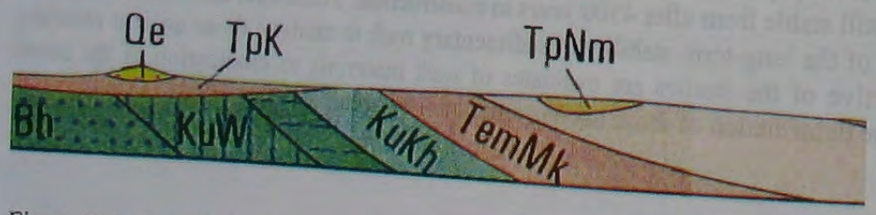


Figure-2 Geological section near Giza area

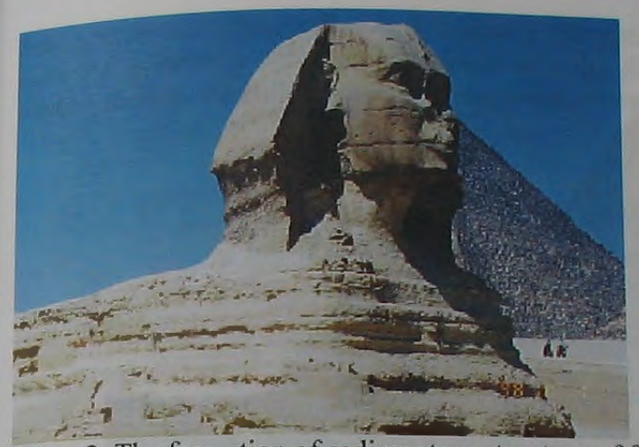


Photo-2 The formation of sedimentary structure of foundation

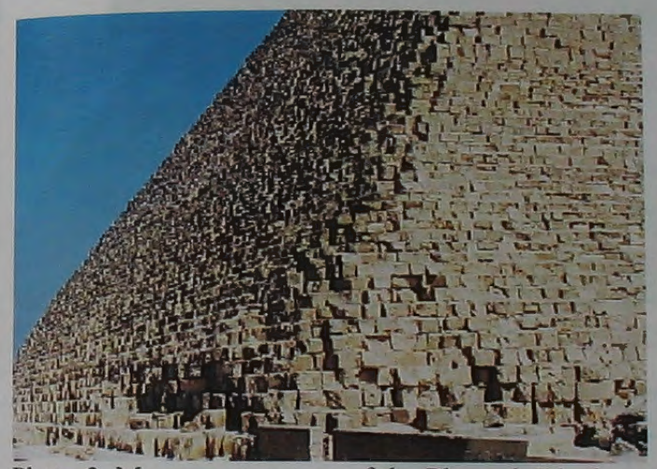


Photo-3 Masonry structure of the Pharaoh Khufu pyramid

3. ANALYSIS OF THE UPPER MASONRY STRUCTURE OF THE PYRAMID

3.1. Analytical models and parameters

The total number of blocks of the pyramid is estimated about 2300 thousand. The height of the Pyramid is 147 m and the width of the foundation is 230m. The total story of the masonry is 203. The total volume is estimated about 2 million and 595 thousand and the total weight is estimated about 5.62 MN. The height of each level, the lower level is about 1.2 m and the upper level is about 75 cm which those are smaller towards the upper level. The unevenness of each level is 2 to 3 cm and those are surprisingly horizontal. The block length of horizontal direction, the lower level is 1 to 1.5 m and the upper level is 10 cm to 1 m at random of the places [1]. Figure-3 shows two dimensional DDA model of the Pharaoh Khufu pyramid.The total story of DDA model is 48 and the average height of step is 2.5 m and the average length of horizontal direction is 5 m for simplicity. The total number of blocks is about 1200.

The material property of limestone blocks was determined by experiments considering size effect of the block as shown Table-1 [5].

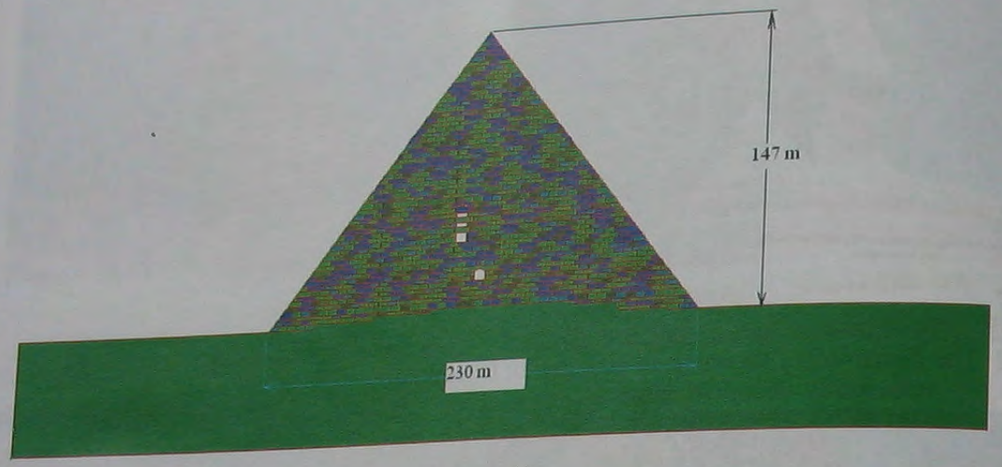


Figure-3 DDA model of the Pharaoh Khufu pyramid

Table-1 Material properties and parameters

Items	Parameters	
Material	Upper block	Foundation
Time increment	0.001 second	
Elastic modulus	1GPa	1 GPa
Unit mass	20 kN/m^3	18kN/m^3
Poisson's ratio	0.30	
Friction angle, Cohesion	ϕ=35°, c=0.0 MPa	
Penalty coefficient (Normal) Penalty coefficient (Shear)	10GN/m^3 4GN/m^3	
Viscosity (Block body)	10%× (unit mass) ×sec	
Viscosity (Normal contact) Viscosity (Shear contact)	10%× (Penalty Pn)×sec 10%× (Penalty Ps)×sec	
Velocity – energy ratio	Rock VS Rock: 0.80	

3.2. Results of the DDA model of Pharaoh Khufu pyramid

Figure-4 shows the principal stress distribution of the static mode calculation. The maximum principal stress distribution around King's chamber is 6 to 7 MPa and this value is almost equivalent what Kerisel (1985) was pointed out by empirical method. The maximum principal stresses of near outside part of the pyramid is distributed along pyramid shape and the inside part is distributed toward perpendicular to the foundation. Figure-5 shows the principal stress distribution of the dynamic mode calculation. The stress distribution of near outside part of the pyramid is distributed

confused and not smoothed comparison with the static mode case. In the dynamic mode calculation, once the unbalance force cause numerically the displacement of the pyramid structure towards development to the collapsed. This phenomenon shows actual physical behavior [7].

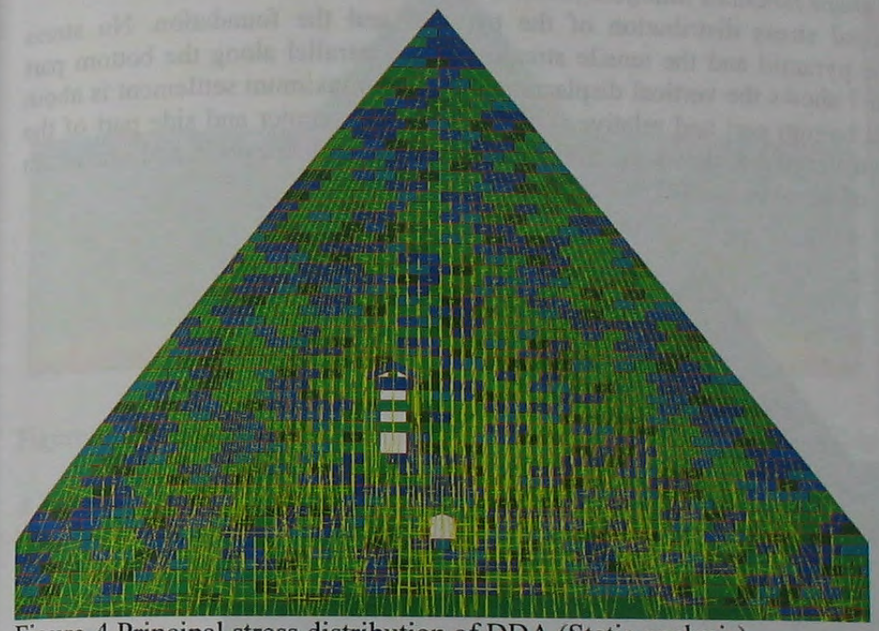


Figure-4 Principal stress distribution of DDA (Static analysis)

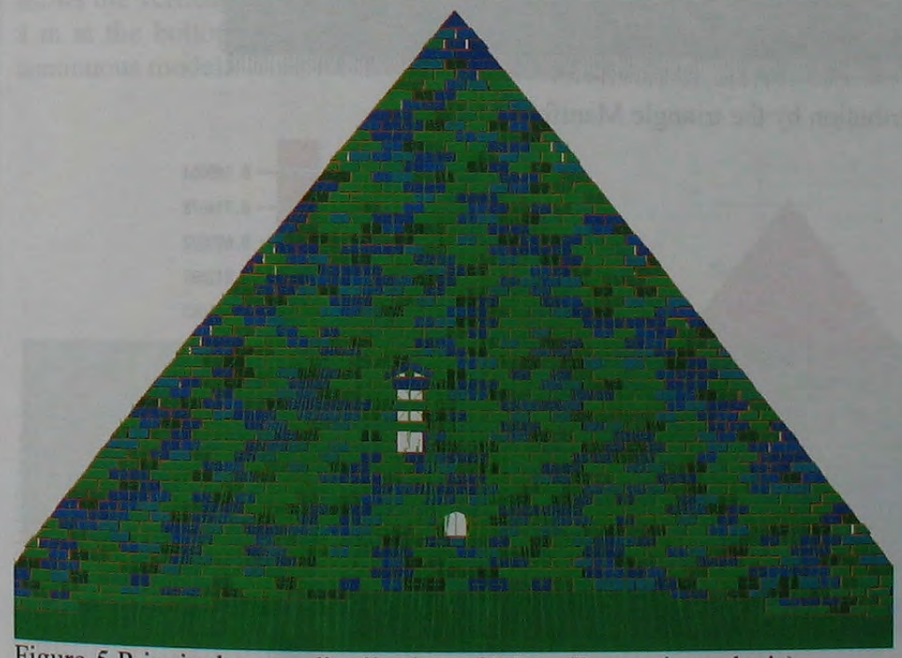


Figure-5 Principal stress distribution of DDA (Dynamic analysis)

4. ANALYSIS OF THE FOUNDATION OF THE PYRAMID BY MANIFOLD METHOD

In order to estimates settlement of the pyramid foundation, the same model as DDA is analyzed by the triangle original and the 4-node iso-parametric Manifold Methods [8][9].

4.1. Results of the triangle shape functions Manifold Method

Figure-6 shows the principal stress distribution of the pyramid and the foundation. No stress concentration caused in the pyramid and the tensile stresses caused parallel along the bottom part near the foundation. Figure-7 shows the vertical displacement and the maximum settlement is about 60 cm at center of pyramid bottom part and relative settlement between center and side part of the pyramid is about 10 to 20 cm. Figure-8 shows the maximum shear strain distribution and maximum value is located central part of the structure [8].

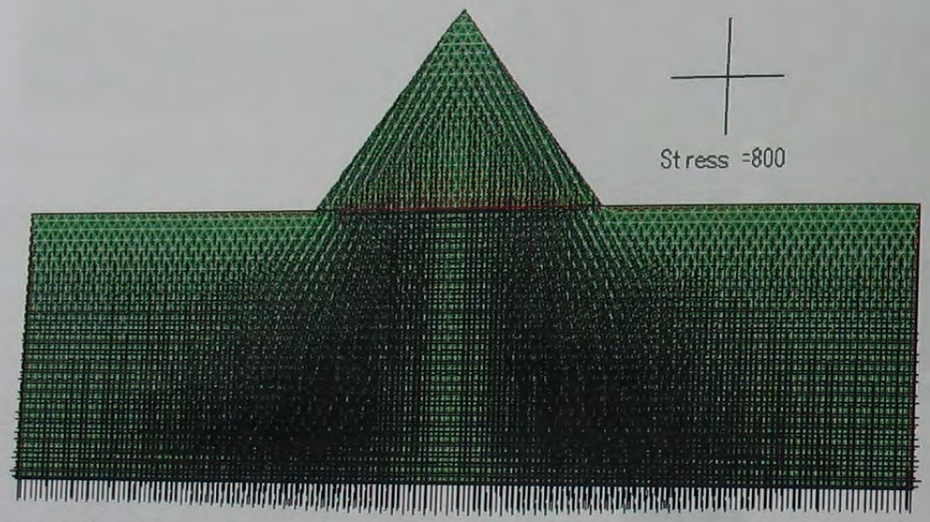


Figure-6 The principal distribution by the triangle Manifold Method

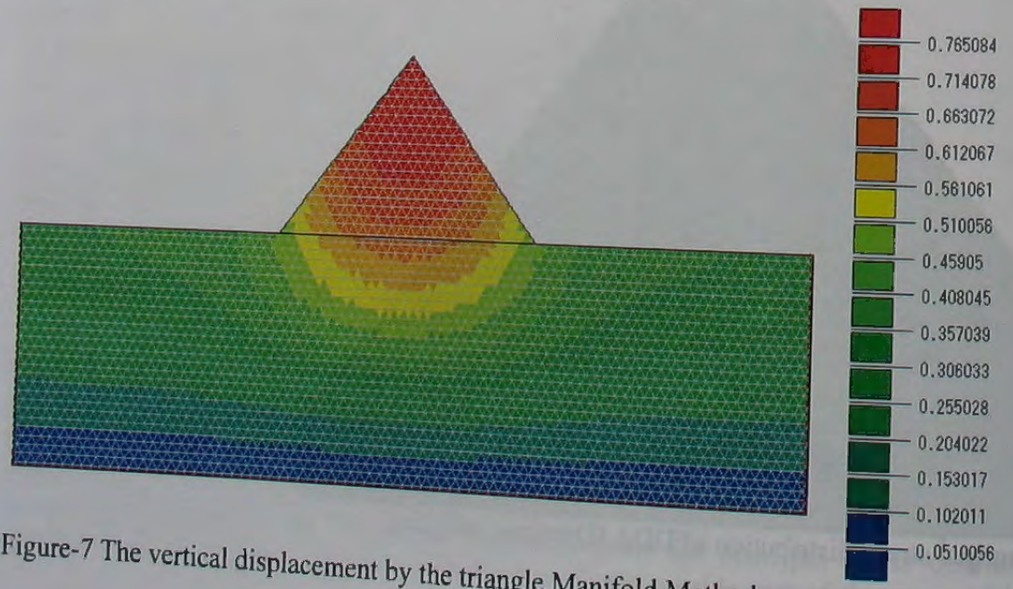


Figure-7 The vertical displacement by the triangle Manifold Method

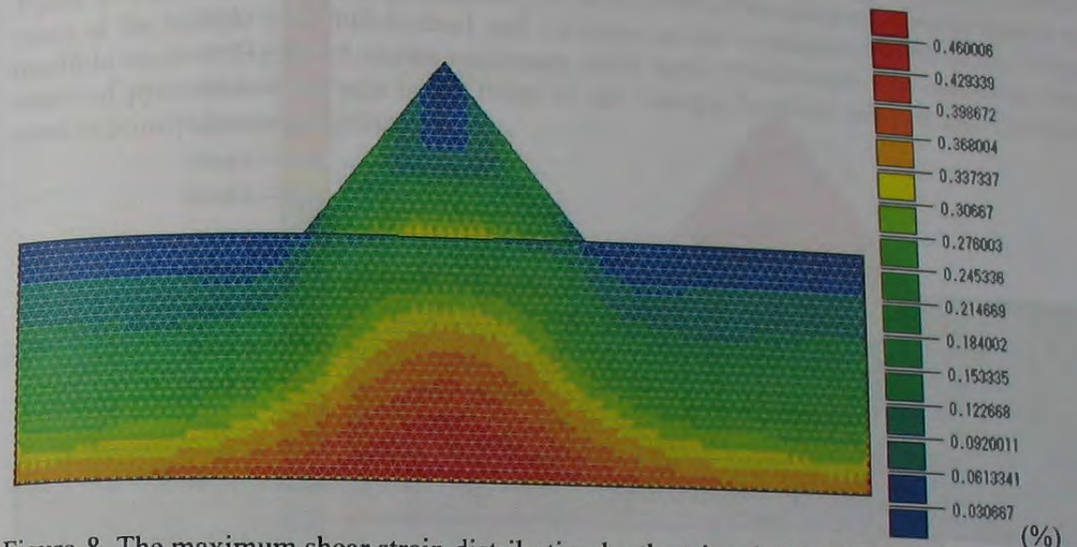


Figure-8 The maximum shear strain distribution by the triangle Manifold Method

4.2. Results of the continuous model of the iso-parametric shape functions Manifold Method

In order to compare between the triangle shape function and the iso-parametric function Manifold Method, the pyramid continuous and the discontinuous models are calculated by the iso-parametric Manifold Method [9]. Figure-9 shows the principal stress distribution of continuous model. In this case, the maximum stress concentrated at the bottom of both side near the foundation. Figure-10 shows the vertical displacement distribution of continuous model. The maximum settlement is about 1 m at the bottom of central part. Figure-11 shows the maximum shear strain distribution of the continuous model.

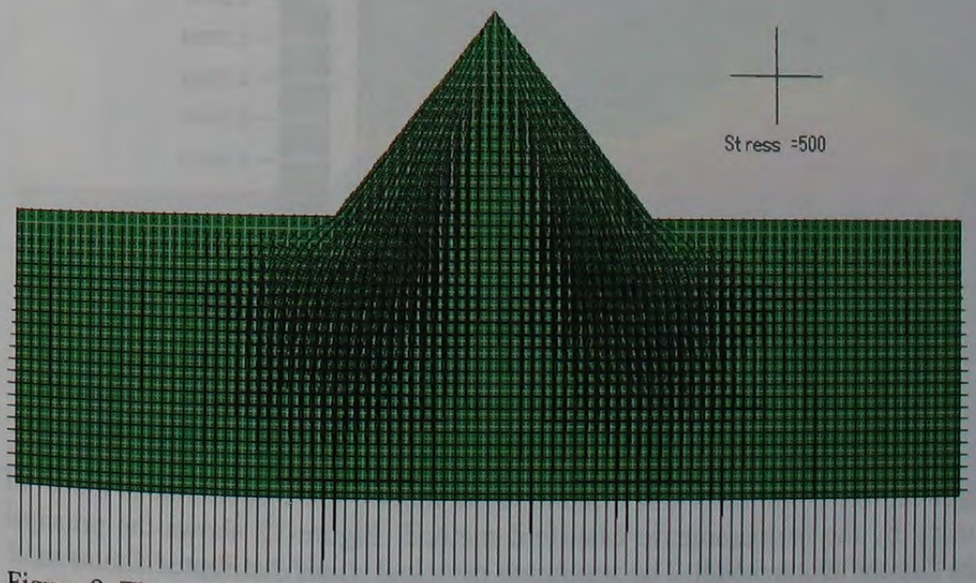


Figure-9 The principal distribution by the iso-parametric Manifold Method

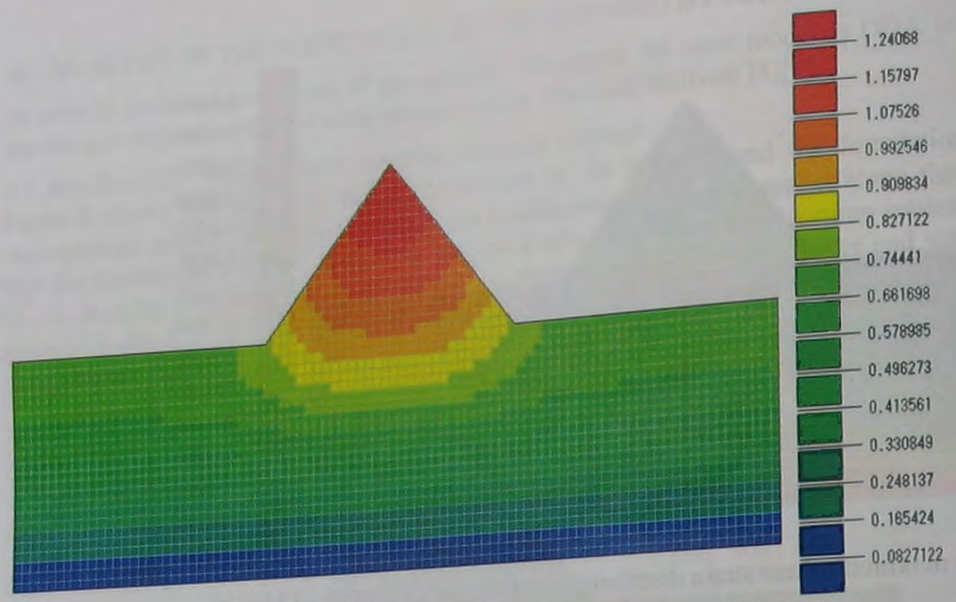


Figure-10 The vertical displacement by the iso-parametric Manifold Method

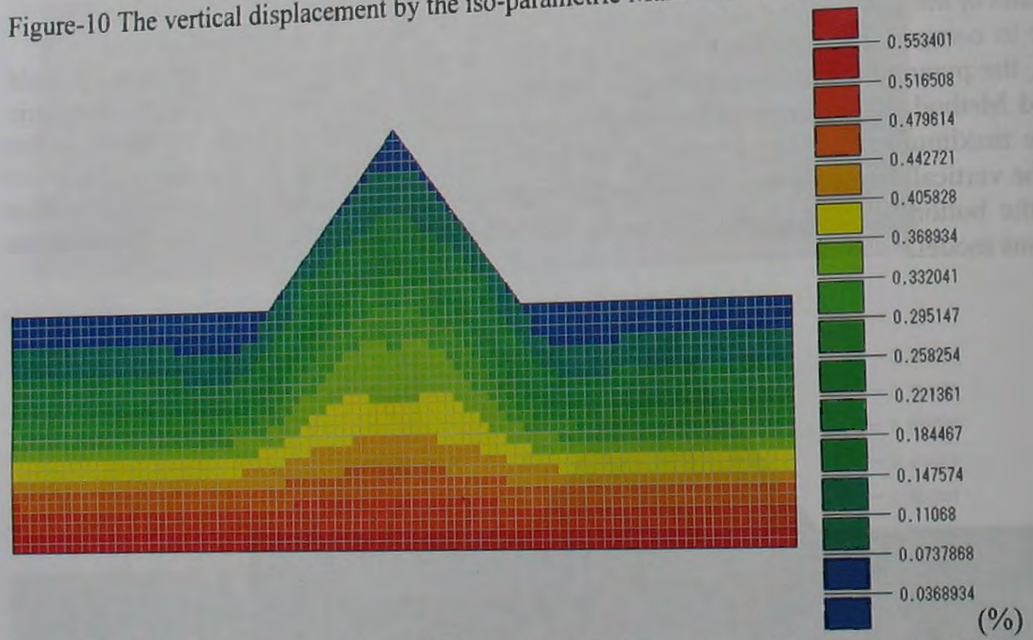


Figure-11 The maximum shear strain distribution by the iso-parametric Manifold Method

4.3. Results of the discontinuous model of the iso-parametric shape functions Manifold Method

In order to compare between the continuous and discontinuous model, the discontinuous model of pyramid is analyzed using by the iso-parametric Manifold method. Figure-12 shows the principal stress distribution of the discontinuous model. The maximum principal stress distributed almost same tendency of the triangle manifold method as shown Figure 6 but the tensile stress distribution along

bottom of the pyramid is relatively large and disturbed compare with the triangle manifold method. Figure 13 shows the vertical displacement. The settlement of the center of pyramid bottom area is 2.0 times of the triangle manifold method and 1.4 times of the continuous model of the iso-parametric manifold method. Figure 14 shows maximum shear strain distribution. The maximum strain at the center of pyramid bottom area is 2.2 times of the triangle manifold method and also disturbed as same as principal stress distribution.

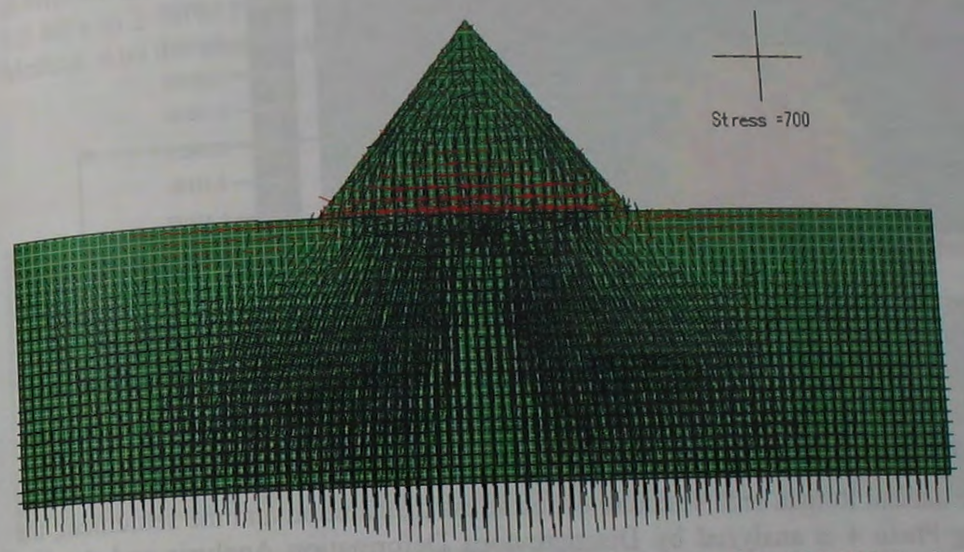


Figure-12 The principal distribution by the iso-parametric Manifold Method
(the discontinuous model)

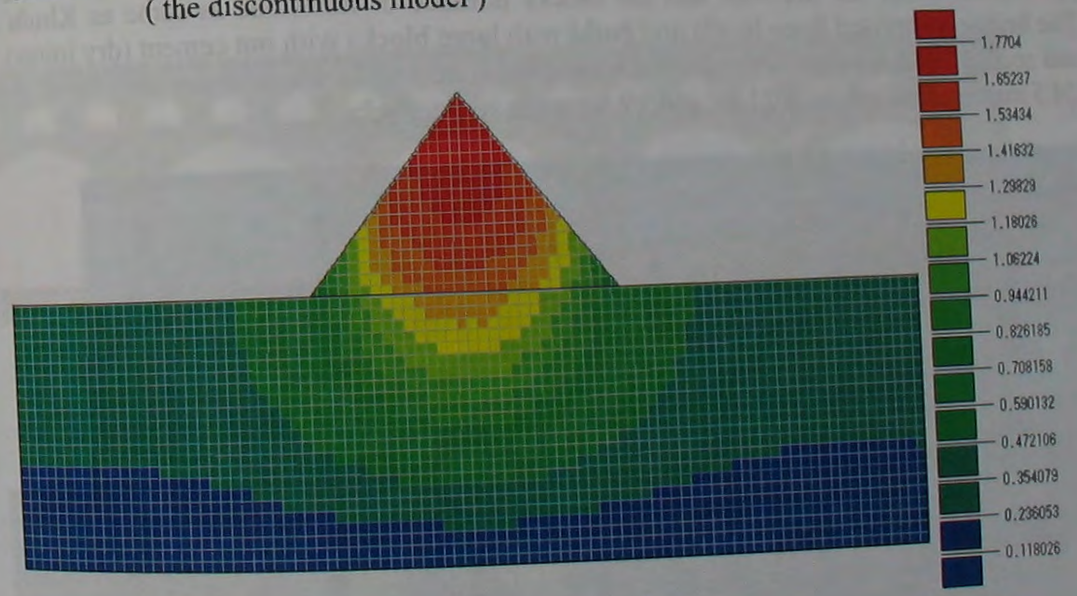


Figure-13 The vertical displacement by the iso-parametric Manifold Method
(the discontinuous model)

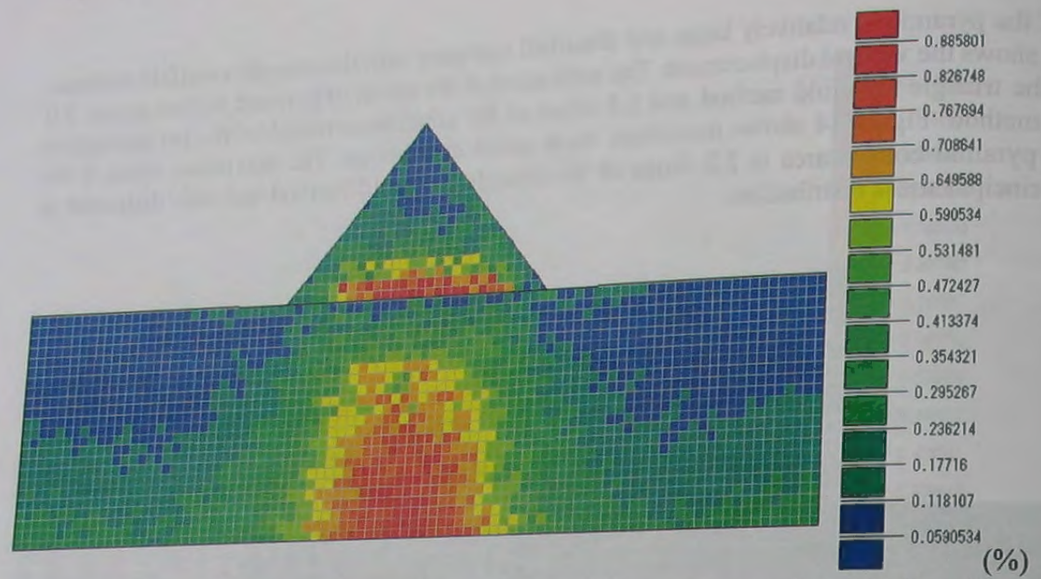


Figure-14 The maximum shear strain distribution by the iso-parametric Manifold Method (the discontinuous model)

5. ANALYSIS OF THE PONT DU GARD ANCIENT ROMAN ARCH STRUCTURE

In order to analyze the ancient Roman arch structure of the stress distribution and the settlement, the Pont of Gard showing Photo 4 is analyzed by Discontinuous Deformation Analysis and the iso-parametric manifold method. The structure was constructed for aqueduct in ancient Roman age B.C.17. The foundation of the structure and the blocks is made of limestone as same as Khufu's pyramid. The bridge comprised three levels and build with large blocks with out cement (dry joints). The first and second level features six and eleven superimposed arches whose spans vary from 15.5 meters to 24.5 meters. And height is 21.87 and 19.5 meters respectively.



Photo-4 The Pont of Gard ancient Roman arch structure

The third level, which is 490 meters long, comprises forty seven arches (12 of which were destroyed in the middle Ages), supports the aqueduct proper. These thirty-five arches are 4.8 meters wide and height is 7.4 meters. To render them waterproof, the walls of the canal are covered by a reddish-brown plaster-work, a Roman secret call the "malthe".
Figure 15 shows the DDA model and the total block is about 2500. The material properties and the parameter of calculation are same as the pyramid model as shown table 1.
Figure 16 shows the principal stress distribution of around main arch and the major stresses are distributed along each arch shapes. The maximum stresses distribute at the bottom of pillars which is 1.5 MPa to 2 MPa. Figure 17 shows the principal stress distribution by the iso-parametric Manifold Method. And the stresses are disturbed compare with the DDA result.

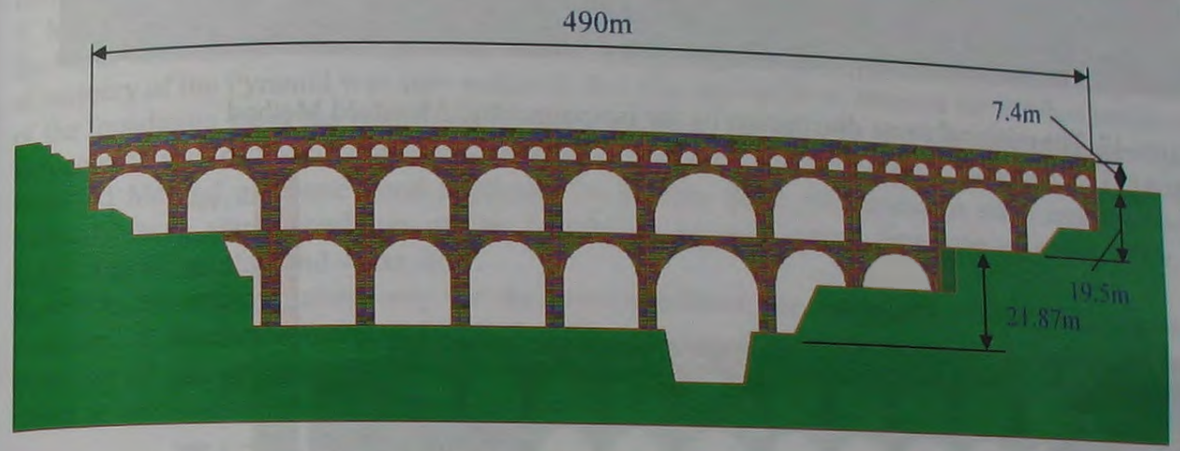


Figure-15 The DDA model of the Pont of Gard

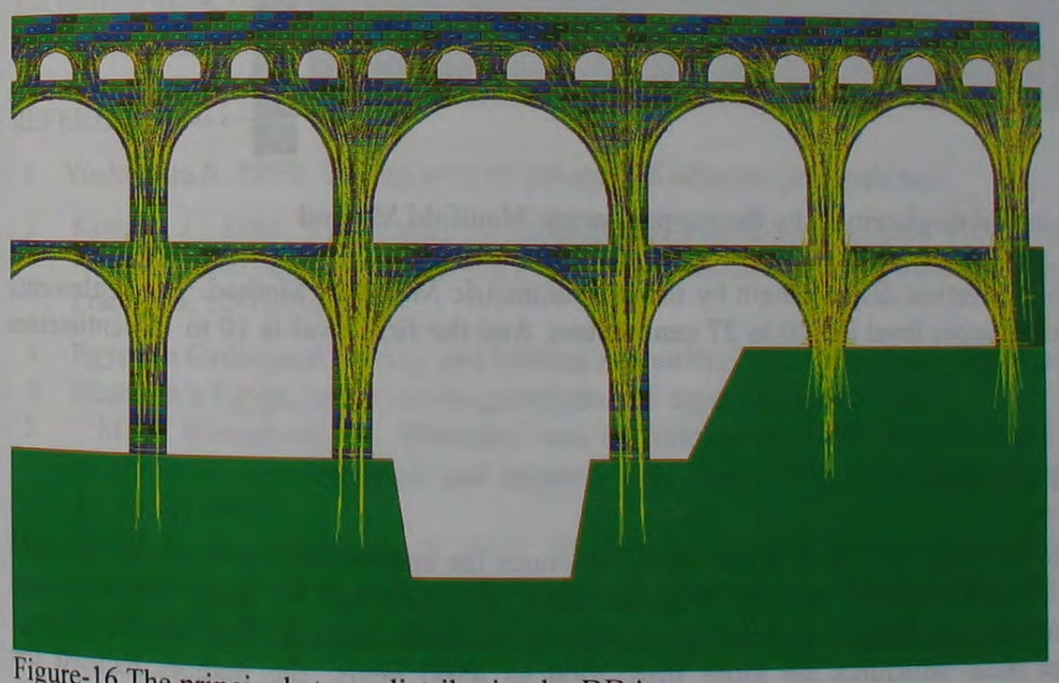


Figure-16 The principal stress distribution by DDA

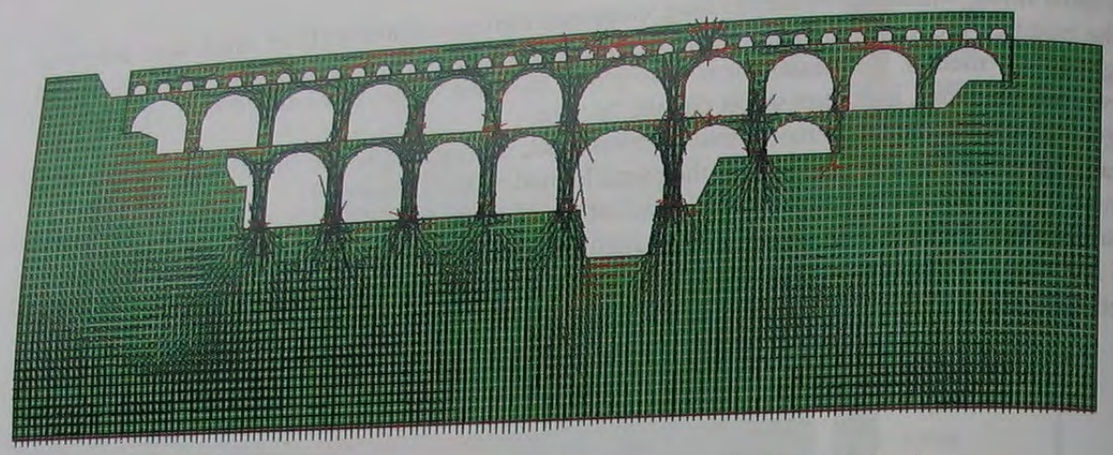


Figure-17 The principal stress distribution by the iso-parametric Manifold Method

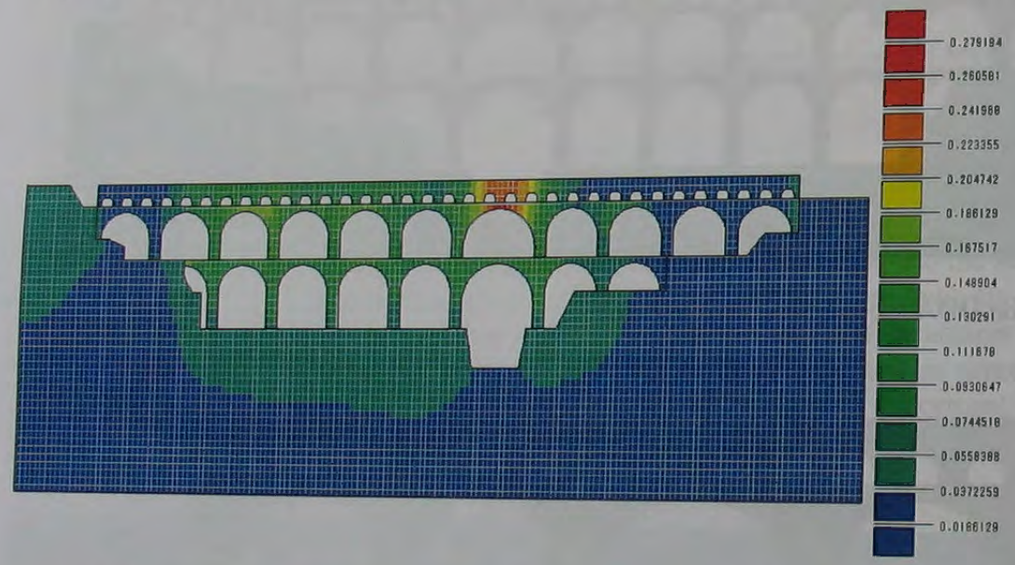


Figure-18 The vertical displacement by the iso-parametric Manifold Method

Figure 18 shows the vertical displacement by the iso-parametric Manifold Method. The settlements around main arch at upper level are 20 to 27 centimeters. And the first level is 10 to 15 centimeters experimentally.

4. CONCLUDING REMARKS

In order to analyze for long term stability of block structures the ancient two international heritages in which the Khuhu's pyramid and the Pont of Gard are analyzed by using Discontinuous Deformation Analysis, the triangle and the iso-parametric manifold method. The reasons of long-term stability of these structures for more than 2000 to 4500 years, the authors focused the

settlements of foundation of the structures and both structures are not collapsed and still keep standing. The first reason is to keep horizontal level of foundations of the structures depends on the mechanical property of the foundation deformability. The second reason that the masonry structure is released surplus shear forces between blocks in its self each others because of compare with the distribution of the principal stresses between DDA and Manifold Method as shown before. And this reason is effective for earthquake motions of the masonry structures also. The third reason, the contemporary design method of structures is estimate the settlement of foundation or the members of beam before construction and finally constructed them considering to keeps horizontal position of the structures. The second bridge of the Gard constructed in 1743 alongside the old aqueduct concealing all the arches on the first level, which the center part of bridge is height about 20 centimeters than the side parts distinguished as shown as Photo 4. According to the measurement by T. Nakagawa in 1978, the difference of horizontal relative level between the South-East corner and the North-West corner was 45 to 30 mm of the first story masonry [1]. In fact, the constructing works of masonry of the Pyramid was very précised. But it is impossible to measure the absolute settlement of the foundation from the initial conditions. Therefore, we imagine that the ancient designers are also considering in this circumstances of their experiments and the presented methods of DDA and Manifold Method are have good applicable to explain those phenomena in static analyses. Both structures have same condition of the foundation as sedimentary limestone which is stable in chemically for rainfall and water flow.

However, this paper studied only for the static condition, the earthquake motion of the dynamic condition is another important factor for the stability of the structure. We will analyze those structures of the dynamic condition of the earthquake motion in the future as we recommended model as considering frequency characteristics of the structure [10][11].

ACKNOWLEDGMENT

The authors thank Dr. Gen Hua Shi for many informative discussions.

REFERENCES

1. Yoshimura S. 1979. The mystery of pyramid, Kodansha (in Japanese)
2. Kerisel J., 1985. The history of geotechnical engineering up until 1700, *Proceedings of the eleventh international conference on soil mechanics and foundation engineering*, San Francisco, 12-16 August.
3. Egyptian Geological Survey and Mining Authority, 1983. Geological map of grater Cairo area
4. Guardian's Egypt, http: / /www.guardians.net/ egypt/ pyramids . htm
5. M. I. Aboushook, Y. Wkizaka, and S. Shinagawa, 1999. Environmental impact on the durability of some Egyptian and Japanese lime stones Proc. Of 9th ISRM Congress Paris, Vol. 2, , pp.991-996
6. Sasaki T. and Yashinaka R.,2002. Studies of masonry structures by using Discontinuous Deformation Analysis and Manifold Method, *Proceedings 7th Japan Society for Computational Engineering and Science*, pp.431-434, May.

7. Shi G.H. 1989. Block system modeling by discontinuous deformation analysis, *Univ. of California*, Berkeley, Dept. of Civil Eng. August.
8. Shi, G. H. 1991. Manifold method of material analysis, *Trans. 9th Army Conf. on Appl. Math. and Comp.*, Rep. No. 92-1. U.S. Army Res. Office
9. Sasaki T. and Ohnishi Y. 2001. Analysis of the discontinuous rock mass by four node iso-parametric Manifold method, *Fourth International Conference for Analysis of Discontinuous Deformation*, Glasgow, Scotland pp.369-378, UK, 6th-8th June.
10. Yoshinaka R., Sasaki T., Sasaki K., Horikawa S. 2007. Consideration on stability and collapse at earthquake of soft rock slope based on an example, *11th ISRM Congress* Lisbon, Portugal , pp. 1109-1112
11. Sasaki T., Hagiwara I., Sasaki K., Ohnishi Y., Ito H. 2007. Fundamental studies for dynamic response of simple block structures by DDA, *Eighth International Conference on the Analysis of Discontinuous Deformation*, pp. 141-146

Motion Analysis of Deformable Discrete System by Vector Form Intrinsic Finite Element (VFIFE) Method

Wang, C. Y.
Professor, Department of Civil Engineering, National Central University, Chungli, Taiwan
Chen, S. H.
Graduate Student, Department of Civil Engineering, National Central University, Chungli, Taiwan
Wang, R. Z.
Assistant Research Fellow, National Center for Research on Earthquake Engineering, Taipei, Taiwan

ABSTRACT: A novel vector form computational method for solids and structure is applied to analyze the nonlinear motion behavior of discrete deformable bodies. Algorithms for contact searching and interaction analysis are included into the Vector Form Intrinsic Finite Element (VFIFE) method developed by Edward Ting in 2004. The VFIFE method models the analyzed domain to be composed by finite particles and the Newton's second law and Euler's equation of motion are applied to describe each particle's motion. By tracing the motions of all the mass particles in the space, it can simulate the large geometrical and material nonlinear changes during the motion of structure without using geometrical stiffness matrix and iterations. The analysis procedure is vastly simple, accurate, and versatile. The formulation of VFIFE type solid element includes a new description of the kinematics that can handle large rotation and large deformation, and includes a set of deformation coordinates for each time increment used to describe the shape functions and internal nodal forces. A convected material frame and an explicit time integration scheme for the solution procedures are also adopted. Numerical examples are presented to demonstrate capabilities and accuracy of the VFIFE method on the nonlinear motion analysis of deformable discrete system.

1. INTRIDUCTION

The main objective of mechanical analysis is to predict the behaviors of structural system under various types of loading. Modeling of the system together with the associated loading conditions is the essential task of an engineering analysis. Computational mechanics is an effective mean for engineers to study the complicated engineering problems admitted in industrial designs and evaluation works that usually cannot be handled by analytical methods. The finite element method (FEM) developed in the last century has demonstrated its capabilities of analyzing engineering problems. However, there still are some problems that exhibiting discontinuities, multiple cracks formation and propagation, multi-body dynamics, large deformation that cannot be well and effectively analyzed by the FEM. Therefore, it is worth reinvestigating the limitations and the fundamental principles inherited in the theories that we have being used in conventional analyses. Then, it is possible to develop a new method to solve the difficulties admitted in applying the conventional methods from different points of view.

The development of the FEM is originated from the matrix analysis and slope deflection method of the structural mechanics. It promoted the concept of member-connection of structure to the continuous medium. The equilibrium condition is satisfied within all the members (elements) according to the deformation modes characterized by the connections (nodes) and a set of linear equations is obtained by equilibrating internal forces assembled from surrounding members (elements) of each connection (node). This intrinsic concept of physically modeling of the structural system obtains good results in analyzing continuous medium by using constant triangle elements. However, this member-connection modeling of linear structure admitted difficulties when it was applied to the higher order finite element, plate/ shell and 3D deformable

bodies. The finite element method entered its new era after adopting the theory of the calculus of variation and some numerical techniques of approximation and discretization. The FEM currently known to the researchers can be identified as a mathematical modeling of continuous medium and is a computational modeling of Ritz-Galerkin analysis. Nevertheless, the analysis method based on the theory of the calculus of variation and the balance of energy inside the simply connected continuous medium still has its limitations on solving some real world problems especially with multiple discontinuities. Some methods like the discrete element method (DEM) (Cundall & Strack 1979), the jointed element method (JEM) (Goodman & Taylor & Katona 1968), the discontinuous deformation method (DDA) (Shi 1988) and the manifold method (MM) (Shi 1992,1996) proposed in the last decade were intent on solving this type of engineering problems. The concept of these methods is close to the physical modeling of a system. But, the accuracy and the stability of these methods are not competitive to the FEM at the moment and can only provide qualitative analysis most of the time.

A new computational method so called the Vector Form Intrinsic Finite Element (VFIFE) is developed by Ting, Shih & Wang (2004) to handle engineering problems with the following characters: (1) containing multiple deformable bodies and mutual interactions, (2) material non-linearity and discontinuity, (3) large deformation and arbitrary rigid body motions of deformable body. Since the conventional FEM based on variational method requires the total virtual work to be zero but does not require the balance of forces at nodes. These unbalanced residual forces will do some non-zero work under virtual rigid body motion and cause the inaccuracy and un-convergence of the calculation results. The computation procedure and some concepts of this VFIFE method are similar to the FEM. But the major difference is that the VFIFE does not apply the variational principle on the stress expressed equilibrium equations in its formulation. Instead, VFIFE maintains the intrinsic nature of the finite element method and makes strong form of equilibrium at nodes, the connections of members. All the forces balanced at each node are obtained from the principle of virtual work and the associated deformations are satisfied with the compatibility condition of deformation.

Due to mechanical loading, chemical reactions and thermal treatment during the manufacturing processes or from damage during service, discontinuities in the physical field of an engineering system might exist at different scope levels. Complicated behaviors due to these discontinuities lead to difficulties in interpretation and analysis. In the past decades, topics concerning such discontinuities as the behavior of jointed rock masses, ice plates or granular materials, the delamination of a layered medium, blasting fragmentation, the damage/fracture progression of a material etc., have been worked by a number of researchers and engineers (Munjiza, 2004).

In the present paper, the VFIFE method is used to study the dynamics of deformable discrete system with large displacement and rotation. Numerical examples are given to demonstrate the capabilities of this new method to predict the complicated behaviors that were not easily conducted by the conventional computational methods.

2. FUNDAMENTALS OF A VECTOR FORM INTRINSIC FINITE ELEMENT (VFIFE)

2.1. Deformation coordinate and Convected Material Reference Frame

Structures will exhibit distinct geometrical deformation when it is under damage and fracturing. Any numerical simulation code must have the capabilities of modeling the large displacement and large deformation that the structure undergoes. The profound theories of nonlinear continuous mechanics developed in last century were based on mathematical analysis. Total stress-strain theory was used to model the behaviors of material. The kinematics description of material point is based on the material frame of initial configuration. However, the usage of total deformation theory in numerically analyzing nonlinear continuous media will cause some difficulties, for example the requirement of positive definite of matrix is not satisfied. Therefore,

there are some restrictions on the size of deformation and displacement in conventional nonlinear finite element analysis methods.

To study the behaviors of structure under damage and fracturing, we must develop an algorithm that can exclude this kind of restrictions and can do predictions stably and accurately. Based on these concepts, Ting (2004) developed the VFIFE method. In this method, explicit formulation is used to avoid the difficulties that are caused by iterations of material non-linearity and an incremental theory based on the material reference frame of current configuration is used to define the stress-strain relations. In the calculation process, the external loads are applied to the deformable body incrementally. These incremental forces apply to a continuous body with stress and motion. All the material properties, stress distribution, particle velocities and geometry are defined from the calculation results of previous time step. The motion path and loading history of material points in the system are independent to the incremental type computational algorithm. The history dependency is inherited in the adjusting of parameters of material model during the calculation. Hence, we can call this explicit calculation is based on the convected material frame. The incremental theory may not be so complete and accurate as the total deformation theory since errors are introduced in every incremental step. But, we are benefited from the simplification and convenience it provides to the code development.

Figure 1 can explain the general concept and the incremental algorithm of the VFIFE method. At time t, the material point is located at $\mathbf{x}$ and it moves to $\mathbf{x}'$ after a time increment Δt. $\Delta\mathbf{F}$ is the deformation gradient increment calculated from the equations of motion and the load increment at time $t+\Delta t$. To calculate the internal forces applied at each node, the deformation of material has to be identified. Since the rigid body motion of material point has no effects on the values of virtual work, stress and strain, the VFIFE method decomposed the motion within this time increment into $\Delta\mathbf{F}^d$ and $\Delta\mathbf{R}$. A deformation coordinate system $\hat{x}-\hat{y}$ is constructed in each time step by a rotation matrix $\mathbf{Q}$ from global coordinates based on the deformation calculated at current time step. The objectivity of this deformation coordinate system had been proved by Shih & Wang & Ting (2004). If the rotation matrix $\Delta\mathbf{R}$ calculated in each time step is the true rotation matrix $\Delta\mathbf{R}^*$ of the polar decomposition of $\Delta\mathbf{F}$, then the $\Delta\mathbf{F}^d$ is equal to the pure right stretch matrix $\Delta\mathbf{U}$ in the theory of continuous mechanics (Malvern, 1969). But, the rotation matrix $\Delta\mathbf{R}$ defined in the VFIFE method is just a rough approximation. The difference between $\Delta\mathbf{R}$ and $\Delta\mathbf{R}^*$ can be reduced, if a small time increment is used. The rigid body motion residua existed in $\Delta\mathbf{F}^d$ could be filtered out through the construction of the deformation coordinates in VFIF method. It has to be pointed again that the deformation of the analyzed medium at time $t+\Delta t$ is defined already. The decomposition of $\Delta\mathbf{F}$ into $\Delta\mathbf{R}$ and $\Delta\mathbf{F}^d$ is just made to calculate the internal forces at this current time step. The internal forces are calculated by the relative deformation to this material reference frame. These calculated internal forces at time $t+\Delta t$ will be dynamically equilibrated with the external loads applied at time step $t+\Delta t$ on their corresponding connection nodes. The configuration of the system at time step $t+\Delta t$ can be defined by the new positions of nodal points calculated by the equations of motion.

2.2. Averaged rigid body rotation

For each 2D solid element, we can construct a set of unit vectors $\boldsymbol{e}_i$ from its centroid $\mathbf{c}$ to its nodes at the time t and a set of unit vectors $\boldsymbol{e}_i'$ from its centroid $\mathbf{c}'$ to its nodes at the time $t+\Delta t$. As shown in Fig. 2, the rotation angle θ_i of each unit vector $\boldsymbol{e}_i$ from time t to time $t+\Delta t$ can be determined. The averaged rigid body rotation can be calculated by the following equation

$$\theta=\frac{1}{n}\sum_{i=1}^{n}\theta_i \tag{1}$$

where

$$\theta_i=\cos^{-1}(e_i\cdot e_i') \tag{2}$$

Then, the rotation matrix $\Delta\mathbf{R}$ from time t to time $t+\Delta t$ can be written as

$$\Delta\mathbf{R}=\begin{bmatrix}\cos\theta & \sin\theta\\ -\sin\theta & \cos\theta\end{bmatrix} \tag{3}$$

For the frame element, the angle of rigid body rotation, θ, from the $\hat{x}-\hat{y}$ coordinate system to the $x'-y'$ coordinate system can be calculated by the inner product of unit vectors $\bar{e}_1$ and $\bar{e}_1'$ shown in Fig. 3.

Then the rotation matrix $\Delta\mathbf{R}$ is expressed as

$$\Delta\mathbf{R}=\begin{bmatrix}\cos\Delta\theta & \sin\Delta\theta\\ -\sin\Delta\theta & \cos\Delta\theta\end{bmatrix} \tag{4}$$

where

$$\Delta\theta=\cos^{-1}(\bar{\mathbf{e}}_i\cdot\bar{\mathbf{e}}_i') \tag{5}$$

2.3. Deformational coordinate system

If we define the pure deformation displacement du^d as the difference between the displacement and rigid body displacement,

$$du^d=du-du \tag{6}$$

where the incremental rigid body displacement can be calculated by

$$du^r=(R^T-I)dx \tag{7}$$

where du^r is an averaged rigid body displacement vector and it is not a real physical quantity. Hence, the du^d is just existed inside an element and is not continuous inside the medium.

For the 2D solid element in Fig. 4, we may choose the node 1 as the reference node and define the rigid body translation as the displacement of node 1. Then

$$d\mathbf{u}_2=\mathbf{u}_2-\mathbf{u}_1 \qquad d\mathbf{x}_2=\mathbf{x}_2-\mathbf{x}_1 \tag{8}$$

are the incremental displacement vector and the relative position vector to node 1. The corresponding deformation vector is

$$d\mathbf{u}_2^{\mathrm{d}}=\begin{Bmatrix}du_2\\ dv_2\end{Bmatrix}-(\mathbf{R}^T-\mathbf{I})\begin{Bmatrix}x_2-x_1\\ y_2-y_1\end{Bmatrix} \tag{9}$$

Once the incremental displacement vector of node 2, $d\mathbf{u}_2^{\mathrm{d}}$ is obtained, the unit vectors $\hat{\mathbf{e}}_1$, $\hat{\mathbf{e}}_2$ along $\hat{x}$, $\hat{y}$ coordinate axis respectively can be determined as

Proceedings of International Mini-Symposium for Numerical Discontinuous Analyses, edited by T. Koyama, Hawaii, November, 2008

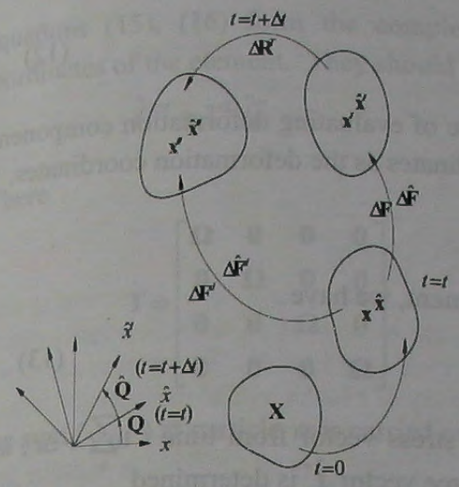


Figure 1. Deformation coordinate and convected material reference frame of VFIFE method.

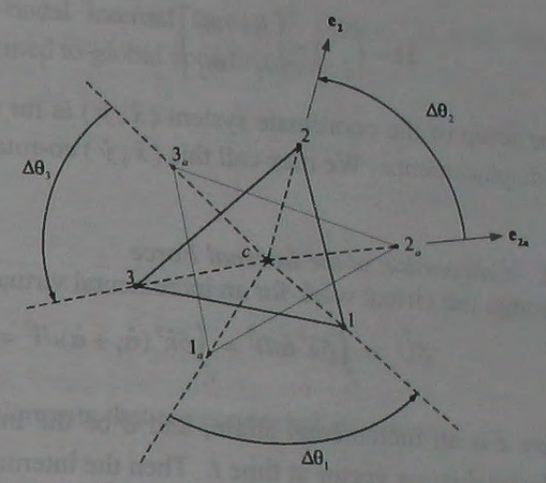


Figure 2. Angle of the rigid body rotation of a 3-node solid element from time t to time $t+\Delta t$

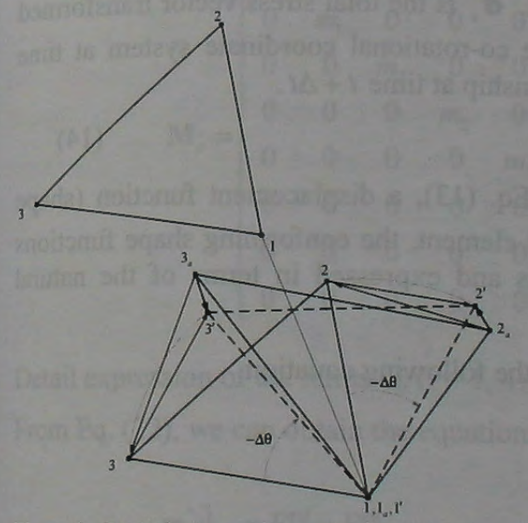


Figure 3. Rigid body rotation of a 2D solid element.

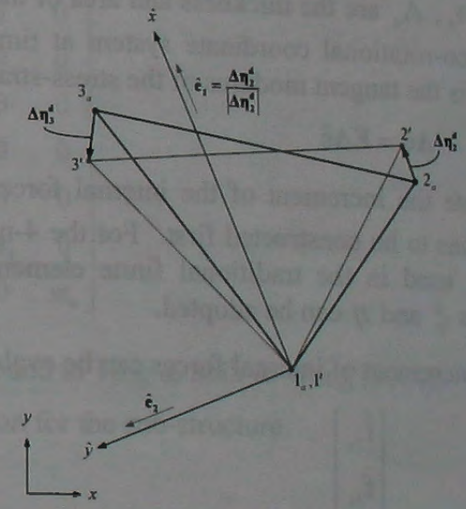


Figure 4. Deformation coordinate system ($\hat{x}-\hat{y}$) of a 3-node solid element.

$$\hat{\mathbf{e}}_1=\begin{Bmatrix}l_1\\ m_1\end{Bmatrix}=\frac{1}{\left|du_2^d\right|}\begin{Bmatrix}du_2^d\\ dv_2^d\end{Bmatrix} \tag{10}$$

$$\hat{\mathbf{e}}_2=\begin{Bmatrix}l_2\\ m_2\end{Bmatrix}=\begin{Bmatrix}-m_1\\ l_1\end{Bmatrix} \tag{11}$$

The coordinate transformation matrix between the convected coordinates and the fixed global coordinates, i.e., $\hat{\mathbf{x}}=\Omega\mathbf{x}$, can be determined as

(12)

$$\mathbf{\Omega}=\begin{Bmatrix}\hat{\mathbf{e}}_1\\ \hat{\mathbf{e}}_2\end{Bmatrix}=\begin{bmatrix}l_1 & m_1\\ l_2 & m_2\end{bmatrix}$$

The setup of the coordinate system $(\hat{x},\hat{y})$ is for the purpose of evaluating deformation components of displacements. We may call this $(\hat{x},\hat{y})$ co-rotation coordinates as the deformation coordinates.

2.4. Calculation of the Internal Force

Through the virtual work for an incremental virtual displacement, we have

(13)

$$\delta U_e=\int_{V_e}\delta\hat{\boldsymbol{\varepsilon}}^T\hat{\boldsymbol{\sigma}}d\hat{V}=\int_{V_e}\delta\hat{\boldsymbol{\varepsilon}}^T(\hat{\boldsymbol{\sigma}}_t+\hat{\boldsymbol{\sigma}})d\hat{V}=\delta(\hat{\mathbf{d}}_e^{\bullet})^T\hat{\mathbf{f}}_e^{\bullet}$$

where $\hat{\boldsymbol{\varepsilon}}$ is an incremental strain, and $\hat{\boldsymbol{\sigma}}$ be the incremental stress vector from time t to $t+\Delta t$, and $\hat{\sigma}_t$ the total stress vector at time t. Then the internal nodal force vector $\hat{\mathbf{f}}_e^{\bullet}$ is determined

(13)

$$\hat{\mathbf{f}}_e^{\bullet}=t_e\int_{A_e}\mathbf{B}^T\hat{\boldsymbol{\sigma}}_t d\hat{A}+t_e\Big(\int_{A_e}\mathbf{B}^T\mathbf{E}\mathbf{B}\,d\hat{A}\Big)\hat{\mathbf{d}}_e^{\bullet}=\hat{\mathbf{f}}_{et}^{\bullet}+\Delta\hat{\mathbf{f}}_e^{\bullet}$$

in which, t_e, A_e are the thickness and area of the element. $\hat{\boldsymbol{\sigma}}_t$ is the total stress vector transformed from the co-rotational coordinate system at time t to the co-rotational coordinate system at time $t+\Delta t$. $\mathbf{E}$ is the tangent modulus of the stress-strain relationship at time $t+\Delta t$.

(14)

$$\Delta\hat{\boldsymbol{\sigma}}=\mathbf{E}\Delta\hat{\boldsymbol{\varepsilon}}$$

To calculate the increment of the internal forces $\Delta\hat{\mathbf{f}}_e^{\bullet}$ in Eq. (13), a displacement function (shape function) has to be constructed first. For the 4-node solid element, the conforming shape functions commonly used in the traditional finite element analysis and expressed in terms of the natural coordinates ξ and η can be adopted.

Then, the increment of internal forces can be evaluated by the following equation.

$$\Delta\hat{\mathbf{f}}_e^{\bullet}=\begin{Bmatrix}\hat{\mathbf{f}}_{2x}\\ \hat{\mathbf{f}}_{3x}\\ \hat{\mathbf{f}}_{3y}\\ \hat{\mathbf{f}}_{4x}\\ \hat{\mathbf{f}}_{4y}\end{Bmatrix}=t_e\int_{A_e}\mathbf{B}^T\Delta\hat{\boldsymbol{\sigma}}\mathrm{d}\hat{\mathrm{A}} \qquad (15)$$

The nodal forces $\hat{f}_{1x}$, $\hat{f}_{1y}$ and $\hat{f}_{2y}$ corresponding to $\hat{u}_1^d$, $\hat{v}_1^d$ and $\hat{v}_2^d$ at reference nodes 1 and 2 are not zeros. They can be found from the equilibrium equations. We get

$$\begin{aligned}\hat{f}_{1x}&=-(\hat{f}_{2x}+\hat{f}_{3x}+\hat{f}_{3x})\\ \hat{f}_{1y}&=-(\hat{f}_{2y}+\hat{f}_{3y}+\hat{f}_{3y})\\ \hat{f}_{2y}&=-(-\hat{f}_{2x}\hat{y}_2+\hat{f}_{3y}\hat{x}_3-\hat{f}_{3x}\hat{y}_3+\hat{f}_{4y}\hat{x}_4-\hat{f}_{4x}\hat{y}_4)/\hat{x}_2\end{aligned} \qquad (16)$$

Equations (15), (16) form the complete set of nodal internal forces $\hat{\mathbf{f}}_e^{\bullet}$ written in convected coordinates of the element. They should be transformed to global coordinates as

$$\hat{f}_e^{\text{int}}=T^T\hat{f}_e^{\bullet} \qquad (17)$$

Where

$$\mathbf{T}=\begin{bmatrix}\mathbf{\Omega} & \mathbf{0} & \mathbf{0} & \mathbf{0}\\ \mathbf{0} & \mathbf{\Omega} & \mathbf{0} & \mathbf{0}\\ \mathbf{0} & \mathbf{0} & \mathbf{\Omega} & \mathbf{0}\\ \mathbf{0} & \mathbf{0} & \mathbf{0} & \mathbf{\Omega}\end{bmatrix} \qquad (18)$$

The sum $(\sum_e)$ at particle α is carried out for the elements that are connected at node α.

2.5. Equations of Motion

The mass matrix for the 4-node solid element is

$$\mathbf{M}_e=\begin{bmatrix}m_1 & 0 & 0 & 0 & 0 & 0 & 0 & 0\\ 0 & m_1 & 0 & 0 & 0 & 0 & 0 & 0\\ 0 & 0 & m_2 & 0 & 0 & 0 & 0 & 0\\ 0 & 0 & 0 & m_2 & 0 & 0 & 0 & 0\\ 0 & 0 & 0 & 0 & m_3 & 0 & 0 & 0\\ 0 & 0 & 0 & 0 & 0 & m_3 & 0 & 0\\ 0 & 0 & 0 & 0 & 0 & 0 & m_4 & 0\\ 0 & 0 & 0 & 0 & 0 & 0 & 0 & m_4\end{bmatrix} \qquad (19)$$

Detail expression of the terms m_i (i = 1, 4) can be found in Ting & Shih & Wang (2004).

From Eq. (22), we can obtain the equations of motion for the sub-structure.

$$\begin{aligned}\mathrm{m}_\alpha^*\ddot{\mathrm{d}}_{\alpha x}&=\mathrm{F}_{\alpha x}^{\text{ext}}-\mathrm{F}_{\alpha x}^{\text{int}}\\ \mathrm{m}_\alpha^*\ddot{\mathrm{d}}_{\alpha y}&=\mathrm{F}_{\alpha y}^{\text{ext}}-\mathrm{F}_{\alpha y}^{\text{int}}\end{aligned} \qquad (20)$$

Where F^{ext} is the external force applied on the particles, F^{int} is the internal force due to the element deformation.

If a simple central difference is adopted, the displacement equations can be written as

$$(\mathbf{d}_{n+1})_\alpha=\frac{(\Delta t)^2}{\mathrm{m}_\alpha}(\mathbf{F}_n^{ext}-\mathbf{F}_n^{\text{int}})_\alpha+(2\mathbf{d}_n-\mathbf{d}_{n-1})_\alpha \qquad (21)$$

The detail computational procedure can be found in the papers written by Ting & Shih & Wang (2004).

In the present VFIFE approach, the fundamental structural modeling assumption is that structural behavior can be characterized by the motions of a finite set of mass points. The motion of each mass point follows the Newton's law of motion or the principle of virtual work for a particle. The governing equation is a vector differential equation that describes the trajectory of this set of mass points. Thus the concept of this approach is fundamentally different from the traditional finite element method.

3. CONTACT DETECTION AND ANALYSIS

Contact detection is the core step for any motion analysis of a discrete system. For a discrete system consists of finite blocks patched with finite element meshes, the basic contact detection units can be identified as only vertex-to-edge, and vertex-to-vertex two types (see Fig. 5). In the present paper, the vertex is defined by the nodal points located on the boundary of blocks, while the edge is defined by the boundary between two neighboring nodes. The vertex-to-vertex type contact can be further decomposed into four possible vertex-to-edge type contacts. According to the angles among four edges (Shi 1988, 1996), the penetration time, and the distance criterion, one can determine which one of the four possible cases is occurred first. Figure 6 shows the four possible contact conditions between two vertices of convex polygons. Therefore, the contact evaluation of the vertex-to-edge type is the basis of the multi-body contact analysis.

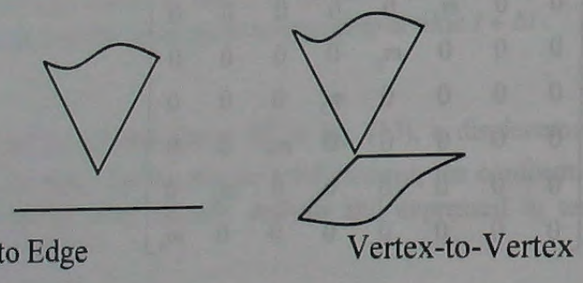


Figure 5. Basic contact detection units for the motion analysis of multi-body system.

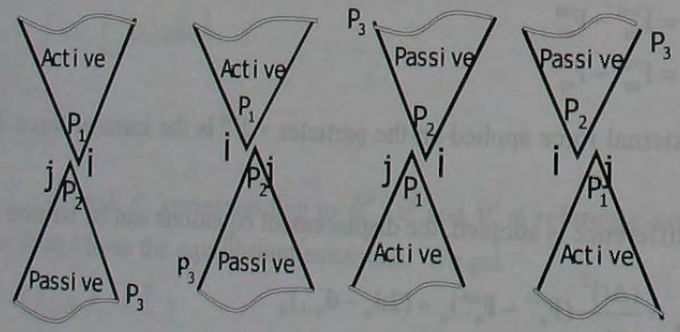
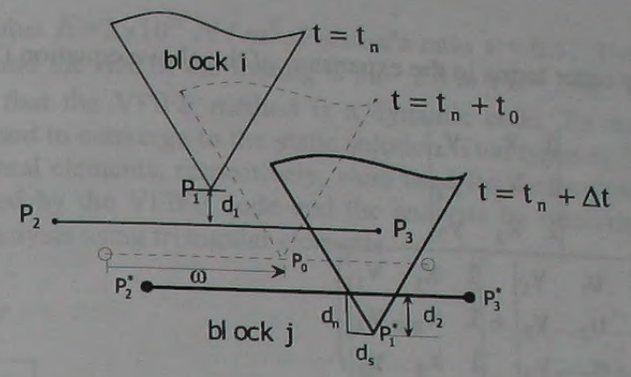


Figure 6. Four possible contact conditions between two vertices.



$d_1 > 0$, $d_2 < 0$

Figure 7. A vertex contacts an edge after a time increment without installing penalty spring.

In the vertex-to-edge contact case, the identification of the penetration condition, happened after one step of time increment, is crucial to the installation of penalty springs and the associated contact forces in any iteration process. Figure 7 shows the positions of a vertex node and two edge nodes before and after one time step. After one time step calculation, nodes located at $P_1(x_1, y_1)$, $P_2(x_2, y_2)$ and $P_3(x_3, y_3)$ move to points p_1^*, p_2^* and p_3^* with displacements (u_1, v_1), (u_2, v_2) and (u_3, v_3), respectively. The distance d_1 between point p_1 and edge $\overline{P_2P_3}$ and the distance d_2 between point p1* and edge $\overline{P_2^*P_3^*}$ can be determined by the following equations:

$$d_1 = \frac{1}{L}\begin{vmatrix} 1 & x_1 & y_1 \\ 1 & x_2 & y_2 \\ 1 & x_3 & y_3 \end{vmatrix}, \quad L = \sqrt{(x_2 - x_3)^2 + (y_2 - y_3)^2} \tag{22}$$

$$d_2 = \frac{1}{L}\begin{vmatrix} 1 & x_1 + u_1 & y_1 + v_1 \\ 1 & x_2 + u_2 & y_2 + v_2 \\ 1 & x_3 + u_3 & y_3 + v_3 \end{vmatrix} \tag{23}$$

The d_2 value is negative when the vertex of block i penetrates the edge of block j. It is assumed that the first contact instant, t_0, is determined by linear interpolation from the data before and after a time increment. Hence, the coordinates of this first contact point P_0 are $(x_1+t_0u_1, y_1+t_0v_1)$ and the area of the triangle formed by the vertex and two edge nodes is zero. One can apply this concept and use Eq. (25) to determine t_0.

$$\begin{vmatrix} 1 & x_1 + t_0u_1 & y_1 + t_0v_1 \\ 1 & x_2 + t_0u_2 & y_2 + t_0v_2 \\ 1 & x_3 + t_0u_3 & y_3 + t_0v_3 \end{vmatrix} = 0 \tag{24}$$

By neglecting the higher order terms in the expansion of the above equation (24), one can get

$$t_0 = -\frac{\begin{vmatrix} 1 & x_1 & y_1 \\ 1 & x_2 & y_2 \\ 1 & x_3 & y_3 \end{vmatrix}}{\left(\begin{vmatrix} 1 & u_1 & y_1 \\ 1 & u_2 & y_2 \\ 1 & u_3 & y_3 \end{vmatrix} + \begin{vmatrix} 1 & x_1 & v_1 \\ 1 & x_2 & v_2 \\ 1 & x_3 & v_3 \end{vmatrix} \right)} \tag{25}$$

Once the location of first contact point P_0 is determined, the magnitude of shear displacement, d_s, along the edge after contact can be determined as the distance between P_0 and the projection point of point p_1* on $\overline{P_2 * P_3 *}$.

The first contact location and the shear displacement d_s calculated from above discussion will be used as the data for establishing the normal and shear penalty springs in the following iterations within the time step. The normal contact force, and shear contact force $\mathbf{F}_n$, $\mathbf{F}_s$ are calculated by the following equations:

$$\mathbf{F}_n = k_n \mathbf{d}_n \tag{26}$$

$$\mathbf{F}_s = k_s \mathbf{d}_s \tag{27}$$

Where k_n, k_s are the spring constants in the normal and shear directions, respectively, $\mathbf{d}_n$, $\mathbf{d}_s$ are the penetration depths in the normal and shear directions, respectively. Besides, the sliding condition has to be considered by

$$F_f = F_s \text{ if }, F_s < \mu F_n \tag{28}$$

$$F_f = \mu F_n, \text{ if } F_s > \mu F_n \tag{29}$$

Where μ is the friction coefficient of the contact surface.

4. NEWMERICAL EXAMPLES

4.1. Contact Pressure between a Footing and Soil Foundation

The analytical solution (Galin, 1953) of the normal contact pressure $\sigma(x)$ between a rigid punch of width $2a$ and a frictionless elastic half plane due to the action of a vertical load P is

$$\sigma = P / \left(\pi \left(a^2 - x^2 \right)^{\frac{1}{2}} \right) \tag{30}$$

To approximate the half plane state, a soil foundation of relatively big size compared with the dimension of the footing is studied by the VFIFE code. The analytical solution expressed by Eq. (30) is used to verify the capability and accuracy of the numerical prediction on contact problem. The soil foundation of Young's modulus $E = 5\times10^6 N/m^2$, Poisson's ratio $\nu = 0.28$, is indented by a

punch of Young's modulus $E = 2\times10^{10} N/m^2$, Poisson's ratio $\nu = 0.1$. The size of the foundation is $L = 20\ m$, $H = 10\ m$ and the size of the footing is $2a = 2.8\ m \times h = 2\ m$. The punching force P is $2\times10^4\ N$. It is noted that the VFIFE method is a dynamic code. To study the static problem, numerical damping is used to converge to the static solution. Two types of finite element meshes of triangular and quadrilateral elements, respectively, were used for the analyses. Figure 9 shows that good results are obtained by the VFIFE code and the analysis by quadrilateral elements provides better results than the analysis using triangular elements.

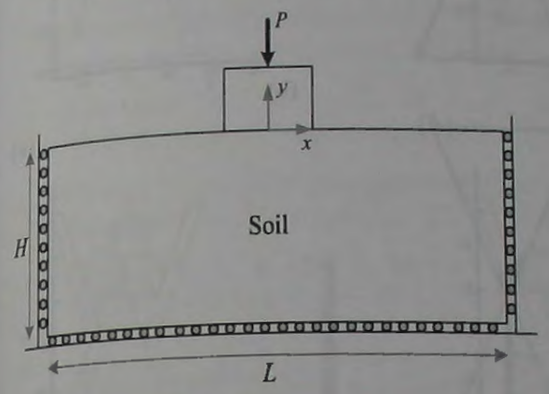


Fig. 8. A footing on the soil foundation

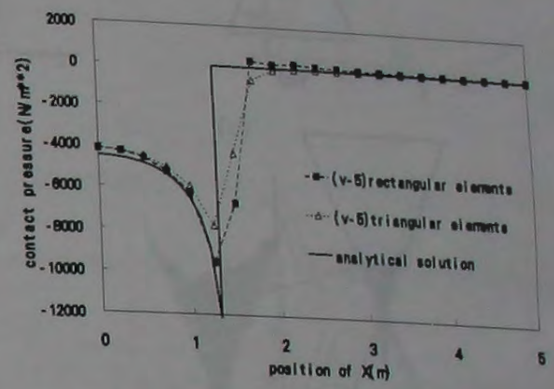


Fig. 9. Comparison of the contact pressure predicted by numerical analysis with the analytical solution.

Table 1. Element type and number of elements used for the analysis

	Nodes	Elements	Element Type
Mesh a	1681	1600	Quadrilateral Element
Mesh b	1681	3200	Triangular Element

4.2. Flowing of Deformable Particles in an Hourglass

The flowing behavior of particles in a silo or hourglass is interested by many researchers. Its complexity is due to the interactions among particles of different geometrical shapes, material properties and distributions. Flowing particles is characterized by the motion with large translation and rotation. Thus far, most of the simulations of granular flow use the rigid particles. If deformable particles are used, then the effect of rigid body motion has to be rigorously considered into the analysis. Sine the VFIFE method can well handle the behaviors of structures and solids moving with large displacement and rotation, it is used to simulate the flow phenomenon of deformable particles. Figure 10 shows the flowing behavior of 644 deformable particle of quadrilateral shape under the action of gravity force. Each particle has Young's modulus $E = 10000 kN/m^2$, mass density $\rho = 100\ Kg/m^3$ and Poisson's ratio $\nu = 0.1$. No frictional effect is considered among particles.

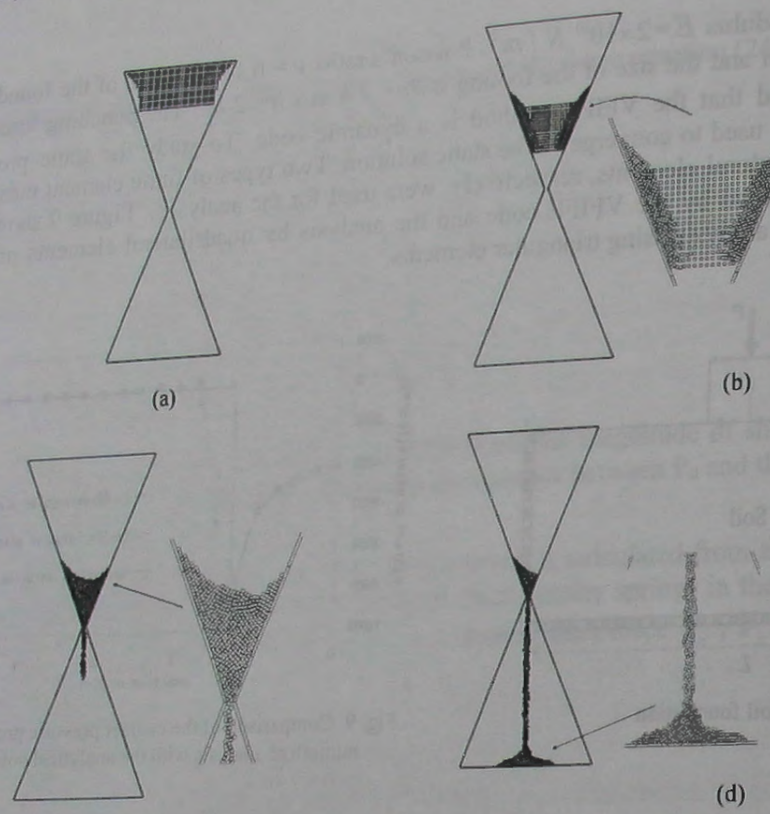


Fig. 10. Motion analysis of deformable particles in an hourglass.

To demonstrate the capability of VFIFE method on the motion analysis of deformable discrete bodies, a flow behavior of five deformable disks through a channel neck due to their own weights is studied. As shown in Fig. 11, the variations of the deformation, stresses and contact forces among particles that are not easily measured from experiments can be obtained through numerical simulation.

Proceedings of International Mini-Symposium for Numerical Discontinuous Analyses, edited by T. Koyama, Hawaii, November, 2008

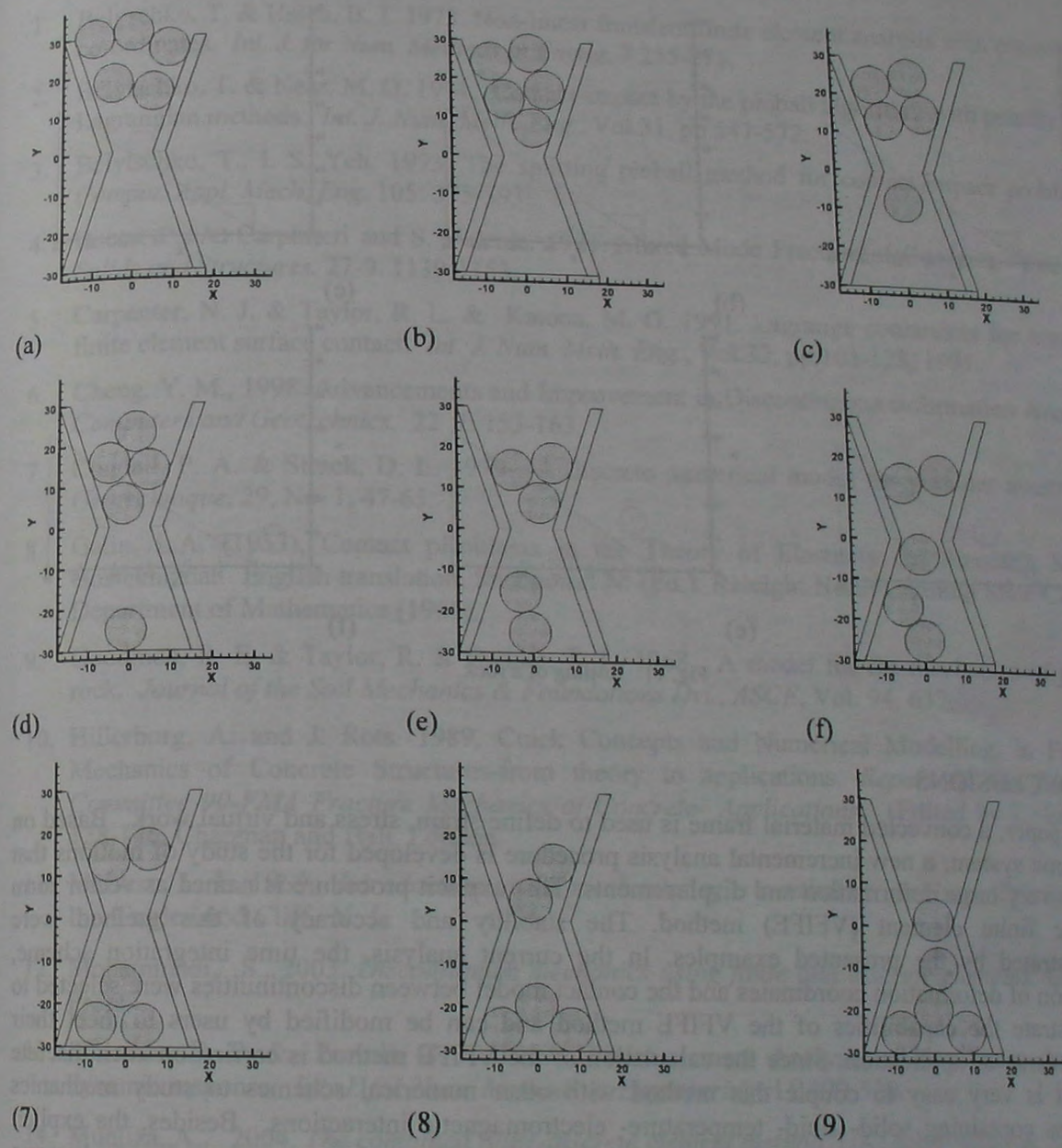


Fig. 11. Flow of five deformable disks through a channel neck.

4.3. Falling Rock

To demonstrate that the VFIFE method can handle problems having large rotation, a falling rock problem is studied numerically. As shown in Fig. 12, both the falling rock and the slope materials are elastic. This is a rolling contact problem. The dynamic contact force and momentum of the rolling rock obtained from the simulation are useful to the design engineers of expressway bureau.

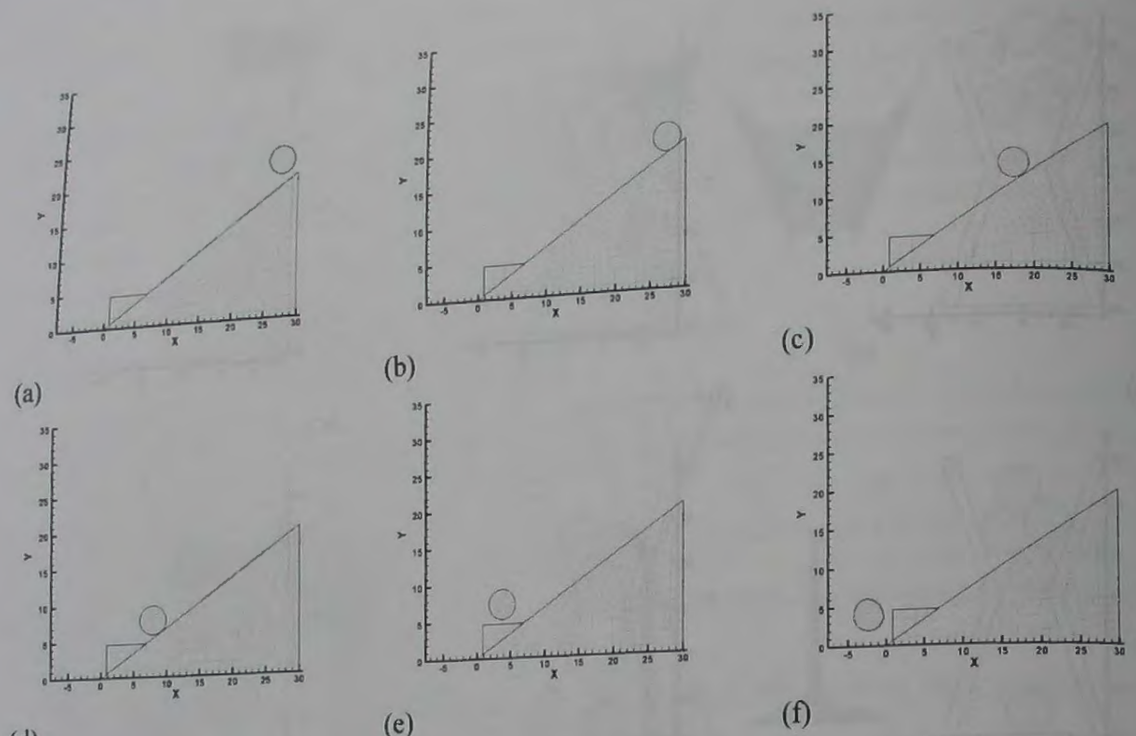


Fig. 11. Rolling of a rock.

5. CONCLUSIONS

In this paper, a convected material frame is used to define strain, stress and virtual work. Based on this frame system, a new incremental analysis procedure is developed for the study of motions that involve very large deformation and displacements. This explicit procedure is named as vector form intrinsic finite element (VFIFE) method. The stability and accuracy of this method were demonstrated by the presented examples. In the current analysis, the time integration scheme, definition of deformation coordinates and the contact model between discontinuities were selected to demonstrate the capabilities of the VFIFE method and can be modified by users to meet their requirements of application. Since the calculation of the VFIFE method is carried on each discrete node, it is very easy to couple this method with other numerical schemes to study mechanics problems containing solid- fluid- temperature- electromagnetic interactions. Besides, the explicit formulation of the VFIFE method allows it to model the discontinuous and nonlinear dynamic behaviors of material easily. It seems that the VFIFE method has the capabilities of analyzing structures with large deformation, large displacement and fragmentation behaviors that are difficult to be conducted by the conventional FEM. The three dimensional formulation of the VFIFE method can be developed based on the presented paper.

REFERENCES

1. Belyschko, T. & Hsieh, B. J. 1973. Non-linear transient finite element analysis with convected co-ordinates. *Int. J. for Num. Methods in Engng*, 7 255-271.
2. Belytschko, T. & Near, M. O. 1991. Contact-impact by the pinball algorithm with penalty and Lagrangian methods. *Int. J. Num. Meth. Eng.*, Vol.31, pp.547-572.
3. Belytschko, T., I. S. Yeh. 1993. The splitting pinball method for contact-impact problems. *Comput. Appl. Mech. Eng*. 105: 375-393.
4. Bocca, P., A. Carpinteri and S. Valente. 1991. Mixed Mode Fracture of Concrete. *Int. J. of Solids and Structures*. 27-9. 1139-1153.
5. Carpenter, N. J. & Taylor, R. L. & Katona, M. G. 1991. Lagrange constraints for transient finite element surface contact. *Int. J. Num. Meth. Eng.*, Vol.32, pp.103-128, 1991.
6. Cheng, Y. M., 1998. Advancements and Improvement in Discontinuous deformation Analysis. *Computers and Geotechnics*. 22 2: 153-163.
7. Cundall, P. A. & Strack, D. L. 1979. A discrete numerical model for granular assemblies. *Geotechnique*, 29, No. 1, 47-65.
8. Galin, L.A. (1953), Contact pRoblems in the Theory of Elasticity (in Russian), Mosco: Gostekhizdat. English translation, Sneddon, I.N. (Ed.), Raleigh: North Carolina State College, Department of Mathematics (1961).
9. Goodman, R. E. & Taylor, R. & Brekke, T. L. 1968. A model for the mechanics of jointed rock. *Journal of the Soil Mechanics & Foundations Dvi., ASCE*, Vol. 94, 637.
10. Hillerborg, A. and J. Rots. 1989. Crack Concepts and Numerical Modelling. in Fracture Mechanics of Concrete Structures-from theory to applications. *Report of the Technical Committee 90-FMA Fracture Mechanics of Concrete- Applications.* (Edited by L. Elfgren), 128-146, Chapman and Hall, London.
11. Malvern, L. E. 1969. *Introduction to the mechanics of a continuous medium.* Printice-Hall, Inc. Englewood Cliff, N. J.
12. Mohammadi, S., 2003. *Discontinuum mechanics using finite and discrete elements.* UK: Wit Press.
13. Mondkar, D. P. & Powell, G. H. 1977. Finite element Analysis of Non-linear static and dynamic response. *Int. J. for Num. Methods in Engineering*, 11 499-520.
14. Munjiza, A., 2004. *The combined finite-discrete element method.* UK: John Wiley & Sons.
15. Rice, D. L. & Ting, E. C. 1993. Large displacement transient analysis of flexible structures. *Int. J. Num. Meth. Eng.*, 36, 1541-1562.
16. Shi, G. H. 1988. Discontinuous deformation analysis-a new numerical model for the statics and dynamics of block system. Ph. D. Dissertation, University of California, Berkeley.
17. Shi, G. H. 1992. Manifold method of material analysis. *Transactions of the Ninth Army Conference on Applied mathematics and Computing*, Minneapolis, Minnesota, USA, 51-76.

18. Shi, G. H. 1996. Manifold method. *Proceedings of the First International Forum on Discontinuous Deformation Analysis (DDA) and Simulations of Discontinuous Media*, Berkeley, California, USA, 52-104.

19. Shih, C., Y. K. Wang, and E. C. Ting. 2004. Fundamentals of a vector from intrinsic finite element: Part II. Plane solid elements. *Journal of Mechanics*. 20-2: 133 143.

20. Taylor, R. L. & Papadopoulos, P. 1993. On a finite element method for dynamic contact/impact problems", *Int. J. Num. Meth. Eng.*, Vol.36, pp.2123-2140,1993

21. Ting, E. C., C. Shih, and Y. K. Wang. 2004. Fundamentals of a vector from intrinsic finite element: Part I. Basic procedure and plant frame element. *Journal of Mechanics*. 20-2: 113 122.

22. Ting, E. C., C. Shih, and Y. K. Wang. 2004. Fundamentals of a vector from intrinsic finite element: Part II. Plane solid elements. *Journal of Mechanics*. 20-2: 123 132.

23. Zhong, Z. H., L. Nilsson. 1989. A contact searching algorithm for general contact problems. *Computers & Structures*. 33 1: 197-209.

24. Zhong, Z. H., L. Nilsson. 1994. Automatic contact searching algorithm for dynamic finite element analysis. *Computers & Structures*. 52 2: 187-197.

Motion Analysis of the Interaction among Discrete Solid Bodies and Multi-Phase Fluid

Tso-Ren Wu
Assistant Professor, Graduate Institute of Hydrological and Oceanic Sciences, National Central University, Jhongli,, 32001, Taiwan
Meihui Chuang
Graduate Student, Graduate Institute of Hydrological and Oceanic Sciences, National Central University, Jhongli,, 32001, Taiwan
Chih-Jung Huang
Graduate Student, Department of Civil Engineering, National Central University, Jhongli,, 32001, Taiwan
Chung-Yue Wang
Professor, Department of Civil Engineering, National Central University, Jhongli,, 32001, Taiwan

1. INTRODUCTION

ABSTRACT: In this paper, we present a two-way coupled moving-solid algorithm to simulate dynamic fluid-solid interaction. This two-way coupled model allows solid bodies moving in the multi-phase fluid to generate realistic motion for both the fluid and solid objects. We discretize the Navier-Stokes equation using finite volume method (FVM) for the fluid part. The volume-of-fluid (VOF) method is used to track the fluid-fluid and fluid-solid interfaces. The moving-solid algorithm which conserves mass and momentum is adopted to transfer the force from solid motion to the multi-phase fluid. The fluid force acting on the solid bodies and solid surfaces are integrated to calculate the movement of the solid objects. The moving-solid algorithm is straightforward to be implemented. The solid objects can be rigid or deformable. Contact analyses among discrete bodies are also included in the simulation algorithm. The solid with different densities can be combined in the same simulation. This algorithm is useful in the fields of Engineering and Earth Sciences, such as structure collapse and landslide generated tsunamis. Examples of falling ice cubes will be demonstrated using the algorithm.

The numerical simulation of water waves interacting with a moving solid body is important for many science and engineering applications, such as landslide generated tsunamis, caisson work, ship maneuvering, and wave energy. However, to analyze unsteady flows with free surfaces poses a great challenge to numerical simulations, because both of the free-surface boundary and the moving solid boundary are presented in the fluid system, and both elements are parts of the solutions.

Over the past decay, many numerical schemes solved the Navier-Stokes (NS) equations have been developed for simulation of wave-structure interactions. Lin and Li [12], (2002) made use of σ-coordinate transformation to map an irregular physical domain on a rectangular computational grid. Lin [11], (2006) further developed a 3D multiple-layer σ-coordinate model to simulate surface wave interaction with structures. However, the use of coordinate transformations and mapping requires a highly accurate method for the calculation of the transformation Jacobians, and generating a body-conformal grid is an iterative process requiring significant devotion of time. As the geometry and free-surface profile become more complicated, the task of generating an acceptable grid becomes increasingly difficult. For the problems of wave-structure interaction, it would be desirable to avoid re-girding all together.

Alternatively, the fixed-grid technique constructed on either simple Cartesian coordinates or complex unstructured girds is adopted to handle moving bodies and complex breaking waves

and is divided into two categories, depending on how the inertial solid boundaries are treated. When virtual forces are utilized to present the moving-body effect on its ambient fluids, the method is termed the immersed boundary method (IB method) (Jia and Nakamusa [9], 1996). The IB method was originally developed by Peskin [19], (1972) to simulate blood flows in mitral valves and was later employed to solve problems in incompressible single-phase fluid flows (e.g., Goldstein et al. [6], 1993; Mohd-Yusof [16], 1997; Fadlun et al. [5], 2000; Balaras [2], 2004). Shen and Chan [20], (2008) combined IB method and VOF to study the fluid interaction with submerged structures. The IB method has the advantage of simulating a moving body (Mittal and Iaccarino [15], 2005) on fixed Cartesian meshes. However, IB method averages solid properties onto the fluid grid and thus it is difficult to stop a fluid leak through solids. The applications are often limited to the submerged obstacles.

Another approach is the Partial-cell (PC) method. The PC (sometimes also called "cut-cell" or "CC") method has been widely employed to represent arbitrary body configuration. Udaykumar et al. [27, 28], (1996, 1997) have implemented the PC method to compute 2D flows with solid-fluid and fluid-fluid interfaces. Compared with IB method, the PC method does not calculate the fluid motion inside the solid obstacle; therefore the leaking problem does not exist during the simulation of the flows with free-surface. Combined with the VOF free-surface treatment, PC method has been developed for the modeling of complex breaking waves interacting with stationary solid boundaries. Kothe and Mjolsness [10], (1992) developed a RIPPLE model to simulate 2D incompressible fluid flows with arbitrary free surfaces and internal obstacles. The free-surface interface was modeled by a volume of fluid (VOF) method developed by Hirt and Nicholes [8], (1981), and the internal obstacles were modeled by PC method. Lin and Liu [13], (1998) coupled the RIPPLE model with the k-ε turbulence model to simulate breaking waves at a sloping beach. The results with high accuracy were predicted in terms of the free-surface profile and wave over-topping rate.

Although the above PC method leaves the possibility of treating the solid-fluid interface and free surface simulation, the application of this method to simulating moving body interaction with free surface was rarely reported. This is due to the numerical difficulty of treating the cells crossed by both solid surface and free surface, especially when a body is moving. However, the problems of moving body interaction with free surface can be found in many important applications in engineering, e.g., ship motion in wave fields, marine operation of pipeline installation, fluid sloshing in an excitation tank, etc. Heinrich [7], (1992) solved 2D NS equations and added a source function to the continuity and momentum equations to represent moving boundary effects. Wu [31], (2004) and Liu et al. [14] (2005) further extended Heinrich's model to simulate the 3D wave generation induced by landslides. In their studies, the movements of the obstacles are prescribed, while we are more interested in the "two-way" fluid-solid coupling which requires the prediction of the solid-body movement.

The body motion with large translation and rotation can be calculated by some computational methods developed in solid mechanics, like the discrete element method (DEM) (Cundall [3, 4], 1988), discontinuous deformation analysis (DDA) method (Shi [21], 1988), and Manifold method (MM) (Shi [22, 23], 1992, 1996), vector form intrinsic finite element (VFIFE) method (Ting et al. [24-26], 2004) and some other nonlinear finite element analysis methods based on up-dated Lagrangian algorithm (e. g., Attaway [1] et al., 1998). For the system containing discrete bodies, the contact detection and contact force analysis are the core parts of the motion analysis. Cundall (1988) proposed the "common plane" concept to do the contact detection among three-dimensional polyhedrons. Recently, Zhao et al [33]. (2006) improved the common plane algorithm to accelerate the contact detection speed of granular particles of irregular shapes. Wang et al [29]. (2008) developed a directed contact analysis algorithm for the motion analysis of mixed polyhedral and ellipsoidal particles. For the

contact analysis of deformable bodies, Zhong and Nilsson [32], (1990) had developed an effective contact searching algorithm for general 3-D contact impact problems. The authors of this paper would like to group these methods by the name as "discrete body motion analysis method".

To include the fluid effect into the analysis of granular medium is highly interested by the researchers in the past two decades. Muller et [17,18] al. (2003, 2005) have used the smooth particle hydrodynamics (SPH) to model the free fluid surface and conducted the fluid-solid particle interaction analysis based on the Eulerian grid-based mode. However, error is accumulated after some interactions among particles, especially for the particles of distinct types.

In this paper, we propose a new method which couples the discrete body motion analysis method and a moving-solid algorithm based on the PC-VOF method. Our method allows robust and accurate solid-fluid coupling in either structure or on unstructured girds. The body motion can either be prescribed or based on DEM. The fluid solver adopts the two-step projection for solving 3D NS equations for fluid-solid interaction by simultaneously conserving the momentum of the fluid and the moving body, while enforcing the conservation of fluid mass.

2. NUMERICAL MODEL FOR THE FLUID SIMULATION

In this section, the numerical algorithm used to simulate fluid motion is introduced. The present model uses VOF method for the free-surface tracking, finite volume method for the discretization, partial-cell method for placing the solid material inside the computational domain, and moving solid algorithm for simulating the fluid motion caused by a moving solid body.

The present model adopts an open source code, "Truchas" (http://telluride.lanl.gov) as the foundation fluid solver.

2.1. Volume of fraction (VOF) method for multi-phase fluids

In order to simulate multi-fluids with interfaces, such as air and water, the VOF method is adopted. In the VOF method, a set of mass and momentum conservation equations is solved on a fixed grid. The volume fraction f , defended as the ratio of the fluid to total volume, is evolved with the advection equation. The governing equation for advecting volume fraction f is the so-called VOF equation:

$$\frac{\partial f}{\partial t}+\nabla\cdot(fu)=0 \tag{1}$$

where u is the velocity field.

$$\nabla\cdot u=0 \tag{2}$$

$$\frac{\partial(\rho u)}{\partial t}+\nabla\cdot(\rho uu)=-\nabla P+\nabla\cdot\left(\mu\left(\nabla u+\nabla^{T}u\right)\right)+g \tag{3}$$

where P is the total pressure, g gravity force, ρ fluid density, and μ fluid viscosity. Because multiple fluids, e.g., water and air, are presented in the simulation, the fluid density and viscosity are defined as

$$\rho=\rho_1 f+\rho_2(1-f) \tag{4}$$

$$\mu = \mu_1 f + \mu_2 (1 - f) \tag{5}$$

where the subscripts 1 and 2 denote fluid 1 and fluid 2, respectively.

The VOF advection equation, Eq. (1), is solved with a PLIC (piecewise linear interface calculation) algorithm (Garrioch and Baliga, 1997; Koth et al., 1996; Rider and Kothe, 1998), and be discretized in the explicit form:

$$\frac{f^{n+1} - f^n}{dt} = - u^n \cdot \nabla f^n \tag{6}$$

Once the volume fractions are advected, fluid properties such as density are updated using Eq. (4) and . The momentum equation is solved by the projection method and is split into a predictor and a corrector step. In the projection method, momentum equations (3) can be described by two fractional steps:

$$\frac{\rho^{n+1} u^* - \rho^n u^n}{\Delta t} = -\nabla \cdot (\rho uu)^n - \nabla P^n + \nabla \cdot \left(\mu^n \left(\nabla u + \nabla^T u \right)^n \right) + \rho^n g^n \tag{7}$$

$$\frac{\rho^{n+1} u^{n+1} - \rho^{n+1} u^*}{\Delta t} = -\nabla \delta P^{n+1} + \rho^{n+1} g^{n+1} - \rho^n g^n \tag{8}$$

where the superscripts n and n+1 represent the current and next time level, respectively. The superscript * represent an intermediate level. The change in pressure is $\delta P^{n+1} = P^{n+1} - P^n$. Eq. (7) is an explicit expression for the interim velocity u^*, referred to as the predictor step. Equation (7) is termed the projection step. Combining Eq. (7) and (8) exactly produces the time discretization of Equation (7):

$$\frac{\rho^{n+1} u^{n+1} - \rho^n u^n}{\Delta t} = -\nabla \cdot (\rho uu)^n + \nabla \cdot \left(\mu^n \left(\nabla u + \nabla^T u \right)^n \right) - \nabla p^{n+1} + \rho^{n+1} g^{n+1} \tag{9}$$

Equation (8) relates u^{n+1} to u^*. By adopting the solenoidal condition (Equation (2)), we have:

$$\nabla \cdot \frac{\nabla \delta P^{n+1}}{\rho^{n+1}} = \nabla \cdot \left(\frac{u^*}{\Delta t} \right) \tag{10}$$

Equation (1) is named the Poisson Pressure Equation (PPE) and is solved for the change in pressure using two-level preconditioned GMRES solution technique (Tel Telluride team, 2003). New time-step cell-centered pressure P^{n+1} can be solved from Eq (10). Eq (11) is then used to calculate the solenoidal velocity field:

$$u^{n+1} = u^* - \Delta t \left(\frac{\nabla \delta P^{n+1}}{\rho^{n+1}} \right) \tag{11}$$

The readers are referred to Francois et al. (2006) for detailed projection numerical schemes.

2.2. Finite Volume Method and Partial-cell (PC) method

The flow fields are discretized by Finite Volume Method (FVM). Consider a general conservation equation for an arbitrary quantity ϕ:

$$u^{n+1} = u^* - \Delta t \left(\frac{\nabla \delta P^{n+1}}{\rho^{n+1}} \right) \tag{12}$$

where S is a source term which is generally dependent upon ϕ. After applying the volume integral and Gauss Divergence theorem, Eq (12) can be approximated by a discrete numerical scheme:

$$\frac{\phi_i^{n+1} - \phi_i^n}{\delta t} + \frac{1}{V_i} \sum_f \left[A \cdot u^n \right]_f [\phi]_f^n = S_i^n \tag{13}$$

where n indicates the n^{th} time step, V_i is the i^{th} cell volume, and subscript f indicates the cell (control volume) face.

To deal with the solid material inside the fluid domain, the PC method is adopted. The partial cell method can be easily applied to FVM and can be used to adopt moving solid algorithm function and to deal with unstructured interior obstacles.

Since the obstacle inside the computational domain occupies a part of the interior fluid volume, the effective cell volume will be a fraction of the original cell volume:

$$V_{eff} = (1 - f_{solid}) V = \theta V \tag{14}$$

where V_{eff} is the effective cell volume, f_{solid} is the volume fraction occupied by solid material in each cell, V is the original cell volume, and θ is the effective volume fraction.

If a cell contains partial volume of solid material, the flow solver has to deal with it. Cell faces are defined either to be entirely closed, or not. Cell faces are "closed" only if at least one of the two immediately neighboring cells is entirely occupied by solid material. If the cell faces are "closed", the face velocity of the cell is set to zero, and the face pressure is no longer calculated in the pressure solution. On the other hand, if any face between two cells, containing at least a partial cell volume of fluid, is "open", the code solves the velocities and pressure gradients.

Compared to the conventional way to treat the irregular solid material that creates the "saw-tooth" boundary, the partial cell treatment introduced here is a better choice to represent the smooth real geometry of the boundary.

2.3. Moving-solid algorithm

In order to simulate the movement of a moving solid body, the PC method and an internal source function are added to the program. Consider a volume V containing an obstacle (Fig.(1).), which is defined by its volume $V_{obs(t)}$ and its surface $A_{obs(t)}$. If the obstacle volume increases, i.e. $DV_{obst} / dt > 0$, the volume of the fluids decrease, and vice versa. The conservation of mass in the volume V can be expressed as follow:

$$\oint_A u \cdot n dA = \frac{dV_{obs(t)}}{dt} \tag{14}$$

The new continuity equation for the volume V can be expressed as:

$$\nabla \cdot u = \frac{1}{V} \frac{dV_{obs(t)}}{dt} = \phi(x, y, z, t) \tag{15}$$

where ϕ = internal source function.

The main procedure of moving-solid algorithm can be expressed as:

(i) Update the new time step solid body VOF (Fig. (2).).

(ii) Add a positive source function to the region where fluids will be pushed out, and a negative source function in the wake zone where fluids will be sucked in (Fig. (3).)

(iii) Solve the new time step velocities.

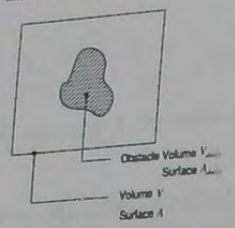


Fig.1. Motion analysis of the interaction among discrete solid bodies and multi-phase fluid.

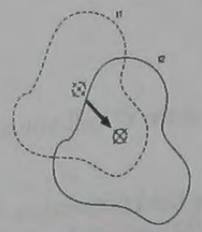


Fig.2. Update the solid body VOF from old time step (t1) to new time step (t2).

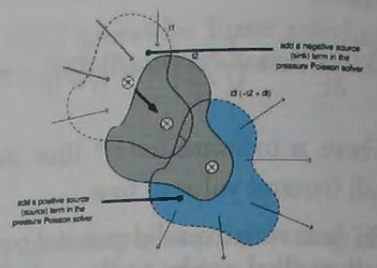


Fig.3. Add a positive source term in front of the solid body and a negative source term (sink term) in the wake zone. Where dt = t2 – t1, t3 = t2 + dt.

The advantages of using the moving solid algorithm can be concluded as follow:

(i) The solid boundary doesn't need to fit the mesh grid

(ii) There is no constrains on the number of fluids. In other words, the moving-solid algorithm can be applied to simulate the fluids with interfaces.

(iii) Compare to the IB method, the moving-solid algorithm doesn't require the velocity interpolation inside the fluid domain.

2.4. Validation for the moving-solid algorithm

To validate the Moving-solid algorithm, two benchmark cases are simulated. The first case is the horizontal displacement of a vertical wall. The second case is the two-dimensional landslide generated waves.

The moving vertical wall often used to generate wave in laboratories. Kennard (1949) derived a theoretical linear solution to relate the motion of the vertical wall and the wave amplitude:

$$\eta(x,t)=\frac{2}{\pi}\int_0^{\infty} dk \int_0^{t} d\tau \int_{-d}^{0} \cos(\sigma(t-\tau))\cosh(k(y+d))\cos(kx)\,F(y,\tau)/\cosh(kd)\,dy \qquad (16)$$

where $\sigma^2 = gk\tanh(kd)$ is the dispersion relationship.

$F(y,\tau)=v_{wall}(t)$ is the wall velocity.

Because the analytical solution is derived from the linear theory, some conditions have to be satisfied (Wiegel, 1972):

(i) The wall displacement has to be small compared to the still water depth.

(ii) The acceleration of the moving wall has to be small compared to the gravity.

(iii) C The Froud number $v_{wall}/\sqrt{gd}$ has to be small compared to unity. Compare to the IB method, the moving-solid algorithm doesn't require the velocity interpolation inside the fluid domain.

We adopted the case propose by Heinrich (1991) which satisfy these conditions:

d = water depth = 1 m; 'T' = total time the wall is in motion = 2 sec; S = wall motion = 0.10 m

Fig. (4).shows the displacement time history of the wall.

The free-surface profiles predicted by the moving-body method and the theoretical equation are plotted at different times: t = 1 sec, t = 2 sec, and t = 3 sec (Fig. (5).). The comparisons show that the moving-body method is able to generate desirable waves.

The second case is the landslide generated waves. Heinrich (1992) performed the experiment by allowing a triangular box to slide freely down an inclined plane with a 45° slope. The shore was modeled by a second incline with a 15° slope, the intersection of the two inclines being 1 m above the channel horizontal bottom. The still water depth is 1 m. The triangular box in cross section 0.5 m x 0.5 m and was a wide as the flume (Fig. (6).). The experiments were filmed by a 35 mm camera. It allowed study of the wave generation, propagation, and runup. At selected times, wave profiles and box coordinates were digitized with an error of ± 4 mm and ± 3 mm in the x- and y- coordinates, respectively.

The submarine landslide is simulated in the present study. By implementing the trajectory of the sliding box (Fig. (7).), the moving-body method is able to simulate the waves generated by the landslide. Fig. (5). shows the comparisons of computed and experimental wave profiles at time t = 0.5 sec, 1.0 sec, and 1.5 sec. Excellent agreement can be seen.

These two cases demonstrate the accuracy of adopting moving-body method to simulate wave-moving structure interaction. However, both the simulations require prescribed trajectories for the body movements. In the following sections, the two-way coupling of fluids and moving body will be introduced.

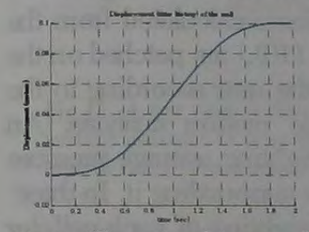


Fig.4 The time-history displacement of the wall motion.

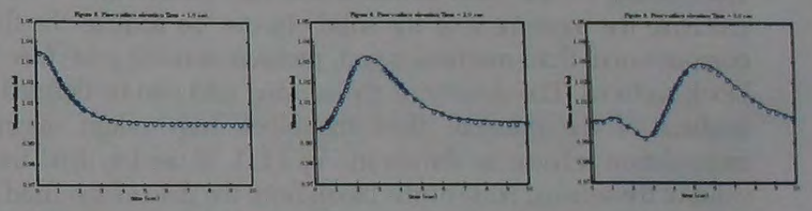


Fig.5. Snapshots of the free-surface elevation caused by a moving vertical wall.

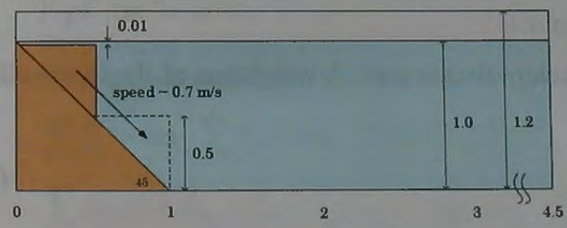


Fig.6. The setup of the 2D landslide benchmark case. The initial top face of the wedge is 0.01 m below the still water level.

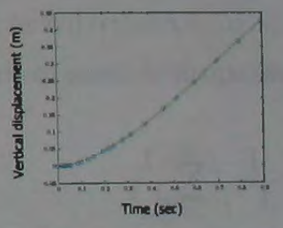


Fig.7. The time-history vertical displacement of the triangle slide motion.

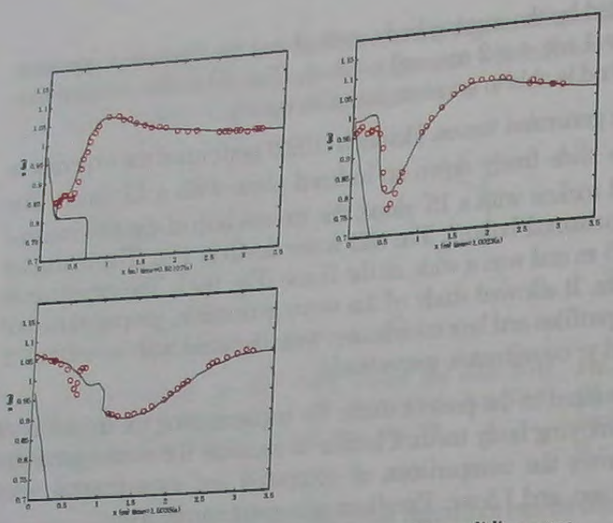


Fig.8. Snapshots of the free-surface elevation caused by a sliding mass.

2.5. Motion Analysis of Discrete Bodies:

To predict the movement of the solid body, DEM model is adopted. The multi-phase fluid force acting on the solid bodies and solid surfaces as shown in Fig. (9). are integrated to calculate the movement of the solid objects. To acquire the fluid force calculated from the computational fluid mechanics part, pressure sensing grids (see Fig. (10).) are patched on the block surfaces. The density of the sensing grid can be defined by the user according to the gradient of the pressure field the block may admit during the motion analysis. An interpolation scheme as shown in Fig. (11). is used to find the weighting average pressure value at the sensing node of the block from the data of the fluid cells surrounding it. In three-dimension cases, there are seven cells to be considered and the weighting of each cellular data is inverse proportional to its distance between the sensing node and the center of the cell. Once the external loads excited on a discrete body are found, the motion analysis of it can then be conducted no matter it is rigid or deformable.

Inverse square distance method is used in the interpolation part. A weighting of the fluid cell is:

$$\omega_i = \frac{1}{d_{0i}^{\ 2}} \Big/ \sum_{i=1}^{N} \frac{1}{d_{0i}^{\ 2}} \tag{17}$$

where d_{oi} is the distance between integral point and the ambient fluid cells, N is the total number of the weighting points. In the current Cartesian grid, N= 7. However, only the fluid cells ($\theta > 0$) will be included in the calculation..

Sum up the weighted pressure of fluid cells, we can get the pressure of integral point:

$$P_0^* = \sum_{i=1}^{N} \omega_i P_i \tag{18}$$

In the present paper, rigid blocks are used to demonstrate the capability and accuracy of this two-way coupled moving-solid algorithm in fluid-solid interaction analysis. After finding the external forces exert on the rigid block, an equivalent force-moment system (see Fig. (12).) applied on the block centroid can be determined for the motion analysis of the block in the next time step.

It is noted that contacts among blocks may happened during their motion. The contact analysis scheme for polyhedrons developed by the authors (Wang [30]et al., 1997) is adopted into the present study. The normal contact force, and shear contact force are calculated by the following equations:

$$\mathbf{F}_n = k_n \mathbf{d}_n \tag{19}$$

$$\mathbf{F}_s = k_s \mathbf{d}_s \tag{20}$$

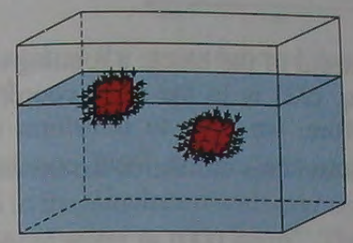


Fig.9. Motion analysis of the interaction among discrete solid bodies and multi-phase fluid.

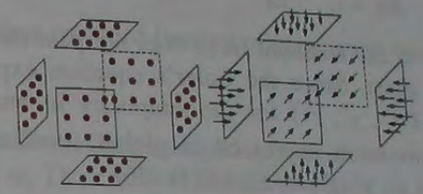


Fig.10. (a) A 3x3 pressure integration grid on each surface of a cubic block, (b) the loading distribution on the block surfaces.

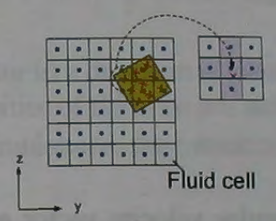


Fig.11. A top view of the interpolation scheme of the surface pressure of a block at a sensing grid from the data of its surrounding fluid cells.

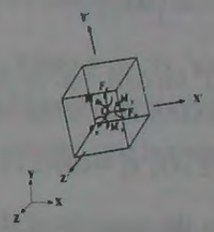


Fig.12. Equivalent force-moment system for a cube exert by the hydrodynamic forces.

where k_n, k_s are the spring constants in the normal and shear directions, respectively, $\mathbf{d}_n$, $\mathbf{d}_s$ are the penetration depths in the normal and shear directions, respectively. As shown in Fig4, the resultant forces and moments applied on each block contain the effects from the fluid forces and the contact forces. Newton's equations (Eq. (21)) and Euler's equations (Eq. (22)) are applied to prescribe the motion of block of mass m in the spatial-temporal space.

$$\sum F_x = ma_x; \sum F_y = ma_y; \sum F_z = ma_z \tag{21}$$

$$\sum M_{x'} = I_{x'}\alpha_{x'} - (I_{y'} - I_{z'})\omega_{x'}\omega_{z'}; \sum M_{y'} = I_{y'}\alpha_{y'} - (I_{z'} - I_{x'})\omega_{z'}\omega_{x'};$$
$$\sum M_{z'} = I_{z'}\alpha_{z'} - (I_{x'} - I_{y'})\omega_{x'}\omega_{y'} \tag{22}$$

where a_i is the i-th component of the acceleration vector, the α_i is the i-th component of the angular acceleration vector, the ω_i is the i-th component of the angular velocity vector, the subscripts x, y, z are the global coordinate axes, and the subscripts x', y', z' are the principal axes of the mass moment of inertias $I_{x'}$, $I_{y'}$, $I_{z'}$.

Explicit central difference time integration scheme is used to solve these equations of motion. The velocity value at time $t + \frac{\Delta t}{2}$ can be obtained as

$$v_i^{(t+\frac{\Delta t}{2})}=\left[(1-\frac{\alpha\Delta t}{2})v_i^{(t-\frac{\Delta t}{2})}+(\frac{F_i}{m}+g_i)\Delta t\right]\frac{1}{1+\frac{\alpha\Delta t}{2}} \tag{23}$$

where α is the numerical damping and g_i is the i-th component of the gravity acceleration. Then, the component of the displacement increment within a time step Δt is

$$\Delta x_i = v_i^{(t+\frac{\Delta t}{2})}\Delta t \tag{24}$$

If the resultant force does not pass through the centroid of the block, a rotating moment will exist. Since the Euler's equation expressed by Eq. (22) is in the local coordinate system (x', y', z') for the simplicity in analysis. Therefore, we have to transform the external moment expressed in global coordinate system into the current local coordinate system (x', y', z') by Eqs. (25)-(26).

$$\begin{bmatrix}M_{x'}\\M_{y'}\\M_{z'}\end{bmatrix}=[\mathbf{A}]\begin{bmatrix}M_x\\M_y\\M_z\end{bmatrix},\quad [\mathbf{A}]=\begin{bmatrix}a_1 & a_2 & a_3\\b_1 & b_2 & b_3\\c_1 & c_2 & c_3\end{bmatrix} \tag{25}$$

$$\begin{aligned}&a_1=\cos(x',x),\ a_2=\cos(x',y),\ a_3=\cos(x',z)\\&b_1=\cos(y',x),\ b_2=\cos(y',y),\ b_3=\cos(y',z)\\&c_1=\cos(z',x),\ c_2=\cos(z',y),\ c_3=\cos(z',z)\end{aligned} \tag{26}$$

Similar to the analysis of displacement vector, the angular velocity vector $\boldsymbol{\omega}'$ at time $t+\frac{\Delta t}{2}$ calculated by the central difference scheme can be calculated as the following.

$$\omega_{z'}^{(t+\frac{\Delta t}{2})}=\left[(1-\frac{\beta\Delta t}{2})\omega_{z'}^{(t-\frac{\Delta t}{2})}+(\frac{M_{z'}^{(t)}}{I'_z}+\frac{(I_{x'}-I_{y'})}{I_{z'}})\omega_{x'}\omega_{y'}\Delta t\right]\frac{1}{1+\frac{\beta\Delta t}{2}} \tag{27}$$

where β is the damping ratio of rotation. This angular velocity vector is further inversely transformed back to the global coordinate system by Eqs (25)-(26). Finally, the increment of rotation within this time step is determined as

$$\Delta\theta_i=\omega_i^{t+\frac{\Delta t}{2}}\Delta t \tag{28}$$

Those two displacement increment vector and the rotation increment vector are used to update the new position of each block in the computational space for the next step analysis.

2.6 Floating body simulation

In this study, we present the simulation results of a cube interacting with fluids. The movement of the cube is determined by the DEM which integrates the fluid pressure acting on the cube surface. The density of the cube varies from 600 kg/m^3 to 1000 kg/m^3 to demonstrate the force balance among the solid cube and fluids.

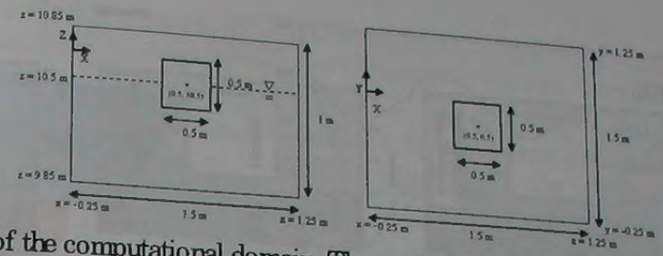


Fig. 12. sketch of the computational domain. The vertical center of floating of cube is the still water level.

The computational domain is sketched in fig. 12. A uniform Cartesian grid system is employed in the simulation with grid size $\Delta x = 0.04$ m, $\Delta y = 0.04$ m and $\Delta z = 0.0167$ m. The density of water is 1000 kg/m^3. The density of air is 1.2 kg/m^3. In the fluid simulation, both air and water are calculated. The length of cube is 0.5 m in each direction. The still water level is located at z = 10.5 m while the bottom the computational domain locates at z = 9.85 m. All the boundaries are no-slip boundary except for the zero pressure at the ceiling (z = 10.85 m).

The cube center in z direction is located same as the still water level (z = 10.5 m). Three different densities of the cube are simulated: ρ = 600 kg/m^3, 800 kg/m^3 and 1000 kg/m^3. From these simulations, the interaction between wave pressure, gravity, and buoyancy can be observed.

The numerical results of x-z plane at y = 0.5 m with different densities are shown in Fig. 13. At time = 0.05 sec, the displacements of blocks are close to zero. At time = 0.5 sec, the cubes affected by gravity and water pressure which causes the difference of cube displacement. From t = 0.5 to 1.0 sec, because of the unsteady water surface, the pressure field of ρ = 1000 kg/m^3 is asymmetrical and the cube rotates. The asymmetric phenomenon is obvious when the local fluid velocity is large.

Fig. 15 shows the angle view of the free-surface profile (ρ = 1000 kg/m^3). At the time = 0.65 sec, cube moves downward and the water floods onto the top of the cube.

Time-history displacements of the cube center location are shown in fig. 15. From time = 0 sec to 0.5 sec, all the cubes move downward. Cubes with larger density move faster. From time = 0.5 sec to 1.0 sec, the pressure force is increasing and is able to support the cube. The pressure force, e.g. the buoyancy force is then makes blocks move up. However, the unstable phenomena can be observed during this process. It might be caused by the unbalance forces or simply caused by the numerical instability.

The cubes moves up and down in the fluid after t = 1.0 sec (Fig. 16). The averaged locations of cube centers are located at z = 10.45, 10.35, and 10.25 m with density = 600 kg/m^3, 800 kg/m^3 and 1000 kg/m^3 respectively which are close the to theoretical values for cubes in the calm water.

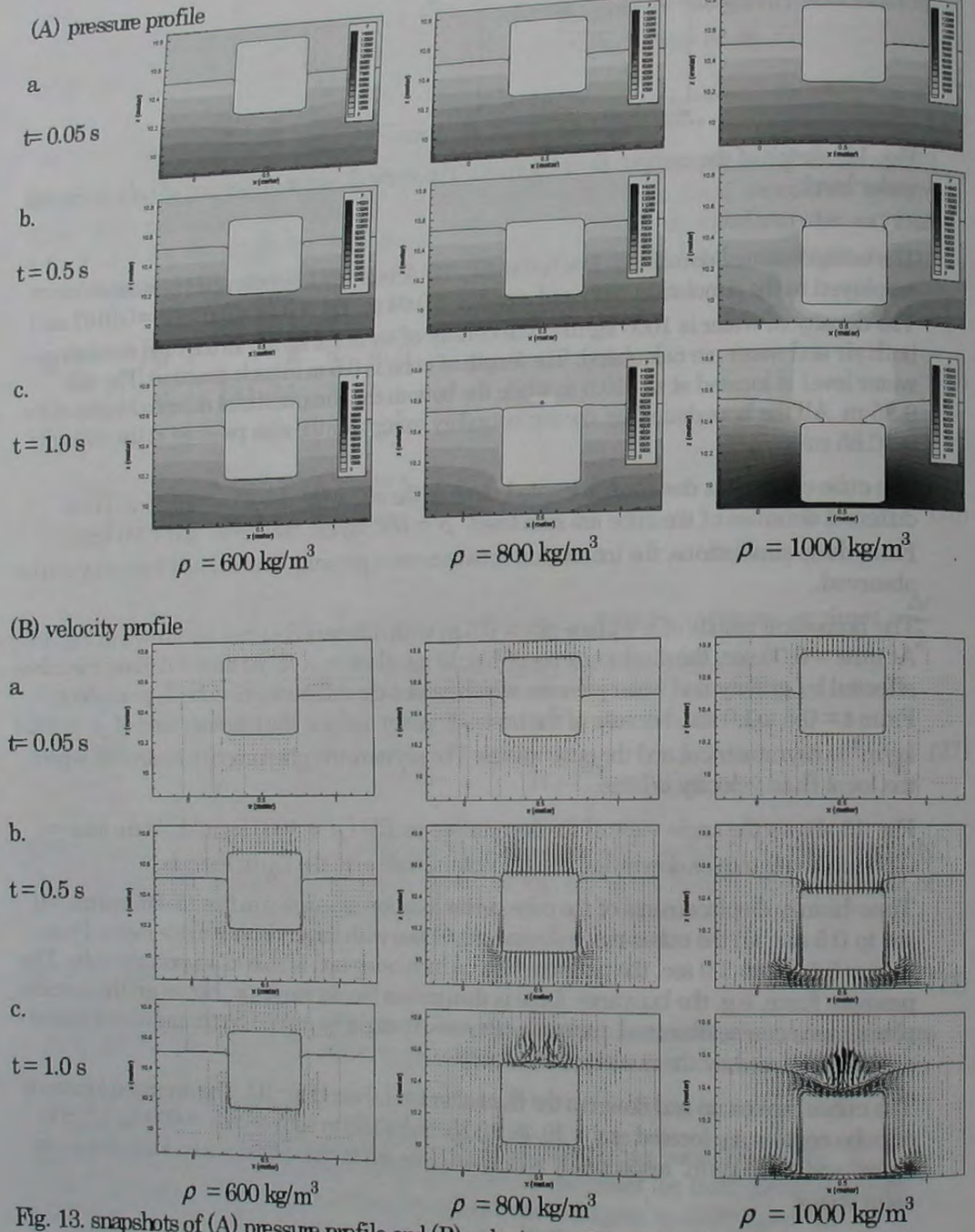


Fig. 13. snapshots of (A) pressure profile and (B) velocity profile of the density of different floating cubes with $\rho = 600$ kg/m^3, 800 kg/m^3 and 1000 kg/m^3.



Fig. 15. free surface and with $\rho = 1000$ kg/m^3 at time = 0.65 sec

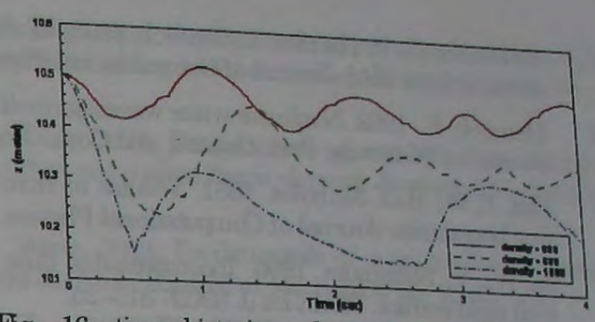


Fig. 16. time histories of the cube center vertical displacement. Solid line denotes $\rho = 600$ kg/m^3, dashed line denotes $\rho = 800$ kg/m^3, and dash dot line denotes $\rho = 1000$ kg/m^3

3. Conclusion

In this study, we developed a two-way coupled moving-solid method which is able to predict both the fluid and solid motions. Two benchmark problems are presented for the validation of the moving solid algorithm. Good results can be seen in the comparisons with analytical solutions and experimental data. By coupling with DEM model, the moving solid method is able to simulate both fluid and solid motion. Floating cube cases with different cube density are simulated for demonstrating the performance of two-way coupled moving-solid algorithm. The results show that the floating cubes move up and down in the water and generate waves. The oscillations of the cubes have mean elevations which are close to the theatrical cube location in the calm water.

As for the future development, the parallelism will be implemented to increase the computational domain, to improve the accuracy, and to shorten the simulation time. The pressure interpolation scheme will also be improved to have better accuracy on the solid surface. The simulation results will be compared with the experimental data.

REFERENCES

1. Attaway, S.W., B.A. Hendrickson, S.J. Plimpton, D.R. Gardner, C.T. Vaughan, K.H. Brown, and M.W. Heinstein. 1998. A Parallel Contact Detection Algorithm for Transient Solid Dynamics Simulations Using PRONTO3D. Computational Mechanics. 22: 43-159.

2. Balaras, E. 2004. Modeling complex boundaries using an external force field on fixed Cartesian grids in large-eddy simulations. Computers and Fluids. 33: 375–404.

3. Cundall, P.A., 1988. Formulation of Three-dimensional Distinct Element Model—Part I: A Scheme to Detect and Represent Contacts in a System Composed of Many Polyhedral B locks. Int. J. Rock Mech. Min. Sci. & Geomech. Abstr. 25: 107-116.

4. Cundall, P.A., 1988. Formulation of a Three-dimensional Distinct Element Model—Part II: Mechanical Calculations for Motion and Interaction of a System Composed of Many Polyhedral B locks. Int. J. Rock Mech. Min. Sci. & Geomech. Abstr. 25: 117-125.

5. Fadlun, E.A., R. Verzicco, P. Orlandi, J. Mohd-Yusof. 2000. Combined immersed-boundary finite-difference methods for three-dimensional complex flow simulations. Journal of Computational Physics. 161: 35–60.

6. Goldstein, D., R. Handler, L. Sirovich. 1993. Modeling a no-slip flow boundary with an external force field. Journal of Computational Physics. 105: 354–366.

7. Heinrich, P., 1992. Nonlinear water waves generated by submarine and aerial landslides. Journal of Waterway, Port, Coastal, and Ocean Engineering. 118(3): 249–266.

8. Hirt, C.W., B.D. Nicholes. 1981. Volume of fluid (VOF) method for the dynamics of free boundaries. Journal of Computational Physics. 39: 201–225.

9. Jia W., Y. Nakamura. 1996. Incompressible flow solver of arbitrarily moving bodies with rigid surface. JSME Int J. 39(2): 315–25.

10. Kothe, D. B., R.C. Mjolsness. 1992. RIPPLE: a new model for incompressible flows with free surfaces. AIAA Journal. 30: 2694–2700.

11. Lin, P., 2006. A multiple-layer σ-coordinate model for simulation of wave–structure interaction. Computers and Fluids. 35: 147–167.

12. Lin, P., and C.W. Li. 2002. A σ-coordinate three-dimensional numerical model for surface wave propagation. International Journal for Numerical Methods in Fluids. 38:1045–1068.

13. Lin, P., P.L.-F. Liu. 1998. A numerical study of breaking waves in the surf zone. Journal of Fluid Mechanics. 359: 239–264.

14. Liu, P.L.-F., T.-R. Wu, F. Raichlen, C. Synolakis, and J. Borrero. 2005. Runup and rundown from three-dimensional sliding masses. Journal of Fluid Mechanics. 536: 107-144.

15. Mittal, R., G. Iaccarino. 2005. Immersed boundary methods. Annual Review of Fluid Mechanics. 37: 239–261.

16. Mohd-Yusof, J. 1997. Combined immersed boundaries/B-splines methods for simulations of flows in complex geometries. In: CTR Annual Research Briefs, Center for Turbulence Research, Stanford University. 317–327.

17. Müller, Matthias., D. Charypar, D. Gross. 2003. Particle-Based Fluid Simulation for Interactive Applications. Computer Animation.

18. Müller, Matthias, B. Solenthaler, R. Keiser, M.Gross. 2005. Particle-Based Fluid-Fluid Interaction. Computer Animation. 29-31

19. Peskin C.S., 1972. Flow patterns around heart valves: a numerical method. Journal of Computational Physics. 10:252.

20. Shen, L.W. and E.S. Chan. 2008 Numerical simulation of fluid-structure interaction using a combined volume of fluid and immersed boundary method. OCEAN ENGINEERING. 35:8-9, 939-952.

21. Shi, G. H., 1988. Discontinuous deformation analysis-a new numerical model for the statics and dynamics of block system. Ph. D. Dissertation, University of California, Berkeley.

22. Shi, G. H. 1992. Manifold method of material analysis. Transactions of the Ninth Army Conference on Applied mathematics and Computing, Minneapolis, Minnesota, USA, 51-76.

23. Shi, G. H. 1996. Manifold method. Proceedings of the First International Forum on Discontinuous Deformation Analysis (DDA) and Simulations of Discontinuous Media, Berkeley, California, USA, 52-104.

24. Shih C., Y. K. Wang, and E. C. Ting. 2004. Fundamentals of a vector form intrinsic finite element: Part III. Convected material frame and examples. Journal of Mechanics. 20: 2, 133-143.

25. Ting E. C., C. Shih, and Y.K. Wang. 2004. Fundamentals of a vector form intrinsic finite element: Part I. basic procedure and a plane frame element. Journal of Mechanics. 20: 2. 113-122.

26. Ting E. C., C. Shih, and Y.K. Wang. 2004. Fundamentals of a vector form intrinsic finite element: Part II. plane solid elements. Journal of Mechanics; 20: 2. 123-132.

27. Udaykumar HS, MM. Rao, W. Shyy. 1996. ELAFINT—A mixed Eulerian–Lagrangian method for fluid flows with complex and moving boundaries. Int J Numer Methods Fluids. 22(8):691–712.

28. Udaykumar HS, H-C. Kan, Shyy W, RT-S. Tay. 1997. Multiphase dynamics in arbitrary geometries on fixed Cartesian grids. J Comput Phys. 137:366–405.

29. Wang, C.Y., J. Sheng, C.J. Huang, M.H. Chen. 2008. Motion Analysis of Mixed Polyhedral and Ellipsoidal Particles. Proceedings of 6th International Conference on Computation of Shell and Spatial Structures. 28-31.

30. Wang, S.P., and E.N. Akamachi. 1997. The Inside-Outside Contact Search Algorithm. Int. J. Numer. Meth. Engng. 40: 3665-685.

31. Wu, T.-R., 2004. A numerical study of three-dimensional breaking waves and turbulence effects. Ph.D. Dissertation, Cornell University.

32. Zhong, Z.H., and L. Nilsson. 1990. A Contact Searching Algorithm for General 3-D Contact-Impact Problems. Computers and Structures. 34(2):327-335.

33. Zhao, D., E.G. Nezami, Y.M.A. Hashash, J. Ghaboussi. 2006. Three-dimensional discrete element simulation for granular materials, Engineering Computations: International Journal for Computer-Aided Engineering and Software. 23: 749- 770.

Proceedings of International Mini-Symposium for Numerical Discontinuous Analyses, edited by T. Koyama, Hawaii, November, 2008

Stability analysis of reinforced slope by using hybrid-type penalty method

Norio Takeuchi
Hosei University, Tokyo, Japan
Morito Kusabuka
Hosei University, Tokyo, Japan

ABSTRACT: We propose the Hybrid-type Penalty Method (HPM) which applied the concept of the penalty method to the principle of hybrid type virtual work. HPM applies the concept of the spring of RBSM in Lagrange multiplier and assume independent displacement field to each sub-domain. In the nonlinear analysis by using HPM, a result equal to FEM is obtained about elastic deformation, and a result with a collapse pattern and limit load equal to Rigid-Bodies Spring Model is obtained. This paper presents the new approach for the modelling of Geotextile Reinforced soil Wall (GRW) by using HPM with penalty density function. Firstly, we show the brief formulation of HPM and concept of the penalty density function. Then, we introduce the method and results of model experiment. Finally, we discuss about the result of present method by comparing with the experiment and FE analysis.

1. INTRODUCTION

In this work for obtaining numerical results for slope stability problems with Geotextile Reinforced soil Wall (GRW), we have used Hybrid-type Penalty Method (HPM), which applied the concept of the penalty method [1] to the principle of hybrid type virtual work [2]. The HPM is based on the discontinuous Galerkin (dG) method [3], and applies the concept of the spring of RBSM [4] (Rigid Bodies-Spring Model) in Lagrange multiplier. In each subdomain, we assume independent displacement field. Because compatibility requirements of the intersection boundary on adjacent sub-domain are secured by using the penalty method, the displacement field can be assumed regardless of the shape of sub-domain [5]. However, it cannot obtain high accuracy solutions when it uses shape other than the triangle at the linear displacement field. For the reason, use of the mesh division of arbitrary shape is difficult. To solve such a problem, we propose the method of applying the second-order displacement field where added the gradient of the strain to linear displacement field of HPM [6].

Usually for finite element method, it is requiring C^1 continuity. However many elements and results are not completely satisfactory this condition. So alternatively using C^0 elements and impose the continuity of slope weakly. This method is called discontinuous Galerkin method [7].

In the following paper, we analyzed slope stability problems with GRW by using HPM based on the dG method. In the first part of the paper, we have given brief formulation of proposed method, and in second part, we have given some experimental results. Finally, we have discussed some numerical result for this problems comparing with FE analysis and the experiment.

2. GOVERNIG EQUATION AND HYBRID TYPE VIRTUAL WORK

2.1. Governing Equation

Let $\Omega \subset \mathbb{R}^{n_{dim}}$, with $(1 \le n_{dim} \le 3)$, be the reference configuration of a continuum body with smooth boundary $\Gamma := \partial\Omega$ and closure $\overline{\Omega} := \Omega \cup \partial\Omega$. Here $\mathbb{R}^{n_{dim}}$ is the n_{dim} dimensional Euclidean space.

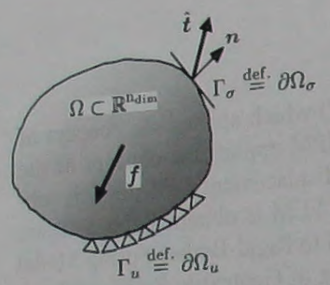


Fig. 1. Reference configuration Ω and smooth boundary $\partial\Omega$

The local form of the equilibrium equation for a deformable body is as follows:

$$\mathrm{div}\boldsymbol{\sigma} + \boldsymbol{f} = 0 \quad \text{in}\ \Omega \quad (\boldsymbol{\sigma} = \boldsymbol{\sigma}^t) \tag{1}$$

where $\boldsymbol{f} : \Omega \to \mathbb{R}^{n_{dim}}$ is the body force per unit volume, $\boldsymbol{\sigma} : \overline{\Omega} \to \mathbb{S}$ is the Cauchy stress tensor respectively. Here $\mathbb{S} = \mathbb{R}^{(n_{dim}+1)\cdot n_{dim}/2}$ is the vector space of symmetric rank-two tensor and $\boldsymbol{e}_i$ is the standard base vector of $\mathbb{R}^{n_{dim}}$, so that the stress tensor becomes $\boldsymbol{\sigma} = \sigma_{ij}\boldsymbol{e}_i \otimes \boldsymbol{e}_j$, where $\otimes$ denotes a tensor product. $\boldsymbol{u} : \overline{\Omega} \to \mathbb{R}^{n_{dim}}$ is a displacement field of particles with reference position $\boldsymbol{x} \in \Omega$. We write $\boldsymbol{u}(\boldsymbol{x})$ and denote the infinitesimal strain tensor by

$$\boldsymbol{\varepsilon} = \nabla^s \boldsymbol{u} := \frac{1}{2}\{\nabla \boldsymbol{u} + {}^t(\nabla \boldsymbol{u})\} \tag{2}$$

where $\nabla := (\partial/\partial x_i)\boldsymbol{e}_i$ is the differential vector operator, ∇^s shows the symmetry part of ∇.

In what follows, we assume that the boundary $\Gamma = \Gamma_u \cup \Gamma_\sigma$ ($\overline{\Gamma} = \overline{\Gamma_u \cup \Gamma_\sigma}$, $\Gamma_u \cap \Gamma_\sigma = \emptyset$). Here $\Gamma_u := \partial_u\Omega \subset \partial\Omega$ where displacement are prescribed as

$$\boldsymbol{u}|_{\Gamma_u} = \overline{\boldsymbol{u}} \ \text{(given)} \tag{3}$$

Where as $\Gamma_\sigma := \partial_\sigma\Omega \subset \partial\Omega$ where tractions $\boldsymbol{t} := \boldsymbol{\sigma}\boldsymbol{n}$ are prescribed as

$$\boldsymbol{\sigma}|_{\Gamma_\sigma}\hat{\boldsymbol{n}} = \hat{\boldsymbol{t}} \ \text{(given)} \tag{4}$$

Here $\hat{\boldsymbol{n}}$ is the field normal to the boundary Γ_σ. The constitutive equation to the elastic body is provided as follows by the use of the elasticity tensor C.

$$\boldsymbol{\sigma} = \boldsymbol{C} : \boldsymbol{\varepsilon} \tag{5}$$

2.2 Virtual Work Equation (Weak Forms)

Let denote by $\mathbb{U}$ the space of admissible displacement field, defined as

$$\mathbb{U} \overset{\text{def.}}{=} \{\boldsymbol{u} : \Omega \to \mathbb{R}^{n_{dim}} \mid \boldsymbol{u}|_{\Gamma_u} = \hat{\boldsymbol{u}}\} \tag{6}$$

Moreover, let denote by $\mathbb{V}$ the space of admissible virtual displacement field, defined as

$$\mathbb{V} \overset{\text{def.}}{=} \{\delta\boldsymbol{u} : \Omega \to \mathbb{R}^{n_{dim}} \mid \delta\boldsymbol{u}|_{\Gamma_u} = \boldsymbol{0}\} \tag{7}$$

We can now use Equation (1) and integrate volume of the body to give a weak statement of the static equilibrium of the body as

$$\delta W = \int_\Omega (\mathrm{div}\,\boldsymbol{\sigma} + \boldsymbol{f}) \cdot \delta\boldsymbol{u}\, dV = 0 \qquad {}^\forall\delta\boldsymbol{u} \in \mathbb{V} \tag{8}$$

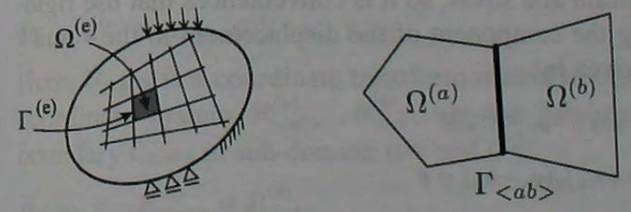
Using the Gauss theorem enable Equation (8) to be rewritten as

$$\int_\Omega \boldsymbol{\sigma} : \mathrm{grad}\delta\boldsymbol{u}\, dV - \int_\Omega \boldsymbol{f}\cdot\delta\boldsymbol{u} dV - \int_{\Gamma_\sigma} \hat{\boldsymbol{t}}\cdot\delta\boldsymbol{u}\, dS = 0 \quad {}^\forall\delta\boldsymbol{u} \in \mathbb{V} \tag{9}$$

This equation is virtual work equation. If $\boldsymbol{u}$ is the weighing function, this is a weak forms. It is $\mathbb{U} \subset \mathbb{H}^1(\Omega)$ and $\mathbb{V} \subset \mathbb{H}^1(\Omega)$ where denotes the Sobolev space $\mathbb{H}^1(\Omega)$ of function possessing space integrable derivatives.

2.3 Hybrid Type Virtual Work Equation

Let Ω consist of M sub-domains $\Omega^{(e)} \subset \Omega$ with the closed boundary $\Gamma^{(e)} := \partial\Omega^{(e)}$ as shown in Figure 2(a). That is $\Omega = \bigcup_{e=1}^{M} \Omega^{(e)}$, here $\Omega^{(r)} \cap \Omega^{(q)} = 0 \quad (r \ne q)$. In what follows, we assume that the closure $\overline{\Omega}^{(e)} := \Omega^{(e)} \cup \partial\Omega^{(e)}$.



(a) Sub-domain $\Omega^{(e)}$ (b) Common boundary $\Gamma_{<ab>}$ of sub-domain $\Omega^{(a)}$ and $\Omega^{(b)}$

Fig. 2. Sub-domain and its common boundary

We denoted by $\Gamma_{<ab>}$ the common boundary for two subdomain $\Omega^{(a)}$ and $\Omega^{(b)}$ adjoined as shown in Figure 2(b), and which is defining as $\Gamma_{<ab>} \overset{\text{def.}}{=} \Gamma^{(a)} \cap \Gamma^{(b)}$. The relation for $\tilde{\boldsymbol{u}}^{(a)}$ and $\tilde{\boldsymbol{u}}^{(b)}$ are following:

$$\tilde{\boldsymbol{u}}^{(a)} = \tilde{\boldsymbol{u}}^{(b)} \ \text{ on } \Gamma_{<ab>} \tag{10}$$

They are the displacements on $\Gamma_{<ab>}$ that is intersection boundary in $\Omega^{(a)}$ and $\Omega^{(b)}$ sub-domain. It introduces this subsidiary condition into the framework of the variational equation (9) with Lagrange multipliers $\boldsymbol{\lambda}$ as follows:

$$H_{ab} \overset{\text{def.}}{=} \delta \int_{\Gamma_{<ab>}} \boldsymbol{\lambda}\cdot(\tilde{\boldsymbol{u}}^{(a)} - \tilde{\boldsymbol{u}}^{(b)})\, dS \tag{11}$$

where $\delta(\bullet)$ shows the variation of $(\bullet)$. Physical meaning of the Lagrange multiplier $\boldsymbol{\lambda}$ is equal to the surface force on the intersection boundary $\Gamma_{<ab>}$.

As described above, the hybrid type virtual work equation is as follows about M subdomain and N intersection boundary:

$$\sum_{e=1}^{M}\left(\int_{\Omega^{(e)}}\boldsymbol{\sigma}:\mathrm{grad}\delta\boldsymbol{u}\,dV-\int_{\Omega^{(e)}}\boldsymbol{f}\cdot\delta\boldsymbol{u}dV-\int_{\Gamma^{(e)}}\boldsymbol{t}\cdot\delta\boldsymbol{u}\,dS\right)-\sum_{s=1}^{N}\left(\delta\int_{\Gamma_{<s>}}\boldsymbol{\lambda}\cdot(\tilde{\boldsymbol{u}}^{(a)}-\tilde{\boldsymbol{u}}^{(b)})\,dS\right)=0 \qquad {}^{\forall}\delta\boldsymbol{u}\in\mathbb{V} \tag{12}$$

3. INDEPENDENT DISPLACEMENT FIELD AND DISCRIZATION

3.1. *Displacement Field*

In the following work, we considers a two-dimensional displaced field $\boldsymbol{u}\in\mathbb{U}$ with $\mathrm{n_{dim}}=2$. Taylor's expansion is carried out to this displacement $\boldsymbol{u}(\boldsymbol{x})$ about the any point $\boldsymbol{x}_P=(x_P,y_P)\in\Omega^{(e)}$ in a domain $\Omega^{(e)}$ as follows:

$$\boldsymbol{u}^{(e)}=\boldsymbol{u}^P+(x-x_P)\boldsymbol{u}_x^P+(y-y_P)\boldsymbol{u}_y^P+\frac{1}{2}(x-x_P)^2\boldsymbol{u}_{xx}^P+\frac{1}{2}(y-y_P)^2\boldsymbol{u}_{yy}^P+(x-x_P)(y-y_P)\boldsymbol{u}_{xy}^P+\cdots \tag{13}$$

here,

$$(\bullet)_x=\frac{\partial}{\partial x}(\bullet),\ (\bullet)_y=\frac{\partial}{\partial y}(\bullet),\ (\bullet)_{xy}=\frac{\partial^2}{\partial x\partial y}(\bullet),\ (\bullet)_{xx}=\frac{\partial^2}{\partial x^2}(\bullet),\ (\bullet)_{yy}=\frac{\partial^2}{\partial y^2}(\bullet).$$

Here, $(\bullet)^P$ indicates the value of the physical quantity in the point $\boldsymbol{x}_P$. The second-order displaced filed can take even the second-order term of Taylor's expansion.
The stress analysis often needs the check on the strain and stress, so it is conveniences that use rigid-displacement, strain and slope of strain. Denoting the component of the displacement to the x and y direction by u and v, strain and its derivative are given by

$$u_x=\varepsilon_x,\ u_{xx}=(\varepsilon_x)_x,\ u_{xy}=(\varepsilon_x)_y,\ v_y=\varepsilon_y,\ v_{yy}=(\varepsilon_y)_y,\ v_{yx}=(\varepsilon_y)_x$$
$$\frac{1}{2}(u_y+v_x)=\gamma_{vy},\ \frac{1}{2}(u_y+v_x)_x=(\gamma_{vy})_x,\ \frac{1}{2}(u_y+v_x)_y=(\gamma_{vy})_y(v_x-u_y)=\theta$$

Consequently, the second-order displaced field in the arbitrary sub-domains $\Omega^{(e)}$ by matrix form will be:

$$\boldsymbol{u}^{(e)}=\boldsymbol{N}_d^{(e)}\boldsymbol{d}^{(e)}+\boldsymbol{N}_\varepsilon^{(e)}\boldsymbol{\varepsilon}^{(e)}+\boldsymbol{N}_g^{(e)}\boldsymbol{\varepsilon}_x^{(e)} \tag{14}$$

where

$$\boldsymbol{N}_d^{(e)}=\begin{bmatrix}1&0&-Y^{(e)}\\0&1&X^{(e)}\end{bmatrix},\ \boldsymbol{N}_\varepsilon^{(e)}=\begin{bmatrix}X^{(e)}&0&Y^{(e)}/2\\0&Y^{(e)}&X^{(e)}/2\end{bmatrix}\qquad \left.\begin{matrix}X^{(e)}=x-x_P\\Y^{(e)}=y-y_P\end{matrix}\right\}$$
$$\boldsymbol{N}_g^{(e)}=\begin{bmatrix}(X^{(e)})^2/2&0&X^{(e)}Y^{(e)}&-(Y^{(e)})^2/2&0&(Y^{(e)})^2/2\\0&(Y^{(e)})^2/2&-(X^{(e)})^2/2&X^{(e)}Y^{(e)}&(X^{(e)})^2/2&0\end{bmatrix}$$
$$\boldsymbol{d}^{(e)}=\lfloor u^P,v^P,\theta^P\rfloor^t,\ \boldsymbol{\varepsilon}^{(e)}=\lfloor\varepsilon_x^P,\varepsilon_y^P,\gamma_{xy}^P\rfloor^t,\ \boldsymbol{\varepsilon}_x^{(e)}=\lfloor(\varepsilon_x^P)_x,(\varepsilon_y^P)_y,(\varepsilon_x^P)_y,(\varepsilon_y^P)_x,(\gamma_{xy}^P)_x,(\gamma_{xy}^P)_y\rfloor^t$$

The displacement field is expressed with this model using the parameter in the arbitrary point in each sub-domain, so that the displacement is not defined by the node such as displacement model of FEM.

Therefore, an arbitrary polygon, a polyhedron, and a curved surface body can be used as sub-domain without limiting the element shape.

3.2. *Lagrange Multiplier and Penalty Function*

Physical meaning of the Lagrange multiplier $\boldsymbol{\lambda}$ is equal to the surface force on the intersection boundary as described. Generally, in a hybrid-type variational principle, this multiplier is dealt with as an unknown parameter. Sinee it has the meaning that Lagrange multiplier $\boldsymbol{\lambda}$ is the surface force on the boundary $\Gamma_{<ab>}$ in sub-domain $\Omega^{(a)}$ and $\Omega^{(b)}$, the surface force is defined as follows:

$$\boldsymbol{\lambda}_{<ab>}=\boldsymbol{k}\cdot\boldsymbol{\delta}_{<ab>} \tag{15}$$

Here, $\boldsymbol{\delta}_{<ab>}$ shows relative displacement on the sub-domain boundary $\Gamma_{<ab>}$, and it is shown in two dimensional problems as follows:

$$\begin{Bmatrix}\lambda_{n<ab>}\\\lambda_{t<ab>}\end{Bmatrix}=\begin{bmatrix}k_n&0\\0&k_t\end{bmatrix}\begin{Bmatrix}\delta_{n<ab>}\\\delta_{t<ab>}\end{Bmatrix} \tag{16}$$

where, $\delta_{n<ab>}$, $\delta_{t<ab>}$ are relative displacement in the normal and the tangential direction to the sub-domain boundary $\Gamma_{<ab>}$. Similarly, $\lambda_{n<ab>}$, $\lambda_{t<ab>}$ are Lagrange multipliers in the normal and tangential direction of the surfaee forces. The hybrid type penalty method can be described as follows by penalty function p use as coefficient k.

$$k_n=k_t=p \tag{17}$$

By the way, the subsidiary condition shown by equation (10) can be described with a local coordinate system along the intersection boundary as follows.

$$\boldsymbol{R}_{<ab>}\tilde{\boldsymbol{u}}^{(a)}=\boldsymbol{R}_{<ab>}\tilde{\boldsymbol{u}}^{(b)}\quad\text{on}\quad\Gamma_{<ab>} \tag{18}$$

Here, $\boldsymbol{R}_{<ab>}$ is a coordinate transform matrix to change from a global coordinate system to the local coordinate system. $\boldsymbol{R}_{<ab>}^{(a)}$, $\boldsymbol{R}_{<ab>}^{(b)}$ are the geometric transformation in each area of the common boundary $\Gamma_{<ab>}$ in sub-domain $\Omega^{(a)}$ and $\Omega^{(b)}$.

$$\boldsymbol{R}_{<ab>}=-\boldsymbol{R}_{<ab>}^{(a)}=\boldsymbol{R}_{<ab>}^{(b)} \tag{19}$$

Therefore, relative displacement is shown as follows:

$$\delta_{<ab>}=\boldsymbol{R}_{<ab>}^{(a)}\tilde{\boldsymbol{u}}^{(a)}+\boldsymbol{R}_{<ab>}^{(b)}\tilde{\boldsymbol{u}}^{(b)}=\sum_{l=1}^{2}\boldsymbol{R}_{<ab>}^{(l)}\tilde{\boldsymbol{u}}^{(l)} \tag{20}$$

Equation (11) can be described as follows by the use of the relation between these and the relation of equation (15).

$$H_{ab}\overset{\mathrm{def.}}{=}\delta\int_{\Gamma_{<ab>}}\boldsymbol{\lambda}_{<ab>}(\boldsymbol{R}_{<ab>}\tilde{\boldsymbol{u}}^{(a)}-\boldsymbol{R}_{<ab>}\tilde{\boldsymbol{u}}^{(b)})\,dS=-\delta\int_{\Gamma_{<ab>}}\boldsymbol{\delta}_{<ab>}^t\cdot\boldsymbol{k}\cdot\boldsymbol{\delta}_{<ab>}\,dS \tag{21}$$

3.3. *Discretization Equation by Matrix Form*

When equation (12) is rewritten by the matrix form to make the discretization equation, it is possible to describe it as follows:

$$\sum_{e=1}^{M}\left(\int_{\Omega(e)}[\boldsymbol{L}\delta\boldsymbol{u}]^t\boldsymbol{D}\boldsymbol{L}\boldsymbol{u}dV-\int_{\Omega^{(e)}}\delta\boldsymbol{u}^t\boldsymbol{f}dV-\int_{\Gamma_\sigma}\delta\boldsymbol{u}^t\hat{\boldsymbol{T}}dS\right)+\sum_{s=1}^{N}\left(\delta\int_{\Gamma_{<s>}}\delta^t\boldsymbol{k}\delta\,dS\right)=0 \tag{22}$$

In a plane strain of two dimensions, each coefficient is as follows:

$$L^t = \begin{bmatrix} \frac{\partial}{\partial x} & 0 & \frac{\partial}{\partial y} \\ 0 & \frac{\partial}{\partial y} & \frac{\partial}{\partial x} \end{bmatrix}, D = \frac{(1-\nu)E}{(1+\nu)(1-2\nu)} \begin{bmatrix} 1 & \frac{\nu}{1-\nu} & 0 \\ \frac{\nu}{1-\nu} & 1 & 0 \\ 0 & 0 & \frac{1-2\nu}{2(1-\nu)} \end{bmatrix}, f = \begin{Bmatrix} f_x \\ f_y \end{Bmatrix}, u = \begin{Bmatrix} u \\ v \end{Bmatrix}, \delta u = \begin{Bmatrix} \delta u \\ \delta v \end{Bmatrix}, \hat{T} = \begin{Bmatrix} \hat{t}_n \\ \hat{t}_t \end{Bmatrix}$$

Here, E and ν are the elastic coefficient and Poisson's ratio. f_x and f_y show the body force in the direction of x and y, u and v are the displacements of the direction of x and y, δu and δv are virtual displacement in the direction of x and y, $\hat{t}_n$, $\hat{t}_t$ are the given surface force in the normal and tangential direction on the boundary.

The displacement shown by the second order function in Equation (14) is substituted for Equation(22). Similarly, we assumed virtual displacement as follows:

$$\delta u^{(e)} = N_d^{(e)} \delta d^{(e)} + N_\varepsilon^{(e)} \delta \varepsilon^{(e)} + N_g^{(e)} \delta \varepsilon_x^{(e)} \tag{23}$$

To make the discretization equation, equation (14) and equation (23) are changed as follows.

$$u^{(e)} = N^{(e)} U^{(e)}, \delta u^{(e)} = N^{(e)} \delta U^{(e)} \tag{24}$$

Here,

$U^{(e)} = \lfloor d^{(e)}, \varepsilon^{(e)}, \varepsilon_x^{(e)} \rfloor^t$, $\delta U^{(e)} = \lfloor \delta d^{(e)}, \delta \varepsilon^{(e)}, \delta \varepsilon_x^{(e)} \rfloor^t$, $N^{(e)} = \lfloor N_d^{(e)}, N_\varepsilon^{(e)}, N_g^{(e)} \rfloor$.

Therefore, the following expression is obtained.

$$Lu^{(e)} = LN^{(e)} U^{(e)} = B^{(e)} U^{(e)} \tag{25}$$

here, $B^{(e)} = LN^{(e)}$. When one dimension array that arranges all degree of freedom in the reference configuration is assumed to be U, the degree of freedom $U^{(e)}$ concerning the sub-domain $\Omega^{(e)}$ is shown as follows:

$$U^{(e)} = \mathcal{A}^{(e)} U \ , \ \delta U^{(e)} = \mathcal{A}^{(e)} \delta U \tag{26}$$

Here, $\mathcal{A}^{(e)}$ is a procession who relates all degree of freedom in the reference configuration and degree of freedom in the attention sub-domain.

On the other hand, the relative displacement $\delta_{<ab>}$ is described as follows:

$$\delta_{<ab>} = B_{<ab>} U_{<ab>} \tag{27}$$

here,

$B_{<ab>} = \lfloor R_{<ab>}^{(a)} N^{(a)} \ , \ R_{<ab>}^{(b)} N^{(b)} \rfloor$, $U_{<ab>} = \lfloor U^{(a)} \ , \ U^{(b)} \rfloor^t$.

When one dimension array that arranges all degree of freedom is assumed to be U, the degree of freedom $U_{<ab>}$ of the sub-domain boundary $\Gamma_{<ab>}$ can be described as well as equation (26) as follows:

$$U_{<ab>} = \mathcal{M}_{<ab>} U \ , \ \delta U_{<ab>} = \mathcal{M}_{<ab>} \delta U \tag{28}$$

Here, $\mathcal{M}_{<ab>}$ is a procession which relates all degree of freedom to degree of freedom concerning the attention sub-domain boundary.

The following is obtained by substituting these relations for Equation (22).

$$\delta U^t \left(\sum_{e=1}^{M} K^{(e)} + \sum_{s=1}^{N} K_{<s>} \right) U - \delta U^t \left(\sum_{e=1}^{M} P^{(e)} \right) = 0 \tag{29}$$

here,

$$K^{(e)} = (\mathcal{A}^{(e)})^t \int_{\Omega^{(e)}} (B^{(e)})^t D^{(e)} B^{(e)} \, dV \, \mathcal{A}^{(e)} \ , \ K_{<s>} = \mathcal{M}_{<s>}^t \int_{\Gamma_{<s>}} B_{<s>}^t k B_{<s>} \, dS \, \mathcal{M}_{<s>}$$

$$P^{(e)} = (\mathcal{A}^{(e)})^t \left(\int_{\Omega^{(e)}} (N^{(e)})^t f \, dV + \int_{\Gamma_\sigma} (N^{(e)})^t T \, dS \right)$$

Since Virtual displacement δU of equation (29) is arbitrary, we obtain the following discretized equations.

$$KU = P \tag{30}$$

here,

$$K = \sum_{e=1}^{M} K^{(e)} + \sum_{s=1}^{N} K_{<s>} \ , \ P = \sum_{e=1}^{M} P^{(e)}$$

The discretization equation of this model becomes a simultaneous linear equation shown in equation (30). Left coefficient matrix K consists of stiffness in the sub domain and subsidiary condition on the intersection boundary for the adjacent sub-domain. The discontinuous phenomenon of opening etc. can be expressed without changing degree of freedom by changing the value of k of equation (29) to zero.

4. NUMERICAL ARGORITHM FOR NONLINEAR ANALYSIS

4.1. Constitutive Relation

For determination of spring constants in slip (shear) failure, the ordinary plastic flow rule is adopted. It is assumed that the plastic yielding will occur if the tractions on intersection boundary satisfy the following condition.

$$f(\lambda) = 0 \ , \ Q(\lambda) = 0 \tag{31}$$

where, $f(\lambda)$ is the yield function in the flow theory of plasticity and $Q(\lambda)$ is the plastic potential, and λ is the surface force on the intersection boundary.

Based on the associated flow rule in which yield function f is equal to plastic potential Q, the relation between stress increments and strain (relative displacement) increment can be finally obtained in the following form:

$$\Delta\lambda = k^{ep} \cdot \Delta\delta \ , \ k^{ep} = \left(k^e - \frac{k^e \frac{\partial f}{\partial \lambda} \frac{\partial f}{\partial \lambda} k^e}{\frac{\partial f}{\partial \lambda} k^e \frac{\partial f}{\partial \lambda}} \right) \tag{32}$$

where, k^e is the matrix for penalty function and superscript e indicates the status of elasticity.

In each sub-domain, yield function g and plastic potential Φ is expressed by:

$$g(\sigma)=0\ ,\ \Phi(\sigma)=0 \tag{33}$$

where, σ is the stress in the sub-domain. In each sub-domain, we assume the relation of the stress-strain with the plastic flow rule. Then, we obtain following relation.

$$\sigma = D^{ep}\cdot\varepsilon^{e}\ ,\ D^{ep}=\left(D^{e}-\frac{D^{e}\frac{\partial g}{\partial\sigma}\frac{\partial\Phi}{\partial\sigma}D^{e}}{\frac{\partial g}{\partial\sigma}D^{e}\frac{\partial\Phi}{\partial\sigma}}\right) \tag{34}$$

In the above equation (34), it obey the associated flow rule if $g\equiv\Phi$.

4.2. *Nonlinear Algorithm*

The numerical algorithm is proposed by applying the incremental load procedure developed by YAMADA for the nonlinear problem of soil foundations whose failure condition is described the above.

The load $P^{(i+1)}$ at the (i+1)th step can be calculated by using the load $P^{(i)}$ at the i-th step:

$$P^{(i+1)}=(1-r_i)P^{(i)} \tag{35}$$

where r_i is a rate of load increment at the present step (i) which we can calculated using following equation:

$$f(\lambda+r\Delta\lambda)=0 \tag{36}$$

If crack initiation will cause stress relaxation, relieved forces are taken into account as follows:

$$P^{(n)}=\prod_{i=0}^{n-1}[(1-r_i)]\,P+\sum_{k=1}^{n}\left(\prod_{i=k}^{n}[(1-r_i)]\,F^{(k-1)}\right) \tag{37}$$

where $F^{(k)}$ is the relieved force at the *k*th step.

Here r_{TOTAL} implies the cumulative rate of load increment and it can be defined as follows:

$$r_{TOTAL}=\sum_{k=1}^{n}\left(\prod_{i=0}^{k-1}[(1-r_i)]\right)r_k \tag{38}$$

The calculation must be repeated until $r_{TOTAL}=1$ in each stage of loading.

5. EXPERIMNENTAL AND NUMERICAL RESULT

5.1. *Experiment of Model Slope with GRW*

In this section, we describe the outline of the model experiment for discussing the compatibility of the numerical result. Figure 3 shows the model slope. In the experiment, we packed the Toyoura standard sand of 5% of the moisture content by free fall, and compact the banking by a rammer for every 60mm in height. The model foundation has depth of 250mm, width of 700mm, height of 450mm and extension of slope is a 3-bu.

We lay reinforcement of wide 250mm (Figure 4(a)) with rectangular arrangement. The laying height from the bottom of the foundation is 100mm, 200mm, 300mm, and 400mm. As shown in Figure 4(b),

the length of geogrid is three patterns (150mm, 200mm, and 250mm) We apply the load in position of 150mm from the toe of slope.

Figure 5 shows the load-settlement curve by experiment. On the non-reinforced foundation, the slope caused general shear failure and collapsed. The ultimate bearing capacity was 28.31kN/m^2 and the settlement at that time was 0.1. On the other hand, the hardening phenomenon occurred in reinforcement soil. When the geogrid length is 150mm and 200mm, the hardening rate was almost the same, but in the case of 250mm, the hardening rate became larger than other's. This result shows that the geogrid controlled the slip, and demonstrates the effect of reinforcement.

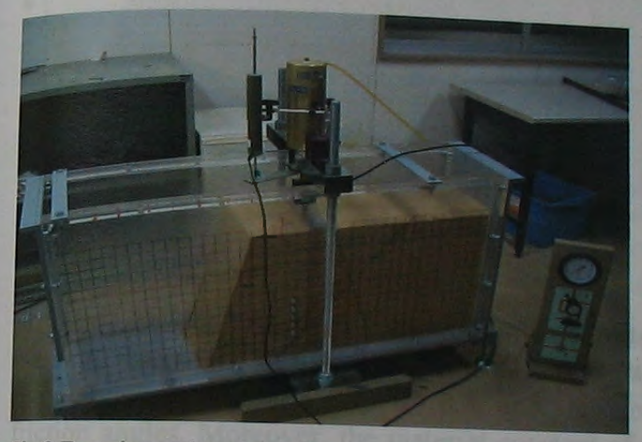
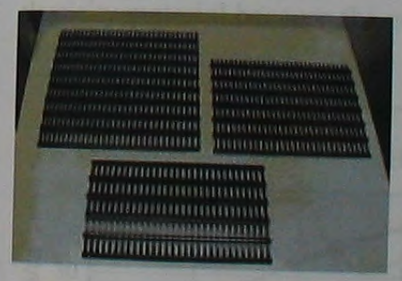
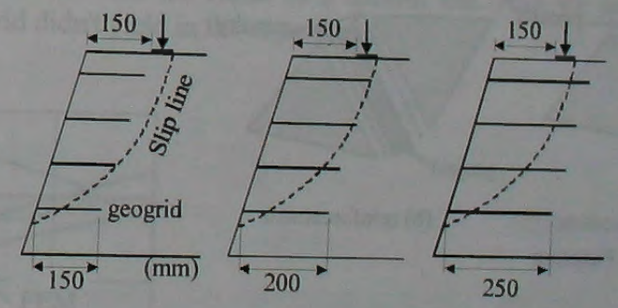


Fig.3 Experimental model



(a) geogrid



(b) arrangement of the geogrid

Fig.4 Reinforcement

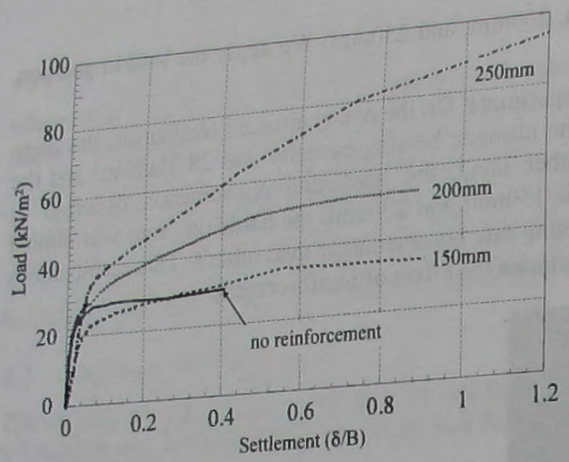
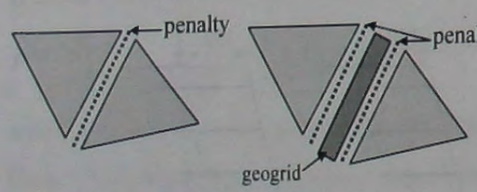


Fig.5 Load-settlement curve

5.2. *Numerical Model of GRW*

In HPM, the penalty function distributed over the intersection boundary is arranged as shown in Figure 6(a). Therefore, the penalty function is arranged also between the foundation and the reinforcement as shown in Figure 6(b).



(a) no reinforcement (b) reinforcement

Fig.6 Penalty Function

In this case, since a geogrid is thin, a penalty function is arranged densely. Then, we newly introduce penalty density function shown in the following:

(penalty density function) $\beta = \dfrac{1}{h_1 + h_2}$ (39)

$k_n = k_t = \dfrac{p}{h_1 + h_2} = \beta \cdot p = p'$ (40)

Here, h1 and h2 express the length of the perpendicular taken down from the center of figure of each element to the intersection boundary.

5.3. *Numerical Result*

Figure 7 shows the mesh division with the geogrid of the construction length of 250mm. As a boundary condition, the bottom of the foundation fixes x and y direction and the right side fixes only x direction.

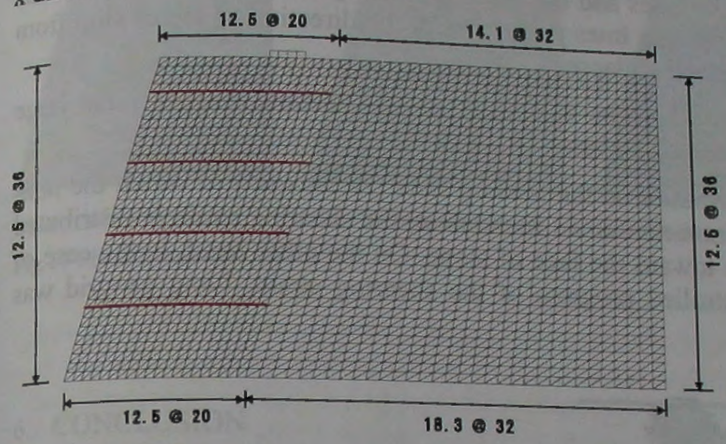


Fig.7 Mesh Division

We analyze on the basis of assumption of a plane strain with Mohr-Coulomb's yield condition. The material constants of the model foundation (sands) used for analysis are elastic-modulus $E=2500kN/m^2$, Poisson's-ratio $\nu= 0.3$, and cohesion $c=1.8kN/m^2$ and $\phi= 35$ degrees of internal-friction angles. Moreover, the material constant of the geogrid is elastic-modulus $E=16\times10^5 kN/m^2$ and cross-sectional-area $A=1.0\times10^{-4}m^2/m$ from the result of a tension test. And we assumed that elasticity material because the geogrid didn't yield in the experiment.

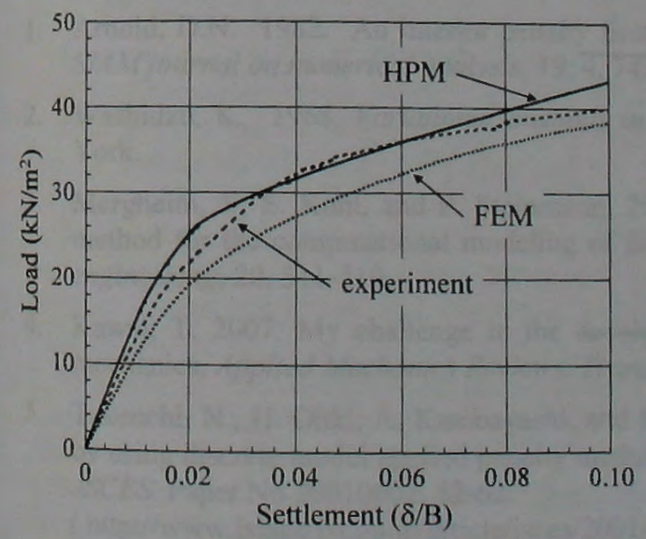


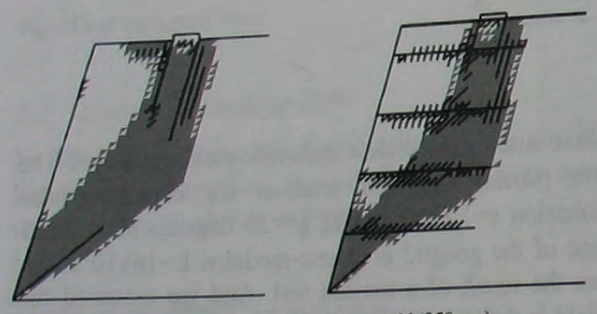
Fig.8 Load-Settlement Curve

Figure8 shows the load-settlement curve of HPM, FEM and experiment in the construction length of 250mm. Although these are similar results, the collapse load of FEM is a little small.

Figure 9 shows the slip line pattern of non-reinforced foundation and reinforced foundation with geogrid length of 250mm in the loading state (28.5kN/m^2) in which the non-reinforced foundation collapsed. The solid line expresses the slip lines and the shading part expresses that the element has yielded. On the non-reinforced foundation, slip lines progresses in the direction of toe of slop from directly under the loading plate, and the slope collapse.

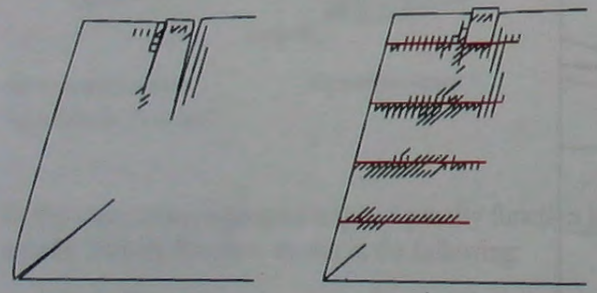
Figure 10 shows the displacement mode when the non-reinforced foundation collapses, and large deformation has arisen on the non-reinforced foundation.

Figure 11 shows the shearing-strain distribution in the loading state (28.5kN/m^2) in which the non-reinforced foundation collapsed. On the non-reinforced foundation, the shearing strain is distributed over the slip line from loading-plate like toward the face of slope. On the other hand, in the case of reinforcement soil, the geogrid had controlled progress of the shearing strain. Long geogrid was effective in control of failure.



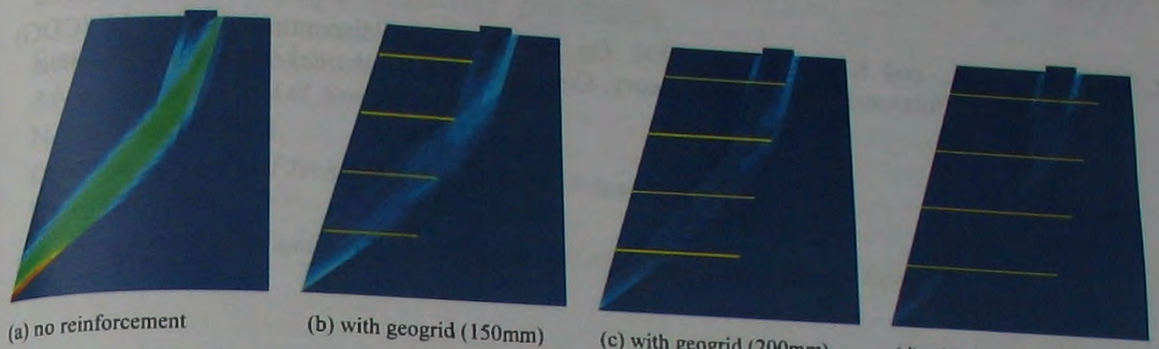
(a) no reinforcement (b) with geogrid (250mm)

Fig.9 Slip Lines (28.5kN/m^2)



(a) no reinforcement (b) with geogrid (250mm)

Fig.10 Displacement Mode (28.5kN/m^2)



(a) no reinforcement (b) with geogrid (150mm) (c) with geogrid (200mm) (d) with geogrid (250mm)

Fig.11 Shear Strain (28.5kN/m^2)

6. CONCLUSION

As one of the approaches by the dG method, we introduced the discrete limit analysis of the reinforcement soil by HPM. We have expressed the similar result, when load settlement behavior was compared with the experimental result. Moreover, about the collapse mode of the foundation, we obtained the result which can explain the diseontinued progressive in the foundation. We think that HPM which is discontinuous analysis such as dG method becomes one tool of soil and rock mechanics.

REFERENCES

1. Arnold, D.N. 1982. An interior penalty finite element method with discontinuous elements. *SIAM journal on numerical analysis,* 19, 4, 742-760.
2. Washidzu, K. 1968. *Variational methods in elasticity and plasticity*, Pergamon Press, New York.
3. Mergheim, J., E. Kuhl, and P. Steinmann, 2004. A hybrid discontinuous Galerkin/interface method for the computational modeling of failure, *Communications in numerical methods in engineering*, 20, 511-519.
4. Kawai, T. 2007. My challenge in the development of a mixed variational method in solid mechanics, *Applied Mechanics Reviews, Transaction of the ASME,* 60, 51-64.
5. Takeuchi, N., H. Ohki, A. Kambayashi, and M. Kusabuka, 2001. Material nonlinear analysis by using discrete model applied penalty method in hybrid displacement model, *Transactions of JSCES,* Paper No 20010002, 52-62.
(http://www.jstage.jst.go.jp/article/jsces/2001/0/20010002/_pdf/-char/ja/)
6. Ohki, H., and N. Takeuchi, 2006. Upper and low bound solution with hybrid-type penalty method, *Transactions of JSCES*, Paper No 20060020, 1-10.
(http://www.jstage.jst.go.jp/article/jsces/2006/0/20060020/_pdf/-char/ja/)

7. Hughes, T.J.R., and K. Garikipati, 2004. On the continuous/discontinuous Galerkin(CDG) formulation of Poisson-Kirkhoff plate theory, *Computational mechanics-Theory and practice*

Development of simplified discrete limit analysis for three-dimensional slope stability problem

Eisaku HAMASAKI
Advantechnology Co.,Ltd. Sendai , Japan
Norio TAKEUCHI
Department of Art and Technology, Hosei Univ., Tokyo, Japan.
Yuzo OHNISHI
Department of Urban and Environmental Engineering, Kyoto Univ., Kyoto, Japan.

ABSTRACT: In this study, a new simplified discrete limit analysis technique for a three-dimensional slope stability problem is proposed, using divided columns which are three-dimensional elements of RBSM (Rigid Body Spring Model). This approach is easy to use such as the slice method currently used in the conventional slope stability analysis and it helps to develop a very effective slope protection work plan taking into account displacement of each column. In this model, a sliding surface consists of squares, since a column is square. Then, the concept of the isoparametric element is introduced to define this surface. Using this model to analyze a three-dimensional slope stability problem, we showed that the safety factor of a landslide is calculated, and it can predict a movement of the whole body of the slope from combination of displacement direction of each column.

1. INTRODUCTION

When we review the recent improvements in the analytical ability of computers, it is certain that the three-dimensional stability analysis of landslides at the level of the limit equilibrium method is not a special analysis but that is now quite common [1]. And, the frequency of utilizing the three-dimensional limit equilibrium method, based on slope analysis that assumes that slip surfaces is known is still quite high, compared with three-dimensional numerical analyses, such as the finite element method. For the slope stability analysis, the three-dimensional finite element analysis requires expertise in setting boundary conditions, specifying physical properties, and it is difficult to interpret results in many cases, so the use of such method is still limited to special cases, when taking the costs and time for analysis into consideration.

Meanwhile, when an engineer performs three-dimensional stable analysis of a slope, they adopt Hovland's method[2], which is an extension model of two-dimensional Fellenius' method. Hovland's method assumes that the inter-column forces are zero, like the two-dimensional Fellenius' method assumes that the resultant of the internal forces acting on the slice side is parallel with the slip surface (it is ignored, in a strict sense). Therefore, as pointed out by Ugai[3] and Enokida et al[4], Hovland's method finds it difficult to taking into account three-dimensional geometric effects such as lateral constraint.

In order to consider three-dimensional geometric effects, Ugai et al. expanded the two-dimensional Janbu's method, Bishop's method, or Spencer's method to the three-dimensional one and assumed that there is a resultant of internal forces acting on the lateral side of column in the direction toward the point of action, to propose an analysis method, etc. [5].

However, their method also needs to make assumptions regarding the point of action of and the direction of the resultant between lateral sides of column, and in the case of three dimensions, a movement direction is set in only one direction on the horizontal plane to obtain the safety factor. If the movement direction is not determined, it is necessary to obtain the safety factor of the slope by calculating the safety factor for each possible movement direction and seeking the direction of the minimum safety factor [4].

But, when seeing the displacement directions of observation posts and GPS devices traced in most landslide sites, for example, the landslide in Washiodake [6], it was often observed that the moving body in a landslide does not move only in one direction. On the other hand, the limit equilibrium model assumes that the hypothetical slide directions of the entire slope are in one direction, to calculate the safety factor, and so, however little there may be, we still do fined gaps within actual conditions.

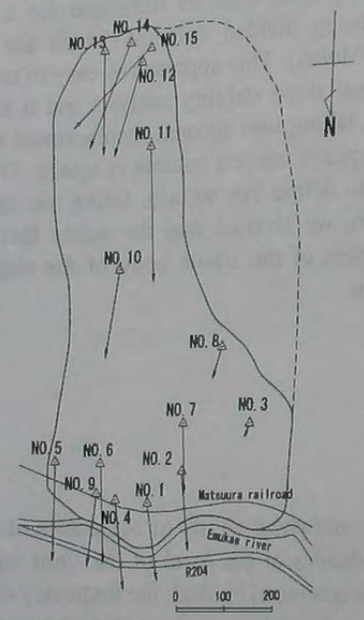


Fig. 1 Movement direction of observation posts in Washiodake landslide area (Kinoshita,2001) [6]

In order to solve such problems, the authors adopted the RBSM (Rigid Body-Spring Model), which obtains a discretization equation using the energy stored between elements[7]. RBSM has been developed as a computational model generalizing limit analysis in plasticity. In this model structures or solids are idealized as a set of rigid elements interconnected by two types of spring systems, one of which resists the dilatational deformation, the other, the shearing deformation. Thus, RBSM is extremely useful for fracture analysis of rock or concrete cracking, which can be regarded as a well-known discrete crack model.

According to this method, by introducing lateral springs that applied the penalty function between the lateral sides of columns, which underwent mesh division on the horizontal plane, it becomes possible to produce a mechanism in which force is transmitted with the displacement of columns, and then it is possible to calculate the safety factor of the slope from the surface force on the slip surface[8].

The input data used in this method is the same as that for the conventional limit equilibrium method, that is, the unit weight (γt), the cohesion (C), and the internal friction angle (ϕ) of the moving body, and pore water pressure (U). Namely, it becomes possible to obtain the

displacement of each column with easy condition-setting, and also to clearly reflect the three-dimensional geometrical effects, especially the lateral constraint condition.

This paper describes the theory and formulation of this method, and with simple model analysis, we show that these three-dimensional stable analyses can consider a restriction effect of landslide's side. And, according to this method, the configuration of a landslide's slip surface is consists of quadrangular, so, we propose a technique of modeling with isoparametric elements.

2. MODEL DEVELOPMENT

2.1. Modeling based on RBSM

In slice methods such as those in Hovland's method, the three-dimensional slope is represented by the aggregate of columns (square poles) standing on the X-Y plane, as illustrated in Fig. 2, and the safety factor of each column on the sliding surface is calculated by the limit equilibrium method.

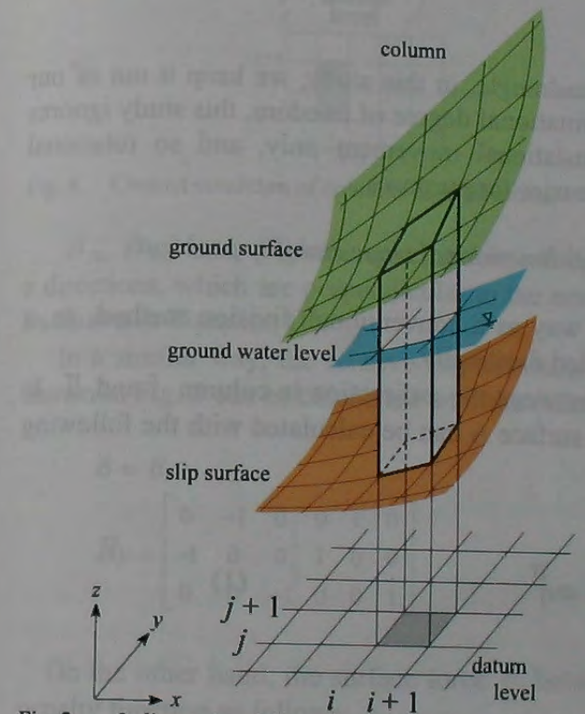


Fig. 2 3-dimensional discretization of sliding body by using columns.

When a discrete limit analysis is conducted under the assumption that these columns are three-dimensional elements of RBSM, the surface force on the sliding surface can be calculated, and the safety factor is calculated from this. The objective of this study is to carry out an analysis easily like a slice method, and a column is defined as an element in RBSM, and the degree of freedom is 3 directions —x, y, and z — to be shown in Fig. 3.

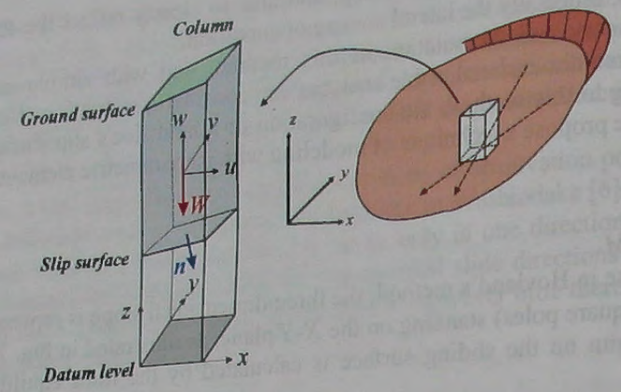


Fig.3 Degree of freedom for column

When we cannot constitute slip surface in a quadrangle, in this study, we keep it out of our calculation. Although generally RBSM considers rotational degree of freedom, this study ignores the deformation of columns and treats the translational movement only, and so rotational displacement is not considered in order to make it easier for purposes.

2.2. Formulation for Simplifying Analysis of three-dimensional slope stability problem

(i) Lateral sides of columns

In this study, columuns are made in the same way as a conventional division method, so, a calculation of stiffness matrix by RBSM is simplified drastically.

Fig. 4 shows the adjacent element relationship between the x-direction in column Ⅰ and Ⅱ. In this case, the relative displacement on the contact surface A can be calculated with the following equations:

$$\delta = B_x u$$

$$\delta = \{\delta_n \ \delta_{sx} \ \delta_{sy}\}^T \quad u = \{ u_{\mathrm{I}} \ v_{\mathrm{I}} \ \omega_{\mathrm{I}} \mid u_{\mathrm{II}} \ v_{\mathrm{II}} \ \omega_{\mathrm{II}} \}^T \qquad (1)$$

$$B_x = \left[\begin{array}{ccc|ccc} -1 & 0 & 0 & 1 & 0 & 0 \\ 0 & -1 & 0 & 0 & 1 & 0 \\ 0 & 0 & -1 & 0 & 0 & 1 \end{array}\right]$$

Here, u represents the displacement vector, and u, v, ω depict the displacement components in the x, y, and z directions, respectively. The suffixes Ⅰ and Ⅱ correspond to the columns shown in Fig. 4.

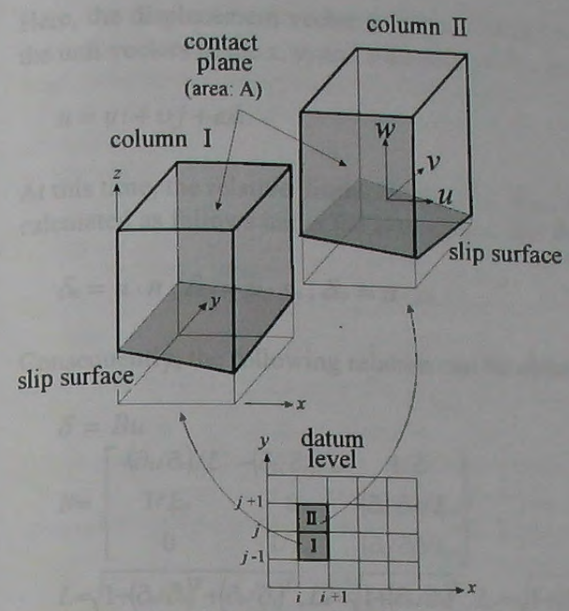


Fig. 4 Contact condition of columns in X-direction.

δ_n, δ_{sx}, and δ_{sy} represent the relative displacements in the normal direction, and the y and z directions, which are perpendicular to the normal direction on the contact surface, respectively, as shown in Equation (1).

In a similar way, the relative displacement δ for the adjacent element in the y direction as shown in Fig. 5 can be calculated with the following equation:

$$\delta = B_y u$$

$$B_y = \left[\begin{array}{ccc|ccc} 0 & -1 & 0 & 0 & 1 & 0 \\ -1 & 0 & 0 & 1 & 0 & 0 \\ 0 & 0 & -1 & 0 & 0 & 1 \end{array}\right] \qquad (2)$$

On the other hand, the surface force σ between columns at lateral sides is obtained using the penalty function as follows:

$$\sigma = D_{side}\delta$$

$$\sigma = \{\sigma_n \quad \tau_{sy} \quad \tau_{sy}\}^T \quad , \quad D_{side} = \left[\begin{array}{ccc} \lambda & 0 & 0 \\ 0 & \lambda & 0 \\ 0 & 0 & \lambda \end{array}\right] \qquad (3)$$

Here, σ_n represents the surface force in the vertical direction per unit area on the column's lateral side, and τ_{sx} and τ_{sy} depict the surface force in the shear directions.

Therefore, the energy stored on the columns at lateral side can be calculated by conducting integration on the contact surface A as follows:

$$V_{side} = 0.5 \cdot u^T \int_A B_x^T D_{side} B_x dAu + 0.5 \cdot u^T \int_A B_y^T D_{side} B_y dAu \qquad (4)$$

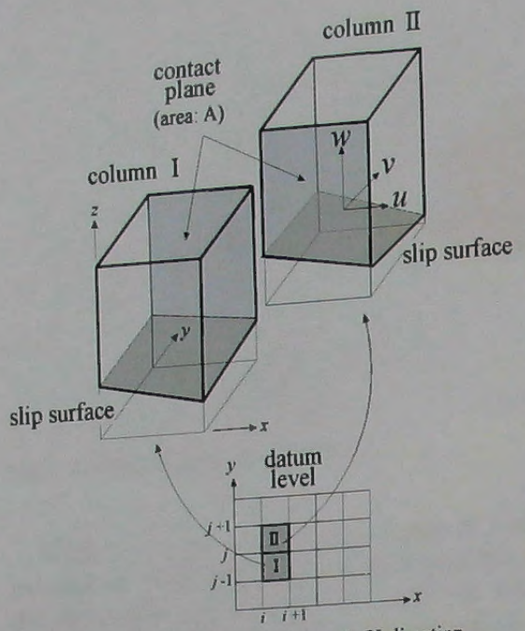


Fig. 5 Contact condition of columns in Y-direction.

(ii) Sliding Surface

As shown in Fig. 6, it is assumed that the sliding surfaee is given by the following equation:

$$z = z(x, y) \tag{5}$$

At this time, the normal vector can be expressed by the following equation:

$$n = \{-(\partial_z/\partial_x)\,i - (\partial_z/\partial_y)\,j + k\} \Big/ \sqrt{1+(\partial_z/\partial_x)^2+(\partial_z/\partial_y)^2} \tag{6}$$

The tangent vectors S_x and S_y in the x and y directions can be calculated in a similar way as follows:

$$S_x = \{\, i + (\partial_z/\partial_x)k\} \Big/ \sqrt{1+(\partial_z/\partial_x)^2}$$
$$S_y = \{\, j + (\partial_z/\partial_y)k\} \Big/ \sqrt{1+(\partial_z/\partial_y)^2} \tag{7}$$

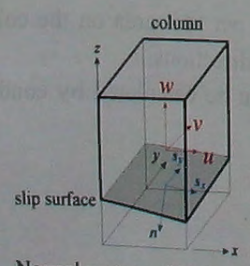


Fig.6 Normal vector and its direction at sliding surface

Here, the displacement vector u of the column can be expressed by the following equation with the unit vectors in the x, y, and z direections — i, j, and k.

$$u = ui + \upsilon j + \omega k \tag{8}$$

At this time, the relative displacement δ_n, δ_{sx}, and δ_{sy} on the sliding surface can be calculated as follows under the assumption that there is no movement of the bedrock.

$$\delta_n = u \cdot n\ ,\ \delta_{sx} = u \cdot s_x\ ,\ \delta_{sy} = u \cdot s_y \tag{9}$$

Consequently, the following relation can be obtained.

$$\delta = Bu$$
$$B = \begin{bmatrix} -(\partial_z/\partial_x)/L & -(\partial_z/\partial_y)/L & 1/L \\ 1/L_x & 0 & (\partial_z/\partial_x)/L_x \\ 0 & 1/L_y & (\partial_z/\partial_y)/L_y \end{bmatrix} \tag{10}$$
$$L = \sqrt{1+(\partial_z/\partial_x)^2+(\partial_z/\partial_y)^2}\ ,\ L_x = \sqrt{1+(\partial_z/\partial_x)^2}\ ,\ L_y = \sqrt{1+(\partial_z/\partial_y)^2}$$

When the relation between the relative displacement and surface force on the sliding surface is expressed as follows:

$$\sigma = \mathrm{D}\delta\ ,\ \mathrm{D} = \begin{bmatrix} \lambda_n & 0 & 0 \\ 0 & \lambda_{sx} & 0 \\ 0 & 0 & \lambda_{sy} \end{bmatrix} \tag{11}$$

the energy on the sliding surface (contact surface A) can be estimated with the following equation:

$$V_{slip} = 0.5 \cdot u^T \int_A B^T DB\, dAu \tag{12}$$

Here, D represents the matrix of the spring of the penalty (λ).
Therefore, the energy of the entire system becomes as follows:

$$V = V_{side} + V_{slip} \tag{13}$$

By deriving a discrete equation from this relation, it becomes possible to conduct a three-dimensional discrete analysis based on RBSM.

2.3. *Gradient of the Sliding Surface*

As mentioned in the previous section, the equation representing the sliding surface: $z = z(x, y)$ is defined using bilinear isoparametric quadrangle elements, and then the gradient of the sliding is calculated[9]. Fig. 7 shows one example of the shape function of this element, and there is the following relation between the natural coordinate system and the physical coordinate system.

$$\mathrm{x}(\xi,\eta) = \sum_{\alpha=1}^{4} \mathrm{N}\alpha(\xi,\eta)\mathrm{x}_\alpha\ ,\ \mathrm{y}(\xi,\eta) = \sum_{\alpha=1}^{4} \mathrm{N}_\alpha(\xi,\eta)\mathrm{y}_\alpha \tag{14}$$

Here, Nα represents the shape function. Since α is the quadrangle element, α is equal to 1 to 4. As for isoparametric elements, physical quantities are interpolated using the same shape function as coordinate transformation. Here, the z-coordinate is considered as the physical quantity, and an area is defined with the following equation:

$$z(x,y)=z(\,x(\xi,\eta),\,y(\xi,\eta)\,)=\sum_{\alpha=1}^{4}N_\alpha(\xi,\eta)z_\alpha \tag{15}$$

At this time, the gradient of the sliding surface can be expressed by the following equation:

$$\begin{Bmatrix}\partial z/\partial x\\ \partial z/\partial y\end{Bmatrix}=\begin{bmatrix}\partial\xi/\partial x & \partial\eta/\partial x\\ \partial\xi/\partial y & \partial\eta/\partial y\end{bmatrix}\begin{Bmatrix}\partial z/\partial\xi\\ \partial z/\partial\eta\end{Bmatrix}=J^{-1}\begin{Bmatrix}\partial z/\partial\xi\\ \partial z/\partial\eta\end{Bmatrix} \tag{16}$$

Here, J represents a Jacobian matrix. By substituting Equations (14)-(16) into Equation (7), it is possible to calculate the normal vector and gradient of the rectangular surface (Fig. 8). Therefore, the gradient of the sliding can be obtained for each integration point by means of numerical integration.

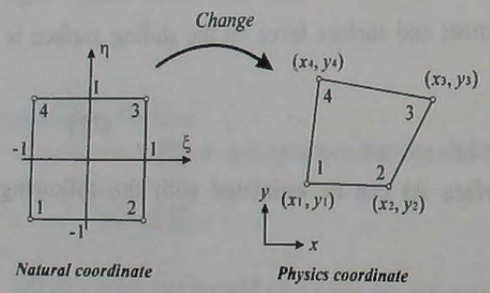


Fig.7 Isoparametric element for a quadrilateral area

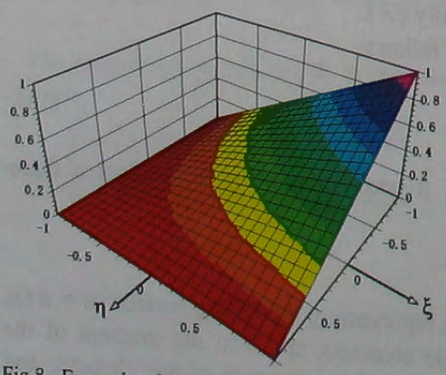


Fig.8 Example of shape function

In this study, an integration point is set at a central point, and the gradient at this central point is defined as the gradient of the sliding surface. In the natural coordinate system, the central point becomes (ξ, η) = (0, 0), and equal to the normal vector that is derived from the midpoint vectors in the x and y directions on the rectangular area.

Proceedings of International Mini-Symposium for Numerical Discontinuous Analyses, edited by T. Koyama, Hawaii, November, 2008

2.4. *Weight and Head Height of the Column*

By defining the intersection of the two lines that are drawn by connecting the weight and head height of the column, and the central point of the column's bottom on the x-y plane, that is, the midpoint of the diagonal line, as the representative point, the average of the height components are calculated.

Therefore, as for a square pole, the following equations are used as shown in Fig. 9.

- Altitude of the column's ground level (Ht)

$$Ht=(Zt_1+Zt_2+Zt_3+Zt_4)/4 \tag{17}$$

- Altitude of the column's groundwater level (Hw)

$$Hw=(Zw_1+Zw_2+Zw_3+Zw_4)/4 \tag{18}$$

- Altitude of the column's sliding surface (Hb)

$$Hb=(Zb_1+Zb_2+Zb_3+Zb_4)/4 \tag{19}$$

- Column's weight (W)

Assuming that the unit weight is(γt),

$$W=dx\cdot dy\cdot \gamma t(Ht-Hb) \tag{20}$$

- Head height of the column's center (U)

$$U=Hw-Hb \tag{21}$$

In this method, when adding the weight term to water pressure including pore water pressure, the body force acts on the sliding surface and the column's lateral side in the perpendicular direction to each surface at the head height. Accordingly, the surface force on the sliding surface is the outcome after summing up all acting forces including the pore water pressure.

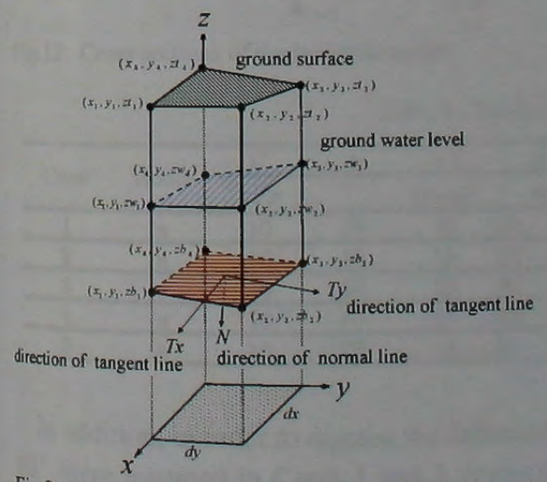


Fig.9 Coordinate to calculate weight of column and water head

2.5. *Entire Safety Factor*

When RBSM-based discrete analysis is conducted, the normal force (N) and tangent forces (Tx, Ty) on the sliding surface of each column is obtained. In this analysis, the safety factor is calculated from these surface forces with the following equation:

$$Fs = \Sigma\{\tan\phi \cdot N + C \cdot A\} / \sqrt{(\Sigma Tx)^2 + (\Sigma Ty)^2} \quad (22)$$
$$= R / D$$

Here, ϕ represents the internal friction angle of the sliding surface, C represents the cohesion, and A depicts the area of the sliding surface. In addition, the numerator R represents the shear strength resisting the sliding, and the denominator D depicts the resultant of the shear strengths on the sliding surface.

3. SENSITIVITY ANALYSIS OF LATERAL CONSTRAINT PRESSURE AND LANDSLIDE CONFIGURATION RATIO

In this section, the effects of constraint pressure are clarified utilizing this method. With regard to the landslide configuration and the safety factor, a model is developed based on the relationship between width (w) and thickness (d) (which is the ratio of "w/d" here) and an analysis is attempted. For comparison, the simplified three-dimensional Janbu's and Hovland's methods are also used for analysis.

3.1. Analysis Conditions

As analysis conditions, the two three-dimensional models (a) and (b) shown in Figs. 10 and 11 were prepared. In addition, Fig. 12 shows the cross sections of the models. Model (a) has a steep crest and a gentle foot like an ordinary landslide, not only its lateral sides, while Model (b) has a homogeneous slope that does not show any change in gradient from its crest to foot. Such a setting was conducted with the purpose of describing clearly the lateral constraint. Here, it was assumed that the gradient of the homogeneous slope is $\tan\theta = 0.3$ ($\theta \fallingdotseq 16.7^\circ$), and Cases 1 to 5 in Table 1 were analyzed.

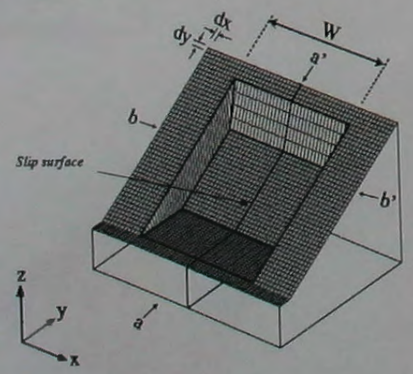


Fig.10 Schematic view of landslide model (model a)

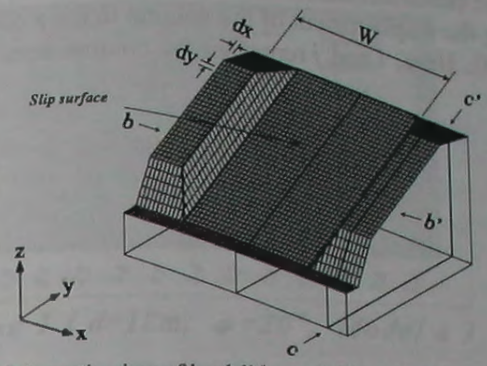


Fig.11 Schematic view of landslide model (model b)

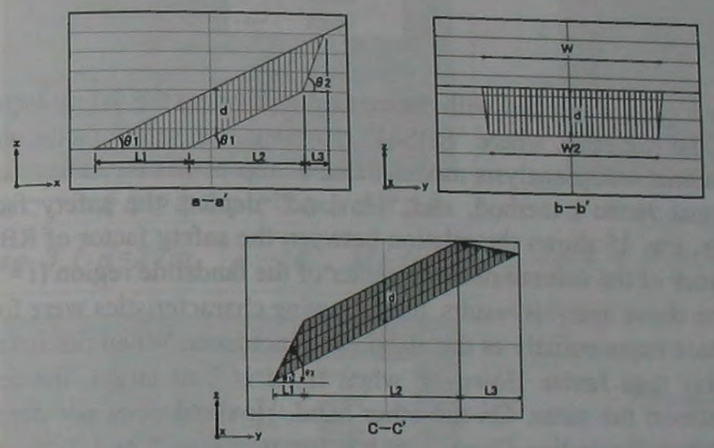


Fig.12 Cross sections of the landslide model

Table 1 Parameters used in calculation models

Case	Model	C	ϕ	γt	w	L1	L2	L3	d	$\tan\theta 1$	$\tan\theta 2$
		kPa	°	kN/m^3	m	m	m	m	m		
1	a	10	20	18	20 - 130	40	50	10	12	0.3	1.5
2	a	10	10	18	20 - 130	40	50	10	12	0.3	1.5
3	a	10	10	18	20 - 190	90	100	11.25	27	0.3	1.5
4	a	10	10	18	40 - 520	180	210	45	54	0.3	1.5
5	b	10	20	18	30 - 120	12.5	75	25	10	0.3	1.9

In addition, in order to discuss the difference in the internal friction angle ϕ, $\phi = 20^\circ$ and $\phi = 10^\circ$ were assumed in Cases 1 and 2, respectively, where the same analysis model was used for Cases 1 and 2. Moreover, the three models of landslide thickness of 12 m, 27 m, and 54 m were used for Cases 2, 3, and 4, respectively for the sensitivity analysis with respect to the landslide thickness (d).

In Cases 1, 2, and 5, it was assumed that the grid widths "dx" and "dy" are both 2.5 m, and in Case 3, the grid width was 5.0 m, and in Case 4, it was 10.0 m. The "$W2$" of the bottom surface of the sliding surface shown in Fig. 12 was calculated with the equation: $W2 = W - 2 \cdot dx$. Moreover, to directly grasp the constraint condition of this method, the work of the column

located at $(i, j) = (29, 22)$, in the right side of the center of landslide of Model (b), Case 5, per m^2 in the x direction, was calculated by multiplying the displacement of the column in the x direction and the surface force in the x direction (Fig. 13). Here, i and j represent the column numbers in the x and y directions, respectively.

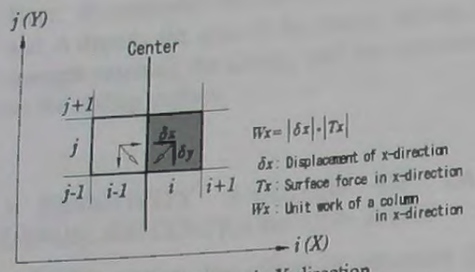
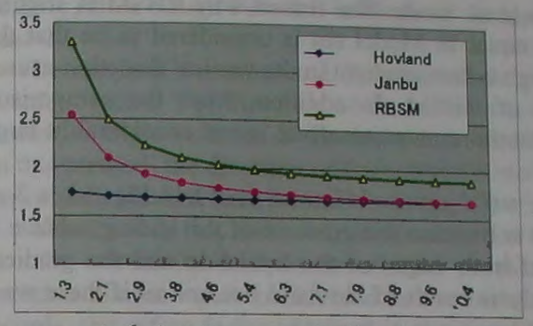


Fig.13 Unit work of column in X-direction

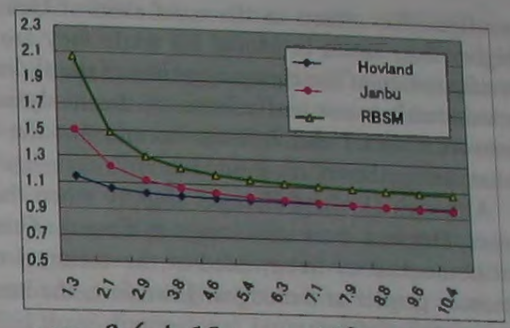
3.2. *Analysis Results*

In Fig. 14, the results of each case are plotted with the vertical axis being the safety factor (Fs) and the horizontal axis being the w/d ratio, where "RBSM" represents the safety factor obtained in the simplified three-dimensional safety analysis model, "Janbu" represents the safety factor in the simplified three-dimensional Janbu's method, and "Hovland" depicts the safety factor in Hovland's method. In addition, Fig. 15 shows the relation between the safety factor of RBSM of Case 5 of Model (b) and the work of the column near the center of the landslide region ($i = 29, j =$ 22) in the x direction. From the above analysis results, the following characteristics were found:

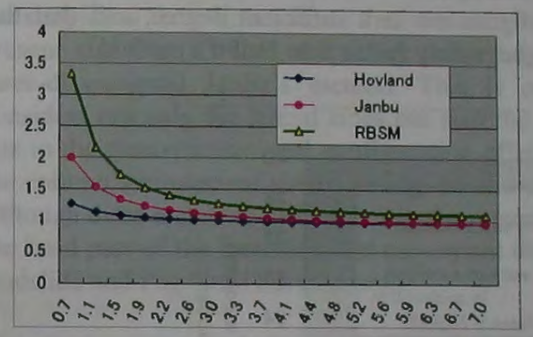
1) RBSM and Janbu decrease exponentially as the w/d ratio increases. When the w/d ratio is small, RBSM is higher than Janbu. However, when w/d is 2 or larger, the decrease behaviors of both are almost the same. On the other hand, Hovland does not depend on w/d and is nearly constant, excluding Cases 2 and 3, but in Cases 2 and 3, the rate of change of Hovland is small compared with Janbu and RBSM.
2) In Model (b), which has no effects of edge configurations such as foot and crest, there are no differences in safety factor between this method and the simplified three-dimensional Janbu's method. On the other hand, in Model (a), the safety factor in this method tends to be higher (constraint effect is stronger) than that in the simplified three-dimensional Janbu's method.
3) From the comparison between Cases 1 and 2, it was found that RBSM and Janbu become higher as ϕ increases and they decrease in the same way as the w/d ratio increase. When Cases 1, 3, and 4, whose ϕ are the same and whose d are different from one another, are compared, the change in safety factor at a small w/d becomes smaller as d is thicker, but there are no significant differences among Cases, and $w/d = 7$~10, and the safety factor is constant.
4) In Model (a), when the w/d ratio exceeds 7~10, Hovland and Janbu become almost the same. In addition, in Model (b), Janbu and RBSM are nearly equal to each other.



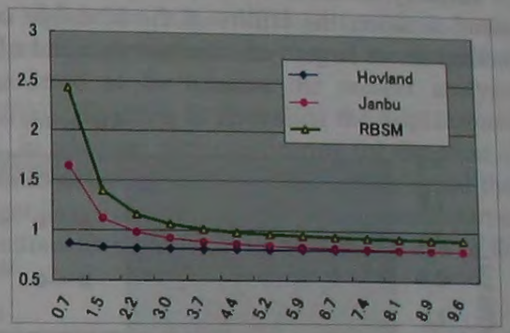
case 1 (d=12m, φ=20°, Model a)



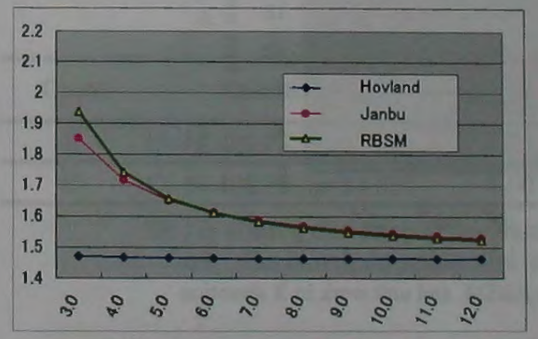
case 2 (d=12m, φ=10°, Model a)



case 3 (d=27m, φ=10°, Model a)



case 4 (d=54m, φ=10°, Model a)



case 5 (d=10m, φ=20°, Model b)

Horizontal axis : Ratio of W/d

Vertical axis : Safety factor (Fs)

Fig.14 Relations between safety factors by various methods with ratio of width (w) and thickness (d) of landslide

3.3. *Discussion of Constraint Condition Analysis*

With regard to discussions on the configuration, scale, and stability of landslides, there is an old report by Watari et al. [10], and Ueno also focused on the relation between the landslide's maximum width (W) and the depth of the sliding surface (D) at a landslide site he investigated, calculated the cross dimensional ratio "W/D" with a simplified equation, demonstrated that the safety factor becomes almost constant when W/D is 10 or larger, and provided a logical explanation for the result that $W/D = 3.0$~10.7, which was obtained at the site he studied [11].

Also in the analysis of this study, RBSM and Janbu become constant suddenly when the w/d ratio exceeds 7~10. In addition, the fact that the work in the x direction, which is shown in Fig. 15, becomes almost zero when the w/d ratio exceeds 11 demonstrates that the same

configuration effects as the w/d ratio of Ueno et al. work. The reason why RBSM is slightly higher than Janbu in Model (a) while they are equal in Model (b) is considered to be that the configuration of the changing points of the sliding surface gradient in the vertical direction causes considerable constraint effects in the analysis of RBSM. In addition, from the comparison between Cases 1 and 2, it can be said that the lateral constraint effect is not considerably large when seeing the w/d ratio.

Although Hovland changes slightly when the w/d ratio of Cases 2 and 3 in Fig. 14 is 3 or lower, Hovland does not change in Case 5. This is because the gradient of the sliding surface is not homogeneous but twisted at the columns of both edges of the landslide and the gradient becomes gentler at the edges. Therefore, the analysis result of Hovland became as if there were the constraint effects.

Anyway, it was found that this analysis, in which the limit discretization method of RBSM is used, considers the effects of the landslide configuration to a sufficient degree, and that this method shows larger vertical constraints and a higher safety factor than Janbu's method.

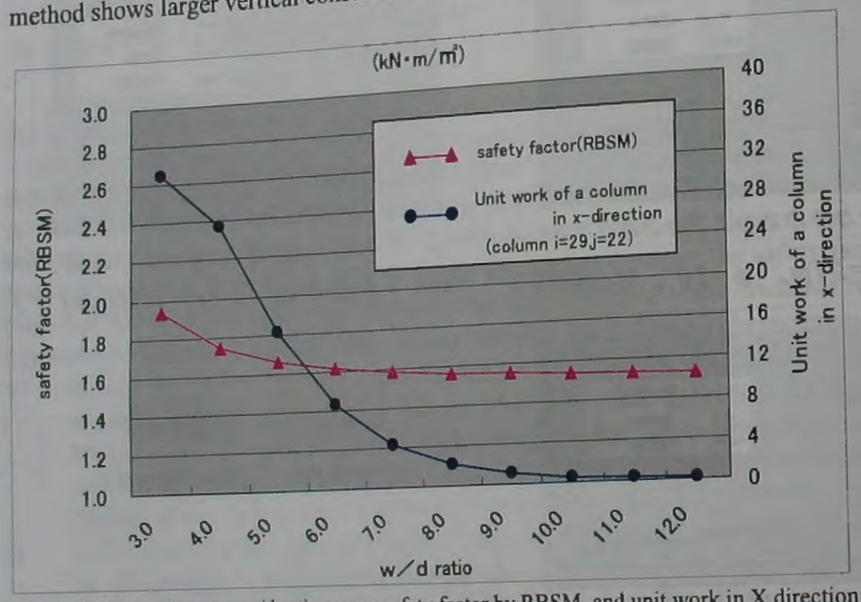


Fig.15 Relations between w/d ratio versus safety factor by RBSM and unit work in X direction

4. ANLYSIS CASES

As mentioned in the previous section, it is a fact that the landslide movement direction varies on the surface of the moving body, according to the observation of moving pegs.

In the reports of Kinoshita[6] and Rou [12], the landslide of Washio-dake shown in Fig. 1 shows the three-dimensional topology and sliding surface, and so the stability analysis with this method was attempted based on them. The location of groundwater was estimated three-dimensionally based on the high water[12] and the flow distribution map[6]. In addition, considering that there exists basalt above an altitude of 210 m, the landslide moving body has a two-layered structure: layers of basalt and of other substances. Then, it was assumed that the unit weight of the soil mass of the former (rt) is 27 kN/m^3 and that of the latter is 26 kN/m^3. With regard to cohesion (C) and internal friction angle (ϕ), it was assumed that C = 16.4 kPa and ϕ= 21.7° , which are the results of the ring shear test, in Case 1, and that C = 16.4 kPa and ϕ= 11.35° , from which Fs = 1.0 is obtained via the back calculation with this method (RBSM), in Case 2.

Proceedings of International Mini-Symposium for Numerical Discontinuous Analyses, edited by T. Koyama, Hawaii, November, 2008

The Hovland's method and the simplified three-dimensional Janbu's method were compared in safety factor. The direction of the minimum safety factor in each method was defined as the clockwise angle from the downward y axis. The results are shown in Table 2. As for Case 2 based on this method, the direction of the column's movement (solid line) and the maximum gradient of the column (dashed line) are shown in Fig. 16.

Table 2 states that the safety factor obtained in the present method indicates tbe highest value like the sensitivity analysis mentioned previously. However, in the previous section, Janbu becomes almost equal to Hovland as the w/d ratio becomes higher, but according to research records, the safety factor obtained in the simplified three-dimensional Janbu's method is higher. This is endorsed by the study of the collapse of Ontake by Ugai [3] in which the safety factor in the simplified three-dimensional Janbu's method is higher than that in Hovland's method. In the present analysis (RBSM), the safety factor becomes further higher than that in the simplified three-dimensional Janbu's method. This is considered to be because the present analysis considers not only the lateral sides but also the vertical direction in discussing the displacement due to the three-dimensional configuration effects. In addition, when comparing the direction of the column's movement shown in Fig. 16 and the moving pegs shown in Fig. 1, it is found that although there are some differences in the movement direction at the east edge and central part of the head part of the landslide, the movement directions from the western edge to the end of the landslide and Peg No. 11 are the same.

Table 2 Comparison for safety factors and movement directions between RBSM, Janbu method and Hovland method at Washiodake area

Case	Condition	Safety factor (Three dimensions method)		
		RBSM	Janbu's method	Hovland's method
①	C=16.40kPa, φ=21.70°	1.88	1.66 (3°)	1.53 (10°)
②	C=16.40kPa, φ=11.35°	1.00	0.89 (3°)	0.83 (10°)

※( ) is sliding direction of minimum safety factor.
And, 0°is North direction and proceeds around watch.

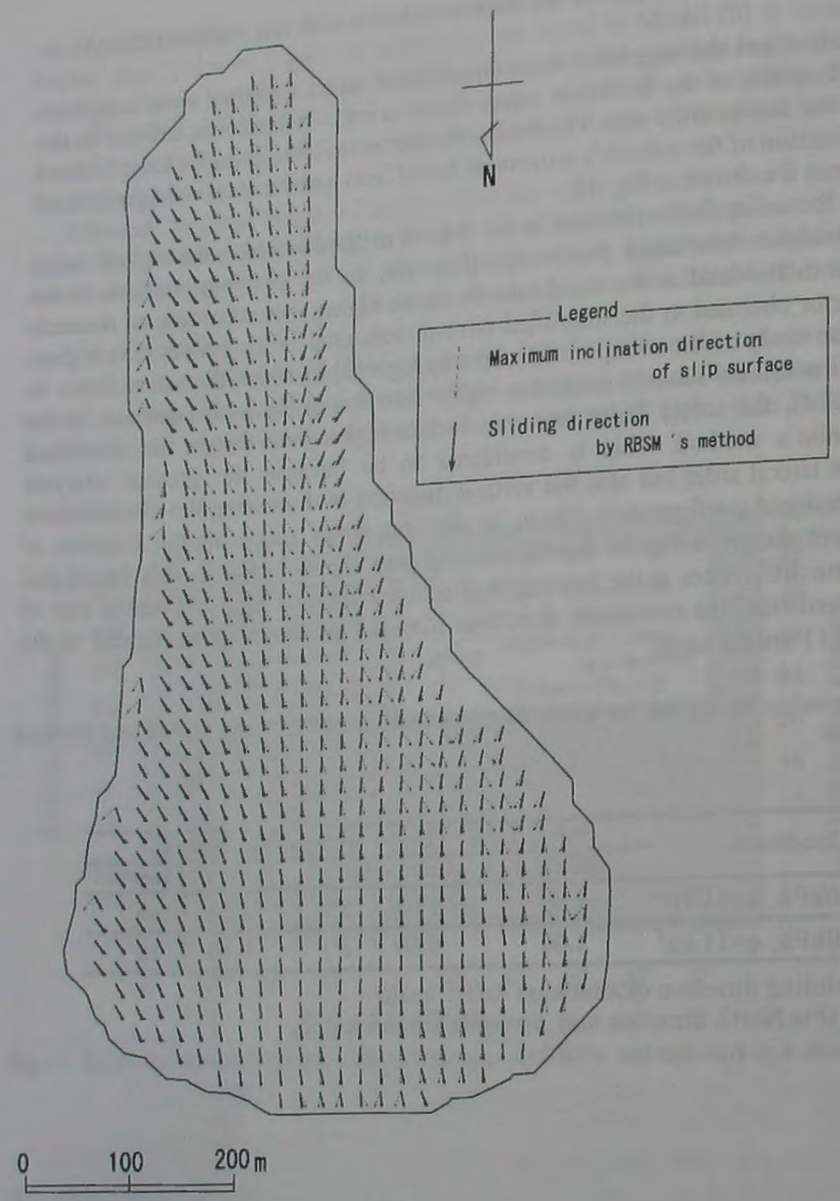


Fig.16 Comparison of calculated movement direction of column and maximum inclination direction using by RBSM.

5. CONCLUSION

The proposed method is based on the discretization limit analysis method similar to RBSM, and differs from the conventional Hovland's method and simplified three-dimensional Janbu's method.

1) With this method, it is possible to obtain a safety factor taking into account each column's displacement.
2) In addition, the three-dimensional configuration effects could not be described by Hovland's method, but the present method induces the lateral constraint like the simplified three-dimensional Janbu's method and higher constraints in the direction of the sliding surface than the simplified three-dimensional Janbu's method. And therefore the safety factor becomes higher as a whole.
3) Anyway, the present analysis method can conduct comparison with the movement directions, according to the analysis of the case of the landslide at Washio-dake, and it can be found from such data that the present method is one of the clues to judging the stability of the sliding surface structure.

When the deformation analysis of a slope is conducted, it is necessary to further segment the column, considering strata and groundwater surface, etc. and input parameters describing the ground properties such as deformation coefficients. However, the present method is almost the same as the conventional limit equilibrium method in necessary parameters, assumed landslide structures, and analysis time, and so the easiness in carrying out analysis is retained.

REFERENCES

1. Takatoshi Kimura, Kouji Kawaba. 2000. On the Preventive Construction Method Plan based on Three-Dimensional Stability Analysis, the Lecture Record of the 39th Conference of the Japan Landslide Society, pp. 253-256
2. Hovland, H. J., Asce, M. 1977. Three-Dimensional Slope Stability Analysis Method, Journal of the Geotehnical Engineering Division, pp. 971-986
3. Keizou Ugai. 1988. Discussion of the Three-Dimensional Stability of Slopes with the Decomposition Method, Soil and Fundamentals, Vol. 36, No. 5, pp. 19-24
4. Mitsuya Enokida. 2003. Discussion on Lateral Wall Effects and Movement Directions Using the Simplified Three-Dimensional Janbu Method, the Lecture Record of the 42nd Conference of the Japan Landslide Society, pp. 177-180
5. Keizou Ugai, Kenji Hosomizo. 1988. Three-Dimensional Extension of the Simplified Bishop Method, the Simplified Janbu Method, and the Spencer Method, the Journals of the Japan Society of Civil Engineers, Issue No. 394/Ⅲ-9, pp. 21-26
6. Shinitsu Kinoshita, Hizuki Tanaka, Tetsuya Sakai, Hiroyuki Yoshimatsu. 2001. Three-Dimensional FEM Analysis Case of Deep Pegs at Landslide Sites, Landslide, Vol. 38, No. 3, pp. 268-275
7. Norio Takeuchi. 1991. Discretization Limit Analysis in Ground Mechanics, Baifuukan, pp. 1-204
8. Norio Takeuchi, Eisaku Hamasaki, Morito Kusabuka. 2003. Simplified Slope tability Analysis Using Finite Elements, Transactions of the Japan Society for Computational Engineering and Science, Vol. 8, No. 2, pp. 567-570
9. Eisaku Hamasaki, Norio Takeuchi, Morito Kusabuka. 2003. Three-Dimensional Slope Stability Analysis Approximating the Sliding Surface with Finite Elements, the Lecture Record of the 38th Conference of the Japan Landslide Society, pp. 3-4
10. Masasuke Watari, Hiroyuki Nakamura, Osamu Itagaki. 1975. Statistics of the Actual Conditions of Landslides (Part 1), Reference from Public Works Research Institute, pp. 6-34
11. Masashi Ueno. 2001. Discussion of Topographic and Geological Factors in Constraining the Configurations and Scale of Landslide, Landslide, Vol. 38, No. 2, pp. 1-10

Proceedings of International Mini-Symposium for Numerical Discontinuous Analyses, edited by T. Koyama, Hawaii, November, 2008

12. Yu-Hua Lang, Hirohuki Nakamura. 2003. Three-Dimensional Stability Analysis of a Landslide at Washiodake and the Stress Distribution of Deep Pegs, the Lecture Record of the 42nd Conference of the Japan Landslide Society, pp. 317-320

A Simulation Analysis of Loading Test on Two-layer Brickwork Arch Model by RBSM

Okano, N.
Railway Technical Research Institute, Kokubunji-shi, Tokyo Metropolitan, Japan
Shigeta, Y.
Dia Consultants Co.,Ltd, Saitama-shi, Saitama pref., Japan
Matsunaga, T.
Pacific Consultants Co LTD., Shinjuku-ku, Tokyo Metropolitan, Japan
Yasui, K.
Daitetsu Kogyo Co LTD., Osaka-shi, Osaka Pref., Japan
Asakura, T.
Kyoto University, Kyoto-shi, Kyoto Pref., Japan

ABSTRACT: It is necessary to estimate the strength of masonry tunnels in order to maintain these tunnels or assess the influence of adjacent construction work, etc. However, the methods of estimation have not been established yet. We performed two-dimensional tunnel lining tests for brickwork lining tunnels by using a part of arch of 1/2-scale tunnel lining model loading device to examine the mechanical characteristics of their linings. Then we simulated the test by the rigid body spring model. As a result, it was concluded as follows.

(i) We can fit the relationship between load and vertical displacement at the crown as follow conditions.
(ii) If boundary condition of edge in horizontal direction changes, situation of cracks and slope of load-displacement curve change.
(iii) Tensile strength of joint material hardly affects the load-displacement curve.

1. INTRODUCTION

Many Japanese railway operators, especially Japan Railway Group (JR group) have a number of masonry lining tunnels consisting of stones, bricks and/or concrete blocks, and joint materials.

It is necessary to understand the structural strength and the mechanical characteristics for evaluation of reinforcement design and the influence of adjacent construction work of tunnels, but the technique for quantitative estimation is not established.

In order to understand them, loading tests by 1/2-scale two-layer brickwork arch model and simulation analysis by the rigid body spring model (RBSM) were carried out, then the results of a loading test and a simulation analysis were discussed in this paper.

2. MODEL TEST

2.1. Test method

This test is conducted by using a 1/2-scale two-layer brickwork arch model of the direct load system to simulate an arch part of single-tracked section. The test unit is shown in Fig. 1.

A two-dimension brick lining model of one ring, which is not restrained in the tunnel axial direction, is made by stacking 68 bricks (the lower layer: 33 bricks, the upper layer: 35 bricks) one by one applying joint materials toward the crown from the leg. The joint material is mortar.

The physical property values of bricks, joint materials are shown in Table 1. It is carried out by the load control based on deformation of the loading plate. The loading direction is vertical, or position in Fig. 1.

2.2. Result of the test

(i) Relationship between load and vertical displacement at the crown

The relationship between load and vertical displacement at the crown is shown in Fig. 4 with results of simulation analysis. The load-deformation curve was almost linear at the initial stage before first crack was generated at the joint between the inner layer and the outer layer. The maximum load was 94kN at the crown displacement of 4.9mm before the second crack generated between the inner layer and the outer layer.

(ii) Situation of crack generation

A crack progress situation is shown in Fig. 3. First, tensile cracks generated on inner surface at the loading point. Second, tensile cracks generated between the inner layer and outer one. Final, compressive failure occurred near the loading point.

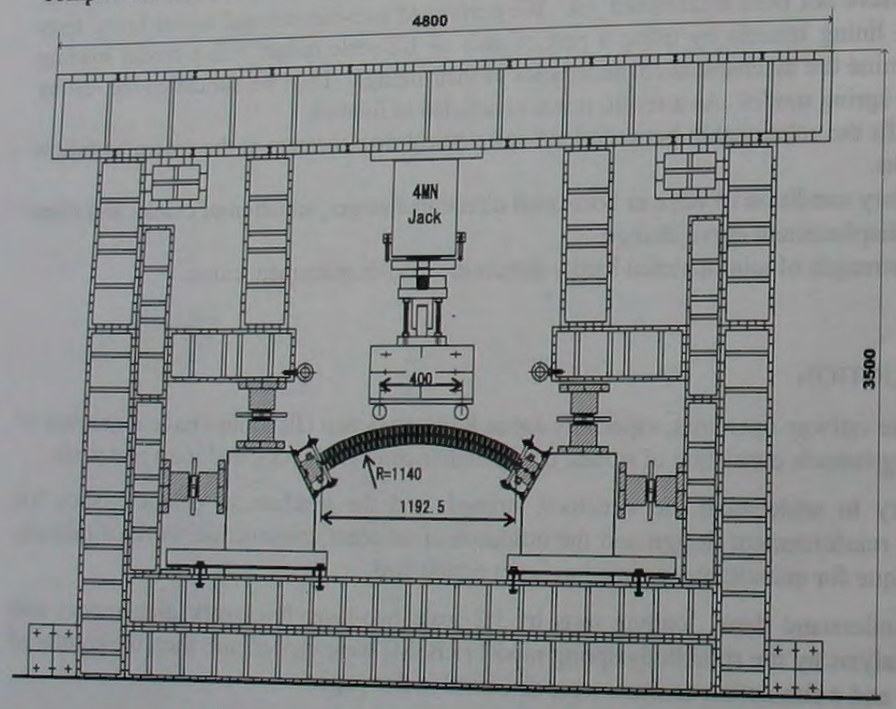
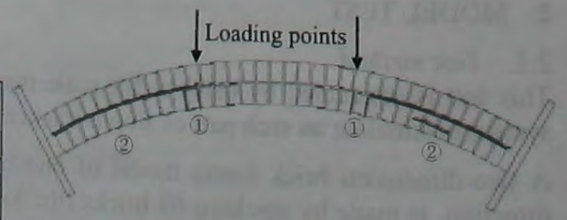


Fig. 1. Probability of failure of the sample wedge.

Table 1. Physical properties of brick and joint material

	Density (g/mm^3)	Compressive strength (N/mm^2)	Elastic modulus (N/mm^2)	Poisson's ratio	Tensile strength (N/mm^2)
Brick	1.85	17.6	5,130	0.112	1.16
Joint material	1.93	7.9	7,800	0.206	1.69



3. SIMULATION ANALYSIS OF THE TEST

3.1. Analysis condition

We used RBSM[1)] for simulation analysis of the test. The analysis model is shown in Fig. 2. The input property data are shown in Table 3.

Physical properties of brick from the material test results were applied to the Young's modulus and the Poisson's ratio. One of joint material was applied to tensile strength because bending tensile cracks generated at the part of joint material. The parameters are boundary conditions of both edges in the horizontal direction and tensile strength of joint material. Loading to the model was applied the obtained data on the test.

We performed 3 cases in change of boundary condition of both edges. The analysis cases are shown in Table. 2.

3.2. Result of the analysis

(i) Relationship between load and vertical displacement at the crown

Relationship between load and vertical displacement at the crown on the test is shown in Fig. 4. But case 2 was excepting from this figure because the load was very small. Case 1 fit the test result relatively. Slopes of the other cases are smaller than Case 1.

(ii) Situation of crack generation

No cracks occurred in Case 1 and 3. In Case 2, bending tensile cracks gradually generated with the increase of load, but cracks between layers did not occur. (See Fig. 4.) In Case 4, bending tensile cracks generated right under the loading point. In Case 5, first, bending tensile cracks generated right under the loading point, and then crack between layer generated between the loading points.

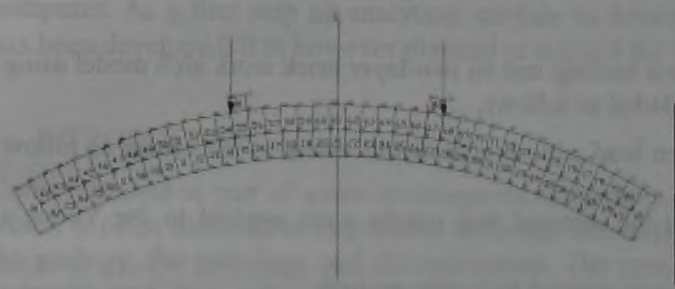


Fig. 3. Analysis model

Table 3. Input properties data

Elastic modulus	5,130 (N/mm^2)
Poisson's ratio	0.112
Compressive strength	7.9 (N/mm^2)
Tensile strength	1.69. (N/mm2)
Cohesion	500 (N/mm2)
Angle of internal friction	0 (°)

Table 2. Analysis cases

Case No.	Boundary condition of both of edges in the horizontal direction	Tensile strength of joint material
1	Both of sides: Fix	Material test result
2	One side: Fix. The other side: Free	Material test result
3	One side: Fix. The other side: Horizontal displacement on the test	Material test result
4	One side: Fix The other side: Horizontal displacement on the test x 5	Material test result
5	One side: Fix the other side: Horizontal displacement on the test x 5	Material test result / 5

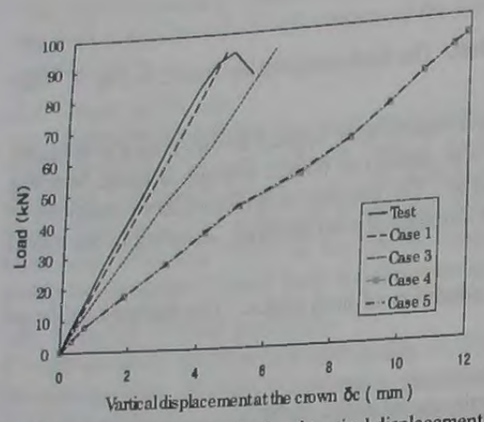


Fig. 4. Relationship between load and vertical displacement at the crown

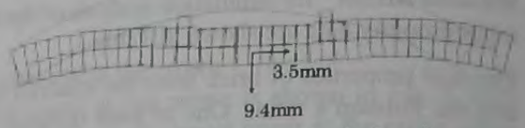


Fig. 5. Situation of crack generation in Case 2

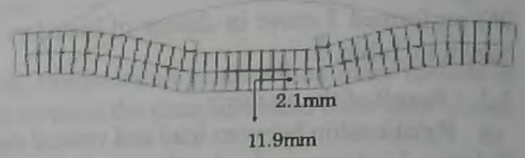


Fig. 6. Situation of crack generation in Case 5

(iii) Considerations

Case 1 fitted the test result on relationship between load and vertical displacement at the crown relatively, but no cracks occurred. If fivefold horizontal displacement at the edge and one fifth of joint material tensile strength were applied, bending tensile cracks and crack between two layers generated. However, the location of a crack between two layers did not fit.

4. CONCLUSION

In this examination, we tried to simulate a loading test on two-layer brick work arch model using RBSM analysis. As a result, it was concluded as follows.

(iv) We can fit the relationship between load and vertical displacement at the crown as follow conditions.

- Physical properties of brick from the material test results were applied to the Young's modulus and the Poisson's ratio.
- Physical property of joint material was applied to tensile strength.
- Boundary condition of both edges was fixed in horizontal direction.

(v) If boundary condition of edge in horizontal direction changes, situation of cracks and slope of load-displacement curve change.

(vi) Tensile strength of joint material hardly affects the load – displacement curve.

However, the situation of cracks generation did not fit. We think that the causes are a problem of mesh division or input property data, and so on. We will continue examinations on simulation of structures consist of bricks and joint material.

REFERENCES

1. Kawai, T. 1977. New element models in discrete structural analysis. *J. of the society of Naval architects of Japan.* No.141, pp.187-193, 1977.

Proceedings of International Mini-Symposium for Numerical Discontinuous Analyses, edited by T. Koyama, Hawaii, November, 2008

Three-dimensional core picture system

Takumi NAKAI
Earthtech Toyo Corporation, Japan
Kenichi ANDO and Patrick BRUINES
Obayashi corporation, Tokyo, Japan
Yuzo OHNISHI
Kyoto University, Japan

ABSTRACT: Core imaging is a standard item of a borehole investigation. For a long time, only simple two-dimensional pictures have been taken. As not all information is captured on these two-dimensional pictures the cores are usually stored for long periods of time in case a closer look at the cores is needed. The cost of keeping the cores can become high and the retrieving the wanted core section requires physical access to the cores and usually involves moving around heavy core cases. We therefore propose a methodology for constructing, storing, retrieving and analyzing high quality, three-dimensional core images on the computer. Already methods have been developed for obtaining 3D images of boring cores, however the cost of the equipment is high and technical problems arise when the quality of the core is low. The newly proposed methodology uses core pictures taken with a digital camera from several angles to develop the three-dimensional model. Nowadays even regular consumer level digital camera can capture images with a level of detail more than adequate for making a very detailed three-dimensional model. The newly proposed method consists of (1) taking digital pictures, (2) correcting for the distortion due to the camera and the curved nature of the core, (3) stitching the different photos together, (4) generation of a three-dimension model and (5) interpretation of the three-dimensional model. The resulting three-dimensional model is accessible at anytime on the computer. As a first step an analytical module to detect discontinuities on the computer screen has been developed. It is however planned to expand the analytical capabilities in the near future.

1. INTRODUCTION

Cores retrieved as part of a site investigation campaign contain a wealth of important information which is often difficult or impossible to obtain otherwise. The cores can give information about the geology, the petrology and discontinuities. The core samples can also be used for mechanic, hydraulic and chemical testing. With the advent of ever cheaper and higher resolution digital cameras it is common place to collect digital photographic evidence of the cores. Especially in cases when cores are subject to the deterioration due to for instance changes in water content, photos can be important to preserve a record of the petrography and geological structures as encountered in the cores.

Both the core and the discontinuities such as joints, bedding planes and faults are however three-dimensional features and a single picture of the cores, as is usually taken, therefore contains only limited information about the orientation of the discontinuities. In this paper we suggest a method to reconstruct the cores in three dimensions by using photogrammetry. The 360 degree core photo can then be used to determine the orientations of discontinuities and for comparison with borehole imagery obtained with other methods.

Section 2 describes the method for taking pictures. In section 3 the software package, ProBoring, that has been developed to generate the three-dimensional model is shown. In section 4 the determination of the orientation of discontinuities is shown. In section 4 the new method is applied to a real site and the results are compared with those of the more conventional methods.

Section 5 gives a short discussion about the results and points out the advantages and disadvantages of the new method. In the final section the improvements that we plan to make to the method in the near future as mentioned.

2. TAKING THE PICTURES

Right after the cores have been retrieved the pictures can be taken. Pictures are taken from four different directions as shown in the figures 1. Pictures are taken at an angle of 45 degrees from two different sides before being turned 180 degrees to repeat the procedure. This method assures that the handling of the core is minimal to prevent disturbing the sample too much which is especially important for weak rocks. For reasons of consistency a NIKON D80 camera with a fixed focal length lens (50mm) has been used, other cameras can however be used. At a distance of 1 meter and the usage of the 50mm lens, 50 cm sections can be photographed without too much distortion allowing them to be pasted lengthwise directly.

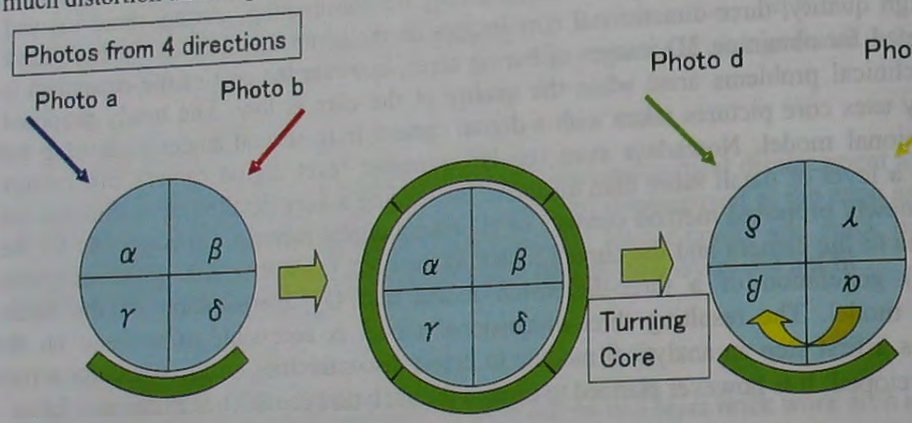


Figure 1 Schematic of procedures to take the four needed photographs

3. PROBORING SOFTWARE

To generate the three-dimensional model the ProBoring software has been developed. The basic treatment procedure comprises the following steps:

- open a picture taken from one direction
- crop the picture so that only the picture of the core remains
- correct for the distortion due to the curvature of the core
- crop again to a section slightly larger than a 90 degree section of the core
- repeat for pictures from the other directions
- stitch all pictures together
- wrap the picture around and display in three dimensions

The original pictures of the core include, except the core, also the fore- and the background (Figure 2). The program has the possibility to rotate and crop the picture so that only the core can be isolated.

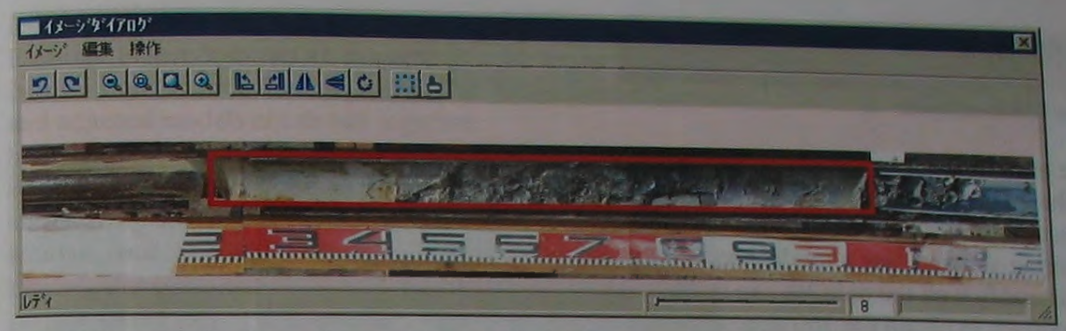


Figure 2 Example of a picture of a core as taken in the field

To correct for the distortion due to the curvature of the core, the program needs three measurements (figure 3). With the length of the core, the core diameter and the angle of the core section, the surface orthogonal to the surface of the core can be calculated.

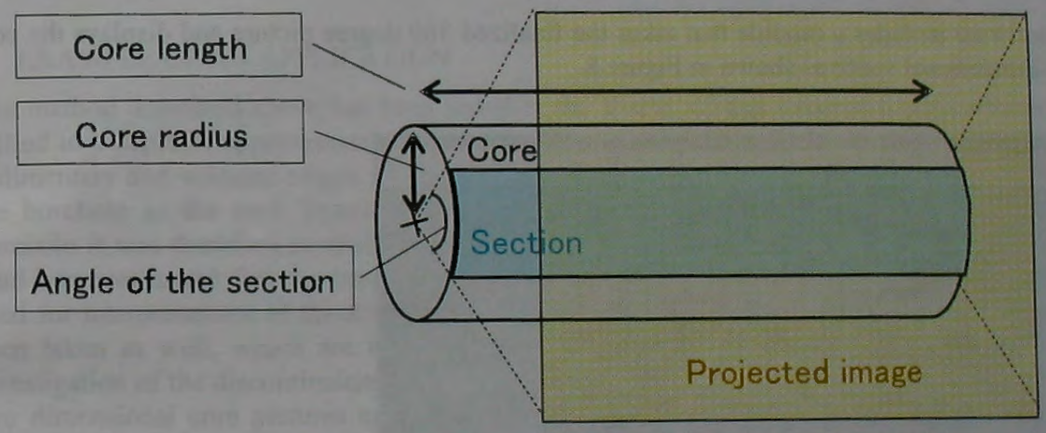


Figure 3 Geometric relations between core sections and photograph taken

Figure 4 shows the core picture after cropping with on the right side a representation of the curvature, where the distance between two lines represents a section of 20 degrees. Figure 5 shows the same model after correction for the curvature. The four pictures from four directions include a large amount of overlap. Especially the data on the edges is of poor quality and additional cropping to a section that represents slightly more than 90 degrees, as is shown in figure 6, will be helpful in the next step.



Figure 4 Core with background cropped



Figure 5 Core curvature corrected section



Figure 6 Sides cropped

Once all four pictures have been treated, cropped and stretched the four pictures can be stitched together. This is done by shifting the pictures over each other to obtain the best fit. As the photos are usually taken at the site, the lighting conditions might be variable. For this reason the ProBoring software has a module to lighten and darken specific sections. When all four pictures fit reasonably well the pictures can be pasted together (figure 7). Some additional cropping might be necessary to obtain the 360 degree model.



Figure 7 Stitched core picture

The software includes a module that takes the finalized 360 degree picture and displays the core three-dimensional space as shown in Figure 8.

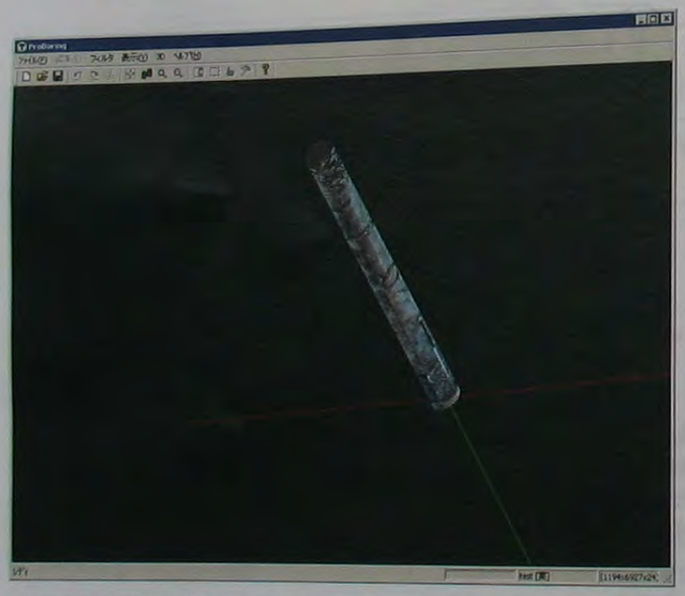


Figure 8 Three-dimensional model of photogrammetric data

When a core is drilled and retrieved it is usually not possible to determine how the core was orientated. Other information is therefore needed if the orientation of the discontinuities is to be determined. Orienting a core might be straightforward if the rock mass is a tilted sedimentary rock and the orientation of the layers is known. In other cases borehole televiewer (BHTV) data could be used. Although the resolution of the BHTV data is not as good as core photography, it might be possible to calibrate the core photography data using large discontinuities clearly visible in both.

The software includes a tool to calibrate all data. Known orientations can be indicated on the core picture with a little mark. The picture can than be "scrolled". Using this scroll method, a row or

Proceedings of International Mini-Symposium for Numerical Discontinuous Analyses, edited by T. Koyama,
Hawaii, November, 2008

column of pixels can be shifted from one side to the other until the marker reaches the required location. Figure 9 shows an example of a 90 degree shift using a marker as a reference resulting in a shift in the three-dimensional model. In the three-dimensional modeling window, the original and adjusted models are shown together.

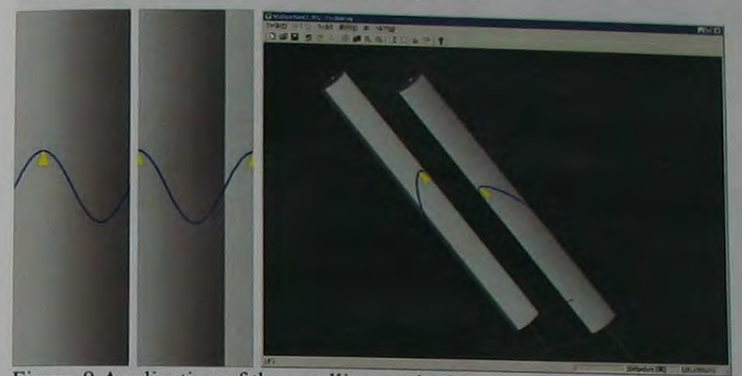


Figure 9 Application of the scrolling method

4. EXAMPLE OF AN APPLICATION

The method described above has been tested at the Y-site. At this location a borehole has been drilled to a depth of approximately 350 meter. The rock formations encountered were mainly of sedimentary and volcanic origin. During drilling problems were encountered with the stability of the borehole as the rock layers encountered were weaker than anticipated. To stabilize the borehole it was therefore neeessary to use drilling mud to prevent further cave-ins. The use of mud however meant that the borehole TV measurements (BTV) were unclear and could not be used for interpretations of the discontinuities. Borehole televiewer measurements (BHTV) have been taken as well, which are less sensitive to the presence of drilling mud. For a detailed investigation of the discontinuities both the two- and three-dimensional models can be used. The two dimensional core pictures are most appropriate for use in reports. As both the BTV and BHTV data collected at the Y-site are presented in this way, an example of a core photo interpretation will be given first. Figure 10 shows the core photo, the BTV and the BHTV models of the same section. The core photo model is not oriented; the center in the BTV model is oriented to the north whereas the center in the BHTV model is oriented to the south.

Having the three models next to each other clearly shows a number of points. The most detail can be found in the core photo model. However at those locations where the core is severely damaged such as in the upper and lower part, no discontinuity data can be obtained.

The BTV model is of especially poor quality. Except for three faint traces segments at the depth of 289.5 meter, not much detail can be determined due to the use of drilling mud for stabilizing the borehole. The lowest of the three trace fragments in the west side of the borehole are maxima, and corresponds approximately with a maximum that can be observed on the BHTV data in the 270 degree direction at the same depth. Although this maximum and the discontinuity are relatively clear in the BHTV model, it has not been interpreted as such. Being able to compare the results of the different models would be helpful to identify discontinuities with more certainty.

The diameter of the core is smaller than that of the borehole itself, this means that the amplitude of the same fracture is larger on the BTV and BHTV plots. Small relative shifts of the measurements are also possible. It is most likely that the center of the core photo points towards the north.

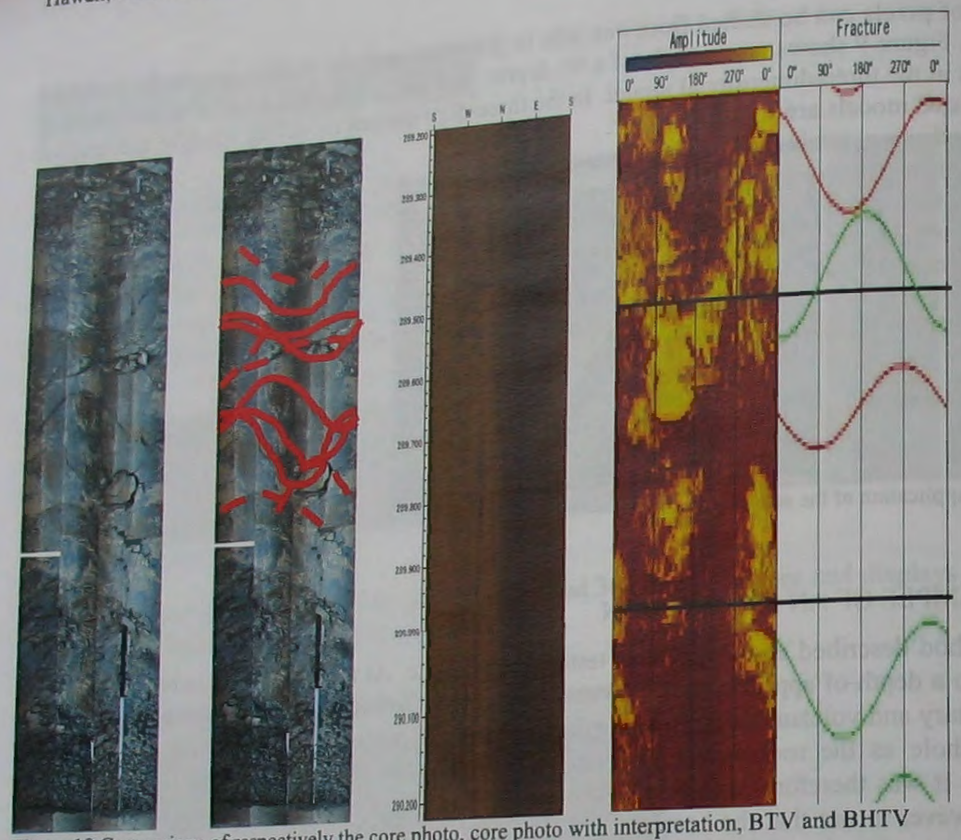


Figure 10 Comparison of respectively the core photo, core photo with interpretation, BTV and BHTV

After the core photo has been produced it is also possible to integrate the core picture in a three-dimensional model as is shown in figure 11. In this application the core can be investigated in three-dimensional space. Additionally it is possible to identify the location of fractures by clicking on three points belonging to the same discontinuity. The normal vector and location of each identified fracture is being written to a console from which the data can be copied to other applications. Simple planar fractures can usually be identified adequately from a two dimensional picture. Partial fracture traces, irregularly shaped fractures as well as fracture endings are much easier identified in a three-dimensional model. If a borehole is located close to other boreholes or underground structures, the three-dimensional can be used to investigate the relations between them which is impossible with two dimensional pictures only.
Although the three-dimensional model presented here has been developed as part of the borehole photography project, the method can be used with BTV or BHTV data as well.

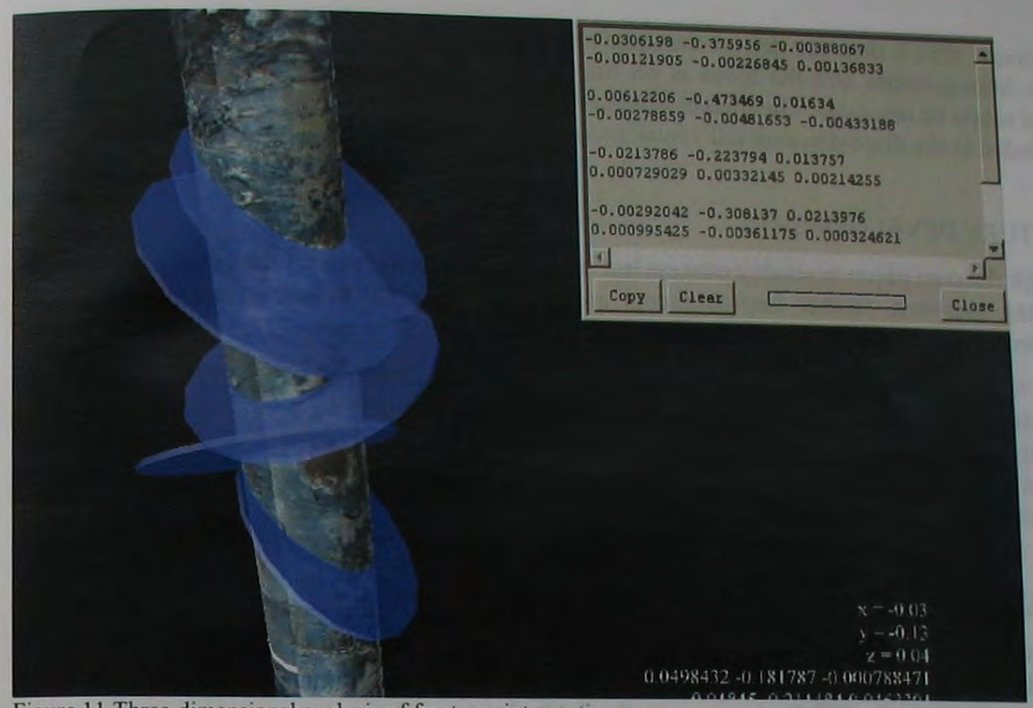


Figure 11 Three-dimensional analysis of fractures intersecting a core.

5. DISCUSSION

The core photo method can be applied in the field as has been shown in this paper. The method has its advantages and disadvantages.

Taking the core pictures from different directions is uncomplicated and can be done quickly in the field. In comparison with alternative methods (BTV, BHTV and core scanner) the costs of obtaining the data is low.

The level of detail of core photos is very high and can be used for a detailed evaluation of a core.

Having a detailed three-dimensional virtual model of the cores can reduce the amount of handling and storing of cores which is beneficial from an occupational safety and health, as well as a cost point of view.

The three-dimensional virtual model of the cores can be observed and investigated off-site.

The three-dimensional model is more intuitive for interpretation than two-dimensional pictures. By aggregating the data of several boreholes as well as additional data into the same model additional interpretation possibilities will be available.

In the current version of the ProBoring software the construction of the core photo from all partial photos is still a time consuming process and needs to be improved.

Some disadvantages are due to the use of the core as a method of characterizing the subsurface. Sections from where no core can be retrieved might be of particular interest for interpretation, reliable aperture measurements can not be obtained from cores, and cores might show fractures that have opened due to stress release and do not represent the situation at depth.

Alternative methods should therefore also be mentioned. If the cores are solid and clean, a core scanner might give better results. If no drilling mud is used, BTV measurements might be more

appropriate. BHTV does not deliver the same resolution as the core photo method. If however the rock is homogeneous and the focus is on finding the most important discontinuities only, the method might be adequate. The images obtained with these alternative methods can however also be included in the three-dimensional visualization part of the software.

6. FUTURE DEVELOPMENTS

Although the core photo assembly process has been greatly speed up with the development of the ProBoring software, further improvements are needed. Especially further automation of the fitting process is needed.

Several ideas to improve the three-dimensional model exist. Different boreholes can already be investigated in the same three-dimensional model. In following steps we would like to include the possibility to include additional data (e.g. tunnel, shaft, and excavation face data) as well as additional interpretation tools (e.g. delimitation of boundaries in three dimensions, identification of discontinuities, key-block analysis).

REFERENCES

1. Bruines, P., Y. Ohnishi, T. Nakai, S. Hanaoka, K. Kimura. 2006. Extension of the underground space information management system: maintenance and 3-D surfaces. *Proceedings of the 35th Symposium on Rock Mechanics*. p1-6.